

Investigations on suprathermal particles in the solar wind and Earth's magnetosphere

A thesis submitted in partial fulfilment of
the requirements for the degree of

Doctor of Philosophy

by

Bijoy Dalal

(Roll No. 19330006)



Department of Physics
Indian Institute of Technology Gandhinagar, Gandhinagar, India

2024

Under the guidance of

Prof. Dibyendu Chakrabarty

Space & Atmospheric Sciences Division

Physical Research Laboratory, Ahmedabad, India

Dedicated to
Chandan Da

Declaration

I declare that this written submission represents my ideas in my own words and where others' ideas or words have been included, I have adequately cited and referenced the original sources. I also declare that I have adhered to all principles of academic honesty and integrity and have not misrepresented or fabricated or falsified any idea/data/fact/source in my submission. I understand that any violation of the above can cause disciplinary action by the Institute and can also evoke penal action from the sources which have thus not been properly cited or from whom proper permission has not been taken when needed.

Bijoy Dalal
(Roll No: 19330006)

Certificate

I feel great pleasure in certifying that the thesis entitled "**Investigations on Suprathermal Particles in the Solar Wind and Earth's Magnetosphere**" by **Mr. Bijoy Dalal** has been carried out under my supervision and this work has not been submitted anywhere else for any degree or diploma.

Prof. Dibyendu Chakrabarty
(Thesis Supervisor)
(Space and Atmospheric Sciences Division)
Physical Research Laboratory
Ahmedabad-380009, Gujarat, India

Acknowledgements

This thesis could not have been completed without the help and support of the following individuals:

The first person who must be at the top of the list is my esteemed supervisor, Prof. Dibyendu Chakrabarty. I find in him the three most important qualities that a person should have in life: a friend to discuss any topic with, a philosopher who provides insightful arguments, and a guide who shows the right path. I feel privileged to have a mentor like him. I am immensely grateful for Prof. Chakrabarty's patience, motivation, enthusiasm, and extensive knowledge, which have been instrumental in navigating the ups and downs of my doctoral journey. His academic support has been indispensable, offering guidance at every stage of my research and thesis writing. I owe a great debt to him for his exceptional mentorship throughout my Ph.D. studies. His visionary outlook, dedication, and motivation have deeply inspired me. He has taught me not only valuable research methodologies but also the importance of presenting research findings clearly and effectively. He has been there beside me every step of my Ph.D. tenure.

I express my sincere gratitude to the members of my Doctoral Study Committee (DSC): Prof. Nandita Srivastava (USO, PRL, India), Prof. Santosh Vadawale (PRL, India), and Dr. Sanjay K. Mishra (PRL, India). They have always asked thought-provoking questions that helped me understand the topic of my research in a better way. Their insights, suggestions, and constructive criticisms have greatly enhanced the quality of this thesis. I have learned a lot regarding energetic particle detection by solid-state detectors from Prof. Vadawale. I feel privileged to work with Prof. Srivastava as a collaborator. Her insights and suggestions have always increased the quality of the work. I am very grateful to her for being so polite and affectionate with me. Dr. Mishra has helped me understand the physical significance of every piece of work I have done during the course of my Ph.D. I owe him a lot. I thank all the members of the Academic Committee for critically

reviewing my research progress throughout my research journey.

I am also thankful to Dr. Aveek Sarkar (PRL, India) and Prof. Christina M.S. Cohen (Caltech, USA) for their invaluable suggestions on my thesis work. Their inputs not only increased the quality of the work but also taught me how to extract meaningful insights from an analysis. I would like to continue working with them in the future as well.

I thank the principal investigators of ULEIS, EPAM, SIT, PALSTIC, MAG on board STEREO, SEPT, STEP, SEISS on board GOES satellites for their commitment to open data.

Being a part of the ASPEX team at PRL is indeed a great pleasure and privilege for me, thanks to my supervisor, Prof. Chakrabarty. I express my heartfelt gratitude to the ASPEX team for making me feel welcomed. Special thanks to Prof. Vadawale and Dr. Shiv Kumar Goyal for bearing with my numerous queries regarding the working of STEPS/ASPEX. They have always tried to answer my questions in befitting ways. I will always remember their contributions to my career.

During the course of my doctoral study, I got the opportunity to attend the Heliophysics Summer School-2023 both in online and in-person modes. The trip to Boulder, USA, to attend the in-person component of the summer school will be one of the most cherished memories of my life. I am grateful to UCAR Cooperative Programs for the Advancement of Earth System Science (CPAESS) for covering all the expenses of my trip to Boulder.

I am grateful to The Astrophysical Journal for waiving the publication charges of two articles, which are included in this thesis. Their contribution to my thesis is appreciable.

I express my gratitude to all the esteemed mentors from the SPASC division of PRL (Prof. D. Pallamraju, Prof. D. Chakrabarty, Prof. Lokesh Sahu, Prof. Som Kumar Sharma, Dr. Harish Gadhavi, Dr. R. P. Singh, Dr. T. A. Rajesh, Dr. A. Guharay, and Dr. N. Ojha) for teaching me the intricacies of space and atmospheric sciences during the coursework. I am also thankful to Dr. Arvind

Singh (PRL, India) for teaching me the concepts of statistics. I really enjoyed discussions with Dr. Arvind Singh regarding statistics, errors, MATLAB, etc. Thank you, Sir, for giving your valuable time. The writing course conducted by Dr. Umasankar Singh (IITGN, India) immensely helped me write scientific articles and this thesis. I sincerely acknowledge his contribution.

My sincere gratitude to Prof. Anil Bharadwaj, Director, PRL, for his kind support in various aspects related to academics, administration, research, etc. I am grateful to the Dean of PRL and the Registrar of PRL for supporting me in academic and administrative affairs during my Ph.D. tenure. I must acknowledge the contribution of Dr. Bhushit Vaishnav, Head of Academics at PRL, for motivating me to join the SPASC division. I thank him for shaping my career in the early stages of my Ph.D. I deeply appreciate the continuous support and provision of essential facilities by the staff members of PRL's Computer Center, Library, Administration, Accounts, Canteen, and CMG. Their dedication and efforts have been instrumental in creating a conducive research environment. I am also thankful to the PRL medical facility and Dr. Samir Dani and Dr. Sheetal Patel for their availability and assistance whenever needed. Their care and support have been invaluable during my time at PRL. Additionally, I extend my gratitude to the academic and administrative personnel of IITGN for their support and efficient handling of official formalities, which have significantly contributed to the smooth progress of my research endeavors.

I have enjoyed a lot during the trips of Science Express organized by PRL at various places. I cordially thank the concerning persons for giving me such opportunity.

The Space Weather Lab (Lab-651) has become my family for the last four years. I am indebted to my past (Kuldeep, Suman, Sumanjit, Yogesh) and present (Mitesh, Anil, Aaditya, Rahul, Ankit, Aakash, Jacob, Abhishek, Maanyash) lab mates and colleagues. Their presence in the lab has greatly enriched the vibrancy of the working environment. I am deeply grateful for the time we have spent together, the valuable interactions, and the unforgettable moments we have shared,

including the memorable parties. I have learnt great life lessons from my immediate senior (Yogesh) and super-senior (Ankit). I would like to express my heartfelt gratitude to them. Their guidance and support have been instrumental in my doctoral journey. Their unwavering encouragement, insightful feedback, and invaluable mentorship have significantly enriched my learning experience. Yogesh and Ankit have always been generous with their time, patiently answering my questions and offering suggestions from their own experiences. Their dedication to their work and their commitment to helping others have inspired me to strive for excellence. I am deeply thankful for their kindness, and I look forward to continuing to learn from their example. In addition to science and research, I have learnt how to keep balance in life from my lab-mates. Anil, Aaditya, and Rahul have taught me the ABCs of stock market and mutual funds. Jacob and Abhishek have been always ready to help me with any kind of technical issues I faced during the past two years. I am thankful to them for their time and kind cooperation. I am also grateful to my lab-mates for bearing with my rude behavior, at times, and making me feel welcomed with any queries related to life, finance, science etc.

I have learned to play volleyball and table tennis during my stay at PRL Hostel, Navrangpura. I am thankful to all the individuals with whom I have played these games and sports. Your enthusiasm and team spirit have not only made our matches enjoyable but have also significantly contributed to my personal growth and well-being. The lessons learned, the challenges faced together, and the victories celebrated have been invaluable. Your dedication and encouragement have been a source of inspiration, fostering a sense of community and resilience that I will always cherish. Thank you for making this journey memorable.

I am profoundly grateful to my batch mates (Gourav, Saurabh, Swagatika, Kimi, Ajayeta, Kshitiz, Santunu, Tanya, Vardaan, Soumya, Vineet, Birendra, Bharati, Rithvik, Yogesh, and Satyam) at PRL for their incredible support and camaraderie throughout our academic journey. Your kind gestures towards me are appreciable. I will always remember the memories we have shared. I am grateful to all my seniors (Sovan, Sunil, Subarana, Meghna) for the suggestions and

motivations during the course of my Ph.D. at PRL. I am thankful to my juniors (Kamran, Dharmendra, Mansi, Akanksha, Debasis, Gurucharan, Harithasree, Kiran, Komal, Nitin, Aakash, Sandip, Shivam, Ankita, Harsh) for their unwavering support and camaraderie, which have made this PhD journey more enjoyable and fulfilling.

I would not have reached this position without the kind help of all my teachers. My heartfelt reverence goes to all of them. Their contributions to my upbringing, building concepts of science, and developing my moral character are immense. I have learned many important life lessons in addition to academic subjects from them. These lessons have always helped me make decisions in critical situations throughout my life. The seed of curiosity sown by them in my mind during my school days has driven my academic journey up to this level and will continue to motivate me in the future.

The person who has always been a source of motivation for my studies is my beloved sister, Rupali. Despite not having a chance for higher education, she has always pushed me to study hard. Her affection, dedication to my studies and personal growth, and care have encouraged me to excel in my studies. Without her support, I could not have reached this level. I express my sincere gratitude to my sister for being so kind to me. My brother-in-law has also motivated me in every aspect of life. I thank him for his care and encouragement. I express my warm love and affection to my niece, Prerana and my nephew, Probuddha. They have always made me feel special and happy.

The most important person whose contribution to my studies is indispensable is Chandan Da. He stood behind me when I found it difficult to continue my studies in the early days of my schooling due to various reasons. He not only taught me himself but also bore all the expenses for my education up to high school. He has always motivated me to overcome all odds in my life. I sincerely dedicate this thesis to him.

I am indebted to my mother for all her care, affection, and love. I know how much pain she has suffered to bring up me and my sister.

Last but not least, I would like to express my sincere gratitude to all the individuals who have helped me in my research and personal well-being. Without your help, I could not have succeeded in overcoming the challenges during my research journey. Thank you all for your kind support.

Abstract

Suprathermal particles/ions (with energies in the range of $\sim 0.01 - 1.0$ MeV per nucleon) are ubiquitous in the heliosphere. Unlike solar wind particles, suprathermal particles are non-thermal and exhibit inverse power law distributions. These particles are essentially the bridge between solar wind (< 3.0 keV) and solar energetic particles (SEPs) with energies from hundreds of keV per nucleon to hundreds of MeV per nucleon. A clear distinction between solar wind and suprathermal particles in the lower energy side is often difficult to establish. The same is true for the upper limit of energies where suprathermal particles and SEPs overlap. Presence of suprathermal particles is observed even in the absence of any transient solar events (i.e., during quiet times) like coronal mass ejections (CMEs); solar flares etc., and this suggests that these particles originate from a pool of ions in the interplanetary (IP) medium. Enhancements in fluxes of these particles are observed during passages of interplanetary CMEs (ICMEs); stream/corotating interaction regions (SIRs/CIRs) etc. It is believed that suprathermal ion pool supplies the seeds for further acceleration in IP shocks to eventually produce SEPs. Suprathermal particles are also observed to propagate towards the Sun. Planetary bow shocks, forward and reverse shocks associated with SIR/CIRs are some of the sources of these sunward propagating particles. Despite studies in the past, the sources and energization processes of suprathermal particles are poorly understood till date. Earlier studies reported a “universal” spectral index (slope of differential directional flux vs energy spectra) of 1.5 as one of the characteristic features of quiet time suprathermal particles. However, recent observations seem to suggest that this is violated on many occasions. This thesis provides a detailed understanding on the generation and modulation of these particles during quiet IP conditions, passage of SIRs, upstream of the terrestrial bow shock, and the impact of IP suprathermal particles on the energetic particle environment in the terrestrial magnetosphere.

In quiet times, fluxes of different suprathermal particles (i.e., different species) are observed to vary with solar cycles (nearly 11-year cycle in the sunspot numbers) with noticeable lags (i.e., time delay between sunspot number variation and the flux variation) of the order of a year or two, as observed from the L1 point

measurements. Correlation between suprathermal fluxes with the sunspot number reveals that solar processes inject suprathermal particles in the IP medium. Lags in suprathermal fluxes with respect to the sunspot number essentially suggest that these particles wander and are accelerated in the IP medium. One of the major outcomes of the thesis is the determination of differential lags of suprathermal ^4He and Fe in solar cycle 24. While ^4He exhibits negative lags (meaning higher fluxes of ^4He corresponding to lower number of sunspot), Fe does not show any lag with respect to the sunspot number in solar cycle 24. Differential behavior of ^4He and Fe is also observed in the spectral indices of these elements in solar cycle 24. In addition, similar variations in lags and spectral indices are observed for C and O fluxes. Keeping in mind the contrasting first ionization potential (FIP) and different mass-to-charge ratio (m/q) of ^4He and Fe, it is argued that the long-term modulation of suprathermal particles in the IP medium depends on FIP and m/q of species. The similar behaviors of C and O (having similar FIP and m/q) seem to support this proposition. The spectral indices of quiet time suprathermal particles are observed to vary in the range ~ 1.5 – 2.6 . Therefore, the thesis suggests that the “universal” spectral feature of suprathermal particles does not seem to hold good on most of the occasions. Instead, it appears that there is mixing of particles from different sources in the quiet time suprathermal ion pool.

Enhancements in suprathermal particles are observed during the passage of SIR/CIR events even when there are no well-formed forward and reverse shocks at 1 AU. Some past studies suggested the compressed interaction regions as possible particle accelerators. In this thesis, it is shown that the spectral indices of ^4He , O, and Fe during shock-less SIR/CIR events vary in the range ~ 1.5 – 4.5 . There could be many factors that contribute to such wide variation in the spectral indices of SIR-associated suprathermal ions. It is conjectured that mixing of seed populations, stochastic nature of acceleration mechanism, and difference in compressional characteristics might lead to this variation. Interestingly, softer spectra (i.e., higher spectral indices) than quiet times are observed in SIR-associated suprathermal particles, the reason for such behavior is still unknown. No systematic dependence of spectral indices of ^4He , O, and Fe on m/q of species is observed. A special event is also identified when ^4He , O, and Fe exhibit almost identical spectral indices very close to 1.5. On further investigations, it is found

that merging and contraction of small-scale magnetic islands near the spacecraft at 1 AU might energize these particles and produce nearly equal spectral indices regardless of m/q of elements. This also suggests that suprathermal particles associated with SIRs can get accelerated locally in the IP medium.

Suprathermal particles upstream of the Earth's bow shock sometimes get enhanced for very short (1–2 hour) periods. These are called upstream events. These particles generally exhibit softer spectra during the events. In this chapter, it is shown that a systematic modulation in the spectra of upstream ions is observed at the Sun-Earth first Lagrange point (L1) depending on the m/q of different species, when compared with the spectra of incoming solar wind suprathermal ions. It is noticed that for most of the events, a radial magnetic field that connects the satellite (at L1) with the bow shock is an important condition for detecting these upstream events. In the presence of radial magnetic fields, cross-field diffusion of ions increases with increasing m/q of ions. Therefore, lighter particles (say, H) reach the spacecraft from the bow shock in a focused manner. On the other hand, heavier ions (say, CNO) get mixed up with different sources of suprathermal ions and exhibit relatively harder spectra very similar to the solar wind suprathermal particles. Contribution of heavier ions having solar wind origin in the upstream events is also reflected in the abundance ratio of heavier ions.

Geomagnetic storms are generally observed with varying intensities during the passage of ICMEs past the Earth's location. High energy SEPs (> 10 MeV) associated with ICMEs can penetrate the terrestrial bow shock/magnetopause and affect the energetic particle environment in the terrestrial magnetosphere. In this thesis, by using the measurements by the Aditya Solar wind Particle EXperiment (ASPEX) payload on board the Aditya-L1 mission of India, it is shown that the suprathermal ions and the low energy SEPs (< 2 MeV) can also affect the particle environments of magnetosphere and magnetosheath region if the original SEP spectra at the Sun-Earth L1 point are hard. More importantly, it is demonstrated that although "stealth" CMEs can affect the Earth's magnetosphere geomagnetically similar to typical CMEs, the "stealth" CMEs do not seem to modulate the energetic particle environment of the magnetosphere. Therefore, this work suggests that the space assets in the magnetosphere are at risk when an energetic particle detector detects harder spectra at L1.

Overall, this thesis gives a comprehensive view on the sources and acceleration mechanisms of suprathermal particles in the IP medium and in the terrestrial magnetosphere. It also underscores the importance of multi-point, multi-directional, species-separated observations combined with physics-based modeling to decouple different processes.

Keywords: Solar wind, Solar Energetic Particles (SEPs), Interplanetary Coronal Mass Ejections (ICMEs), Solar cycle, Solar flares, Stream/Corotating Interaction Regions (SIR/CIRs), Bow shock, Magnetosphere.

List of Abbreviations and Acronyms

Abbreviation	Definition
3DP	Three-Dimensional Plasma and Energetic Particle Investigation
ABI	Advanced Baseline Imager
ACE	Advanced Composition Explorer
ACIS	Advanced CCD Imaging Spectrometer
ACR	Anomalous Cosmic Rays
AIA	Atmospheric Imaging Assembly
AL1	Aditya-L1
ASPEX	Aditya Solar wind Particle EXperiment
AU	Astronomical Unit
CC	Correlation Coefficient
CCD	Charge-coupled Device
CIR	Corotating Interaction Region
CME	Coronal Mass Ejection
CRIS	Cosmic Ray Isotope Spectrometer
DC	Direct Current
DSA	Diffusive Shock Acceleration
EPACT	The Energetic Particles: Acceleration, Composition, and Transport
EPAM	Electron, Proton and Alpha Monitor
ESP	Energetic Storm Particle
EXIS	Extreme Ultraviolet and X-ray sensors
FIP	First Ionization Potential
FOV	Field of View
GCR	Galactic Cosmic Ray
GEO	Geosynchronous Earth Orbit
GLM	Geostationary Lightning Mapper
GOES	Geostationary Operational Environmental Satellites
GSE	Geocentric Solar Ecliptic
GSEP	Gradual Solar Energetic Particle
HCS	Heliospheric Current Sheet
HEL1OS	High Energy L1 Orbiting X-ray Spectrometer
ICME	Interplanetary Coronal Mass Ejection
IMF	Interplanetary Magnetic Field

IMPACT	In-situ Measurements of Particles and CME Transients
IP	Interplanetary
ISEP	Impulsive Solar Energetic Particle
ISRO	Indian Space Research Organization
LASCO	Large Angle and Spectrometric Coronagraph Experiment
LEMS	Low Energy Magnetic Telescope
MAG	Magnetometer
MFI	Magnetic Field Investigation
MHD	Magnetohydrodynamic
MoE	Margin of Error
MPSH	Magnetospheric Particle Sensor High energy
NASA	National Aeronautics and Space Administration
NP	North Pointing
NOAA	National Oceanic and Atmospheric Administration
PAPA	Plasma Analyzer Package for Aditya
PLASTIC	PLAsama and SupraThermal Ion Composition
PS	Parker Spiral
PSD	Phase Space Density
RTN	Radial Tangential Normal
RTSW	Real-Time Solar Wind monitors
SC	Solar Cycle
SDA	Shock Drift Acceleration
SDO	Solar Dynamics Observatory
SE	Standard Error
SECCHI	Sun Earth Connection Coronal and Heliospheric Investigation
SEISS	Space Environment In Situ Suite
SEP	Solar Energetic Particle
SEPICA	Solar Energetic Particle Ionic Charge Analyzer
SEPT	Solar Electron and Proton Telescope
SIR	Stream Interaction Region
SIT	Suprathermal Ion Telescope
SIS	Solar Isotope Spectrometer
SMI	Small-scale Magnetic Island
SMS	Solar Wind and Suprathermal Ion Composition Experiment
SOHO	Solar and Heliospheric Observatory

SoLEXS	Solar Low Energy X-ray Spectrometer
SSN	Sun Spot Number
STEP	Suprathermal Energetic Particle instrument
STEPS	SupraThermal Energetic Particle Spectrometer
STEREO-A, B	Solar Terrestrial Relations Observatory-Ahead, Behind
SUIT	Solar Ultraviolet Imaging Telescope
SUVI	Solar Ultraviolet Imager
SWE	Solar Wind Experiment
SWEPAM	Solar Wind Electron, Proton and Alpha Monitor
SWICS	Solar Wind Ion Composition Spectrometer
SWIMS	Solar Wind Ion Mass Spectrometer
SWS	Solar Wind Sector
TGRS	Transient Gamma-Ray Spectrometer
TOF	Time of Flight
ULEIS	Ultra Low Energy Isotope Spectrometer
UV	Ultra-violet
VELC	Visible Emission Line Coronagraph
WAP	Suprathermal Ions Wide-Angle Partition Sector
WAVES	Radio and Plasma Wave Investigation

Contents

Acknowledgements	ix
Abstract	xv
Abbreviations	xix
Contents	xxiii
List of Figures	xxvii
List of Tables	xxix
1 Introduction	1
1.1 Energetic particles in the heliosphere	1
1.1.1 Galactic cosmic rays (GCRs)	2
1.1.2 Pick-up ions and anomalous cosmic rays (ACRs)	3
1.1.3 Solar energetic particles (SEPs)	3
1.1.4 Stream interaction regions (SIRs) and associated energetic particles	6
1.1.5 Suprathermal particles	9
1.1.6 Particles upstream of the Earth's bow shock	11
1.1.7 Particles in the Earth's magnetosphere	12
1.2 Sources and sinks of suprathermal particles	12
1.3 Particle acceleration mechanisms	13
1.3.1 Fermi acceleration	14
1.3.2 Acceleration of particles by shocks	16
1.3.3 Particle acceleration by gradual compression regions	21
1.3.4 Pump mechanism	22
1.3.5 Particle acceleration by merging and contraction of magnetic islands	24
1.4 Aim and overview of the thesis	28
2 Instruments, datasets, techniques	31
2.1 Some useful parameters and concepts	31
2.1.1 Parameters related to suprathermal particles	32
2.1.2 Statistical concepts	33
2.2 Instruments	34

2.2.1	Advanced Composition Explorer (ACE)	35
2.2.2	Wind	35
2.2.3	Solar-Terrestrial Relations Observatory (STEREO)	36
2.2.4	Geostationary Operational Environmental Satellites (GOES)- 16, 18	37
2.2.5	Aditya-L1	38
2.3	Measurement techniques	40
2.3.1	Total energy measurement in a solid-state detector	40
2.3.2	Time-of-flight and residual energy measurement technique	42
2.3.3	Top hat analyzer (THA): PLASTIC	44
2.3.4	Tri-axial fluxgate magnetometer: MAG	45
2.4	Data sources	47
2.5	Catalogues	47
2.6	Data used in different thesis chapters	48
2.6.1	Chapter 3	48
2.6.2	Chapter 4	48
2.6.3	Chapter 5	49
2.6.4	Chapter 6	49
3	Quiet time suprathermal particles	51
3.1	Introduction	52
3.2	Data used	55
3.3	Identification scheme for the “quiet” periods	55
3.4	Results	58
3.4.1	Cross-correlation analysis (SSN vs. Flux) and sensitivity analysis for the choice of lags	58
3.4.2	Variations in spectral indices of different elements at differ- ent phases of solar cycles	63
3.5	Discussions and conclusions	70
3.6	Key findings	77
4	SIR-associated suprathermal particles	79
4.1	Introduction	80
4.2	Data used	82
4.3	Selection of events	82
4.4	Spectral analysis	85
4.5	Discussions and conclusions	88
4.6	Key findings	99
5	Upstream energetic ions	101
5.1	Introduction	102
5.2	Data used and instrumentation	105
5.3	Selection of upstream events and method	107
5.4	Results	110
5.5	Discussions and conclusions	112
5.6	key findings	117

CONTENTS

6	First observations by STEPS/ASPEX	119
6.1	Introduction	120
6.2	Data used and instrumentation	123
6.3	Observations	123
6.4	Discussions and conclusions	132
6.5	Key findings	137
7	Summary and Future plans	139
7.1	Summary	139
7.2	Future works	141
	Bibliography	143
	List of Publications	169
	Publications Attached with Thesis	173

List of Figures

1.1	Different types of energetic particles in the heliosphere	2
1.2	Gradual and impulsive SEPs	4
1.3	Schematic diagram of two SIR events	7
1.4	Kappa distribution	10
1.5	Sources and sinks of suprathermal particles	13
1.6	Oxygen fluences vs energy	14
1.7	Schematic for shock jump conditions	17
1.8	Schematic of quasi-parallel and quasi-perpendicular shocks	19
1.9	Schematic for pump mechanism	23
1.10	Magnetic islands in the ripples of heliospheric current sheet	26
1.11	Merging of magnetic islands	26
2.1	Deposited and transmitted energy of proton vs proton's incident energy in Si	41
2.2	Schematic of SIT instrument	43
2.3	Schematic of PLASTIC instrument	45
2.4	Working of fluxgate magnetometer	46
3.1	Method of quiet time selection	56
3.2	Comparison between original and quiet suprathermal fluxes	57
3.3	Solar cycle variations of suprathermal particles	59
3.4	Method describing the estimation of correlation coefficients and lags	60
3.5	Variations of Pearson's CCs with averaging windows	61
3.6	Variations of lags with averaging windows	62
3.7	Variations of Pearson's CCs for 4 sets of cut-off fluxes	66
3.8	Variations of lags for 4 sets of cut-off fluxes	69
3.9	Phases of SC 23 and 24	70
3.10	Spectra of suprathermal particles corresponding to different phases of solar cycles	71
3.11	Comparisons between spectral indices	72
4.1	Sample figures of SIR-associated suprathermal flux enhancements	84
4.2	Spectra of ^4He during all the SIR events	86
4.3	Spectra of O	87
4.4	Spectra of Fe	88
4.5	Locations of STEREO-A and STEREO-B	89
4.6	Comparisons of two SIR events observed by both STEREO-A and STEREO-B	90

4.7	A coronal hole and solar flare observed by SECCHI in 19.5 nm . . .	93
4.8	magnetic connectivity between flare location and STEREO-A . . .	94
4.9	Detailed investigation of SIR-12	96
4.10	Hodograms of IMF showing presence of magnetic islands	97
5.1	Variations in H, ^4He , and CNO fluxes corresponding to upstream event 31	108
5.2	Variations in H, ^4He , and CNO fluxes corresponding to upstream event 1	109
5.3	Spectra of H, ^4He , and CNO during upstream event No. 31	111
5.4	Comparisons of spectral indices from the "Sun sector" and "bow shock sector"	113
5.5	Comparisons of $^4\text{He}/\text{H}$ and CNO/H ratios from the "Sun sector" and "bow shock sector"	114
6.1	First observations from STEPS/ASPEX	123
6.2	Positions of AL1 at different intervals	126
6.3	Orientations of PS and NP detector units of STEPS	129
6.4	Comparisons of ion and proton fluxes corresponding to ICME-1 and ICME-3	131
6.5	Variations of ion and proton fluxes along with solar wind parameters corresponding to two "stealth" CMEs	133
6.6	Variations of ion and proton fluxes along with solar wind parameters corresponding to two typical CMEs	135
6.7	Comparisons between ion and proton fluxes corresponding to "stealth" and typical CMEs	136

List of Tables

2.1	Instruments providing suprathermal flux data	39
4.1	List of SIR events and spectral indices of ^4He , O, and Fe	83
5.1	List of upstream events and flux ratios	107
6.1	List of spectral indices at various intervals	128

Chapter 1

Introduction

1.1 Energetic particles in the heliosphere

The Sun is an ordinary star that moves in the Milky Way along with the solar system. Being a hot ball of plasma, it possesses its own magnetic field. The typical temperature of the visible disk (photosphere) is ~ 5800 K. Surprisingly, the temperature of the Sun's upper atmosphere, called the corona, is of the order of 10^6 K (Alfvén, 1941). How the solar corona is heated to such a high temperature is an ongoing topic of research. The solar corona is considered as the source of supersonic plasma flow from the Sun, which is known as solar wind (Parker, 1965). The major constituents of solar wind are protons, electrons, and doubly ionized helium (i.e. alpha particles). Other heavy elements form a very small fraction of the solar wind ions in terms of abundance. Solar wind carries the Sun's magnetic field into the interplanetary (IP) space. The Sun, with the help of solar wind and interplanetary magnetic field (IMF), creates a bubble in the interstellar medium, which is called the heliosphere. In addition to the solar wind ions, there exists several types of energetic ions in the heliosphere. Throughout the thesis, the words "ions" and "particles" are used interchangeably to mean the positively charged species, distinguishing those from electrons. The origin and characteristics of these energetic ions are different. Figure 1.1 gives a schematic of different types of ions available in the heliosphere. There are galactic cosmic rays (GCRs), anomalous cosmic rays (ACRs), solar energetic particles (SEPs), suprathermal and energetic particles associated with stream/corotating interaction regions (SIR/CIRs) etc.

in the interplanetary (IP) medium. Although this thesis deals with suprathermal particles (with energies ≤ 1 MeV), each type of energetic ion in the heliosphere is discussed briefly in the following section for the sake of completeness.

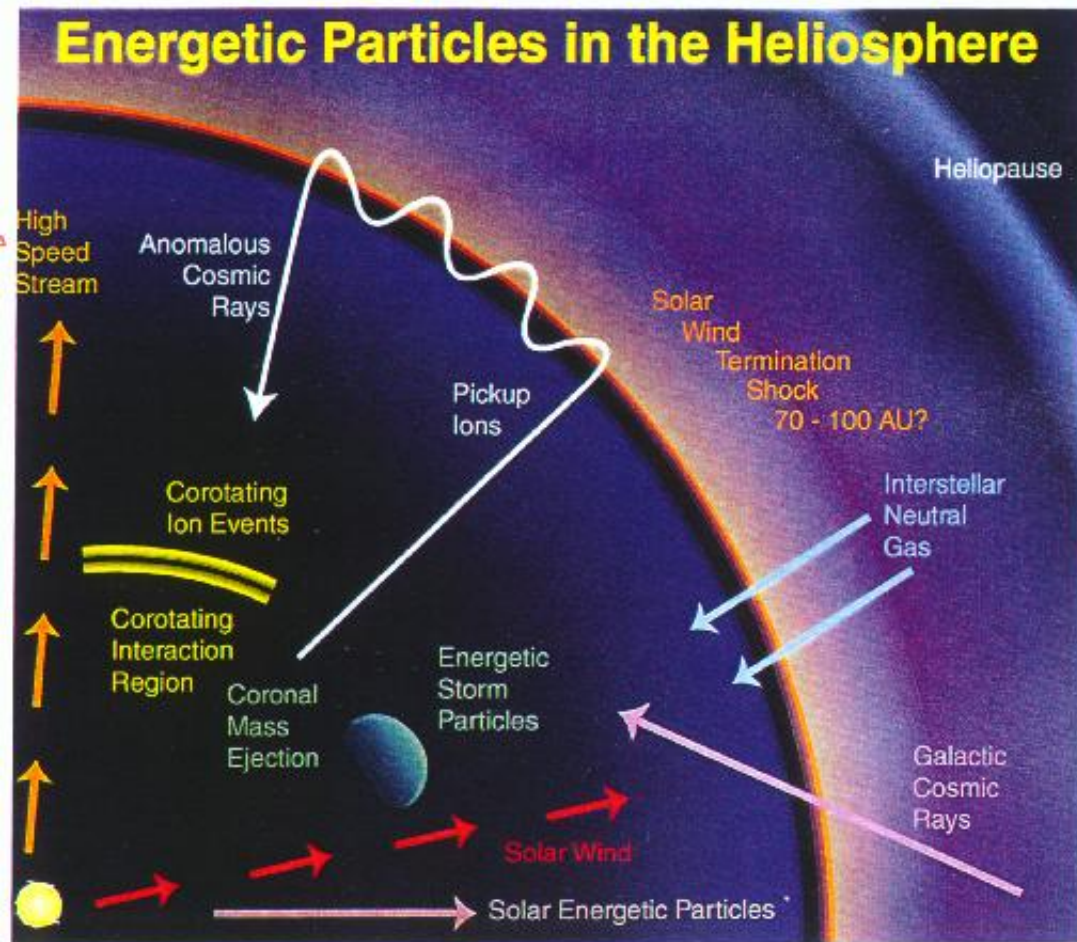


Figure 1.1: Different types of energetic particles and their possible source regions (taken from [Stone et al., 1998c](#)).

1.1.1 Galactic cosmic rays (GCRs)

Galactic cosmic rays (GCRs) are very high energetic (10^8 – 10^{15} eV) ions, generally accelerated by supernovae shocks ([Diehl et al., 2001](#); [Hillas, 2006](#); [Aharonian et al., 2011](#); [Fu et al., 2021](#); [Baral et al., 2023](#) etc.). Shocks and relevant particle acceleration mechanisms are discussed later in this chapter. Protons, heavier ions, and electrons are the major constituents of GCRs. The interface between the he-

liosphere and the interstellar medium filters out most of these ions. The remaining ions form a constant background of GCRs in the heliosphere (e.g., [Rahmanifard et al., 2020](#)). Omnidirectional fluxes of GCRs are observed to vary as power law of energy and the spectral index (γ) is 2.6.

1.1.2 Pick-up ions and anomalous cosmic rays (ACRs)

Interstellar neutral particles enter the solar system due to the relative motion between the solar system and the interstellar medium ([Frisch, 1996](#); [Giacalone et al., 2012](#)). These neutrals gain energy by dropping into the gravitational well of the Sun. These get ionized by interaction with solar wind particles and extreme ultra-violet radiations in the IP medium. These singly ionized ions are picked up finally by the solar wind magnetic field ([Fisk et al., 1974](#)). The so formed pick-up ions typically have energies four times that of solar wind ions and traverse outward with the solar wind. These are thought to be further accelerated to very high energies (~ 100 MeV) by the termination shock of the heliosphere ([Pesses et al., 1981](#)). Due to the presence of these particles and also due to the modulation of GCRs in the heliosphere, the extrapolation of GCR power law (with spectral index of 2.6) to lower energies is mediated by an “anomalous” increase of particle populations peaking around 100 MeV ([Giacalone et al., 2012](#)). This is why these high energy particles are called anomalous cosmic rays (ACRs).

1.1.3 Solar energetic particles (SEPs)

The lions’ share of the energetic particle intensities in the IP medium originates from the Sun or is related to the processes occurring in the heliosphere. SEPs are primarily of two types: gradual SEPs (for a comprehensive review, see [Desai and Giacalone, 2016](#)) associated with interplanetary coronal mass ejections (ICMEs) and impulsive SEPs ([Reames, 2018a](#)) associated with solar flares ([Reames, 1999a, 2013](#)). The characteristics and compositions of these two types of SEP are distinguishably different. Figures 1.2a and b show schematics of the sources of gradual and impulsive SEPs along with longitudinal extends of the interplanetary magnetic

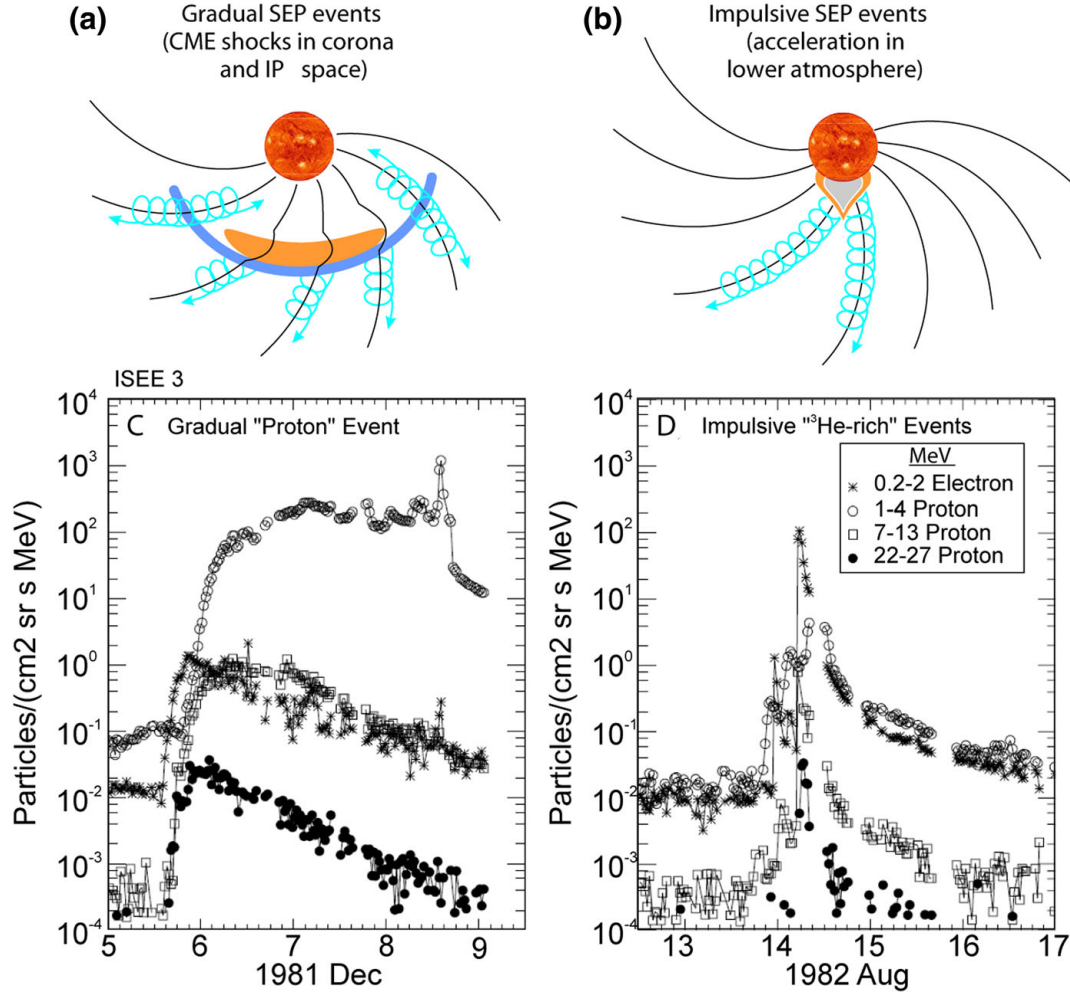


Figure 1.2: Two different classes of SEPs – (a) gradual SEPs from large-scale CME driven shock that accelerate SEPs along IMF over a wide longitudinal regions and (b) impulsive SEPs along IMF over narrow longitudinal region and well connected to a solar flare location. Panel (C) shows variations in the proton fluxes at different energies during a gradual SEP event. Variations in high-energy electron and proton fluxes during a ^3He -rich impulsive SEP event are plotted in panel (D). This figure is taken from [Desai and Giacalone \(2016\)](#) and was originally published in [Reames \(1999b\)](#).

field (IMF) lines populated with these particles, respectively. Impulsive SEPs is generally observed when an observer is magnetically connected to the source location. On the other hand, due to their vast longitudinal spread, gradual SEPs can be detected to a greater extent in the IP medium. Variations in energetic electrons and protons during gradual and impulsive SEP events are shown in Figures 1.2C and D, respectively. The gradual and impulsive variations of electron proton

1.1. ENERGETIC PARTICLES IN THE HELIOSPHERE

fluxes are clear in these figures. Gradual and impulsive SEPs also carry their typical compositional signatures. For example, ${}^3\text{He}/{}^4\text{He}$ shows more than 1000 times enhancement in the impulsive SEPs as compared to the solar wind ${}^3\text{He}/{}^4\text{He}$, which is $\sim 5 \times 10^{-4}$. The increased Fe/C and Fe/O ratios (~ 1) provide a more stable indicator of impulsive SEP. In addition, 1000-fold increases in elements with $76 < Z < 82$ are also observed in many impulsive SEP events (Reames, 2018a). Most importantly, impulsive SEPs are electron rich (Cane et al., 2002). Another important property of the impulsive SEPs is the higher ionization states of heavy elements compared to the normal solar wind ionization states of heavy elements. For example, the ionization state of Fe sometimes goes up to ~ 20 , indicating a temperature of ~ 10 MK in the source region (Klecker et al., 1984; Luhn et al., 1987). On the contrary, gradual SEPs are proton-rich and have Fe/O ratios ~ 0.1 . The mean ionization states of Fe observed in gradual SEPs vary in the range ~ 10 – 14 (Luhn et al., 1984; Reames, 1999a). In addition, it was assumed that ${}^3\text{He}/{}^4\text{He}$ ratios in large SEP events are similar to those of the solar wind. However, after the launch of NASA’s Advanced Composition Explorer (ACE, Stone et al., 1998c) in 1997, the scenario has changed. It is reported by Mason et al. (1999) that the ~ 1 MeV per nucleon (MeV n^{-1}) ${}^3\text{He}/{}^4\text{He}$ ratios are enhanced by factors of ~ 5 – 140 over their solar wind values in many large gradual SEP events. Many authors (Cohen et al., 1999; Wiedenbeck et al., 2000; Torsti et al., 2002) also reported enhancement in ${}^3\text{He}$ above 5 MeV n^{-1} . Not only ${}^3\text{He}$, the Fe / O ratios and the mean ionization states of Fe are also observed to be enhanced in many large gradual events. These observations hint towards the mixing of flare particles with the gradual events. In fact, Reames (2020) described four pathways of SEP production based on element abundance patterns:

1. SEP1: ions accelerated in the islands of magnetic reconnection in solar jets with 1000-fold enhancements in ${}^3\text{He}/{}^4\text{He}$.
2. SEP2: ions produced in jets and subsequently accelerated by CME-driven shocks along with excess amount of energetic protons.
3. SEP3: remnant ions from previous impulsive events and accelerated by

CME-driven shocks

4. SEP4: ions accelerated by extremely strong CME-driven shocks from the ambient coronal plasma

It is clear from the above discussions that IP shocks associated with interplanetary coronal mass ejections (ICMEs) produce gradual SEPs from various background plasmas, like suprathermal tails of the solar wind (Gosling et al., 1981; Desai et al., 2003), remnant flare particles (e.g., Tsurutani and Lin, 1985; Tan et al., 1989). Not only CME-driven shocks, there is another kind of large-scale structure that is sometimes associated with energetic particles at 1 AU.

1.1.4 Stream interaction regions (SIRs) and associated energetic particles

Solar wind generally shows a bimodal distribution in speed - slow solar wind (300-500 km/s) and fast solar wind (600-900 km/s). A stream interaction region (SIR) is formed when a stream of fast solar wind, originated from a coronal hole, interacts in the IP medium with a preceding slow solar wind stream emanated typically from the streamer belt (Belcher and Davis Jr, 1971). A compression region is created due to this interaction, which rotates with the Sun and forms an Archimedean spiral. Coronal holes, sometimes, persist for several solar rotations leading to co-rotation of the interaction regions more than one solar rotation period (Carrington rotation of period ~ 27 days). These structures are then called corotating interaction regions (CIRs). The schematic in Figure 1.3 (taken from Richardson, 2018 and originally published by Belcher and Davis Jr, 1971) shows two SIRs corotating with the Sun, as viewed from above the north pole of the Sun. The typical variations in the in-situ solar wind parameters are also shown in the same figure.

Recurrent enhancements of energetic particles with energies > 1 MeV n^{-1} were observed first almost six decades ago (e.g., Bryant et al., 1965; Wilcox and Ness, 1965 etc.). Some of the initially observed properties of these energetic particles

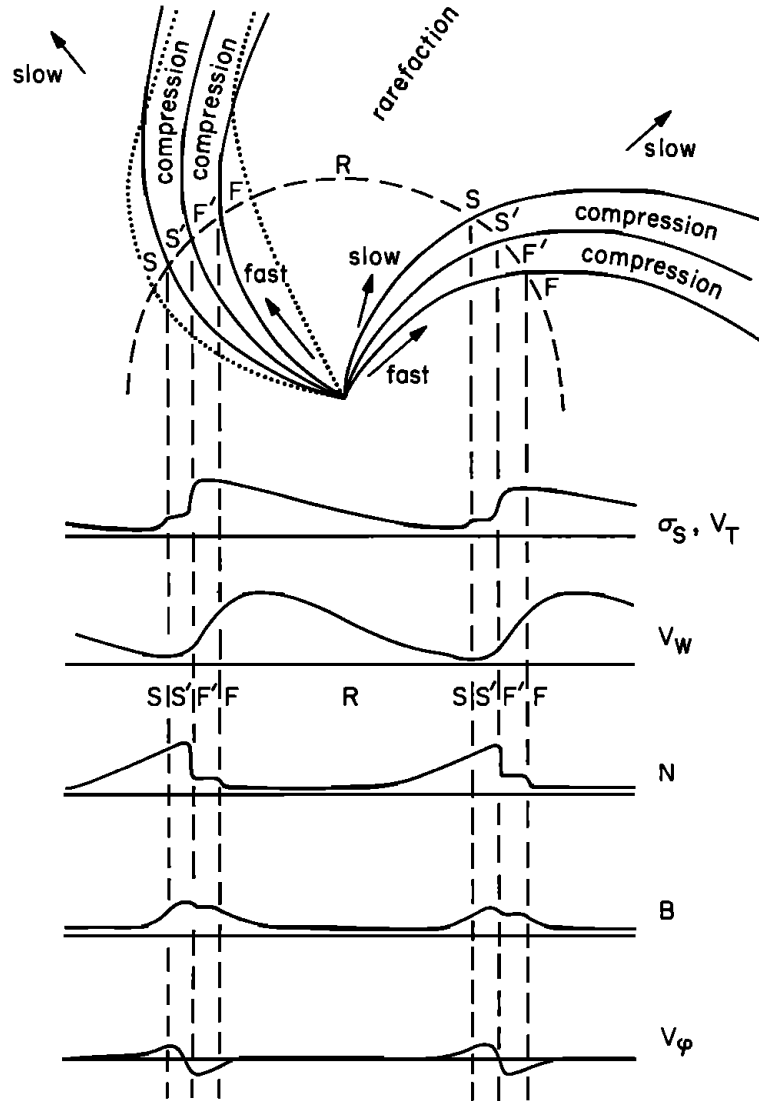


Figure 1.3: Schematic diagram of two SIRs and associated variations in some in-situ plasma parameters at 1 AU. Here, V_T is thermal speed, σ_s represents level of fluctuation in magnetic field, V_W is the solar wind speed, N is the density, B is magnetic field intensity, and V_ϕ is the transverse component of the solar wind velocity. Region S indicates the unperturbed slow solar wind, S' is the region of compressed and accelerated slow solar wind, F' is the compressed and decelerated fast solar wind, and F represents the unperturbed fast solar wind. R represents the rarefaction region after the compressed interface (S'-F'). Dotted lines show the magnetic field lines corresponding to slow and fast solar wind. This image is adapted from Richardson (2018) and was originally published by [Belcher and Davis Jr \(1971\)](#).

include occurrence regardless of solar events or high activity, few hours' of rise and decay times, dispersionless onset of the events, softer and similar spectra at the

onset and event maximum, and weak directional anisotropies. The Pioneer observations (McDonald et al., 1976; Barnes and Simpson, 1976; Kunow et al., 1976; Van Hollebeke et al., 1978; Vanhollebeke et al., 1979; Christon and Simpson, 1979) revealed that these energetic particle events tend to peak near the stream interaction regions and adjacent to the forward and reverse shocks at the leading and trailing edges of the interaction regions, respectively. Van Hollebeke et al. (1978) reported that the peak intensities of SIR events occur at a few AU. Solar origin of these particles was ruled out because of the declining trend in the intensities of these particles towards the Sun. Evidence of particles streaming towards the Sun supports this argument (Marshall and Stone, 1978; Mewaldt et al., 1978; Van Hollebeke et al., 1978; Christon, 1981; Zwickl and Roelof, 1981; Richardson, 1985; Richardson et al., 1993).

To explain the origin of sunward streaming particles in association with SIRs, Fisk and Lee (1980) proposed a model for particle acceleration by reverse shocks adjacent to the fast solar wind streams of the SIRs beyond 1 AU. According to this model, at 1 AU, particle spectra below several 100 keV should show a roll-over if these particles are accelerated beyond 1 AU. This reflects the effect of adiabatic deceleration of low energy particles in the expanding solar wind.

By analyzing 41 SIR events Mason et al. (2008b) showed that the abundances (with respect to O) of energetic particles associated with SIRs are similar to that of solar wind, in particular, fast solar wind. These authors found relatively higher abundances of He and Ne. In addition, their work suggests that the source populations of SIR-associated energetic particles do not directly come from the Sun. Later, Mason et al. (2012) shows that Fe/O ratio in SIR events follows solar cycle in 1997–2012. This indicates that Fe-rich remnant flare particles contribute to the source populations for SIR events. Enhancement in ^3He in these events (Mason et al., 2008b) also suggests this proposition. Some works reported presence of interstellar pick-up ions at 1AU during SIR events (Hilchenbach et al., 1999; Chotoo et al., 2000). However, by analyzing charge states of SIR associated energetic particles Möbius et al. (2002) and Mazur et al. (2002) independently concluded that

majority of the ions have similar charge states to that of the solar wind ions.

1.1.5 Suprathermal particles

So far, all the types of particles mentioned in Figure 1.1 have been discussed. Except for GCRs, all the other types of energetic particles have a common connection, in terms of either source or pool, to suprathermal populations in the solar wind. Suprathermal particles are ubiquitous in the heliosphere (Gloeckler, 2003). These particles have energies (velocities) greater than the bulk solar wind energies (velocities) and lie in the range ~ 10 s of keV per nucleon to ~ 100 s of keV per nucleon. Sometimes, it is hard to differentiate between suprathermal particles and SEPs or other higher energetic particles from their energies. The distribution functions of these non-Maxwellian ions are generally described by power law tails. The transition from the thermal solar wind particles to the suprathermal particles is parameterized by the Kappa (κ) or the generalized Lorentzian velocity-distribution function, which was shown first time by Vasyliunas (1968). The functional form of this distribution can be written as

$$f_i^\kappa(r, v) = \frac{m_i}{2\pi(\kappa\omega_{\kappa i}^2)^{3/2}} \frac{\Gamma(\kappa + 1)}{\Gamma(\kappa - 1/2)\Gamma(3/2)} \left(1 + \frac{v^2}{\kappa\omega_{\kappa i}^2}\right)^{-(\kappa+1)} \quad (1.1)$$

where $\omega_{\kappa i} = \sqrt{(2\kappa - 3)KT_i/\kappa m_i}$ is the thermal velocity, m_i is the mass of the i^{th} species particles, T_i is their equivalent temperature, v is the speed of the particles, n_i is their number density, and $\Gamma(x)$ is the Gamma function. The lower limit of the index κ should be $3/2$ to prevent the distribution function in Eq. 1.1 from collapsing. Figure 1.4 shows the distribution functions for different κ values. As can be seen from Eq. 1.1, for $\kappa \rightarrow \infty$ the Kappa function tends to be the Maxwellian function. The value of κ determines the spectral index of the energy spectrum of suprathermal particles. Many observational and satellite data regarding suprathermal particles in the heliosphere are observed to be fitted with Kappa distribution function. These includes solar wind particles (Gloeckler et al., 1992; Maksimovic et al., 1997), the magnetosheath (Formisano et al., 1973),

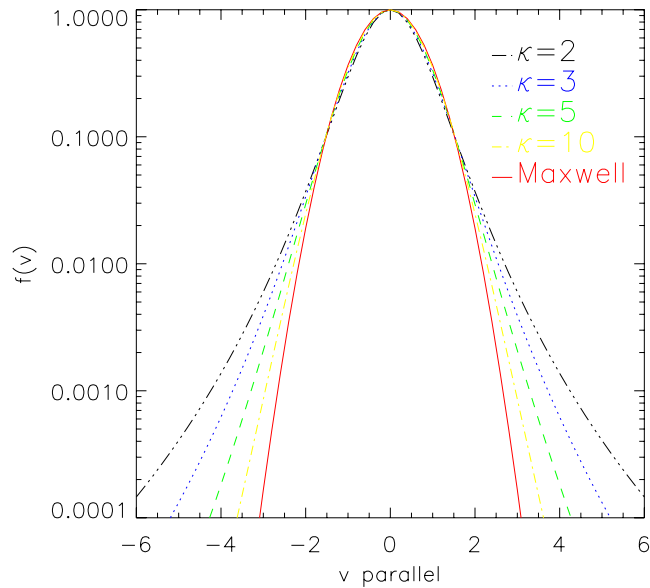


Figure 1.4: Plots for the Kappa distribution function with velocity parallel to magnetic field for different values of κ as shown in the different colors. This figure is taken from [Pierrard and Lazar \(2010\)](#).

the terrestrial magnetosphere ([Gloeckler and Hamilton, 1987](#)), the radiation belts ([Pierrard and Lemaire, 1996](#); [Xiao et al., 2008](#)), the terrestrial plasmashet ([Bame et al., 1967](#); [Christon et al., 1988](#); [Kletzing et al., 2003](#)) etc. In addition, the velocity distributions of the strahl component of solar wind electrons can also be characterized by the Kappa distribution function ([Maksimovic et al., 1997](#)).

Intensities of suprathermal particles increase during the passages of shocks and other IP disturbances like SIR/CIRs at 1 AU. However, “quiet time” tails are observed even in the absence of shocks nearby. This makes it difficult to understand the energization mechanisms of this particle population, and consequently, sources and acceleration mechanisms of these particles have been a field of research for the past few decades.

The distribution functions of “quiet time” suprathermal particles were reported to follow a common power law in velocity and the spectral index happened to be -5 ([Gloeckler, 2003](#); [Fisk and Gloeckler, 2006, 2007, 2008, 2014](#) etc.). According to [Fisk and Gloeckler \(2006\)](#), this kind of spectrum of accelerated ions in the “quiet time” solar wind can be expected if these particles are accelerated by stochastic

process due to compressional turbulence in the solar wind. There are some other theoretical works (e.g., Schwadron et al., 2010; Anteckı et al., 2013 etc.) that tried to explain the common -5 spectral index of suprathermal particles. However, the origin of suprathermal ions has remained highly debated as many authors (Desai et al., 2009; Dayeh et al., 2017) reported deviations in spectral indices of quiet time suprathermal particles from the so called universal -5 spectral index.

1.1.6 Particles upstream of the Earth's bow shock

Some energetic ions are observed to propagate in the sunward direction from the Earth's bow shock (Asbridge et al., 1968; Sarris et al., 1976; Scholer et al., 1979; Paschmann et al., 1980; Desai et al., 2000; Meziane et al., 2002; Kronberg et al., 2011 etc.). These ions are called upstream ions. In the upstream region of the Earth's bow shock; various types of ions are present. Among the suprathermal and energetic ions observed immediately upstream and downstream of the quasi-perpendicular bow shock (where the shock normal angle, θ_{Bn} , is greater than 45°). A brief account of different types of shocks are given in section 1.3.2), the least energetic are the specularly reflected ions, with energies of a few keV. These ions are energized by the solar wind electric field (Gosling et al., 1982) and remain confined within one gyro-radius upstream from the shock (Gosling and Robson, 1985). Slightly more energetic protons, with energies of less than ~ 10 keV, form field-aligned proton beams. These beams are believed to originate either from reflection at the shock or from the leakage of hot proton populations from the magnetosheath into the upstream region (Schwartz and Burgess, 1984). Diffuse ions, in contrast, can reach energies of up to 200 keV per charge and exhibit an almost isotropic distribution in the spacecraft frame (Scholer et al., 1979, 1981). These diffuse ions are consistently associated with large-amplitude hydromagnetic waves (Paschmann et al., 1979). An outstanding problem regarding these diffused upstream ions could be the modulation of these ions during their transport away from the Earth's bow shock.

1.1.7 Particles in the Earth's magnetosphere

Terrestrial magnetosphere is also a great source of energetic particles. High energy SEPs (Paulikas and Blake, 1969; Kaleghev et al., 2018; Filwett et al., 2020 etc.), ACRs, GCRs, particles accelerated at the Earth's bow shock (West Jr and Buck, 1976; Asbridge et al., 1978) can penetrate the magnetopause region and directly contribute to the magnetospheric particle populations. The Earth's magnetosphere is also filled with particles accelerated at the magnetotail region (Fan et al., 1975, 1976) in the night side magnetosphere. Particles with energies < 1 MeV in the magnetosphere are harmful for different space-assets (e.g., O'Dell et al., 2000; Fioretti et al., 2016) rotating in the geosynchronous orbits. ICME-associated low energy SEPs are one of the potential sources for enhanced magnetospheric suprathermal particles. Therefore, assessing the impact of ICME associated SEPs on the magnetosphere is important in the context of space-weather prediction.

1.2 Sources and sinks of suprathermal particles

The various sources and sinks of suprathermal particles are described through the schematic in Figure 1.5 taken from Mason (2000). The suprathermal ion pool provides seed populations for further acceleration by IP shocks, SIR/CIRs leading to SEPs. On the other hand, solar wind particles, particles escaping from planetary bow shocks and magnetospheres, remnant particles from solar flares, pick-up ions, and other energetic ions contribute to the suprathermal ion pool after losing energies (Mason, 2000). Figure 1.6 shows total fluence of oxygen ions with respect to energies ranging from solar wind to GCRs. As can be seen from this figure, fluence of solar wind oxygen (up to say 0.03 MeV n^{-1}) is the highest among all types of particles. Fluence of suprathermal particles comes next followed by solar energetic particles. ACRs and GCRs are highly energetic but their fluences are very less. Space assets are more vulnerable to SEPs, which are produced from the suprathermal ion pool (e.g., Desai et al., 2003) as during impulsive and gradual events, the fluences can increase significantly. Therefore, suprathermal particles

1.3. PARTICLE ACCELERATION MECHANISMS

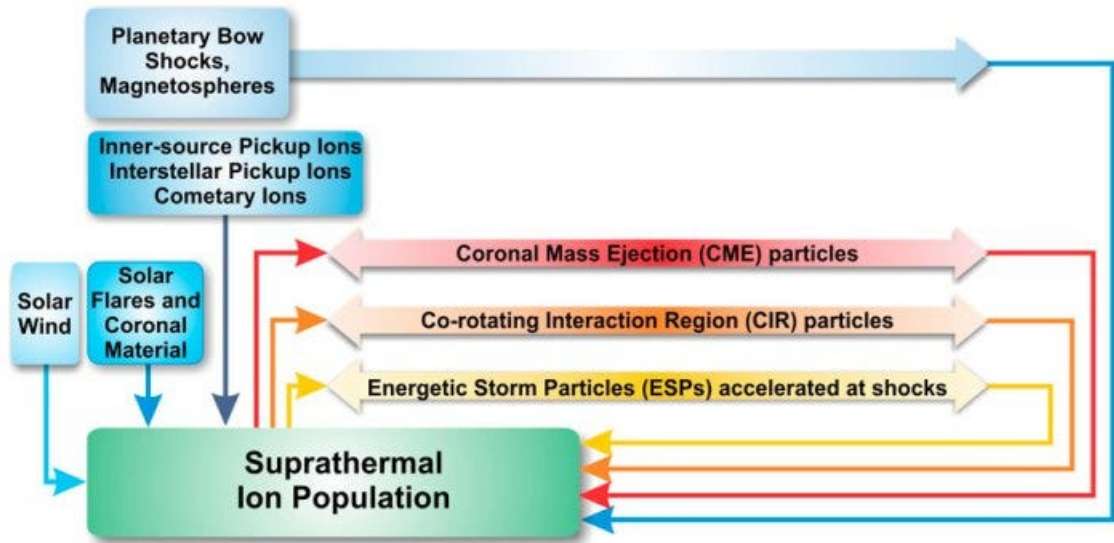


Figure 1.5: A schematic of the various sources and sinks of the suprathermal ion pool in the heliosphere (taken from [Mason, 2000](#)).

and SEPs are of prime importance as long as the risk to space technologies are concerned. Production of large gradual SEPs by IP shocks associated with ICMEs is now well established (a brief description of shock and particle acceleration by shocks is discussed in the next section). Although more studies are required to understand/explain the production and transport of impulsive SEP events, these events are observed mostly during the maximum of solar cycles when the Sun is very active. The present thesis focuses on the suprathermal and low energy SEPs and not on the high energy SEPs. Despite a large volume of work in the field of suprathermal and low energy SEPs, pin-pointing the origin and energization processes remain elusive till date. In the ensuing section, some of the important particle acceleration processes that are relevant for the generation of suprathermal and low energy SEPs, are discussed.

1.3 Particle acceleration mechanisms

A number of particle acceleration mechanisms have been proposed over the years to explain the existence of energetic particles in the heliosphere. In the following

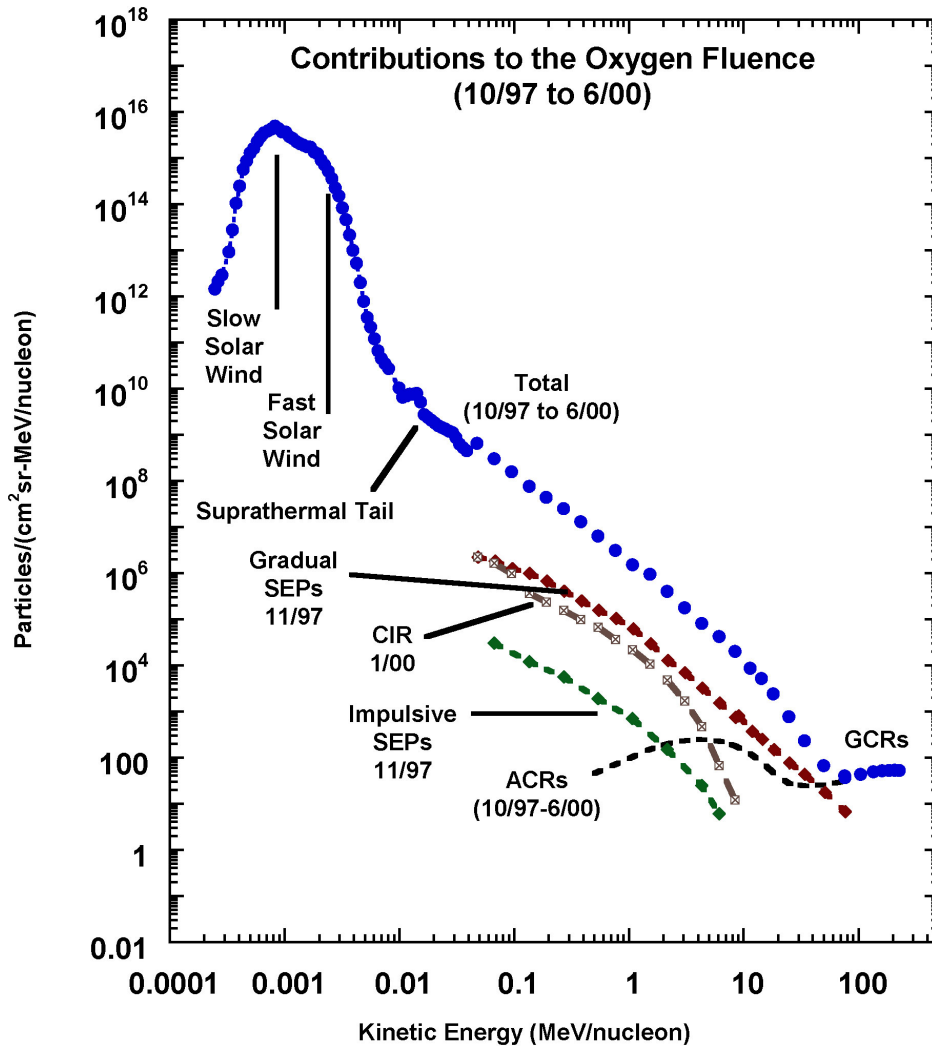


Figure 1.6: Oxygen spectra during October 1997–June 2000 as observed by different particle detector on board the Advanced Composition Explorer (ACE) spacecraft at the L1 point. Blue dots show a composite spectrum of slow-solar wind, fast-solar wind, suprathermal tail, SEPs, ACRs, and GCRs during the said period. Typical spectrum of gradual SEPs, CIR-associated energetic particles, impulsive SEPs are also shown (taken from [Mewaldt et al., 2007](#))

sub-section, some of the most accepted and successful particle energization theories relevant to suprathermal and low energy SEPs are discussed.

1.3.1 Fermi acceleration

Fermi acceleration, named after Enrico Fermi, is one of the most accepted and established theories in the field of particle acceleration. Originally, the Fermi ac-

1.3. PARTICLE ACCELERATION MECHANISMS

celeration was proposed to explain the origin of very high energetic cosmic rays. According to [Fermi \(1949\)](#), cosmic rays are accelerated by collisions with wandering magnetic fields (or rather, magnetized clouds) in the interstellar medium. A simplified version of this theory is described below.

Consider a charged particle with initial kinetic energy E_0 moving in an environment full of magnetized clouds moving with a speed of V_m ($<$ the speed of the particle). In this scenario, the charged particle will collide with the magnetized clouds and undergo random motion after reflection. If the collision is a head-on collision (the particle and a cloud are moving towards each other), then the particle will gain energy. For a follow-on collision (the particle catches up a magnetic cloud from behind), the particle will lose energy. However, the probability of the head-on collisions is more than that of follow-on collisions. In each such collision, the mean energy gain by the particle will be proportional to $(V_m/c)^2$, where c is the speed of light. The spectra of particles thus accelerated will be an inverse power law as observed in case of cosmic ray spectra.

There are some limitations to this theory. The injection energies required for heavy ions to be accelerated by the above-mentioned mechanism should be very high to overcome the ionization loss due to inhomogeneity in the interstellar clouds. According to an estimate by [Fermi \(1949\)](#), the injection energy for protons is 200 MeV. On the other hand, minimum energies required for alpha particles, oxygen, and Fe are 1 BeV, 20 BeV, and 300 BeV, respectively. Therefore, [Fermi \(1949\)](#) discarded the probability of acceleration of heavy ions by this method.

Another important limitation of this theory is the collision frequency. An estimate by [Fermi \(1949\)](#) shows that the mean time difference between two collisions in the interstellar medium is more than a year. This shows that the probability of particle energization by Fermi acceleration is limited. However, keeping in mind the stochastic nature of the acceleration process, similar concept is adopted in many of the particle acceleration theories. For example, diffusive shock acceleration ([Krymskii, 1977](#); [Bell, 1978](#)) requires scattering of particles by magnetic irregularities upstream and downstream of a shock front. In the next section, the

diffusive shock acceleration is discussed more illustratively.

1.3.2 Acceleration of particles by shocks

A shock forms in a medium when the relative speed of an object exceeds the characteristic speed of the medium with which information travels in the medium. For example, if an object moves through air with a speed greater than speed of sound in air, a shock will form ahead of the object. In case of plasma, this speed is fast magnetosonic wave. The region of the medium ahead of a shock is called upstream and the region behind the shock is called downstream. A supersonic flow upstream of the shock is converted to a subsonic flow in the downstream region. Collisions between molecules of air support the propagation of sound through air. In case of solar wind plasma, the collisional mean free path is very large (~ 1 AU) as compared to thickness of shocks (for the Earth's bow shock, the thickness varies in the range of 100 km). Therefore, whatever happens in an IP shock, collisions among particles are not of great importance. For this reason, these shocks are called collisionless shocks. Some examples of such collisionless shocks are the termination shock of the heliosphere, planetary bow shocks, IP shocks ahead of CMEs, forward and reverse shock pairs in the leading and trailing edge of SIR/CIRs etc.

Shocks are regions in space where we see abrupt transition in different properties of the medium between the upstream and downstream regions. It is difficult to say what happens inside a shock. However, the medium properties upstream and downstream of a shock are measurable. In addition, mass, energy, and momentum should be conserved in any physical system like a shock. By using magnetohydrodynamics, one can relate medium properties upstream and downstream of the shock. In case of solar wind plasma, these relations are called shock-jump conditions (also known as Rankine-Hugoniot relations). A brief description of these relations is given below (following [Kivelson and Russell, 1995](#)).

In [Figure 1.7](#), it is considered that a shock front is moving leftward. With respect to a frame of reference where the shock is stationary (shock frame), the

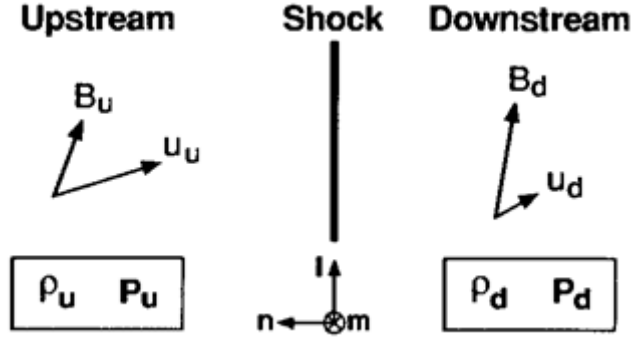


Figure 1.7: A schematic of configuration for shock jump relations (taken from [Kivelson and Russell, 1995](#)).

upstream plasma and embedded magnetic field in it is moving towards the shocks and the downstream plasma is moving away from the shock. The shock plane is the $l - m$ plane and the shock normal is directed along n , as shown in Figure 1.7. The plasma density, pressure, magnetic field intensity, and the velocity of the plasma in the upstream regions are ρ_u , p_u , B_u , and u_u respectively. The corresponding values of these parameters in the downstream region are ρ_d , p_d , B_d , and u_d . Although the shock is a discontinuity, it has a thickness in reality. Two regions of steady flow are basically separated by the shock. Let us consider that the change in quantity X across the two regions is represented by

$$[X] = X_u - X_d \quad (1.2)$$

Assuming the shock to be steady and one dimensional (i.e., variations in quantities in the n direction only), one can express the mass conservation relation as

$$[\rho u_n] = 0 \quad (1.3)$$

where n represents the normal component of mass flow. This relation proves that if the shock decreases the plasma flow speed in the downstream region, the density downstream the shock will increase.

The conservation of momentum normal to the shock surface can be represented

by

$$\left[\rho u_n^2 + p + \frac{B^2}{2\mu_0} \right] = 0 \quad (1.4)$$

Similarly, the transverse component of the momentum conservation leads to

$$\left[\rho u_n u_t - \frac{B_n}{\mu_0} B_t \right] = 0 \quad (1.5)$$

where t stands for transverse to the shock, i.e., parallel to the shock surface. In deriving these equations, we have assumed the pressure to be isotropic. Also, the electric stress term $E = -\mathbf{u} \times \mathbf{B}$ is also considered to be negligible. Considering the plasma to be represented by adiabatic equation of state, so that $p\rho^{-\gamma} = \text{constant}$, the energy conservation equation can be obtained as

$$\left[\rho u_n \left(\frac{1}{2} u^2 + \frac{\gamma}{\gamma - 1} \frac{p}{\rho} \right) + u_n \frac{B^2}{\mu_0} - \mathbf{u} \cdot \mathbf{B} \frac{B_n}{\mu_0} \right] = 0 \quad (1.6)$$

where the first two terms are flow energy and internal energy, respectively. The third and fourth terms are due to electromagnetic energy flux.

In addition to the above equations, another two conservation relations coming from the Maxwell's equations are useful: $\nabla \cdot \mathbf{B} = 0$ leads to the continuity of the normal component of the magnetic field. Therefore,

$$[B_n] = 0 \quad (1.7)$$

and $\nabla \times \mathbf{E} = -\partial \mathbf{B} / \partial t$ produces

$$[u_n B_t - B_n u_t] = 0 \quad (1.8)$$

Here it is considered that $\partial \mathbf{B} / \partial t = 0$. All these conservation relations (Eq. 1.3–1.8) are known as Rankine Hugoniot relations. The solution to these equations produces a number of magneto-hydrodynamic (MHD) discontinuities.

A discontinuity is considered to be a shock when there is plasma flow through the shock and the plasma is dissipated and compressed across the shock. We can

classify a shock with respect to the relative orientation between the shock normal and the upstream magnetic field (shock normal angle). If the shock normal angle (θ_{Bn}) $< 45^\circ$, the shock is called a quasi-parallel shock. If $45^\circ \leq \theta_{Bn} < 90^\circ$, the shock is called quasi-perpendicular. Figure 1.8 shows a schematic diagram of quasi-parallel and quasi-perpendicular shocks.

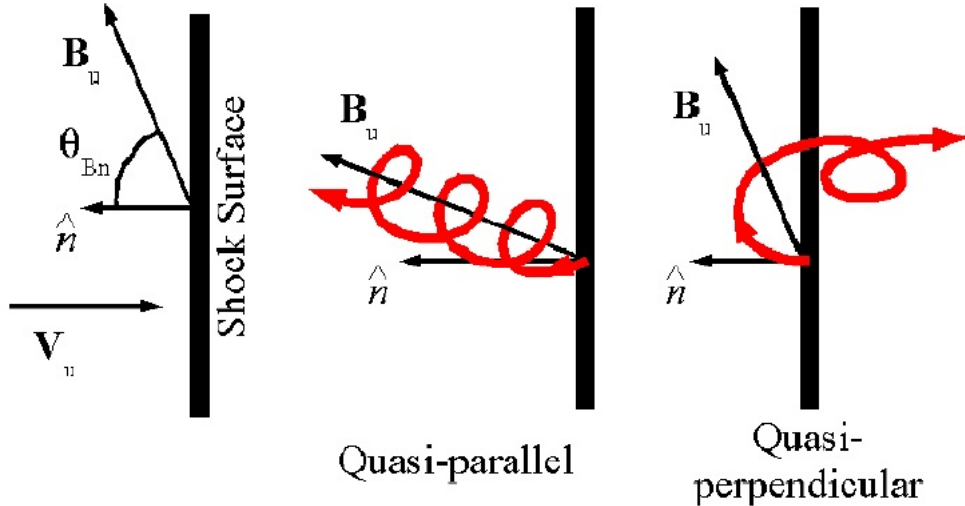


Figure 1.8: Schematic of quasi-parallel and quasi-perpendicular shocks (taken from Schwartz et al., 2004).

From section 1.1.3, it is clear that shock geometry plays very important role in particle acceleration. In general, parallel geometry of shocks suit for diffusive shock acceleration (DSA) and shock drift acceleration mechanism demands perpendicular geometry of the shock. In the following part, we discuss briefly both of the two acceleration mechanisms.

Diffusive shock acceleration (DSA) or first order Fermi acceleration

A comprehensive analytical discussion of diffusive shock acceleration can be found in Drury (1983). There is moving magnetic inhomogeneity both upstream and downstream of a shock due to turbulence. Consider a case of a charge particle with sufficiently high energy (injection energy), so that it can cross the shock, moves from upstream to the downstream region. The particle will be reflected back to the upstream region by any moving magnetic irregularity it encountered

in the downstream region. The diffusion of particles across the shock front is aided by magnetic fields parallel to the shock normal. The energy of the particle will be enhanced due to the motion of the magnetic inhomogeneity. Similar process may occur in the upstream region also. After multiple reflections, the particle will gain sufficiently high energy and the velocity distribution spectrum turns out to be a power law with spectral index $q = 3r/(r - 1)$, where r is the ratio of plasma densities downstream and upstream of the shock (Blandford and Ostriker, 1978). The energy gained by the particle in each collision is proportional to (v_s/c) , where v_s is the shock velocity and c is the speed of light. Since particles are accelerated by diffusion across the shock front, the acceleration process is called diffusive shock acceleration (DSA). This is sometimes termed first-order Fermi acceleration citing the similarity with the classical Fermi acceleration and due to the fact that the energy gain varies with first-order of the velocity of the shock.

A similar distribution of particles was obtained by Bell (1978) where charged particles gain energy by collision with Alfvén waves upstream and downstream of the shock front. In that case, the differential energy spectrum of the energized particles follows a power law with spectral index

$$q = \frac{(2 + \chi) + \chi(2v_w/v_s - 1/M_A)}{(\chi - 1) - \chi(v_w/v_s + 1/M_A)} \quad (1.9)$$

where χ is the shock compression ratio, v_w is the mean velocity of the scattering centres in the downstream region, as viewed by an observer in the rest frame of the downstream plasma, and M_A represents the Alfvén Mach number. In case of a strong shock ($\chi = 4$) and if the shock velocity is very less as compared to the velocity of scattering center, the spectral index $q = 2$. This is very close to the observed spectral index of cosmic rays (a slope of 2.5).

There are multiple limitations of this theory. First is the initial injection energy required by the particles to cross the shock front. These energies typically fall in the suprathermal energy range. How these particles gain sufficiently high energies in the solar wind is still unclear. Secondly, the reaction of back-scattered particles on the velocity field and transmitted spectrum is not taken into account

in these theories. Thirdly, there is high chance of losing energy by the relativistic particles in adiabatic decompression because of the expansion of the shock waves. Despite all these limitations, diffusive shock acceleration has proved to be useful in explaining particle energization by CME and SIR/CIR-associated shock to some extent.

Shock Drift acceleration (SDA)

The DSA theory is mostly valid for parallel or quasi-parallel shocks. In case of perpendicular shocks, the magnetic field is not parallel to the shock normal. This configuration gives rise to a motional electric field. Sometimes, particles may be accelerated by this motional electric field. This process is called shock drift acceleration (SDA). While gyrating around the magnetic field ions and electrons cross the ramp of a shock front multiple times as the shock front is parallel to the magnetic field. Eventually, these particles escape in the upstream region ([Armstrong et al., 1985](#)). The SDA acceleration mechanism is distinct from the DSA mechanism, but in both the cases, particle acceleration takes place while drifting along the shock front within a small distance of the ramp ([Jokipii, 1982](#)).

1.3.3 Particle acceleration by gradual compression regions

While IP shocks are considered major candidates for particle acceleration in the heliosphere, gradual compression regions associated with SIR/CIRs can also accelerate particles by a process similar to the DSA mechanism ([Giacalone et al., 2002](#)). This work investigates the possibility of particle acceleration when the particle mean free path is larger than the width of the compression region. This condition holds good for low energetic particles at 1 AU where the forward and reverse shock-pair has not formed yet. However, particle acceleration in the compression region is possible in the expanding solar wind if the divergence of plasma velocity is negative.

1.3.4 Pump mechanism

So far, particle acceleration mechanisms associated with transient events in the IP medium have been discussed. As mentioned in section 1.1.5, velocity distribution functions of suprathermal particles exhibit power spectra with a common spectral index of -5. This common spectrum is observed mainly during quiet times. To explain the origin of this common spectrum, [Fisk and Gloeckler \(2008, 2014\)](#) proposed a particle acceleration mechanism, known as pump mechanism, which seems to be effective in regions of large-scale compressions and expansions. There should be a source of particles to be accelerated in the region of interest. The volume of the region is considered thermally isolated. It is also assumed that particles are accelerated in the volume only and loss of particles from the volume is negligible. [Figure 1.9](#) shows a volume in space containing regions of compressions and expansions and different types of particles with different speeds. The particle population in the volume primarily consists of three distinct types of particles: (a) the thermal plasma (like thermal solar wind carrying the mass and providing background for compressions and expansions), (b) the source particles with speeds greater than the thermal speed of the bulk plasma and less than an upper threshold speed (v_{th}), (c) the accelerated particles with speeds greater than v_{th} . The source particles cannot escape through diffusion even if they undergo random compressions and expansions. This is the main difference between the source particles and the accelerated particles.

Since the volume considered here is thermally isolated, the source particles will be compressed adiabatically in the compression regions and flow across the threshold boundary $v = v_{th}$. The extension of the compression region in higher particle speeds indicates the enhancement in number of accelerated particles in the compression region.

On the other hand, the flow of particle and energy occurs from the accelerated particles to the source particles. Due to spatial gradients of particle speed, the accelerated particles will spatially diffuse from the compression regions to the expansion regions. Consequently, after some time, the compression regions will

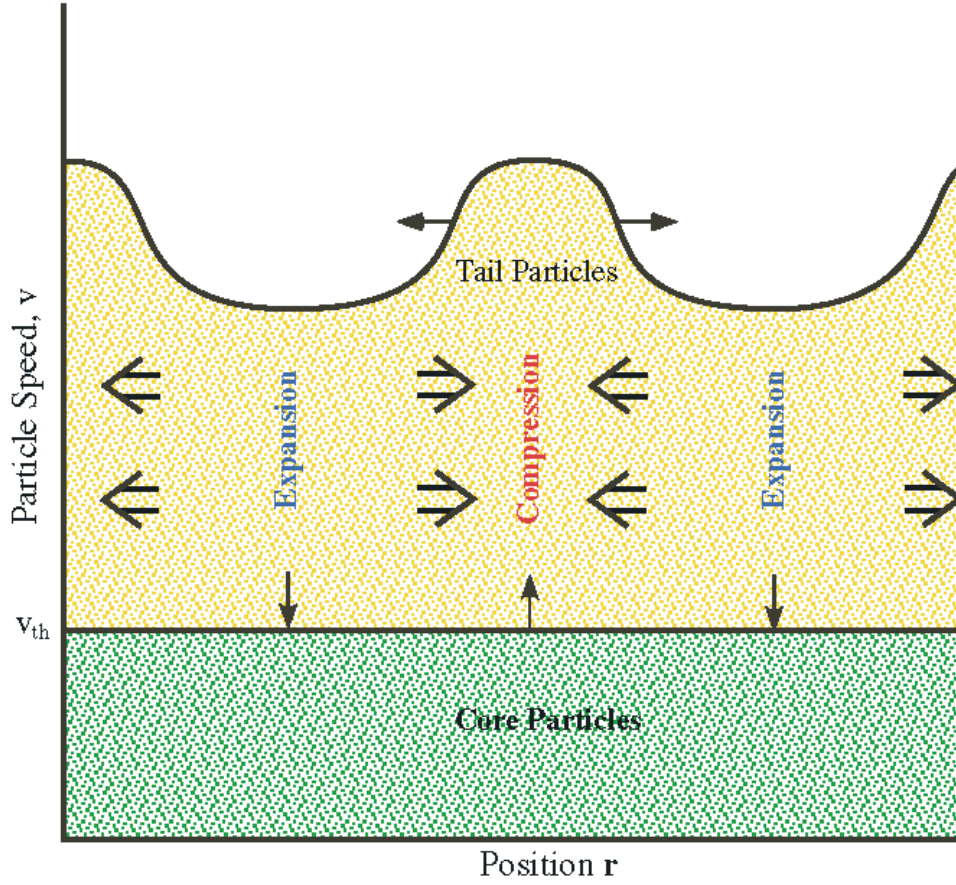


Figure 1.9: A schematic description of the pump mechanism (taken from [Fisk and Gloeckler, 2014](#)).

be expansion regions and vice-versa. The flow of particle and energy between the source particles and the accelerated particles continue repeatedly. This process enhances particle energy systematically with time and is called pump mechanism. Particles from the source population are pumped up in energy by this process without any external influence. The distribution of the accelerated particles can be best represented by the standard Parker transport equation

$$\frac{\partial f}{\partial t} + \delta \mathbf{u} \cdot \nabla f = \frac{\nabla \cdot \delta \mathbf{u}}{3} v \frac{\partial f}{\partial v} + \nabla \cdot (\tilde{\kappa} \cdot \nabla f) \quad (1.10)$$

where $f = f(\mathbf{r}, n, t)$, δu is the convective velocity of the compressions and expansions, and $\tilde{\kappa}$ is the spatial diffusion tensor.

One important aspect of the pump mechanism is that the spatial distribution

of compression and expansion regions in the volume is not random. Every compression region is surrounded by expansion regions. This is fundamentally different from the traditional stochastic acceleration mechanism for which the compression regions are distributed randomly.

The -5 spectral index of accelerated particles via pump mechanism comes from some small assumptions. Since the process of particle acceleration inside the thermally isolated volume is irreversible, the accelerated particles will tend to reach a state of maximum entropy. The compressions and expansions continue after attaining a state of maximum entropy. This indicates that the compressions and expansions are isentropic or adiabatic. The spatial gradient in velocity is negligible at the regions below the rollover in velocity in Figure 1.9. Therefore, we can essentially ignore spatial diffusion of particles for those regions. In such a scenario, the distribution of particles can be described by

$$\frac{\partial f}{\partial t} + \delta \mathbf{u} \cdot \nabla f - \frac{\nabla \cdot \delta \mathbf{u}}{3} v \frac{\partial f}{\partial v} = 0 \quad (1.11)$$

The pressure equation for isentropic compression and expansion is

$$\frac{\partial P}{\partial t} + \delta \mathbf{u} \cdot \nabla P + \frac{5}{3} (\nabla \cdot \delta \mathbf{u}) P = 0 \quad (1.12)$$

Every compression and expansion, at least in the portions with negligible spatial gradient, must follow this pressure equation.

Therefore, if the pump mechanism produces a particle spectrum $f \propto v^{-\alpha}$, the spectral index α must be 5 to satisfy both the distribution and pressure equations.

1.3.5 Particle acceleration by merging and contraction of magnetic islands

It has been discussed in section 1.1.3 that magnetic reconnection during solar flares in the corona accelerate the particles and generate impulsive SEPs. In the supersonic solar wind also, magnetic reconnection can energize particles. Many authors (e.g., [Gouveia Dal Pino and Lazarian, 2005](#); [Kowal et al., 2011, 2012](#)) identified

1.3. PARTICLE ACCELERATION MECHANISMS

acceleration of particles similar to the first and the second order Fermi acceleration due to magnetic reconnection. Typically, direct current (DC) electric fields generated in the reconnection current sheets are thought to accelerate particles. Magnetic islands of different scales are common in magnetospheric plasmas (Greco et al., 2010). In the IP medium, these islands are located near the heliospheric current sheet (Khabarova et al., 2015a). Figure 1.10 gives a schematic illustration of the wavy heliospheric current sheet and magnetic islands of different scales located at the ripples of the current sheet. Below we discuss a mechanism (Zank et al., 2014) of particle acceleration by merging of magnetic islands in a turbulent plasma. Merging of two neighboring magnetic islands is shown in Figure 1.11. Particle energization occurs in these sites because of three main reasons.

1. (i) Particles trapped in magnetic islands will gain energy by repeated reflections from the ends of converging mirrors in the contracting magnetic islands formed during reconnection (Drake et al., 2006a). This process is similar to first order Fermi acceleration. On the other hand, oscillating (both contracting and expanding) magnetic islands energize particles via second order Fermi acceleration
2. Particles are energized via second order Fermi acceleration due to contraction in the magnetic field length during merging of two magnetic islands (Drake et al., 2012). The shortening in the length of magnetic field increases the particle velocity component parallel to the magnetic field. If the particles are sampled in multiple magnetic islands, they will gain sufficient energy.
3. Particles are energized through interaction with the induced reconnection electric field (Oka et al., 2010)

Therefore, total acceleration of the particles is a superposition of these three types of energizations. In this scenario, the force equation can be written as

$$\mathbf{F} = \mathbf{F}_L + \mathbf{F}_c + \mathbf{F}_m + \mathbf{F}_E \quad (1.13)$$

where, \mathbf{F}_L is the Lorentz force, \mathbf{F}_c is the force due to contraction in magnetic

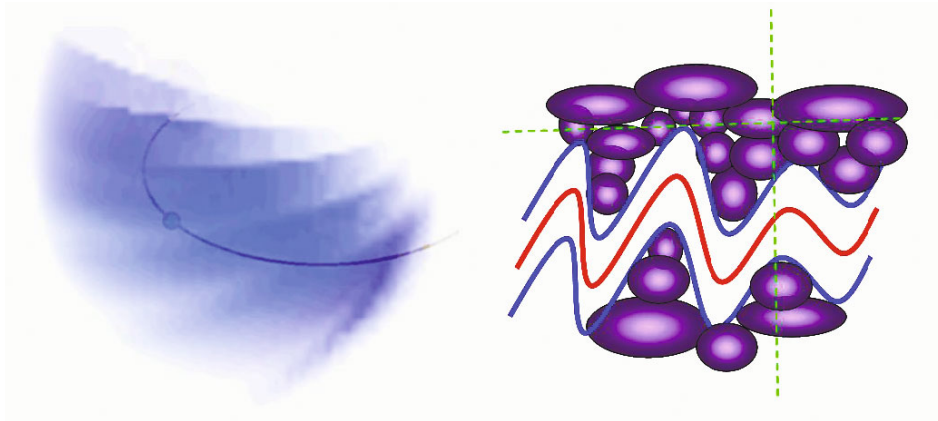


Figure 1.10: Ripples in the heliospheric current sheet and magnetic islands of different sizes. The Earth (blue solid circle in the left image) is shown to move in its orbit (blue curve in the left image) through the heliospheric current sheet (taken from [Mingalev et al., 2019](#)).

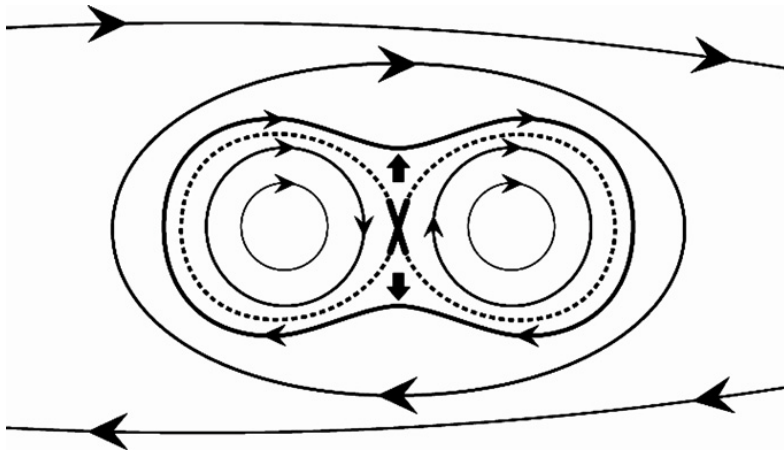


Figure 1.11: Lines with arrows are the local oppositely polarized magnetic field lines of two neighboring magnetic islands experiencing reconnection. The reconnection site is marked by X and the outflows are shown by thick arrows. The induced reconnection electric field is directed into the page (taken from [Zank et al., 2014](#)).

islands, \mathbf{F}_m is the force due to merging of magnetic islands, and \mathbf{F}_E represents the electric force due to reconnection electric field, which is different from the large-scale or mean electric field.

Now, let us consider some test particles with mean speed c_0 are being injected steadily in an incompressible super-Alfvénic flow. It is also considered that the motion of the particles is confined in the x direction only. Half of the test particles

1.3. PARTICLE ACCELERATION MECHANISMS

will be accelerated and the rest will be decelerated to conserve the energy. Due to the contribution from the induced electric field alone, the distribution function of the accelerated particles ($c > c_0$) will be

$$\begin{aligned} f(x, c) &= \frac{n_0}{8\pi c_0^2 |V_E|} \left(\frac{c}{c_0}\right)^{-(3+U/|V_E|)/2} H(c - c_0), \quad \text{for } x > 0 \\ &= \frac{n_0}{8\pi c_0^2 |V_E|} \left(\frac{c}{c_0}\right)^{-(3+U/|V_E|)/2} H(\xi + 2|V_E|x/\kappa), \quad \text{for } x < 0 \end{aligned} \quad (1.14)$$

where n_0 is the initial density of test particles; V_E is the velocity of particles due to induced electric field; $\kappa = c^2\tau/3$, τ being scattering time scale; U is the velocity of the super-Alfvénic flow; $\xi = \ln(c/c_0)$; and $H(x)$ is the Heaviside step function.

The solutions are power laws with spectral index of $-(3 + U/|V_E|)/2 \sim -(3 + M_A)/2$, where M_A is the Alfvén Mach number. For $M_A = 7$, the so called ‘universal’ spectral index (5) for quiet time suprathermal particles can be achieved.

If the particles were to be accelerated by contraction of a magnetic island alone, the distribution of particles with $c > c_0$ would be

$$\begin{aligned} f(x, c/c_0) &= \frac{n_0}{8\pi c_0^2 U} \sqrt{\frac{3\tau_c}{2\tau_{diff}}} \left(\frac{c}{c_0}\right)^{3(\frac{\tau_c}{8\tau_{diff}}+1)} \frac{1}{\sqrt{\pi \ln(c/c_0)}} \\ &\times \exp\left[\left(\frac{1}{2} - \frac{1}{6\ln(c/c_0)} \frac{\tau_{diff}}{\tau_c} \frac{x}{L_{diff}}\right) \frac{x}{L_{diff}}\right] \times H(|\ln(c/c_0)|) \end{aligned} \quad (1.15)$$

Here, $\tau_{diff} = \kappa/U^2$ is the diffusive time scale, τ_c is the contraction time scale, $L_{diff} = \kappa/U$ is the diffusive length scale. The spectral index in this case is $3 \times [(\tau_c/8\tau_{diff}) + 1]$ and depends on the contraction and diffusion time scales. This mechanism is expected to produce a harder spectrum since the contraction time scale is very less as compared to the diffusion time scale though the nature of both of these time scales is not known properly.

Considering effects of both the induced electric field and contraction of magnetic island, the acceleration time scale (τ_{acc}) can be calculated such that $\tau_{acc} - 1 \sim 8V_A/(3l)$ where l is the characteristic size of the magnetic island. A comparison of τ_{acc} with the adiabatic cooling rate (U/R , R being the solar wind spatial scale ~ 1 AU) in the solar wind yields that acceleration rate is 100 times greater than

adiabatic cooling. Therefore, merging and contraction of magnetic islands can essentially generate suprathermal power laws in the IP medium.

In addition to these mechanisms, wave particle interactions (Vocks and Mann, 2003) and transit time damping of magnetohydrodynamic (MHD) waves (Fisk, 1976) are also suggested as potential processes for the acceleration of suprathermal and energetic particles in the heliosphere.

1.4 Aim and overview of the thesis

As discussed in section 1.2, origins and energization mechanisms of suprathermal particles are not understood properly. These particles are present in the IP medium in a consistent manner and enhance during transient events (like ICMEs, SIR/CIRs, and solar flares).

It is difficult to find a fixed energy (velocity) value that distinguishes the suprathermal particles from the solar wind particles in the low-energy limit of suprathermal particles. Similarly, high-energy suprathermal particles and SEPs are inseparable in the high-energy limit. For the sake of uniformity, in this thesis, particles with energies $\sim 0.05 < E < 1.0 \text{ MeV n}^{-1}$ are considered as suprathermal particles. This thesis aims to investigate the origin, energization, and modulation of suprathermal particles in the solar wind. In order to do so, at first, behaviors of quiet time suprathermal particles in the IP medium is investigated. Then, energization of suprathermal particles during SIR events is studied. Subsequently, an effort to understand the characteristics of upstream suprathermal particles from the terrestrial bow shock is made. Last but not the least, the impact of low energy SEPs ($< 2 \text{ MeV}$) associated with ICMEs on the terrestrial magnetospheric energetic particle environment has been evaluated. The subsequent chapters of this thesis are as follows.

Chapter 2 discusses some useful parameters and concepts related to the physics of suprathermal particles. This chapter also includes the measurement techniques of suprathermal and energetic particles, instruments, data sources, and catalogues of different events used in the subsequent chapters.

In Chapter 3, behaviors of different suprathermal species (H, ^4He , ^3He , C, O, and Fe) are investigated during solar cycles 23 and 24 by using the L1 point observations. These particles are shown to follow solar cycles with certain lags with respect to the sunspot number. Variations in spectral indices of these elements during quiet times over the two solar cycles are also discussed in this chapter. Deviation from the “universal” spectral index of suprathermal particles is seen. Modulation of suprathermal particles in the IP medium is observed to be dependent on first ionization potential and mass-to charge ratio of different elements.

Energization of suprathermal particles at 1 AU during 20 shock-less SIR events is investigated in Chapter 4. Spectral indices of ^4He , O, and Fe are found to vary in a wide range. In a special SIR event, the three species exhibit almost identical spectral indices. This particular event is investigated in detail. The role of merging and contraction of magnetic islands in accelerating suprathermal particles with identical spectral indices is observationally shown in this chapter.

Modulation of upstream suprathermal H, ^4He , and CNO during the course of their propagation from the Earth’s bow shock towards the Sun is investigated in Chapter 5 by using simultaneous measurements of solar wind (towards the terrestrial bow shock) and upstream (sunward) suprathermal particles. A systematic hardening of upstream ions is observed with increasing mass-to-charge ratio of these elements.

Chapter 6 presents the first observations by the suprathermal and energetic particle instrument on board the Aditya L1 spacecraft during its earth-bound orbits. Contrasting impacts of SEPs associated with a “stealthy” and a typical ICME on the magnetospheric energetic particle environment is discussed in this chapter.

In Chapter 7, the key findings discussed in chapter 3–6 are summarized. This chapter also includes some potential science problems that will be taken up in near future.

Chapter 2

Instruments, Datasets, Techniques

In-situ measurements of particle fluxes and other solar wind parameters (like bulk solar wind speed, magnetic field, density, pressure etc.) from various space-based instruments have been utilized extensively in this thesis. The salient details of the relevant instruments and corresponding measurement techniques are presented in this chapter. In-situ data from the Advanced Composition Explorer (ACE; [Stone et al., 1998c](#)), Wind (<https://wind.nasa.gov/>), Solar Terrestrial Relations Observatory Ahead, Behind (STEREO-A, B; [Kaiser et al., 2008](#)), and the newly launched Aditya-L1 ([Seetha and Megala, 2017](#)) mission of India are utilized in this thesis. There are multiple instruments on board these spacecraft. For the sake of brevity, a list of all the instruments present in each of the above-mentioned satellites is provided. Only the measurement techniques of instruments which measure the energetic particles, solar wind particles (top hat analyzer), and IMF (fluxgate magnetometer) are discussed briefly.

2.1 Some useful parameters and concepts

Before detailing the instruments, it is necessary to introduce a few useful parameters that will be used in the upcoming chapters. A few standard statistical concepts that are used in the thesis are also discussed.

2.1.1 Parameters related to suprathermal particles

1. **Phase space density (f):** This is defined as the number of particles per unit phase space volume (a multidimensional volume defined by components of coordinate and velocity). In the context of suprathermal particles, phase space density and the velocity distribution function are used interchangeably. The velocity distribution functions are, in general, the key parameter for the theoretical explanations of the acceleration and transport of suprathermal particles. It is expressed in terms of particles $cm^{-6}s^3$ (Gloeckler et al., 1995b; Wüest et al., 2007; Knoll, 2010).

2. **Differential directional flux (j):** This is defined as the number of particles per unit time per unit area per unit solid angle per unit energy. Differential directional flux is, in general, measured over a range of energies and directions. Usually, it is expressed in units of particles $s^{-1}cm^{-2}sr^{-1}MeV^{-1}$.

In general, f and j are connected by the following relation under the assumption of quasi-isotropic particle distribution (Gloeckler et al., 1995b)

$$j \sim fp^2 \tag{2.1}$$

where p is the momentum of the particles.

3. **Fluence:** This is the differential directional flux integrated over time. It is expressed in units of particles $cm^{-2}sr^{-1}MeV^{-1}$ (Wüest et al., 2007; Knoll, 2010).

As mentioned in chapter 1, suprathermal particles exhibit power law spectra. Power law is observed in the f vs v spectra (phase space density description) as well as in the j vs E spectra (differential directional flux description), where v and E are particle's speed and kinetic energy respectively. Since f and j are connected by Eq. 2.1, the power law indices in both the approaches

are also related. If

$$f \sim v^{-a} \quad (2.2a)$$

$$j \sim E^{-b} \quad (2.2b)$$

where a and b are the spectral indices in the f vs. v and j vs. E descriptions, respectively then,

$$b = \frac{a - 2}{2} \quad (2.3)$$

Following Eq. (2.3), it can be seen that a spectral index of 5 in phase space density description is equivalent to a spectral index of 1.5 in differential directional flux description. Spectral index in the j vs E description is considered throughout the thesis.

2.1.2 Statistical concepts

The spectral indices of suprathermal particles are estimated by plotting the differential directional fluxes with respect to the energies of these particles subsequently, by estimating the slopes of the linear fits. Therefore, the accuracy of the estimated spectral indices are dependent on the goodness of the fits even if one does not consider the measurement errors. These errors are statistical in nature and two types of statistical errors in the spectral indices are estimated in the thesis.

1. **Margin of error (MoE):** Margin of error (MoE) of an estimated spectral index gives a measure of the maximum difference between the true population spectral index and the estimated spectral index (e.g., [Tanur, 2011](#); [Ramachandran and Tsokos, 2021](#)). Basically, MoE creates an interval around the estimated spectral index, which is called the confidence interval. In fact, MoE is defined as the half width of the confidence interval. A higher confidence leads to a wider confidence interval and consequently, greater value of MoE. MoE depends on variabilities in the data points, number of data

points used for the fit, and a confidence level (typically 90%, 95%, 99% etc.). MoEs corresponding to 95% confidence level are used as estimation of errors in the spectral indices of suprathermal particles in chapter 3 and chapter 4.

2. **Standard error (SE):** Standard error (SE) of an estimated spectral index is a measure of the variability of the estimated spectral index around the true population spectral index (e.g., [McHugh, 2008](#)). If the spectral index is calculated repeatedly several times, then the variability that arises from this repetition can be captured by SE. SE is not associated with any confidence level.

In fact, MoE can be written in terms of SE as

$$MoE = SE \times t \tag{2.4}$$

where, t value is associated with the Student's t distribution and depends on the confidence level and degrees of freedom ($n = N - K$, N and K being the number of data points and number of parameters to be calculated, respectively). This t value is taken from the t table, which is a standard practice. For most of the cases, $MoE > SE$, because $t > 1$. Sometimes, the higher value of MoE may lead to misinterpretation of the estimated spectral index. Therefore, SE is used for cases when there is no need to calculate the MoE. In fact, in chapter 5 and chapter 6, SE is given preference for the measure of errors in the estimated spectral indices.

2.2 Instruments

Data from a number of space-based instruments have been utilized in this thesis. In this section, brief overviews of different spacecraft and the instruments on board these spacecraft are given.

2.2.1 Advanced Composition Explorer (ACE)

The National Aeronautics and Space Administration (NASA) launched this science exploration mission on August 25, 1997 and injected the spacecraft into a Lissajous orbit around the first Sun-Earth Lagrange (L1) point. An overview of the ACE spacecraft can be found in [Stone et al. \(1998c\)](#). The ACE is a spin-stabilized (5 rpm) satellite with spin axis towards the Sun. Below is the list of instruments on board this spacecraft

1. Cosmic Ray Isotope Spectrometer (CRIS, [Stone et al., 1998a](#))
2. Solar Isotope Spectrometer (SIS, [Stone et al., 1998b](#))
3. Ultra Low Energy Isotope Spectrometer (ULEIS, [Mason et al., 1998](#))
4. Solar Energetic Particle Ionic Charge Analyzer (SEPICA, [Möbius et al., 1998](#))
5. Electron, Proton & Alpha Monitor (EPAM, [Gold et al., 1998](#))
6. Solar Wind Ion Mass Spectrometer (SWIMS, [Gloeckler et al., 1998](#))
7. Solar Wind Ion Composition Spectrometer (SWICS, [Gloeckler et al., 1998](#))
8. Solar Wind Electron, Proton & Alpha Monitor (SWEPAM, [McComas et al., 1998](#))
9. Magnetometer ([Smith et al., 1998](#))
10. Real-Time Solar Wind monitors (RTSW, [Zwickl et al., 1998](#))

2.2.2 Wind

The Wind satellite (<https://wind.nasa.gov/>) was launched on November 1, 1994 by NASA with an intention to study solar wind and magnetospheric radio waves and plasma. Initially, it revolved around the Earth to study the magnetosphere and lunar environment. The spacecraft was injected into a Lissajous Orbit around

the L1 point in May 2004. It was later inserted into a halo orbit in 2020. This is also a spin-stabilized satellite with spin axis almost normal to the ecliptic plane.

The instruments on board the Wind spacecraft are listed below

1. Magnetic Field Investigation (MFI, [Lepping et al., 1995](#))
2. Solar Wind Experiment (SWE, [Ogilvie et al., 1995](#))
3. Three-Dimensional Plasma and Energetic Particle Investigation (3DP, [Lin et al., 1995](#))
4. Solar Wind and Suprathermal Ion Composition Experiment (SMS, [Gloeckler et al., 1995a](#))
5. The Energetic Particles: Acceleration, Composition, and Transport (EPACT, [Von Rosenvinge et al., 1995](#))
6. Transient Gamma-Ray Spectrometer (TGRS, [Owens et al., 1995](#))
7. Radio and Plasma Wave Investigation (WAVES, [Bougeret et al., 1995](#))
8. KONUS ([Aptekar et al., 1995](#))

2.2.3 Solar-Terrestrial Relations Observatory (STEREO)

A pair of identical STEREO ([Kaiser et al., 2008](#)) satellites was launched on October 26, 2006 by NASA to study the structure and evolution of solar transients. One of the satellites was placed ahead of the Earth and other one behind it. STEREO-A takes 347 days to complete one revolution of the Sun and revolution period of STEREO-B is around 387 days. While STEREO-A is still operational, STEREO-B lost contact with the ground segment on October 1, 2014. Each of these satellites carries the following instruments

1. Sun Earth Connection Coronal and Heliospheric Investigation (SECCHI, [Howard et al., 2008](#))

2.2. INSTRUMENTS

2. In-situ Measurements of Particles and CME Transients (IMPACT, [Luhmann et al., 2008](#))
3. PLAsama and SupraThermal Ion Compostion (PLASTIC, [Galvin et al., 2008](#))
4. STEREO/WAVES ([Bougeret et al., 2008](#))

2.2.4 Geostationary Operational Environmental Satellites (GOES)-16, 18

Goes-16 and GOES-18 are among the GOES-R series satellites operated by NASA and the National Oceanic and Atmospheric Administration (NOAA). These satellites are used as weather satellites. GOES-16 was launched on November 19, 2016 and is a replacement of GOES-13 satellite. GOES-18 was launched on March 1, 2022. It replaced GOES-17 on January 4, 2023. The details of these satellites can be found at <https://www.ngdc.noaa.gov/stp/satellite/goes-r.html>. The following instruments are there on board both the GOES satellites

1. Extreme Ultraviolet and X-ray sensors (EXIS, [Machol et al., 2020](#))
2. Magnetometer (MAG)
3. Space Environment In Situ Suite (SEISS)
4. Solar Ultraviolet Imager (SUVI)
5. Advanced Baseline Imager (ABI)
6. Geostationary Lightning mapper (GLM)

The details of these instruments can be found at <https://www.goes-r.gov/downloads/resources/documents/GOES-RSeriesDataBook.pdf>.

2.2.5 Aditya-L1

The first Indian dedicated solar observatory, Aditya-L1 (“Aditya” in Sanskrit means “the Sun”) was launched on September 2, 2023. It was inserted into a halo orbit around the L1 point on January 6, 2024. It is a three-axis stabilized satellite. There are 4 remote sensing and 3 in-situ payloads on board the Aditya-L1 (e.g. [Seetha and Megala, 2017](#)). These are

1. Visible Emission Line Coronagraph (VELC, e.g., [Prasad et al., 2017](#))
2. Solar Ultraviolet Imaging Telescope (SUIT, eg., [Ghosh et al., 2016](#))
3. Solar Low Energy X-ray Spectrometer (SoLEXS, [Sankarasubramanian et al., 2011](#))
4. High Energy L1 Orbiting X-ray Spectrometer (HEL1OS, [Sankarasubramanian et al., 2017](#))
5. Aditya Solar wind Particle EXperiment (ASPEX, [Janardhan et al., 2017](#); [Goyal et al., 2018](#))
6. Plasma Analyzer Package for Aditya (PAPA, e.g., [Janardhan et al., 2017](#))
7. Magnetometer (MAG, [Yadav et al., 2018](#))

In this thesis, differential directional fluxes of different ion species corresponding to energies < 2 MeV (suprathermal and low energy SEPs) of various instruments have been utilized. Some instruments are capable of differentiating between different elements (species) and some provide species integrated ion fluxes. Table [2.1](#) summarizes these instruments and the spacecraft that carry those instruments, field of views (FOVs), energy ranges, measurement techniques, typical thickness of detectors, and the nature of stabilization of the spacecraft.

Here

LEMS120/EPAM: Low Energy Magnetic Telescope, which makes 120° angle with the spin axis of the ACE, of EPAM suite ([Gold et al., 1998](#))

SIT/SEP/IMPACT: Suprathermal Ion Telescope ([Mason et al., 2008a](#)) of the

2.2. INSTRUMENTS

Spacecraft	Instrument	FOV	Energy	Technique	Thickness of detector	Platform
ACE	ULEIS	$24^\circ \times 20^\circ$	0.045–8.2 MeV/n	TOF + residual E	500 μm	Spin stabilized
	LEMS120/EPAM	51° (Cone)	0.047–4.8 MeV	Total E	200 μm	
STEREO-A, B	SIT/SEP/IMPACT	$44^\circ \times 17^\circ$	0.068 – 8.1 MeV/n	TOF + residual E	500 μm	3-axis stabilized
	SEPT/SEP/IMPACT	52° (Cone)	0.06–7 MeV	Total E	300 μm	
Wind	STEP/EPACT	$44^\circ \times 17^\circ$	0.04 – 8.1 MeV/n	TOF + residual E	500 μm	Spin stabilized
Aditya-L1	PS/STEPS/ASPEX	30° (Cone)	0.02 – 10.0 MeV	Total E	300 μm	3-axis stabilized
	NP/STEPS/ASPEX	28° (Cone)	0.02 – 10.0 MeV	Total E	300 μm	
GOES-16, 18	MPSH/SEISS	30° (Cone)	0.05 – 12 MeV	Total E		3-axis stabilized

Table 2.1: List of instruments from which suprathermal particle fluxes are obtained and the necessary specifications.

Solar Energetic Particle (SEP) suite for IMPACT ([Luhmann et al., 2008](#))

SEPT/SEP/IMPACT: Solar Electron and Proton Telescope (Muller Mellin et al., 2008) of the Solar Energetic Particle (SEP) suite for IMPACT ([Luhmann et al., 2008](#))

STEP/EPACT: Suprathermal Energetic Particle instrument of EPACT ([Von Rosenvinge et al., 1995](#))

STEPS/ASPEX: SupraThermal and Energetic Particle Spectrometer, a subsystem of ASPEX payload ([Goyal et al., 2018](#)). Parker Spiral (PS) and north pointing (NP) units are the two sensors of the STEPS subsystems looking towards Parker Spiral, and the ecliptic North respectively.

MPSH/SEISS: Magnetospheric Particle Sensor High energy of SEISS on board GOES-16, 18 (available at <https://www.goes-r.gov/downloads/resources/documents/GOES-RSeriesDataBook.pdf>)

In Table 2.1, the names of the instruments are mentioned in the form of abbreviations and those are expanded below for the sake of completeness. The relevant references are also provided. Based on Table 2.1, it is noted that there are two types of particle detection techniques employed in the above instruments—Total energy measurement (Total E) and the time of flight plus residual energy measurement (TOF + residual E). In addition to the fluxes of suprathermal particles, some other in-situ data such as solar wind speed, proton density, pressure, components of interplanetary magnetic field (IMF) etc. and geomagnetic index, Sym-H are also used in the thesis. The technique for measuring solar wind parameters is different from the above-mentioned techniques to measure energetic particles.

Magnteometers also use different principle of measuring IMF. Brief descriptions of measurement techniques used in PLASTIC (solar wind bulk parameters) and MAG (magnetic field) onboard STEREO spacecraft are also given below.

2.3 Measurement techniques

2.3.1 Total energy measurement in a solid-state detector

When traversing through a solid-state detector (e.g., silicon), energetic charge particles lose energy generally by interactions with nuclei and electrons of the solid-state medium. The amount of energy lost by the charged particle per unit path length through the medium is called the linear stopping power of the medium ($-\frac{dE}{dx}$). Classically, linear stopping power can be expressed by the Bethe formula, which reads as follows.

$$-\frac{dE}{dx} = \frac{4\pi e^4 z^2}{m_0 v^2} N B \quad (2.5)$$

where

$$B = Z \left[\ln \frac{2m_0 v^2}{I} - \ln \left(1 - \frac{v^2}{c^2} \right) - \frac{v^2}{c^2} \right] \quad (2.6)$$

and ze = charge of the particle, m_0 =particle's mass, v = particle's speed, N = number density of medium atoms, Z = proton number of medium atom, and I is the average excitation and ionization potential of the medium atoms. From [Eq. 2.5](#) and [2.6](#), it can be seen that the stopping power of the medium is inversely proportional to the square of the velocity of the charged particle. This means that particles with greater speeds (and with same charged states) will spend less amount of time within a unit length of the medium and will get less time to interact with the atoms of the medium, resulting in less energy deposition within the medium. In addition, it can be further seen that for two particles with same speed, the one with higher charge state will lose more energy. In the thin absorber (solid-state

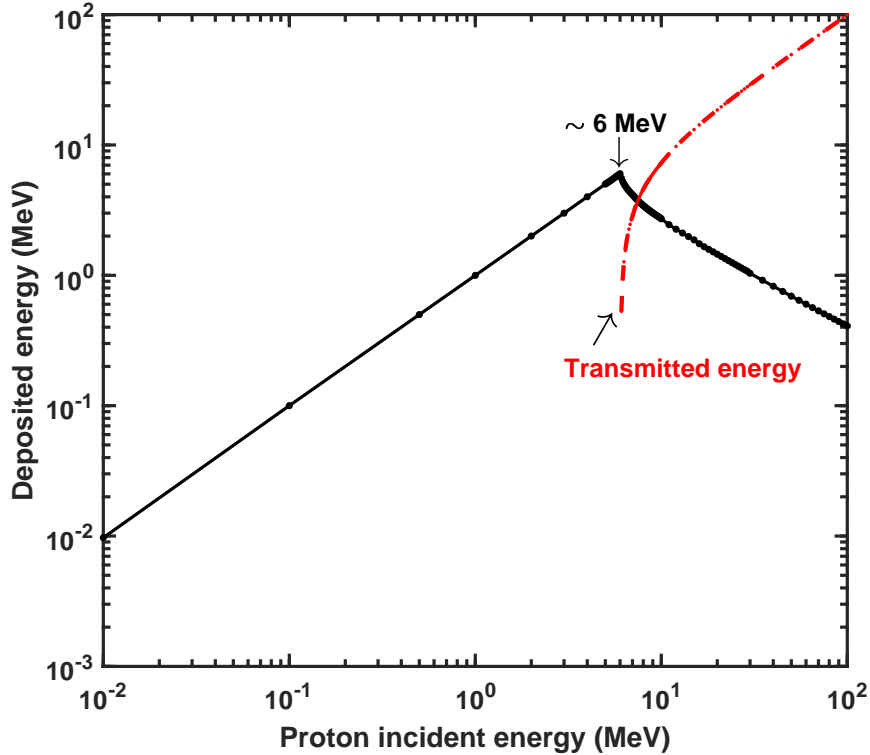


Figure 2.1: Deposited (black) and transmitted (red) energies vs initial energy of protons through a Si detector with thickness of 300 μm .

medium) limit, the energy deposited by a charge particle can be approximated by

$$\Delta E = - \left(\frac{dE}{dx} \right) \times d \quad (2.7)$$

where d is the thickness of the absorber and $\left(\frac{dE}{dx} \right)$ is the linear stopping power inside the absorber. Therefore, any energetic charge particle will continuously lose energy during its course through a solid medium and eventually lose its entire energy. The path length inside the medium up to which a charge particle with a particular energy travels before it loses all of its energy is called the range of the particle through that medium. For two same type of particles with equal charge, the range through a medium will be greater for the particle with greater energy. If the thickness of an absorber is less than the range of a charge particle with particular energy and charge state, a fraction of the particle's initial energy will be deposited inside the absorber. The particle then will penetrate the absorber

thickness travel with the remaining energy.

Figure 2.1 shows that a proton with energies up to 6 MeV will completely deposit their energies in a 300 μm silicon detector. If the proton's incident energy is > 6 MeV, a part of the incident energy will be deposited in silicon and the rest will be carried away by the proton. LEMS120/EPAM, SEPT, STEPS/ASPEX, and MPSH use this technique to detect ions. The thickness of the solid-state detectors of these instruments are mentioned in Table 2.1. A single solid-state detector cannot distinguish between different ion species. One way to separate ions with different masses is the measurement of time-of-flight plus the residual energy of charged particles.

2.3.2 Time-of-flight and residual energy measurement technique

In order to understand this technique, the schematic diagram of SIT instrument (Figure 2.2) is shown. In this configuration, any charged particle has to travel thorough a thin metal foil (here nickel foil is used), which is generally kept at a certain distance (L) above the solid-state detector (Si). Secondary electrons generated from the metal foil due to interaction with the charged particle are collected and the time is recorded. This defines the 'start' of the event (particle detection). A fraction of the particle's energy is lost in this step. When the particle with residual energy (E_{res}) reaches the solid-state detector, again some secondary electrons are produced. These electrons are collected. This defines the 'stop' of the event. The energy of the particle is measured by the solid-state detector. The time of flight (τ) of the particle from the metal foil to the solid-state detector is calculated from 'start' and 'stop' time stamps. The speed of the particle during the course of its journey from the thin metal foil to the solid-state detector is calculated as

$$v = \frac{L}{\tau} \tag{2.8}$$

Suprathermal Ion Telescope (SIT)

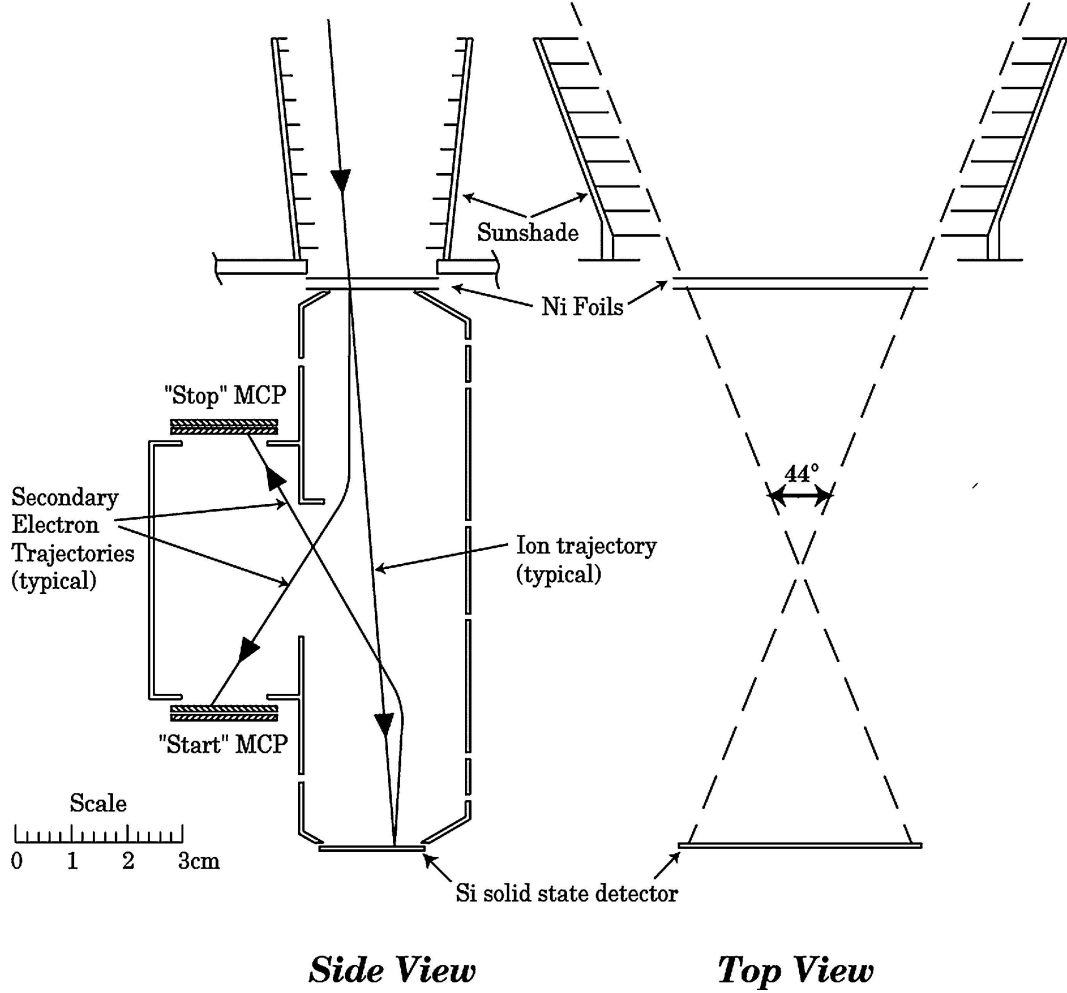


Figure 2.2: Schematic diagram of the cross section of SIT instrument on board STEREO spacecraft. This figure is taken from [Mason et al. \(2008a\)](#).

By using the detected energy $E = \frac{1}{2}mv^2$, mass of the particle can be determined and is given by

$$m = 2E \left(\frac{\tau}{L} \right) \quad (2.9)$$

Once the mass is known, the energy of the particle is corrected for the energy loss in the thin foil. ULEIS, SIT, and STEP use this technique to measure both the energy and mass of different species of the suprathermal and energetic particle populations.

2.3.3 Top hat analyzer (THA): PLASTIC

PLASTIC measures solar wind parameters and elemental composition of low energy heliospheric particles ($\sim 0.3\text{--}80$ keV per electronic charge, keV/e) in the ecliptic plane. The Solar Wind Sector (SWS) of PLASTIC has a FOV of 45° in the ecliptic plane and 40° FOV in the polar plane. There are two channels in SWS instrument: small channel and main channel. The small channel measures the velocity distribution functions of solar wind protons and alpha particles. The final data product of this channel are proton number density, solar wind bulk speed, thermal speed, and alpha to proton ratio. On the other hand, the main channel measures the ionic charge state distribution, compositions of elements, and speeds (both bulk and thermal speeds) of more abundant minor species in the solar wind (e.g., C, O, Mg, Si, and Fe). Another sub-system of PLASTIC is the Suprathermal Ions Wide-Angle Partition Sector (WAP), which measures suprathermal ion distribution in the solar wind in the energy range $0.3\text{--}80$ keV/e. A schematic diagram of PLASTIC instrument is shown in Figure 2.3. It can be seen from Figure 2.3 that energy of incoming particles is selected using a top hat analyzer (energy-per-charge) placed at the top of the unit. Then the selected ions are accelerated and forced to pass through a time-of-flight arrangement. The angle information is extracted using a resistive anode (4 quadrants Q1, Q2, Q3, and Q4). Mass-to-charge ratio of incident ions can be calculated as

$$M/Q = 2 \times (E/Q + |PAC|) \times \alpha \times (\tau/d)^2 \quad (2.10)$$

where E/Q is the energy-per-charge, PAC is the post-acceleration voltage, τ is the time of flight, d is the length of the flight path, and $\alpha(E, M)$ is the mass and energy dependent energy loss in the carbon foil.

The mass of the ions can be determined as

$$M = 2 \times E_{ssd}/\beta \times (\tau/d)^2 \quad (2.11)$$

where $\beta(E, M)$ is a function of the pulse height defect in silicon detector. α and

2.3. MEASUREMENT TECHNIQUES

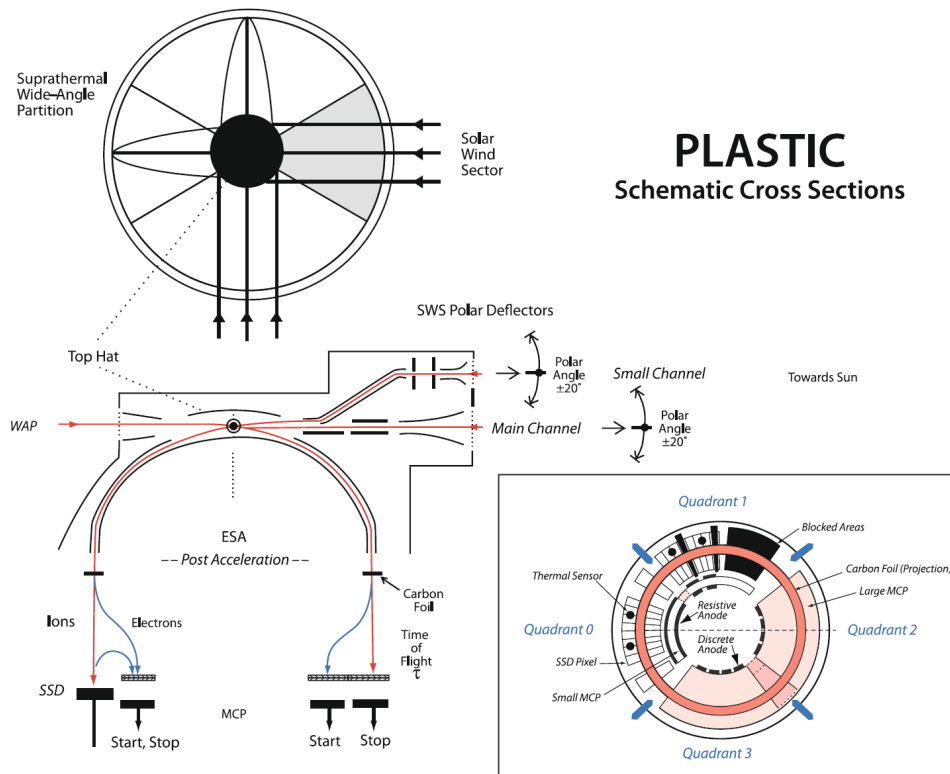


Figure 2.3: Schematic cross section of the PLASTIC instrument on board STEREO spacecraft (taken from Galvin et al., 2008).

β are determined based on pre-flight calibrations and simulations.

2.3.4 Tri-axial fluxgate magnetometer: MAG

The magnetometer (MAG) of IMPACT/STEREO is a tri-axial fluxgate magnetometer that can measure magnetic field vector in two ranges up to 65536 nT and up to 500 nT with 0.1 nT accuracy. A fluxgate magnetometer works on the principle of magnetic induction (Ness, 1970) and is more sensitive in case of fluctuating magnetic field. In order to understand the basic working principle of a fluxgate magnetometer, Figure 2.4 is shown. The magnetic hysteresis of a magnetically saturable transformer, which serves as a sensing element, play a crucial role in the operation of a flux-gate magnetometer. In this case, the second harmonics of the input can provide direct information about the external magnetic field. The non-linear $B - H$ curve is considered a combination of linear segments. A triangular

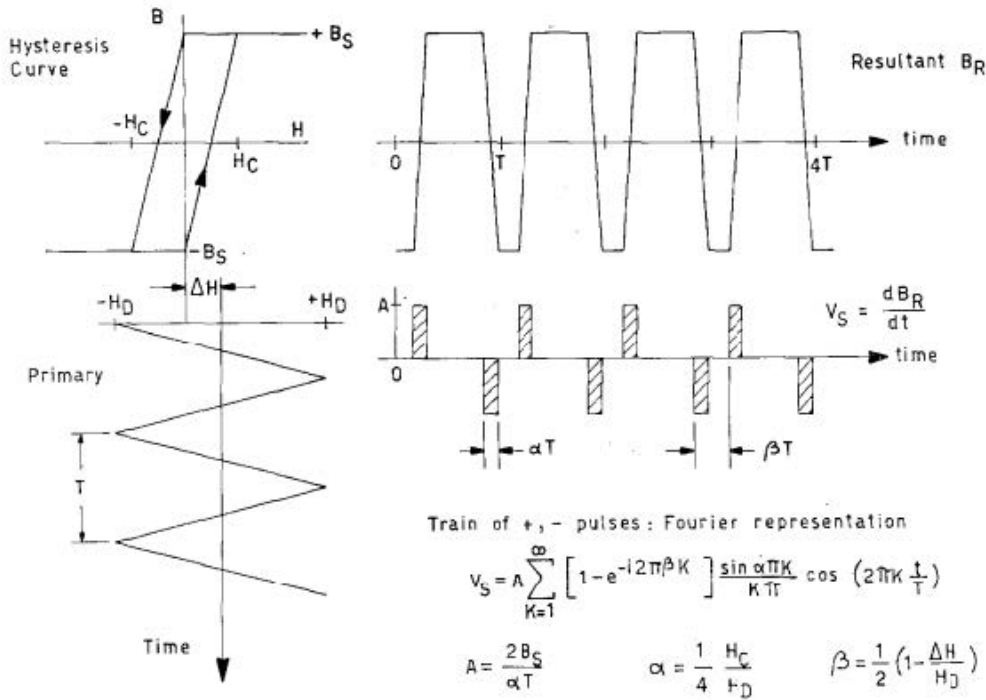


Figure 2.4: Schematic description of working principle of a fluxgate magnetometer (taken from [Ness, 1970](#)).

wave with a frequency of $1/T$ and an amplitude of H_D is applied to the primary coil. The core material within the primary coil saturates when the magnetic field strength, H , reaches $\pm H_C$ (as shown in Figure 2.4) and the magnetic induction B reaches $\pm B_S$. Although a sinusoidal wave is typically used, a simple triangular wave is depicted here for clarity, without compromising the operational principle ([Ness, 1970](#)). It is assumed that the $+\Delta H$ is the bias introduced by the external magnetic field (here the solar wind magnetic field). The resulting magnetic field, B_R is shown in Figure 2.4. The induced output signal of the sensing coil depends on the $\frac{\partial B_R}{\partial t}$. When the flux varies, an output will be observed, but there will be no output when the flux is restricted to positive or negative saturation levels. Figure 2.4 illustrates a consistent pattern of alternating positive and negative pulses. The width of these pulses is denoted as αT , and the interval between successive pulses is βT or $(1 - \beta)T$. The alternating saturation of the core in opposite directions generates the 'gated flux,' which is detected by the secondary coil. Fourier analysis of the output waveform results in the formulas displayed in Figure 2.4. It is noted

2.4. DATA SOURCES

that α is independent of ΔH , while β depends on $\Delta H/H_D$. In the absence of any external field ($\Delta H = 0$), the even harmonics of the square bracketed term in the expression of V_s becomes zero. These are non-zero in the presence of external magnetic field. The amplitudes of the second harmonics are used to calculate the ambient magnetic field. The details of the technique can be found in [Ness \(1970\)](#).

2.4 Data sources

Suprathermal and energetic particle fluxes, sunspot numbers, solar wind parameters, solar images, positions of different spacecraft are obtained from the following sites

1. <https://cdaweb.gsfc.nasa.gov/index.html>: Particle fluxes and solar wind parameters data
2. <https://omniweb.gsfc.nasa.gov/form/dx1.html>: Solar wind parameters
3. <https://www.sidc.be/SILSO/datafiles>: Sunspot number data
4. <http://www.ipshocks.fi/database>: IP shock database
5. <https://www.ngdc.noaa.gov/stp/satellite/goes/dataaccess.html>: GOES data
6. <https://www.ngdc.noaa.gov/stp/satellite/goes-r.html>: GOES-R series data
7. <https://solar-mach.streamlit.app/?embedded=true>: Instantaneous position of satellites
8. <https://cdaw.gsfc.nasa.gov/>: CME properties
9. <https://helioviewer.org/>: Solar activity images and movies

2.5 Catalogues

In thesis, catalogues of various transient events like IP shocks, ICMEs, SIR, stealth CMEs are used. The URLs for these sites are provided below.

1. http://www.ssg.sr.unh.edu/mag/ace/ACElists/obs_list.html#1998: ACE list of disturbances and turbulences:
2. https://stereo-ssc.nascom.nasa.gov/data/ins_data/impact/level3/: STEREO SIR catalogue
3. [https://izw1.caltech.edu/ACE/ASC/DATA/level3/icmetable2.htm#\(c\)](https://izw1.caltech.edu/ACE/ASC/DATA/level3/icmetable2.htm#(c)): Richardson and Cane ICME catalogue
4. <https://doi.org/10.1007/s11214-021-00857-0>: List of ICMEs associated with "stealth" CMEs

2.6 Data used in different thesis chapters

2.6.1 Chapter 3

1. Differential directional fluxes of H, ^4He , ^3He , C, O, and Fe are obtained from ULEIS instrument on board ACE (during 1998–2020)
2. Sunspot number data

2.6.2 Chapter 4

1. Differential directional fluxes of ^4He , O, and Fe are obtained from SIT instrument of SEP suite, a part of IMPACT investigation on- board STEREO-A, B. (during 2007–2014)
2. Solar wind parameters obtained from PLASTIC on board STEREO-A
3. Components of IMF from the Magnetometer on board STEREO-A
4. Solar images in the extreme ultra-violet (19.5 nm) captured by Extreme Ultra-Violet Imager of the Sun Earth Connection Coronal and Heliospheric Investigation (SECCHI)
5. List of SIRs observed by STEREO-A, B

2.6.3 Chapter 5

1. Differential directional fluxes of H, ^4He , and CNO obtained from the STEP instrument of EPACT investigation on board the Wind spacecraft (during 2012–2014)
2. Components of IMF from OmniWeb

2.6.4 Chapter 6

1. Differential directional fluxes of ions obtained from STEPS/ASPEX on board the Aditya-L1 (during September 11–19, 2023)
2. Differential directional fluxes of ions obtained from LEMS120/EPAM on board ACE
3. Differential directional fluxes of ions obtained from SEPT of SEP suite, a part of IMPACT investigation on board on board STEREO-A
4. Differential directional fluxes of protons observed by MPSH/SEISS on board GOES-16, 18

Chapter 3

Characteristics of “quiet” suprathermal particles in the interplanetary medium

Excerpt

The origin and acceleration processes of background “quiet” suprathermal particles in the heliosphere are outstanding science issues where a number of ideas have been floated over the years but the field has still remained wide open as no single process seems to explain all the characteristic observational features. In this chapter, the behaviors of “quiet” time suprathermal particles (H and heavy ions like ^4He , ^3He , C, O, and Fe) are investigated using < 1 MeV per nucleon (MeV n^{-1}) ion flux data from the Ultra-Low Energy Isotope Spectrometer on board the Advanced Composition Explorer over solar cycle 23 and 24. In order to address this problem, a set of criteria is defined first for the identification of “quiet” time. Subsequently, cross correlation investigation of the variation of suprathermal fluxes with the variations in the sunspot numbers is performed to understand the influences of solar processes on the generation of suprathermal particles in the interplanetary (IP) medium. This investigation reveals that maximum cross-correlation coefficient is obtained when the quiet-time suprathermal ^4He shows positive lags in solar cycle 23 and negative lags in cycle 24. Interestingly, Fe shows no negative lag in solar cycle 24. Lags of other elements are found to be inconsistent and mostly around zero. The differential behavior of ^4He and Fe is also visible in their spectral in-

dices calculated over different phases of solar cycles. This contrast is particularly prominent during the descending phase of solar cycle 24. On the contrary, variations in spectral indices for C and O are found to be similar over all the phases of the solar cycles. These observations suggest a modulation of quiet-time suprathermal particles in the IP medium depending on the first ionization potential and mass-to-charge ratio of different ion species.

3.1 Introduction

Suprathermal particles with energies in the range $\sim 0.01\text{--}1.0$ MeV n^{-1} are ubiquitous in the heliosphere. Although not so energetic in terms of damaging space assets, these particles play crucial role in providing the seeds for solar energetic particles (SEPs) accelerated by IP shocks associated with coronal mass ejections (CMEs) (e.g., [Gosling et al., 1981](#); [Desai et al., 2003, 2004](#) etc.) and stream/corotating interaction regions (SIR/CIRs) ([Fisk and Lee, 1980](#); [Chottoo et al., 2000](#); [Giacalone et al., 2002](#); [Ebert et al., 2012](#) etc.). The concerned acceleration mechanisms like diffusive shock acceleration (DSA) ([Krymskii, 1977](#); [Bell, 1978](#) etc.) and acceleration by gradual compression regions (e.g., [Giacalone et al., 2002](#)) are discussed in Chapter 1. One of the most important observations regarding suprathermal ion populations is their presence in the IP medium irrespective of local solar wind conditions at any point of solar cycle. These ions are observed even in the absence of any transient events like shocks or SIR/CIRs. These “quiet” time particles are believed to constitute the suprathermal ion pool in the IP medium. The sources of the suprathermal ion pool are manifold ([Mason, 2000](#)) and are already discussed in Chapter 1.

Earlier observations suggest that the differential directional flux (phase space density, PSD) of suprathermal particles varies as a power of energy (velocity) ([Gloeckler, 2003](#); [Fisk and Gloeckler, 2006, 2007](#) etc.). This power spectrum is essentially the higher energy part of a generalized Maxwellian distribution, called the Kappa distribution ([Pierrard and Lazar, 2010](#); [Lazar et al., 2012](#)). On some occasions, the “quiet” time spectral index is observed to be -5 ([Fisk and Gloeckler,](#)

3.1. INTRODUCTION

2006) in the phase space density vs velocity representation, which is equivalent to -1.5 in the differential flux vs energy approach. Multiple theories have been proposed to explain the generation of the -5 spectral index of suprathermal particles. For example, Fisk and Gloeckler (2007, 2008, 2014) proposed the pump mechanism, according to which, particles are accelerated during quiet times by large-scale compressions and rarefactions in the solar wind. However, there are many studies that have reported suprathermal spectral indices deviating from spectral index of -5 (-1.5) (Gloeckler, 2003; Mason and Gloeckler, 2012; Dayeh et al., 2017 etc.). Many researchers (Dayeh et al., 2009, 2017) have reported double power law spectra in the energy range of 0.11–1.28 MeV n^{-1} . These observations indicate towards the difficulty in characterizing the acceleration mechanism of quiet time suprathermal ions in terms of a single process.

There are variations in the composition of quiet time suprathermal particles also. Kecskemety et al. (2011) investigated the possible sources of low-energy suprathermal ions with the help of composition analysis using ACE, Wind, and SOHO data. They checked abundance ratios of Fe/O, Fe/CNO, Ne-S/O, and C/O during 1998-2011, which encompasses the minimum of solar cycle 23 (SC23). It was found that Fe/O ratio during 50% of the quiet periods, excluding the minimum of SC23, corresponds to the mean coronal Fe/O ratio. It resembles the solar flare abundance during the rest 50% of the quiet periods. Interestingly, Fe/O ratio during the SC23 minimum was reported to be similar to that found in solar wind. Owing to the difference in the Fe/O ratios during quiet time intervals, these authors suggested different seed populations that are accelerated at different phases of the solar cycle. Solar cycle variations of C/O, Fe/O, and $^3\text{He}/^4\text{He}$ at 1 AU have been studied during SC23 and SC24 by Dayeh et al. (2017). These authors have found clear solar cycle dependence of these abundance ratios. They have reported correlation coefficients of -0.62, 0.89, and 0.90 between annual mean sunspot number (SSN) and C/O, Fe/O, and $^3\text{He}/^4\text{He}$, respectively. Fe/O ratio resembles that of gradual solar energetic particles (GSEPs) during solar maxima and that of solar winds during minimum of solar cycle. It has been concluded by Dayeh et al. (2017)

that particles accelerated by shocks and remnant flare particles possibly have the major contribution in the suprathermal population at 1 AU during enhanced solar activity. On the other hand, SIR/CIRs and heated solar wind contributes to the suprathermal ions during minima of solar activity. Interesting, C/O ratio neither matches with GSEPs not with the solar wind values. In addition, these authors have found a spectral rollover in the C–Fe spectra in the energy range of 0.11–1.28 MeV n⁻¹. The low energy (0.11–0.32 MeV n⁻¹) spectral indices lie in the range 1.40–2.97 in the differential flux vs energy representation. The spectra are observed to steepen in higher energy range (0.46–1.28 MeV n⁻¹). No correlation was found between the spectral indices of heavy ions and the SSN. Looking at the wide variations in spectral indices and composition ratios these authors suggested that quiet time suprathermal particles are transported from regions far away from the observation location. These particles are then accelerated locally by different processes as discussed in Chapter 1.

Regardless the exact nature of the seed population and the process(s), it is expected that charged suprathermal population will be modulated while they wander in the IP medium in the presence of interplanetary magnetic field (IMF). During the course of modulation, these particles should exhibit systematic time delay with solar activity proxies (for example, SSN). Time delay (lag) analysis with respect to the SSN has already been attempted for SIR/CIR-associated suprathermal particles (Mason et al., 2012; Allen et al., 2019). However, for quiet time suprathermal particles, this has not been attempted and can be done to gain new insights on the generation of the suprathermal population in the IP medium. Also, the nature of IP modulation for different elements is not known. Therefore, a detailed comparison of lags (associated with cross-correlation) between quiet time suprathermal particles and SSN and spectral indices may give us new insights on the sources and propagation of these ions through the IP medium. In this chapter, these issues are addressed using particle flux measurement from the L1 point during SC23 and SC24. The results reveal interesting differences in the behaviors of different suprathermal elements in SC23 and SC24.

3.2 Data used

Differential directional fluxes of H, ^4He , ^3He , C, O, and Fe (with energies 0.1–1.0 MeV n^{-1}) obtained from ULEIS on board ACE spacecraft and sunspot number data during 1998–2020 have been extensively analyzed in this study. The details of measurement techniques used in ULEIS has already been discussed in Chapter 2.

3.3 Identification scheme for the “quiet” periods

It is observed that suprathermal ion fluxes are enhanced on many occasions by many orders of magnitude above the background level. These increments may be associated with SIR/CIRs, CME-associated shocks etc. Enhancements in fluxes are also different for different elements. An example is shown in Figure 3.1 (a) and (c) where temporal variations of H and ^4He fluxes, respectively, at different energy channels during June 2–August 3, 2007 are shown. The interval bounded by the red and blue dashed vertical lines corresponds to flux enhancement due to a CIR event as reported by [Allen et al. \(2019\)](#). It is not intended to identify the other enhancements seen in Figure 3.1 (a) and (c) and these are called non-CIR transient events. Therefore, in order to identify a “quiet” background, it is essential to remove the intervals associated with the transient enhancements in the observed flux. Choosing a flux cut-off and subsequently removing fluxes above that cut-off value is one way to do that ([Kecskemety et al., 2011](#)). However, in that case, the transient flux enhancement events in which the enhancements are below the defined cut-off will get mixed up with the quiet period. Therefore, in this work, the transient events are removed entirely from start to end by visual inspection to minimize the contribution of any transient event to the “quiet” time data. Further, this is done for the six elements (i.e., H, ^3He , ^4He , C, O, and Fe) independently as the durations of the “quiet” times are not identical for every element. Figure 3.1 (b) and (d) show variations of the quiet time H, and ^4He fluxes corresponding to Figure 3.1 (a) and (c), respectively. Figure 3.2 shows the complete sets of

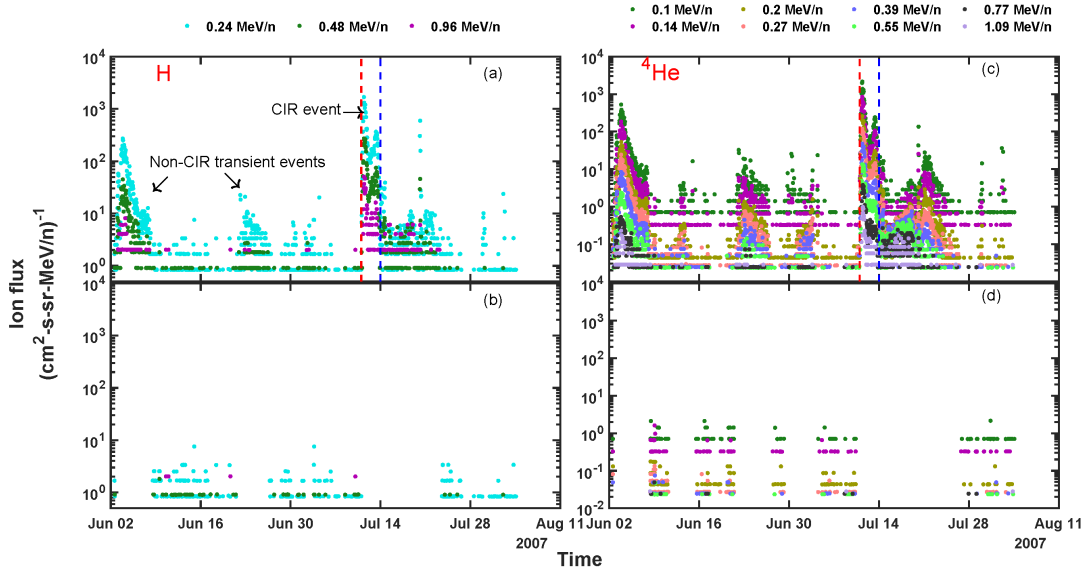


Figure 3.1: Identification of “quiet” time intervals in the variation of suprathermal fluxes . Panel (a) shows the original H fluxes at three energy channels as observed by ACE/ULEIS during June 2 – August 3, 2007. Mean values of the energy channels are mentioned at the top of each panel. Enhancement in H fluxes due to a CIR event (reported in [Allen et al., 2019](#)) is marked between red-blue vertical dashed lines . Other enhancements in H fluxes are termed as non-CIR transient events. The corresponding quiet fluxes are plotted in panel (b). Original and quiet ^4He flux variations at nine energy channels are shown in panel (c) and (d), respectively.

original and quiet background fluxes of the six elements considered during the whole data interval. Note, quiet has been kept within quotes so far to highlight that the selection of “quiet” period can be subjective to some extent. However, to keep the subsequent description simple, the quotes will be dropped around the word quiet from this point onwards. The original variations of H fluxes at different energy channels are shown in panels (a) and (b) represents the corresponding quiet time variations. Similarly, panels (c) and (d) show the original and quiet fluxes, respectively, for ^4He . Original and quiet ^3He fluxes are plotted in panels (e) and (f), respectively. Panels (g), (i), and (k) show the original flux variations of Fe, C, and O, respectively. The corresponding quiet backgrounds are shown in panels (h), (j), and (l). The above exercise automatically brings out the cut-off/threshold values for fluxes of different elements. For example, it comes out that 0.24 MeV

3.3. IDENTIFICATION SCHEME FOR THE “QUIET” PERIODS

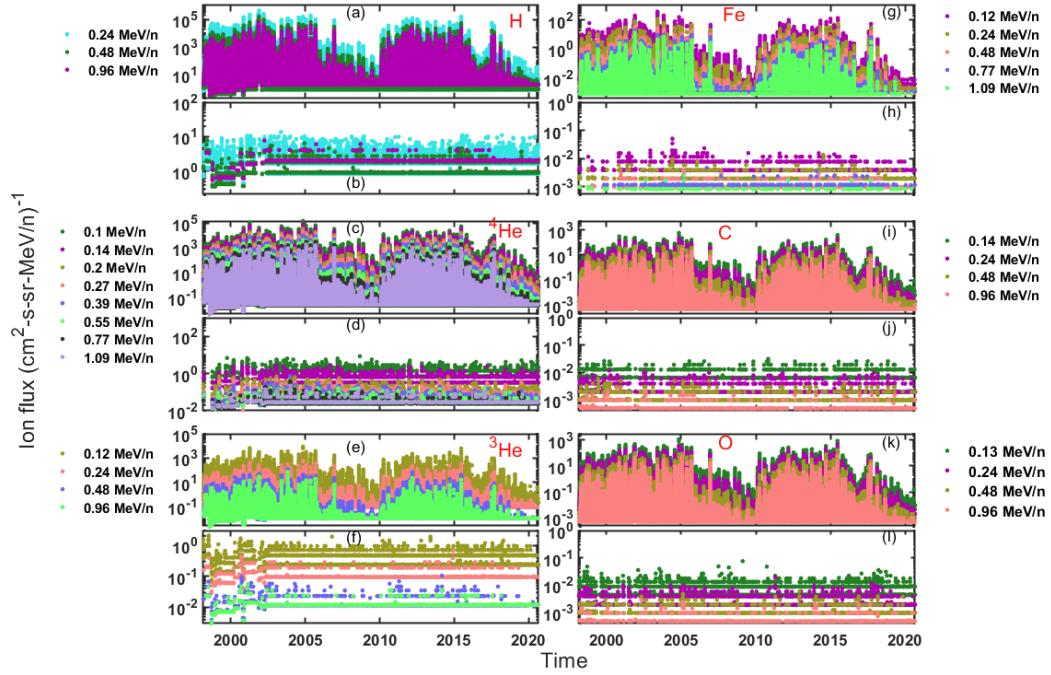


Figure 3.2: Plots for original and “quiet” fluxes for the six elements during the 1998 – 2020. The original flux variations of H, ^4He , ^3He , Fe, C, and O are shown respectively in panel (a), (c), (e), (g), (i), and (k). The corresponding “quiet” fluxes in the similar order are plotted in panel (b), (d), (f), (h), (j), and (l). The mean energies for each of the elements are also mentioned at the left and right of the Figure.

proton flux has a upper threshold value of around 10 particles/($\text{cm}^2\text{-sr-s-MeV}$) during the quiet times. Despite all these, it is still possible that some minor contributions from transient events are still present in the quiet time dataset. To address this issue, a rigorous sensitivity analysis is performed by choosing different cut-off/threshold values for fluxes of different elements at different energy channels. This aspect is discussed later in this chapter. In the subsequent section, a detailed correlation analysis between the particle fluxes at different energy channels and the SSN data is performed after obtaining the quiet time fluxes for the six elements under consideration.

3.4 Results

3.4.1 Cross-correlation analysis (SSN vs. Flux) and sensitivity analysis for the choice of lags

In order to find correlations between the quiet time suprathermal ion flux and SSN, SC23 and SC24 are treated separately. In both the solar cycles, the flux and SSN data are subjected to moving average in which the averaging windows from 240 days to 400 days with an increment of 10 days. This is done to test that the results coming out of the present analyses are invariant regardless of the choice of the size of averaging window. The averaging window is also kept sufficiently more than 180 days so that the variation of the heliospheric current sheet (e.g. [Kasper et al., 2007](#)) with respect to the spacecraft does not affect the correlation analysis. Figure 3.3 shows the variations of 240 days averaged ion fluxes at different energy channels along with 240 days averaged SSN data. For better visuals, ^4He , ^3He , C, O, and Fe fluxes are multiplied by some factors mentioned in the header of each column of Figure 3.3 (a) and (b). These plots show good correlations between the ion fluxes and the SSN.

For each averaging window mentioned above, maximum correlation coefficient and corresponding lag between averaged ion flux at each energy channel and SSN are calculated. To check the significance of these correlation coefficients, first the lags are applied to the time series data. Then, the Pearson's correlation coefficients and corresponding p values (defined as the probability of acceptance of null hypothesis that these correlations are occurring by chance) are calculated between the lagged fluxes and SSN. This method is illustrated in Figure 3.4. 370 days averaged $0.55 \text{ MeV n}^{-1} ^4\text{He}$ flux and SSN data during SC23 and SC24 are shown in panel (a) of Figure 3.4. The flux data are then shifted in the right side or the left side of SSN to maximize the correlation coefficients. Panels (b) and (c) show the results obtained after this analysis scheme is applied. As can be seen from panel (b), maximum cross correlation (marked by red vertical line) occurs in SC23 when the flux data is shifted leftward. On the other hand, the flux data has to

3.4. RESULTS

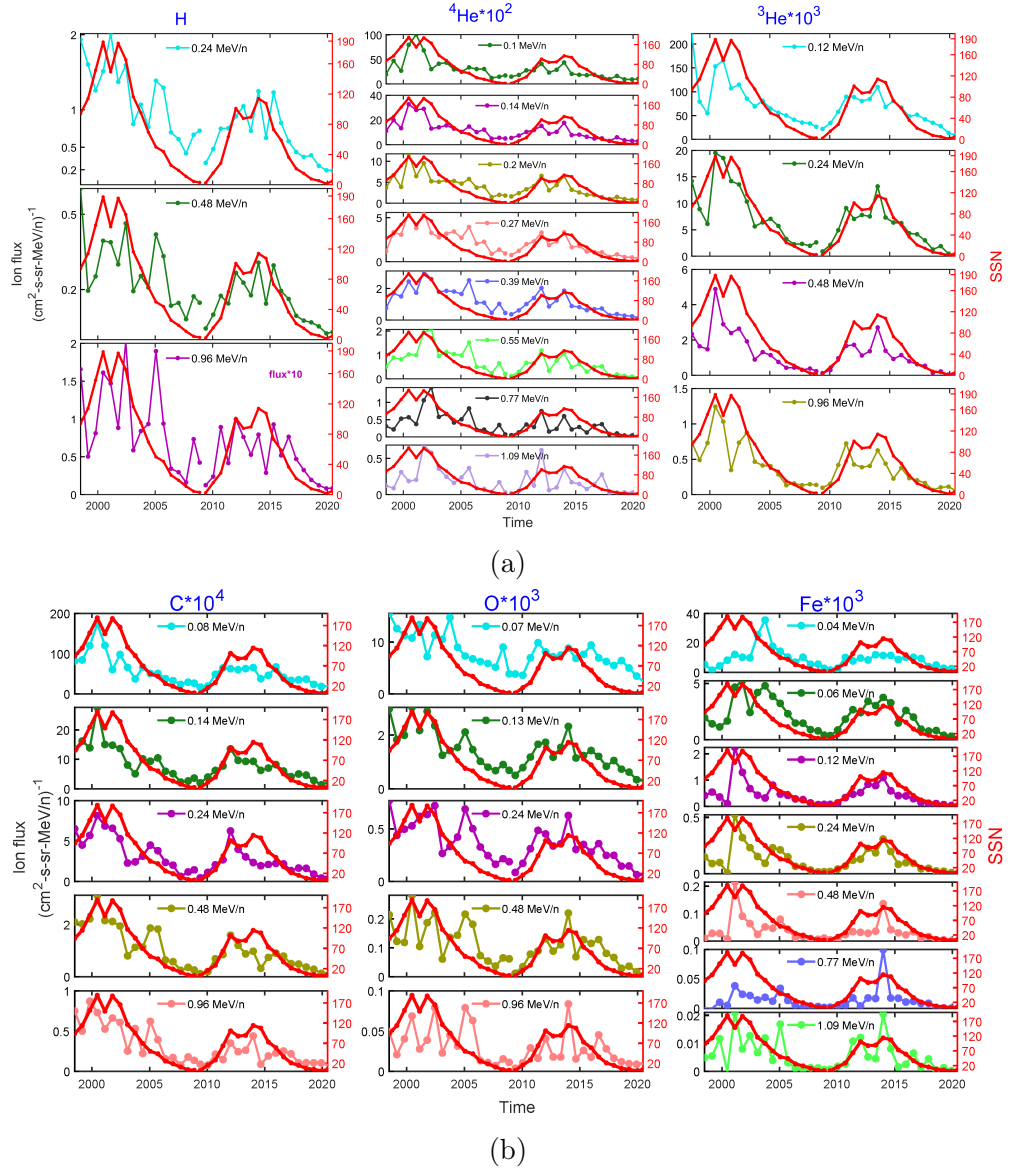


Figure 3.3: Variations in 240 days' averaged fluxes and SSN are shown for each suprathermal element and different energy channels. Figure (a) shows the variations for H, ${}^4\text{He}$ and ${}^3\text{He}$ fluxes and Figure (b) shows the variations of C, O, and Fe fluxes. Individual suprathermal elements are mentioned at the top of each panel. Except for H, all other flux values are multiplied by constant factors mentioned at the top of each panel. Different energy channels are marked by different colors.

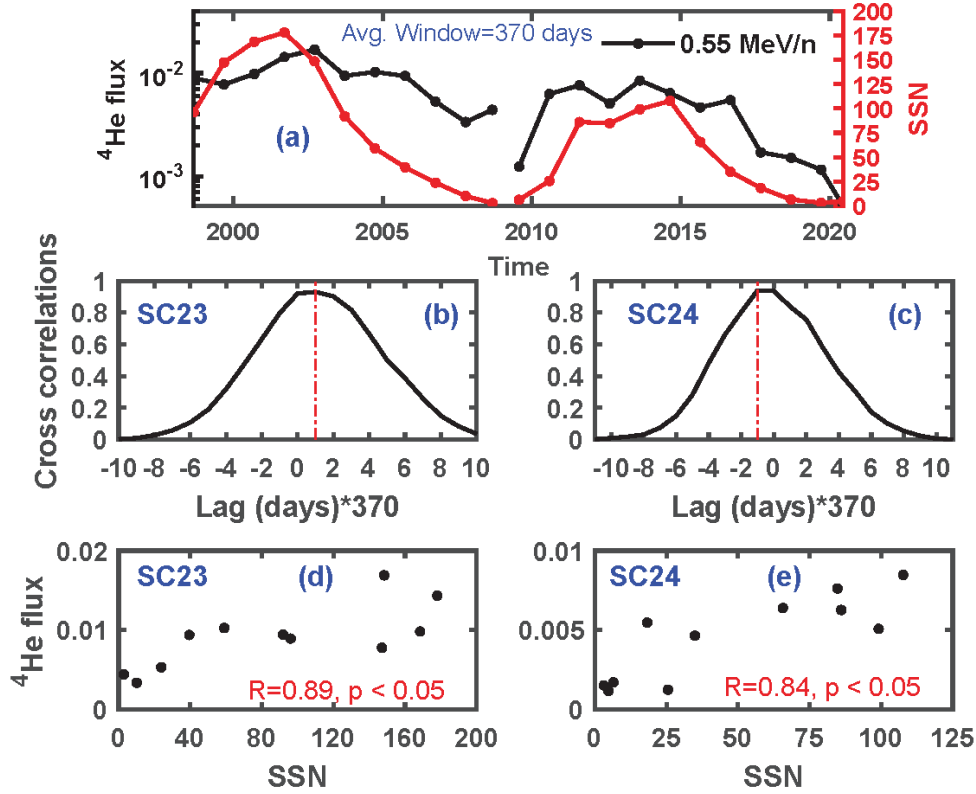


Figure 3.4: Illustration of method for calculating lag and Pearson's correlation coefficients between averaged ion flux and SSN. Panel (a) presents variations of 370 days' averaged 0.55 MeV n^{-1} ^4He flux and SSN data in SC23 and SC24 separately. Variations of cross-correlation coefficients between flux and SSN with respect to the lags in SC23 and SC24 are shown in panels (b) and (c), respectively. The maximum cross-correlations in both the solar cycles are marked by red vertical dashed lines. The lags between ^4He flux and SSN are defined as the value in the abscissa where the red lines intersect. The lag values are then adjusted in the ^4He flux variations to make the ^4He fluxes and SSN in phase. The scatter plots in panels (d) and (e) represent variations of the adjusted ^4He fluxes in SC23 and SC24, respectively, with respect to the SSN. The Pearson's correlation coefficients and p values between these two quantities are also mentioned.

shift rightward in SC24 to maximize the cross-correlation coefficients. Therefore, a positive lag value indicates that the flux variation lags the SSN variation. A negative lag value refers to the situation when increase in flux has started earlier than increase in SSN variation. Once the nature of the lags are known, the flux data are adjusted for these lags in both the cases and the Pearson's correlation coefficients as well as corresponding p values are calculated and shown in panels

3.4. RESULTS

(d) and (e) of Figure 3.4. In both SC23 and SC24, the Pearson's correlation coefficients are > 0.8 and p values (probability of acceptance of the null hypothesis that these correlations do not occur by chance) are < 0.5 . This indicates strong correlations between flux data and SSN data with the presence of noticeable lags. The complete variations of Pearson's correlation coefficients between ion fluxes

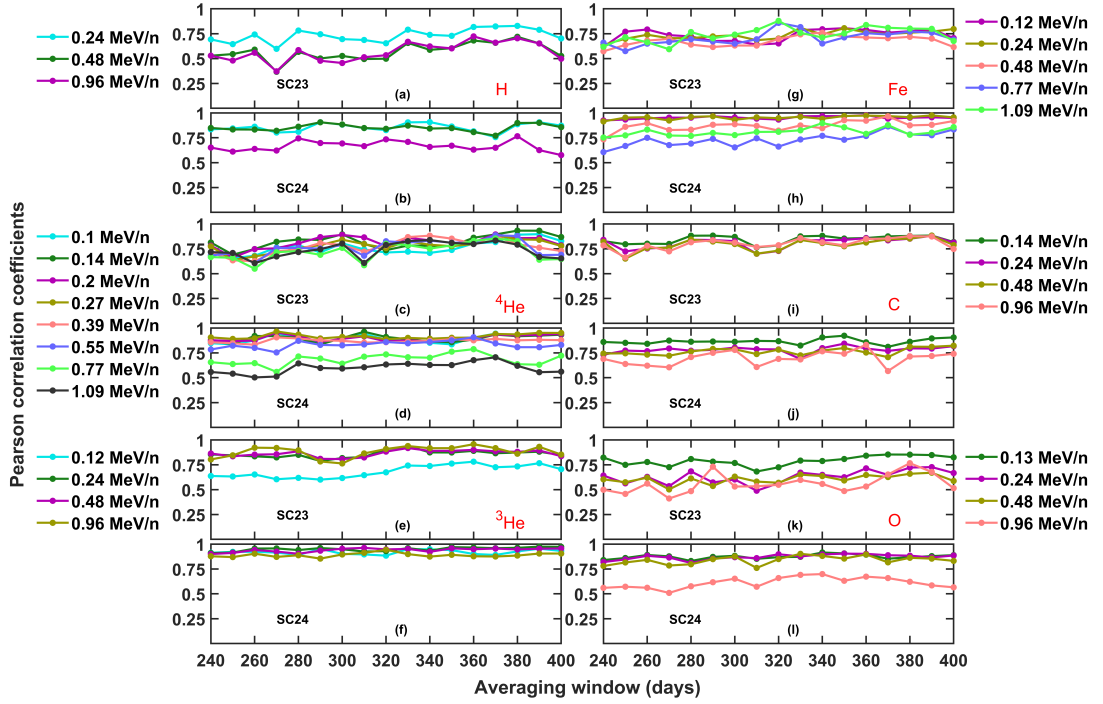


Figure 3.5: Variations of Pearson's correlation coefficients between lag-adjusted quiet time suprathermal ion fluxes at different energy channels and SSN with respect to the averaging windows. The Pearson's correlation coefficients are calculated for both SC23 and SC24. Panels (a), (c), (e), (g), (i), and (k) depict the fluctuations in correlation coefficients for H, ^4He , ^3He , Fe, C, and O, respectively, throughout SC23. Conversely, panels (b), (d), (f), (h), (j), and (l) illustrate the corresponding variations during SC24. The energy channels of concerned elements are mentioned in the left and right side of the figure.

and SSN in SC23 and SC24 are plotted with respect to averaging windows in Figure 3.5. The Pearson's correlation coefficients between lagged flux and SSN data are seen not to vary significantly with the averaging window. The p values in most of the cases are found to be < 0.05 . Variations of lags corresponding to each point in Figure 3.5 are shown in Figure 3.6. This figure reveals some interesting features. It can be seen from Figure 3.6 (a) that H does not lag the SSN for all

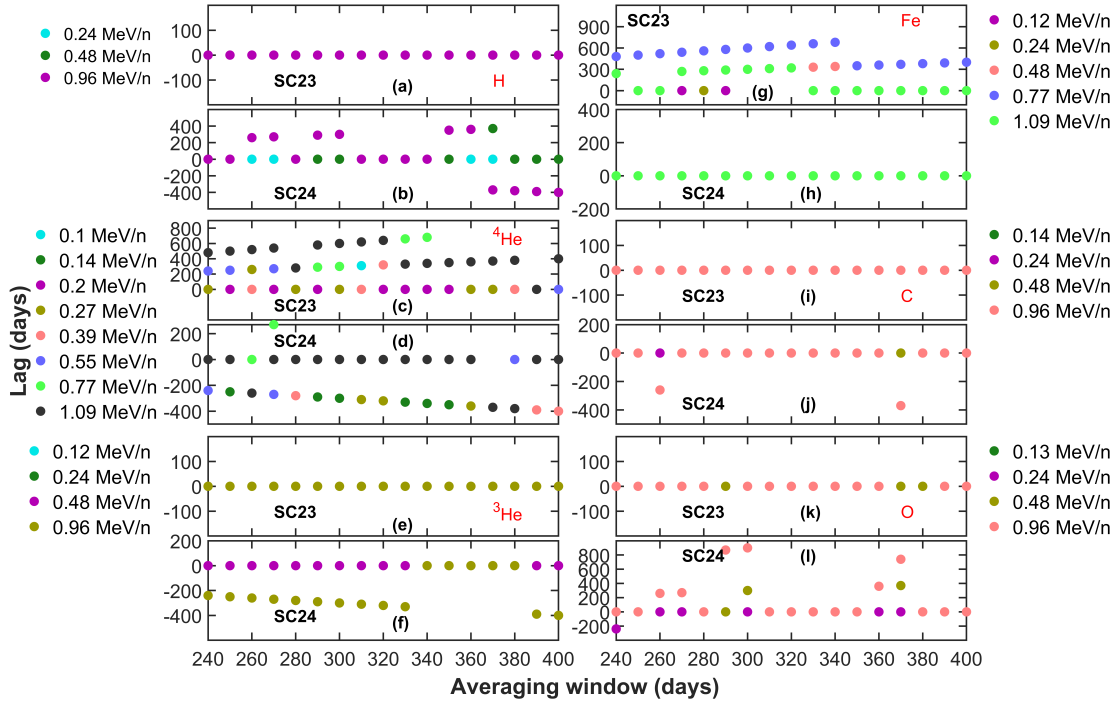


Figure 3.6: Variations of the lags between the quiet-time averaged ion fluxes at different energy channels and SSN with respect to the averaging windows. Panels (a), (c), (e), (g), (i), and (k) illustrate the variations of the lags for H, ^4He , ^3He , Fe, C, and O, respectively, during SC23. Panels (b), (d), (f), (h), (j), and (l) depict the same during SC24. Energy channels corresponding to H, ^4He , and ^3He are written on the left side of the left column of the figure. The same corresponding to Fe, C, and O are mentioned on the right of the right column of the figure.

the energy channels in SC23 while in SC24 (Figure 3.6 (b)), inconsistent lag in H fluxes can be seen. At this point, it must be noted that the differently colored legends for different energy channels are overlapped in the figure making it difficult to identify each color distinctly. This happens for all the subplots. From panel (c), it is clear that ^4He fluxes show zero or positive lags in SC23. On the other hand, there are zero and negative lags (panel (d)) with respect to the SSN in SC24. This indicates that ^4He lags are of opposite natures in SC23 and SC24. Panel (e) and (f) of Figure 3.6 bring out that there is no time delay in the variations of ^3He fluxes with respect to the SSN variations, while only 0.96 MeV n^{-1} ^3He flux shows negative lags on some occasions. It can be seen from panel (g) of Figure 3.6 that Fe fluxes show zero and positive lags with respect to SSN in SC23. In

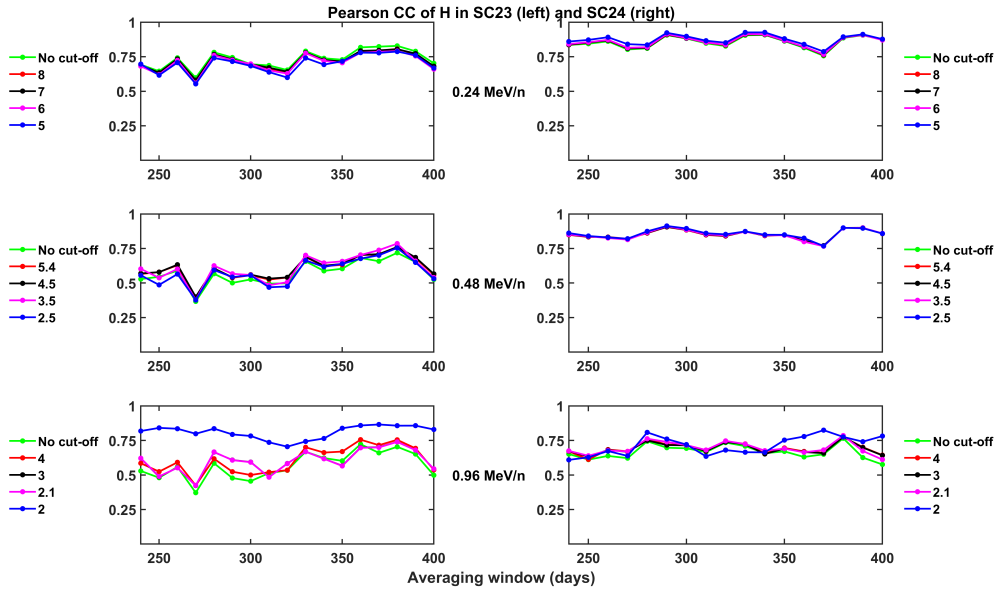
SC24, only zero lags are observed for Fe fluxes. The behavior of Fe fluxes in SC24 is completely opposite to that of ^4He fluxes in SC24. Panel (h) and (i) show that C fluxes exhibit zero lag with respect to SSN in both the solar cycles. Almost similar variation is observed for O fluxes as well, which is depicted in panel (k) and (l).

To validate the values of Pearson's correlation coefficients and lags, rigorous sensitivity analysis is performed by choosing 4 sets of cut-offs in the ion fluxes. The above-described method is repeated for these 4 sets of flux thresholds. Figure 3.7 shows the variations of Pearson's correlation coefficients and lags for the six elements corresponding to the 4 cut-offs in ion fluxes. Figure 3.7 (a)-(f) present the variations in Pearson's correlation coefficients between H, ^4He , ^3He , C, O, and Fe fluxes and SSN with respect to the variations in the averaging window for (1) no-cut-off as far as the background flux level is concerned and (2) four different cut-off levels in the background flux levels. It can be seen that the Pearson's correlation coefficients are, in general, consistent and independent of the levels of cut-offs chosen. Therefore, this exercise reveals that as long as the cut-off levels are below certain flux level, the correlation coefficients do not get affected significantly with the averaging window chosen. Figure 3.8 (a)-(f) reveals the lags are also nearly independent of the averaging window as long as the cut-off levels are below certain flux level. This exercise validates our method for obtaining quiet background flux levels.

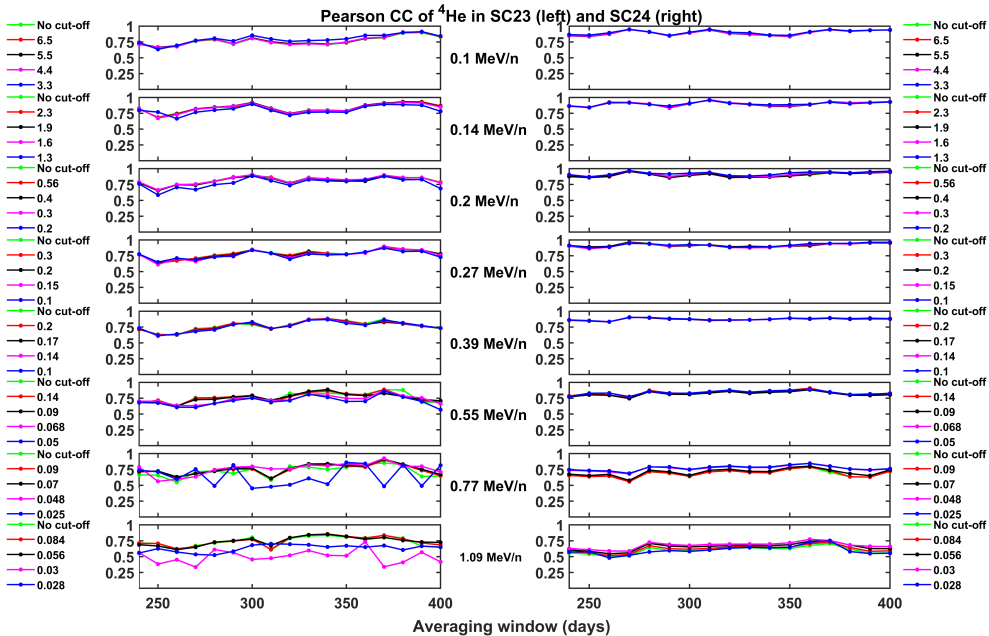
3.4.2 Variations in spectral indices of different elements at different phases of solar cycles

Since Correlation coefficients between SSN and Suprathermal fluxes indicate solar connection and lags indicate IP modulation of these particles, the previous sections indicate that, on many occasions, the IP modulations of the suprathermal particles occur for a large duration which sometimes extends to 100s of days. In this section, the spectral slopes of suprathermal elements are explored during quiet times at various phases of the two solar cycles to investigate the changes

CHAPTER 3. QUIET TIME SUPRATHERMAL PARTICLES

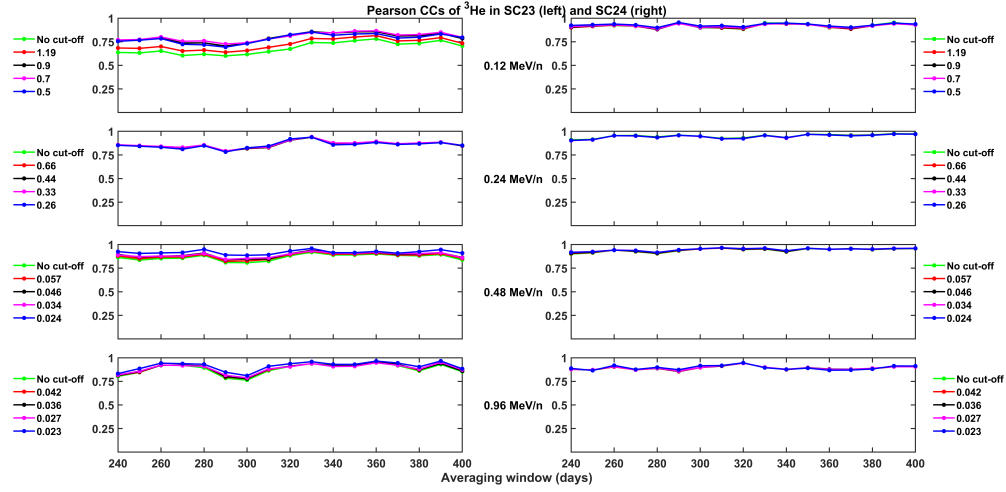


(a) Variations of Pearson CCs with respect to the averaging window for H fluxes at different energy channels (mentioned in between the columns) in SC23 (left) and SC24 (right). Five colors correspond quiet time fluxes of H with no cut-off and for 4 set of cut-off values for fluxes. The cutoff values are written in the left (SC23) and right (SC24) sides of the figure

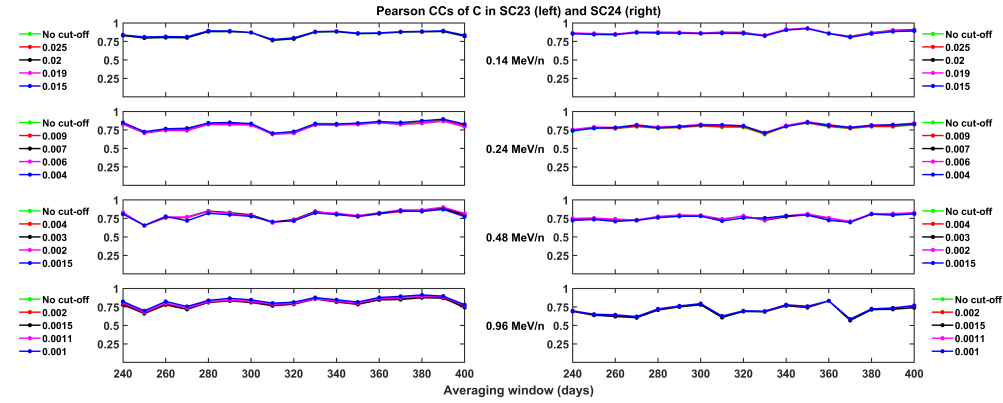


(b) same as 3.7a but for ^4He

3.4. RESULTS

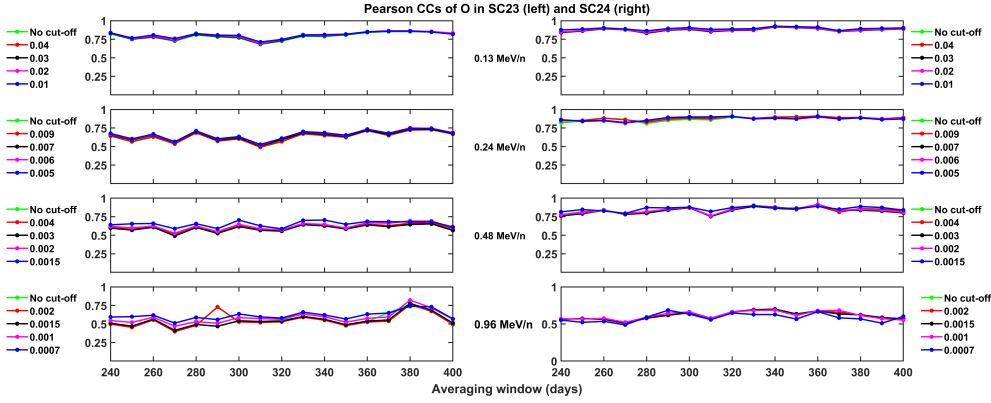


(c) same as 3.7a but for ^3He

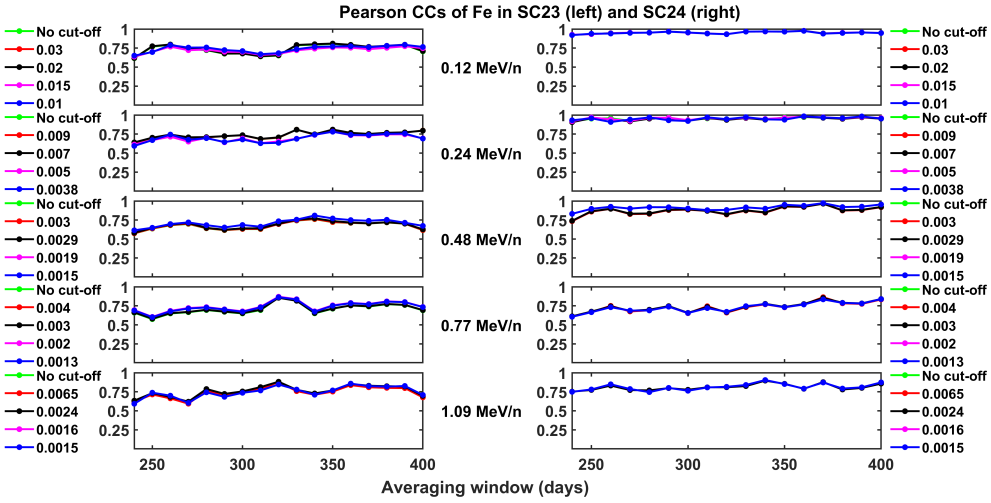


(d) same as 3.7a but for C

in the acceleration/energization processes of these populations. In order to check spectral index variations of different suprathermal elements the two solar cycles are divided into 7 phases with 2 years of duration in each phase. These phases are (1) maximum of SC23 (from November 11, 1999 to November 11, 2001), (2) descending phase of SC23 (from July 15, 2003 to July 15, 2005), (3) minimum of SC23–24 (from July 05, 2007 to July 05, 2009), (4) ascending phase of SC24 (from September 24, 2009 to September 24, 2011), (5) maximum of SC24 (from April 20, 2012 to April 20, 2014), (6) descending phase of SC24 (from July 8, 2015 to July 8, 2017), and (7) minimum of SC24–25 (from August 31, 2018 to August 31, 2020). The solar cycle phases are shown in Figure 3.9. Average of quiet background fluxes are taken over these phases and calculate the spectral indices for all the six elements. The spectral indices are denoted by m_i 's (where $i=1,2, 3, 4,$



(e) Same as 3.7a but for O



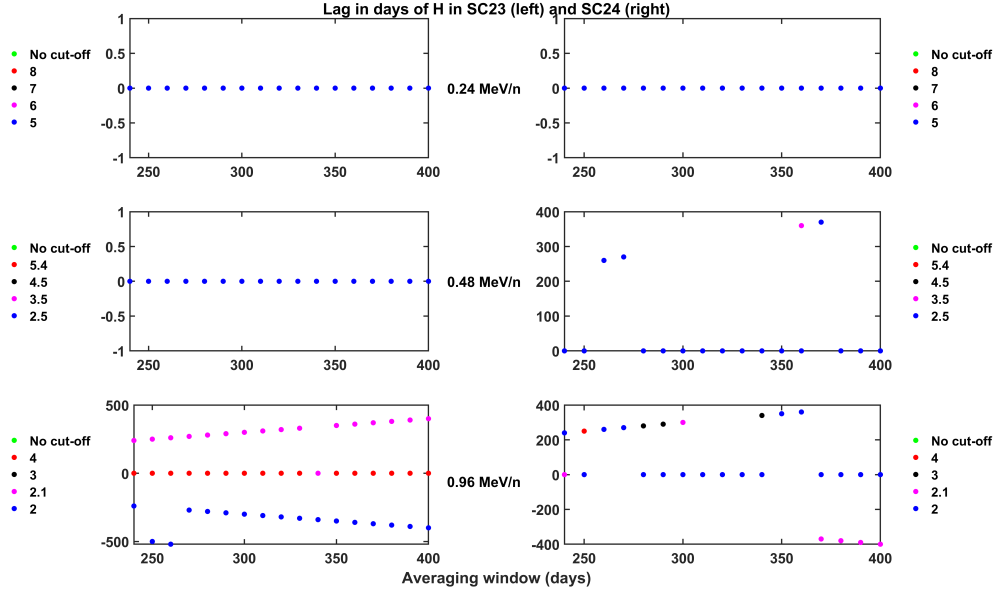
(f) same as 3.7a but for Fe

Figure 3.7

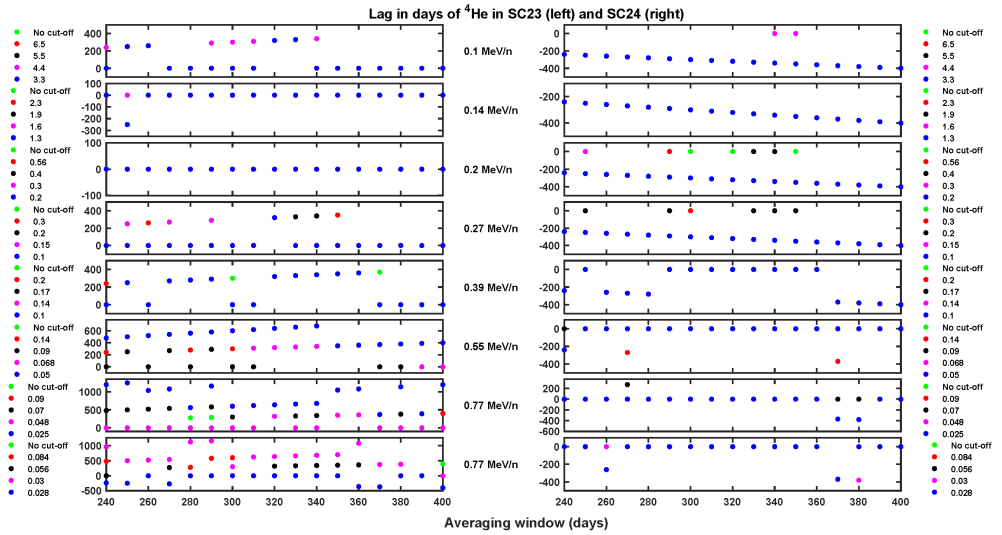
5, 6, and 7) starting from the maximum of SC23 and ending at the minimum of SC24–25. The spectra of the six elements for seven phases are shown in Figure 3.10. The margin of errors (MoEs) are shown as estimates of uncertainties in calculating the spectral indices. Actually, MoE sets a lower and upper bound on the estimated spectral index corresponding to a specified confidence level. The value of MoE depends on the data sample size, variability in the data, and the confidence level. The more one wants confidence on estimated parameters like, spectral index, the wider becomes the confidence interval and consequently, the greater the MoE. One of the methods to calculate MoE in estimated parameters is Bootstrapping (Tibshirani and Efron, 1993).

In order to synthesize the results obtained from Figure 3.10, Figure 3.11 is

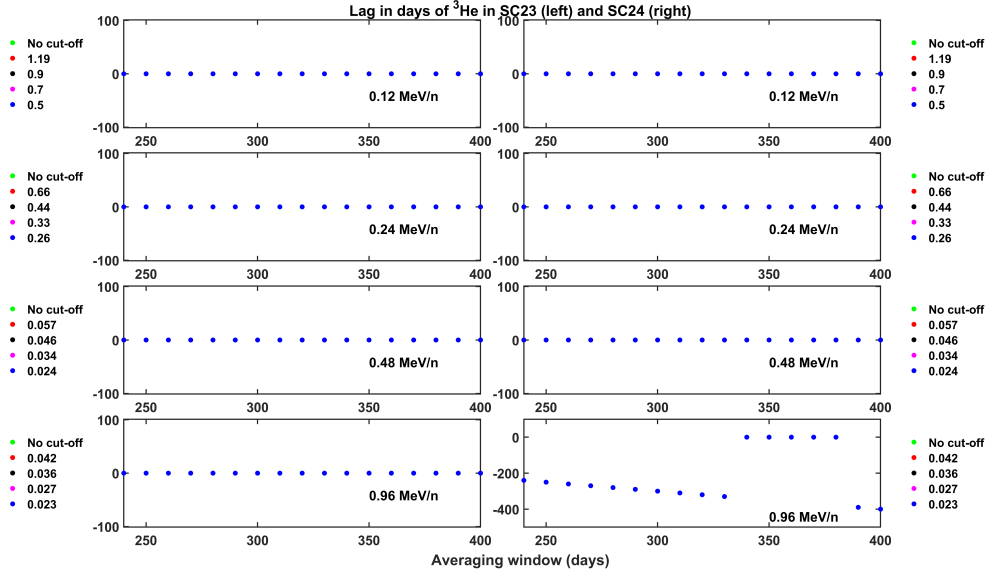
3.4. RESULTS



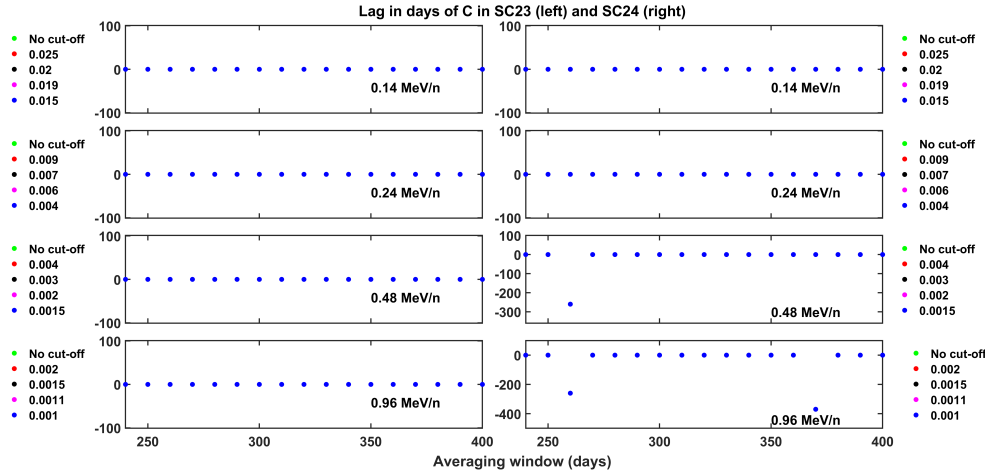
(a) Variations of lags with respect to the averaging window for H fluxes at different energy channels (mentioned in between the columns) in SC23 (left) and SC24 (right). Five colors correspond quiet time fluxes of H with no cut-off and for 4 set of cut-off values for fluxes. The cutoff values are written in the left (SC23) and right (SC24) sides of the figure



(b) same as 3.8a but for ^4He



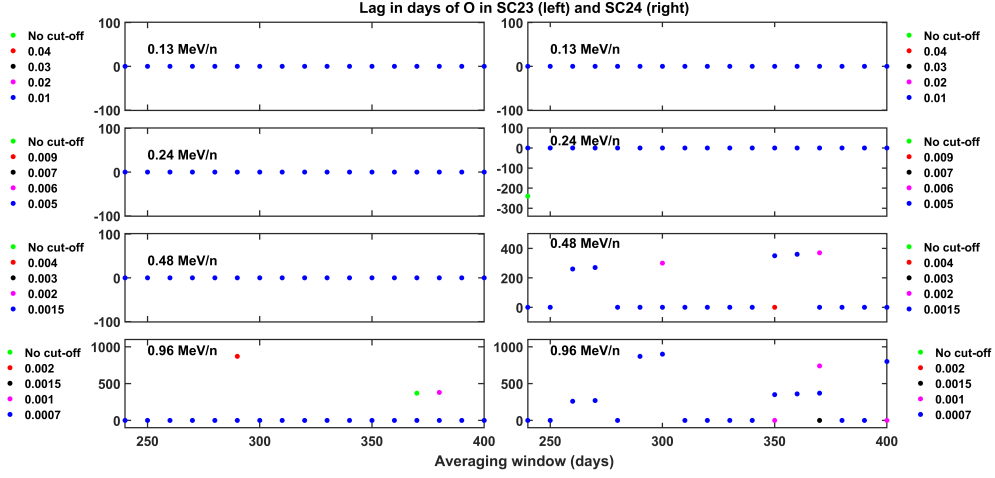
(c) same as 3.8b but for ${}^3\text{He}$. Here, the energy channels are mentioned inside the panels



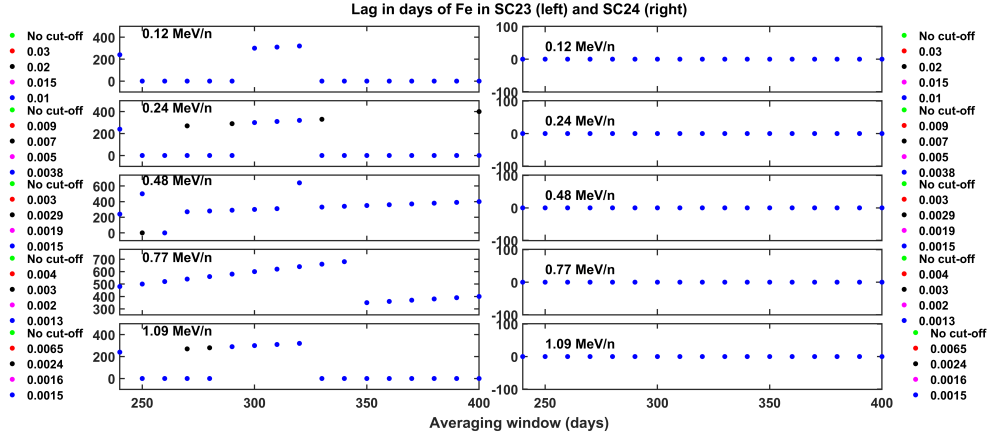
(d) same as 3.8c but for C

created. Panel (a) of Figure 3.11 shows the variations of H spectral indices with different phases of solar cycles. It is found that the spectral index of H varies between 1.51 (m_2) and 2.2 (m_7). The maximum spectral index is seen during the minimum of SC24-25. The MoEs corresponding to the H spectral indices are large possibly because of less number (3) of energy channels to fit the spectra. Solar cycle variations of ${}^3\text{He}$ spectral indices are shown in Figure 3.11 (b). The spectral indices vary in the range 2.35 (m_1) – 2.64 (m_7). Panel (c) presents a comparison between spectral indices of C and O. It can be seen that spectral indices of these two elements vary almost hand in hand for all the phases of solar

3.4. RESULTS



(e) same as 3.8c but for O



(f) same as 3.8c but for Fe

Figure 3.8

cycles with spectral indices for O being consistently greater than those for C. The differences between the spectral indices of O and C appear to be maximum during the minimum of SC23-24. Figure 3.11 (d) shows a comparison of ^4He and Fe spectral indices. The spectral indices (from $m_1 - m_5$) vary almost similarly up to the maximum of SC24 with spectral indices for ^4He having relatively higher values than Fe. However, the scenario changes from the descending phase of SC24 when ^4He spectral index (m_6) becomes less than Fe spectral index. This time ^4He spectral index reaches a minimum value among all the seven values corresponding to seven phases of solar cycles. During the minimum of SC24-25, spectral index (m_7) of ^4He becomes higher than m_7 of Fe. Interestingly, spectral indices of Fe do not show any significant change. Note, mean values are taken as reference while

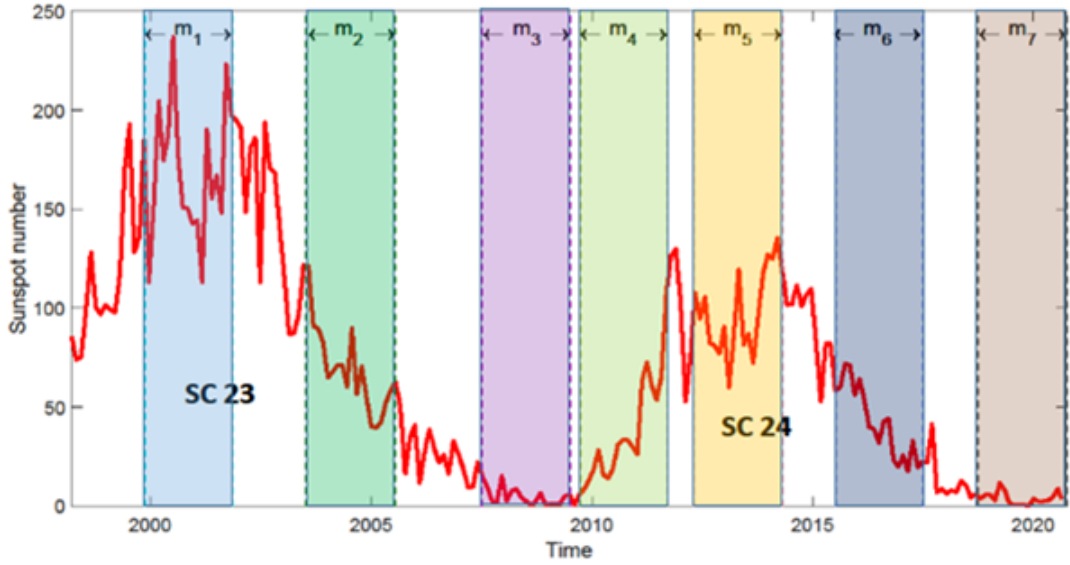


Figure 3.9: Temporal variation of 30 days averaged SSN data in SC23 and SC24. Seven phases of solar cycles, each with durations of 2 years, are shown by shaded intervals of different colors. m_i 's ($i=0, 1, 2, 3, 4, 5, 6,$ and 7) denote the spectral indices (see Figure 3.10) of ions during these phases of solar cycles

concluding the increase and decrease of spectral indices and variation ≥ 0.5 are considered significant.

3.5 Discussions and conclusions

Previous studies (e.g., Dayeh et al., 2009; Kecskemety et al., 2011; Dayeh et al., 2017) have reported variations in suprathermal heavy ion ratios (C/O, Fe/O, and $^3\text{He}/^4\text{He}$) during "quiet" periods with respect to solar activity. These ratios are noted to have SEP-like values during solar maximum and a SIR/CIR/solar wind-like values during solar minimum. This suggests that SEP and CIR events are important contributors to the suprathermal ion pool in the IP medium during solar maximum and minimum, respectively. This investigation not only confirms the dependence on solar activity, as indicated by significant correlation coefficients, but also highlights time delays between solar activity proxies (e.g., SSN) and quiet time suprathermal fluxes suggesting IP modulations of these particles. This also suggests that the so-called quiet time suprathermal population in the IP

3.5. DISCUSSIONS AND CONCLUSIONS

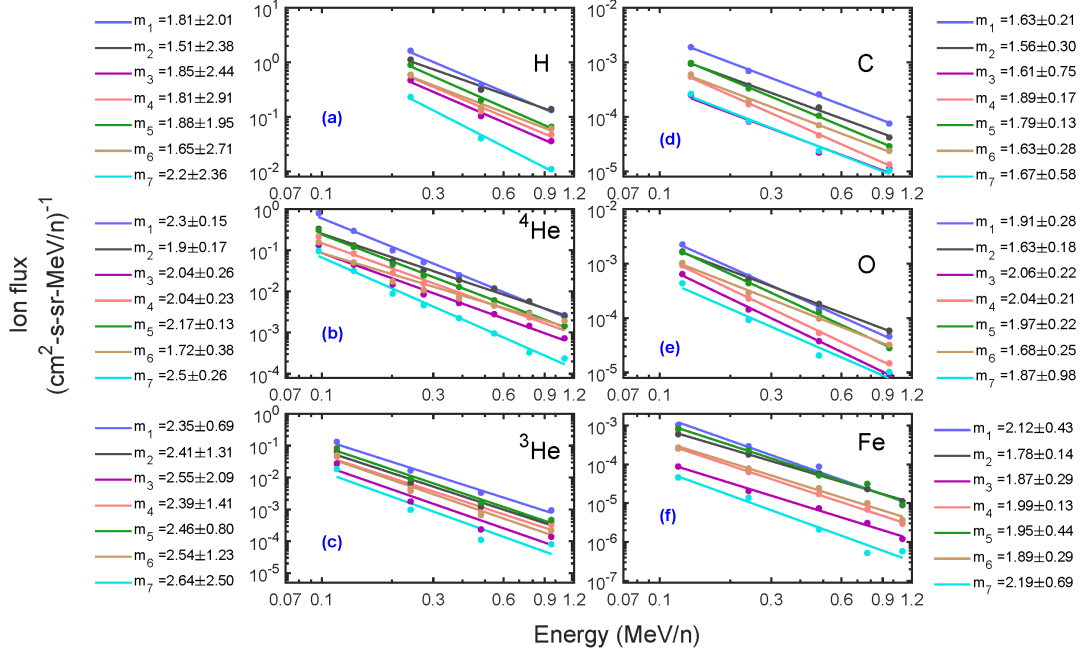


Figure 3.10: Differential directional flux vs energy spectra for (a) H, (b) ${}^4\text{He}$, (c) ${}^3\text{He}$, (d) C, (e) O, and (f) Fe during the seven phases of solar cycles shown in Figure 3.8. The spectral indices (m_i 's) and corresponding margin of errors (MoEs) with 95% of confidence level for H, ${}^4\text{He}$, and ${}^3\text{He}$ are mentioned in the left of panel (a), (b), and (c), respectively. The same for C, O, and Fe are written in the right of panels (d), (e), and (f), respectively.

medium may consist of residual particles from previous solar and IP transient events. Hence, the quiet time population of suprathermal particles may not truly be quiet, even after the contemporaneous transient events are accounted for.

It is observed that different elements exhibit both positive and negative lags of 240–800 days (the lower limit comes from the lower limit of the averaging window) with respect to SSN in SC23 and SC24. These time scales are much larger than any solar transient solar phenomenon such as the passages of ICME (a few days) and SIR (a few months), solar rotation (Carrington rotation of ~ 27 days), solar wind expansion time scale (~ 2 – 3 days) etc. (e.g., [Verscharen et al., 2019](#)). Even, the lags are larger than the first ionization potential (FIP) modulation time, which is a few days ([Laming, 2015](#)). [Zhang and Lee \(2013\)](#) compared time scales of stochastic particle acceleration, adiabatic cooling, and shock acceleration at 1 AU. These authors found that the shock acceleration time scale for particle energy below 60

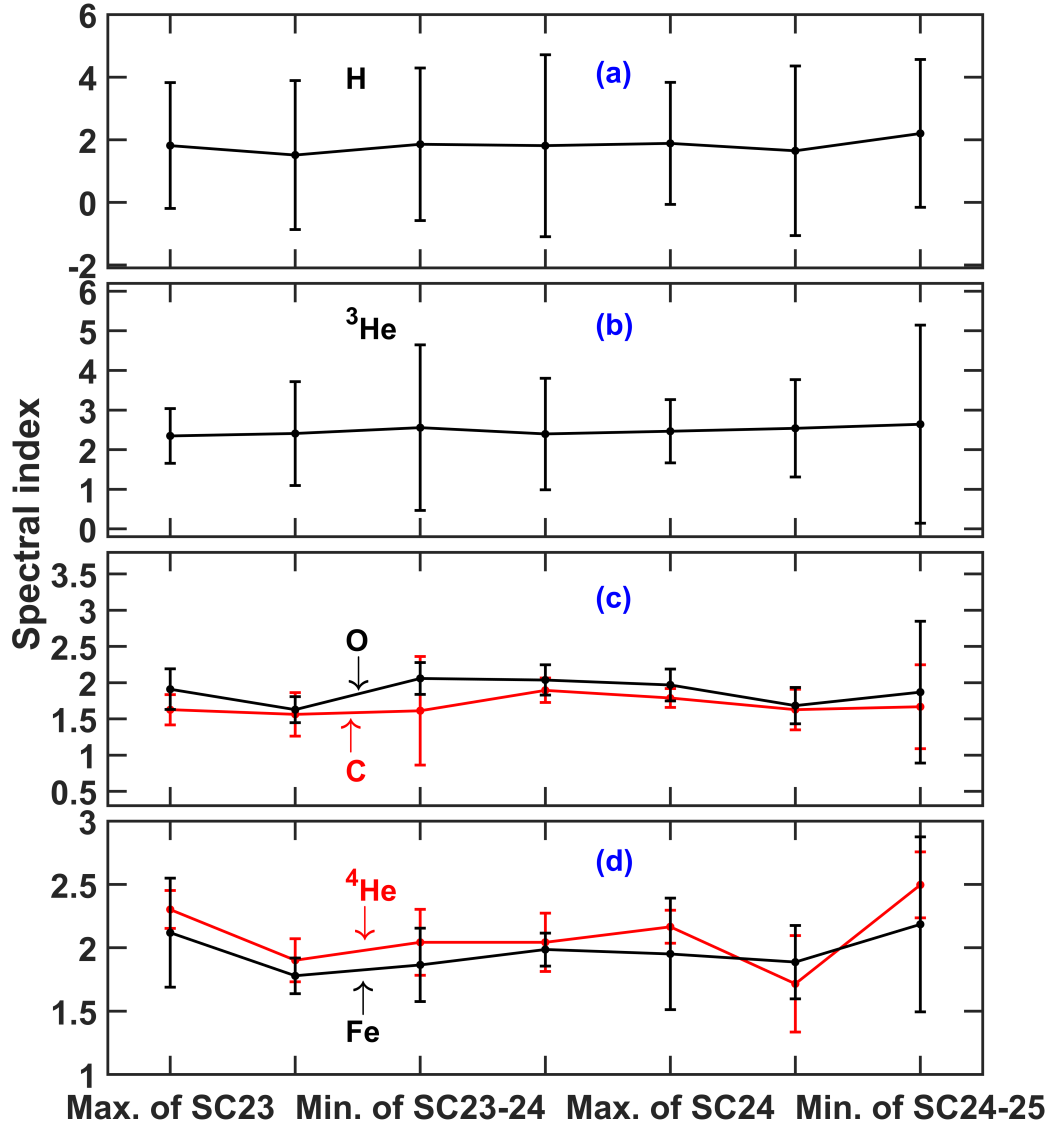


Figure 3.11: Solar cycle variations of spectral indices of (a) H, (b) ^3He , (c) C (red) and O (black), and (d) ^4He (red) and Fe (black). These spectral indices (values are mentioned in Figure 3.10) are calculated at the seven phases of solar cycles as illustrated in Figure 3.9. The error bars are the margin of errors.

MeV is < 10 days. Acceleration time scales for particle with much lower energies are further smaller. Although suprathermal particles with energies ≤ 1 MeV n^{-1} are being discussed in this chapter, the maximum total energy is ~ 56 MeV (for Fe with energy ~ 1 MeV n^{-1}). This essentially means that the shock acceleration time scale for the highest-energy particle also is negligible when compared to the lags observed. However, the time scale of stochastic acceleration by small-

3.5. DISCUSSIONS AND CONCLUSIONS

scale magnetohydrodynamic waves for particles with total energy $< \sim 5$ MeV is comparable to that of lags. This energy corresponds to 5 MeV n^{-1} for H, 1.25 MeV n^{-1} for ^4He , 0.42 MeV n^{-1} for C, 0.31 MeV n^{-1} for O, and 0.1 MeV n^{-1} for Fe. As mentioned in Section 3.4.1, all these smaller time scales are averaged out due to the choice of long-term averaging windows (i.e., 240–400 days). This choice also mitigates the effect of heliospheric current sheet modulation time scales, which is around 6 months (Kasper et al., 2007).

This investigation reveals, for the first time, the presence of negative lags between suprathermal ^4He fluxes and the sunspot number (SSN) in SC24. This implies that suprathermal ^4He flux levels began to increase in the IP medium before the SSN started to rise during SC24. This points towards source processes that are predominant during the solar minimum phase. Given that SIR/CIRs are the primary source of energetic particles in the IP medium during solar minima, the negative lags of suprathermal ^4He during SC23–24 likely indicate the generation of these suprathermal particles from CIR events in the IP medium. The deep minimum of SC23–24 provides an optimal background condition for this phenomenon. This argument is supported by the negative lags observed in the 0.96 MeV n^{-1} ^3He flux in SC24. It is established that impulsive flare events contribute to the energetic ^3He population in the IP medium (e.g., Mason et al., 2002). Therefore, a negative lag in the ^3He fluxes may also suggest the involvement of remnant flare particles that were accelerated by CIR events during the minimum of SC23–24 and contributed to the background suprathermal ion pool.

Mason et al. (2012) utilized ACE/ULEIS data spanning from 1998 to 2011 and observed that the lag between CIR event-averaged suprathermal Fe/O ratios and SSN was initially present in SC23, but this lag diminished and became more synchronized in SC24. These findings were further corroborated and expanded upon by Allen et al. (2019), who utilized ACE/ULEIS data from both SC23 and SC24 (1998–2018) and identified similar trends in CIR-averaged suprathermal Fe/O ratios (specifically in the energy range of $0.32\text{--}0.45 \text{ n}^{-1}$). Interestingly, our current results focusing on quiet time suprathermal populations exhibit consistency with

the observations made by both [Mason et al. \(2012\)](#) and [Allen et al. \(2019\)](#) regarding the differences in lag times of suprathermal Fe between the two solar cycles. This consistency suggests that past CIR events may contribute significantly to the quiet time suprathermal particle population at present.

Significant shifts in the spectral index of ^4He are observed in the descending phase of SC24. During the declining phase of SC24, the mean spectral index (m_6) of ^4He reaches its minimum value at 1.72. In the subsequent phase, the index ($m_7 = 2.50$) attains its peak value, surpassing all other phases. This alteration is more pronounced than any of the MoEs for ^4He . On the other hand, the spectral indices of Fe exhibit a smoother variation and attain their maximum during the minimum of SC24–25. These fluctuations in the spectral indices of ^4He and Fe indicate disparities in the production and/or processing of these two suprathermal elements in the IP medium. As noted earlier, different lags of these two elements were observed in SC23 and SC24. Hence, it is evident that there are significant differences in SC24 when the generation and processing of suprathermal ^4He and Fe are concerned. Actually, SC24 holds particular significance in several aspects. Notably, it stands out as the weakest solar cycle in the last century and follows an extended minimum period. An unusual polar field reversal in the Sun was also reported by [Janardhan et al. \(2018\)](#). Therefore, it appears that changes in the Sun makes ^4He and Fe to behave differently in SC24. This proposition does not get support from the fact that C and O exhibit similar lags and spectral indices in both the solar cycles. This discrepancy prompts a consideration of the selective processing of suprathermal particles within the IP medium. The acceleration of the suprathermal population in this medium has been proposed to hinge on factors such as the mass-to-charge ratio (m/q) (e.g., [Drake et al., 2009](#); [Zhao et al., 2017](#); [Reames, 2018b](#)) and FIP effects (e.g., [Feldman and Widing, 2002](#)). Given the noticeable differences in m/q and FIP between ^4He and Fe, it is possible that the processing of these elements in the IP medium was influenced during SC24. This hypothesis gains support from the observation that carbon (C) and oxygen (O) share closer FIP and m/q values, resulting in no discernible differential changes in the lags

3.5. DISCUSSIONS AND CONCLUSIONS

and spectral indices between SC23 and SC24. Thus, the present study suggests a dependence on FIP and m/q for the generation of suprathermal populations in the IP medium. In the context of SC24's distinctiveness, several additional findings are pertinent. [Mewaldt et al. \(2015\)](#) revealed a marked reduction in the fluence of SEPs during the initial phase of SC24, attributed to two factors: a diminished IMF in the IP medium and a depletion in the seed population (suprathermal particles). It is expected that a reduced IMF can affect the acceleration of particle adversely, leading to less population in the SEP energy domain (e.g., [Gopalswamy et al., 2014](#); [Mewaldt et al., 2015](#); [Allen et al., 2019](#)). Also, the maximum energy attained by particles which are accelerated by interaction with the Alfvén waves at the shock fronts will be limited by the lower densities of the seed population (e.g., [Li and Lee, 2015](#)). Interstellar pick-up ions may also be responsible for changes in spectral indices in the IP medium.

At this juncture, it's crucial to consider the relative significance of acceleration and deceleration processes in the alterations observed in suprathermal ^4He during the minimum of SC24–25. As mentioned earlier, the typical time scale of the stochastic acceleration mechanism differs from energy to energy ([Zhang and Lee, 2013](#)). The second-order Fermi acceleration is prevalent in the interstellar medium ([Fermi, 1949](#)). The time scale of Fermi acceleration is limited by the frequency of collisions between charged particles and magnetized clouds, which is of the order of a year. On the other hand, the time scale for the first-order Fermi acceleration mechanism (or diffusive shock acceleration) varies between 0.001 and 500 days for energies ranging from 0.01 to 10000 MeV ([Zhang and Lee, 2013](#)). Particle acceleration by gradual compression region has an almost similar time scale as shock acceleration. This acceleration process is applicable during the passage of SIR/CIRs in the absence of a forward and reverse shock pair ([Giacalone et al., 2002](#)). The pump mechanism works where there are large-scale compressions and expansions. The heliosheath, the interstellar medium, shocked solar wind downstream of interplanetary shocks etc. are some of the places suitable for particles acceleration by pump mechanism. The details about this mechanism (e.g., [Fisk](#)

and Gloeckler, 2006, 2007, 2008, 2014) is discussed in section 1.3.4 of the thesis. According to Fisk and Gloeckler (2014), particle acceleration in this process is possible only when the particles do not escape the compression and expansion regions by spatial diffusion. The time scale of pump acceleration can vary from hours to days (Fisk and Gloeckler, 2014). Particle acceleration by merging and contraction possibly occurs near the heliospheric current sheet, where the probability of the formation of small-scale magnetic islands is more (e.g., Zank et al., 2014). Since the underlined mechanism is magnetic reconnection, the particle acceleration time scale in this case should be less than an hour.

Dayeh et al. (2017) deliberated on the origins of suprathermal tails, suggesting they arise from either continuous acceleration of seed populations in the IP medium (e.g., Fisk and Gloeckler, 2006, 2008, 2014; Zank et al., 2014 etc.) or deceleration of energetic particles stemming from solar and IP events (e.g., Fisk and Lee, 1980; Giacalone et al., 2002 etc.). In the works of Fisk and Gloeckler (2006, 2008, 2014), these authors introduced pump acceleration mechanism, which is operational in regions containing large-scale compressions and expansions and readily available seed particles (e.g., downstream region of a shock). Previous research has indicated that the lower-energy segment of SIR/CIR-associated suprathermal populations is predominantly influenced by local acceleration processes (e.g., Schwadron et al., 1996; Giacalone et al., 2002; Ebert et al., 2012; Filwett et al., 2017, 2019; Allen et al., 2019, 2020, 2021), whereas the higher-energy segment is affected by shock acceleration occurring at a distance (e.g., Ebert et al., 2012; Filwett et al., 2019). Thus, the significance of acceleration, whether local or shock-induced, cannot be overstated in the observed changes reported in the present study. Schwadron et al. (2010) proposed that a combination of stochastic processes, represented by distribution functions such as exponential and Gaussian functions, could lead to the emergence of a power-law distribution function with an exponent of -5 ($f \propto v^{-5}$) (or -1.5 in terms of differential intensity with respect to energy). This proposition suggests that variable acceleration and heating processes may be operative in the IP medium for the generation of suprathermal particles. Anteck et al. (2013)

3.6. KEY FINDINGS

further explored stochastic acceleration under a pressure balance condition, where the timescale of acceleration is balanced with the timescale of adiabatic cooling in the solar wind, as an effective mechanism for producing a -1.5 spectral index. Conversely, the potential role of deceleration processes in the observed changes in suprathermal ^4He particles during the minimum of SC24–25 cannot be ruled out. This is because particles accelerated at distant shock fronts can be redirected back into the inner heliosphere, leading to increased scattering and magnetic cooling processes. Such phenomena may induce variations in intensity and spectral index (e.g., [Fisk and Lee, 1980](#); [Mason et al., 1999](#); [Zhao et al., 2016](#); [Allen et al., 2021](#)). Importantly, particles accelerated during previous transient events, while traversing the IP medium, undergo adiabatic expansion of the solar wind, resulting in their deceleration. As a result, energetic particles undergo a deceleration process and become part of the suprathermal pool. According to [Fisk and Lee \(1980\)](#), this type of particle is expected to exhibit a rollover below approximately 0.5 MeV n^{-1} in the spectra. However, no such rollover is observed by [Mason et al. \(1997\)](#), and similarly, our present investigation does not reveal such a feature. Nonetheless, while it is challenging to ascertain, the potential impact of deceleration processes on the changes in the spectral slope of ^4He during SC24–25 cannot be dismissed. It appears plausible, therefore, to argue that variable contributions from both acceleration and deceleration processes or distribution functions may lead to variations in spectral indices with changing solar activity levels. These processes might have undergone changes during the minimum of SC24–25, contributing to changes in spectral indices, particularly concerning heavier ions like Fe and ^4He . These aspects warrant further scrutiny in future studies, and the comprehensive suprathermal particle measurements from India’s upcoming Aditya-L1 mission ([Janardhan et al., 2017](#); [Goyal et al., 2018](#); [Tripathi et al., 2022](#)) may shed significant light on some of these unresolved issues.

3.6 Key findings

The key findings of the present chapter can be summarized as follows.

1. Fluxes of quiet-time suprathermal particles vary with solar cycles.
2. ^4He and Fe lag the SSN in SC23 and SC24 differently. There are positive and zero lags in both ^4He and Fe fluxes in SC23. Negative lags are observed in ^4He fluxes in SC24, while no negative lag is there in case of Fe fluxes in SC24.
3. H, C, and O do not lag the SSN
4. The differential behavior of ^4He and Fe is also visible in their spectral indices in different phases of solar cycles, specifically after the maximum of SC24. Spectral indices of C and O vary similarly in both the solar cycles.
5. There appears to be a FIP and m/q dependence of the modulation of quiet-time suprathermal particles. While FIP dependence suggests modulation closer to the Sun, the m/q dependence indicates IP processing of the suprathermal ion pool.

Chapter 4

Suprathermal particles associated with stream interaction regions

Excerpt

Enhancements in suprathermal particles are often observed at 1 AU during the passage of stream interaction regions (SIRs). The forward and reverse shocks formed respectively at the leading and trailing edge of a SIR are thought to accelerate these particles. In the absence of these shock pairs, the compressed interaction regions may also energize particles. The nature and relative roles of the shock pairs and the compression region associated with SIR in accelerating particles are poorly understood as of date. In this work, in order to address some of these issues, suprathermal fluxes of ^4He , O, and Fe associated with twenty shock-less SIR events observed by Solar Terrestrial Relations Observatory-Ahead (STEREO-A) have been analyzed. It is found that the fluxes of heavy elements like O and Fe get enhanced during certain events and do not get enhanced in certain other events. The reason for these selective enhancements could not be ascertained. Moreover, spectral indices of ^4He , O, and Fe are observed to vary in ranges of 1.55–4.08, 1.49–4.56, and 1.46–4.04, respectively. The cause behind the large variations in the spectral indices of these three elements with different mass-to-charge ratio (m/q) is attributed to difference in seed populations or/and stochastic nature of acceleration mechanisms. Interestingly, while variation in spectral indices is found in most of the cases, ^4He , O, and Fe are seen to exhibit nearly identical spectral

indices (close to 1.5) during one particular SIR event. Based on circumstantial evidences, it is argued that the background conditions (like turbulence in the interplanetary (IP) medium due to solar flare, strength of interplanetary magnetic field, IMF, solar wind speed etc.) favored the generation of small-scale magnetic islands (SMIs) near the spacecraft, which accelerated these particles regardless of their m/q .

4.1 Introduction

Association of suprathermal particles with stream/corotating interaction regions (SIR/CIRs) has been known for the past few decades. The first observation of recurrent enhancements in the ~ 1.0 MeV per nucleon (MeV n^{-1}) H and ^4He fluxes at 1 AU was reported by [Bryant et al. \(1965\)](#). It is confirmed by Pioneer 10 and 11 measurements that these particles are accelerated in the IP space between 3–5 AU ([Desai et al., 1998](#)). It is believed that the forward and reverse shocks formed respectively at the leading and trailing edge of a SIR accelerate these particles ([Barnes and Simpson, 1976](#); [Sanderson et al., 1994](#)) at heliocentric distances ≥ 2 AU. According to [Fisk and Lee \(1980\)](#), particles are accelerated at these shocks by being compressed between upstream and downstream magnetic irregularities. These particles experience adiabatic deceleration while steaming into the inner heliosphere. According to this model, an exponential rollover in the spectra of these particles below ~ 500 keV is expected at 1 AU. However, SIR associated particle spectra show power law till about 0.1 MeV n^{-1} ([Mason et al., 1997, 2008b](#); [Chottoo et al., 2000](#)). This raises a concern regarding the true nature of the acceleration mechanism(s) of SIR-associated particles at 1 AU.

As discussed in Chapter 1, a typical SIR has four sectors: S, S', F', and F. [Chottoo et al. \(2000\)](#) showed that the peak intensities of $0.01\text{--}0.5 \text{ MeV n}^{-1} \text{ H}^+$, He^+ and He^{++} ions occur in the compressed fast wind (F' in Figure 1.7.) region. However, as per these authors, this is not the case for MeV n^{-1} ions. Peak intensities in MeV n^{-1} ions are generally observed in the rarefied fast wind (F in Figure 1.7.) region of SIRs. Enhancements in suprathermal ($0.25\text{--}0.8 \text{ MeV n}^{-1}$) pick-up

4.1. INTRODUCTION

ion abundances ($\text{He}^+/\text{He}^{++}$) at 1 AU was also reported (Kucharek et al., 2003; Ebert et al., 2012). Ebert et al. (2012) also investigated 73 CIR events and found that $\sim 0.1 - 0.8 \text{ MeV n}^{-1}$ He peak intensities are well correlated to the magnetic compression ratios (ratio between the downstream and upstream magnetic field) irrespective of the presence and absence of shocks. These authors suggested local acceleration of suprathermal particles near the spacecraft at 1 AU. An acceleration mechanism was suggested by Giacalone et al. (2002) in which low energy particles gain energy in regions of gradual compression. This mechanism is similar to that of acceleration by quasi-parallel shocks and can explain the acceleration of protons up to $\sim 10 \text{ MeV}$ when the mean free path of particles is larger than the width of the compression region. These authors also suggested that the acceleration efficiency inversely depends on the width of the compression region. However, Bučík et al. (2009) did not find any correlation between peak He intensities and the width of the compression regions in shock-less SIRs. Bučík et al. (2011) found that the frequency of occurrence of strong CIR-associated particle events at 1 AU increases with the increase in tilt angle of the heliospheric current sheet (HCS). Therefore, it is clear from the above discussion that no unanimously agreed mechanism could be identified that could fully explain the acceleration mechanism(s) for SIR/CIR-accelerated particles at 1 AU.

One way to get an idea of the acceleration mechanism is to investigate the characteristics of different heavy ions with varying m/q . It has been observed that $0.1\text{--}1.0 \text{ MeV n}^{-1}$ ^4He ions exhibit a wide range (1.3–5) of spectral indices (Mason et al., 2008b; Allen et al., 2021). Correlation between spectral indices of CIR-associated $0.16\text{--}0.91 \text{ MeV n}^{-1}$ ^4He and O was reported by Mason et al. (2008b). These authors did not find any similarity between Fe spectral indices in the same energy and ^4He or O spectral indices. This shows that the acceleration mechanism treats different ion species differently or may be, ions with different m/q are modulated in the IP medium depending on their m/q . This proposition seems to be valid because m/q -dependent modulation of quiet-time suprathermal particles in solar cycle time scale has been suggested by Dalal et al. (2022). This

indicates that although different particles are accelerated locally by SIR, by the time they reach any spacecraft, they are modulated and the information of the source mechanism probably gets modulated as well .

In this work, the behaviors of suprathermal ($\sim 0.1\text{--}1.0$ MeV n^{-1}) ^4He , O, and Fe associated with 20 shock-less SIR events at 1 AU observed by the Solar Terrestrial Relations Observatory Ahead (STEREO-A) have been investigated. The spectral indices of these elements are observed to vary significantly similar to quiet time (Dalal et al., 2022). The possible physical processes responsible for such wide variation in spectral indices of these elements associated with SIR events are discussed. Interestingly, in a particular SIR event, the spectral indices of ^4He , O, and Fe are found to be almost identical and close to 1.5. This event is investigated in detail. The outcomes of this investigation leads to the conclusion that this noticeable similarity in spectral indices of these three elements is possibly due to their acceleration by merging and contraction of small-scale magnetic islands at 1 AU near the spacecraft. The details of the work are discussed in subsequent sections.

4.2 Data used

Instrumentation and data used in this study have already been discussed in Chapter 2.

4.3 Selection of events

20 SIR events occurring between 2007 and 2014 that exhibited significant enhancements in suprathermal ^4He have been identified. These events, labeled as SIR 1–20, are tabulated in Table 4.1. These are characterized as shock-less SIR events based on the in-situ data at 1 AU. However, it is to be noted that the contribution of distant shocks associated with SIRs in accelerating these particles (that are detected at 1 AU) cannot be completely ignored and the energized particles may have the imprint of these shock accelerations. It is important to

4.3. SELECTION OF EVENTS

note that while these events showed enhancements in suprathermal ^4He , not every SIR event correlated with increases in O and Fe fluxes. Specifically, among the selected events, there were 16 instances where O fluxes displayed minor to moderate enhancements and 9 instances where Fe fluxes exhibited enhancements. This selective enhancement is itself enigmatic. This aspect will be briefly discussed in the discussion section. Variations in ^4He , Fe, and O fluxes during SIR 1, 9, 11,

SIR No.	Start time	End time	O/ ^4He	Fe/ ^4He	Spectral index		
					^4He	O	Fe
1	Sep 21, 2007 13:35	Sep 23, 2007 11:32	2.12E-03	2.75E-04	2.67±0.44	2.89±0.87	
2	Oct 25, 2007 18:04	Oct 26, 2007 15:17	2.63E-03	3.60E-04	3.33±0.45	3.88±0.62	
3	Nov 13, 2007 18:00	Nov 16, 2007 03:30	1.67E-03	2.09E-04	3.35±0.60		
4	Dec 11, 2007 18:00	Dec 13, 2007 04:10	1.23E-03	1.58E-04	3.70±0.38		
5	Feb 11, 2008 00:00	Feb 13, 2008 04:40	2.30E-03	2.71E-04	2.92±0.49	2.75±0.45	2.59±0.69
6	Feb 29, 2008 16:00	Mar 03, 2008 03:15	1.80E-03	1.66E-04	2.49±0.38	2.83±0.56	
7	Jun 16, 2008 06:00	Jun 17, 2008 18:36	2.02E-03	3.05E-04	3.12±0.36		
8	Aug 07, 2008 18:10	Aug 12, 2008 00:00	2.54E-03	2.59E-04	3.14±0.38	3.64±0.71	
9	May 31, 2009 08:13	Jun 02, 2009 16:00	2.37E-03	1.40E-04	4.08±0.42	4.14±0.95	
10	Jan 12, 2011 12:03	Jan 14, 2011 08:00	6.50E-03	2.03E-03	3.18±0.28	3.98±0.61	4.04±1.57
11	Nov 12, 2011 02:00	Nov 14, 2011 18:00	8.63E-03	8.82E-04	2.86±0.28	2.61±0.22	2.09±0.27
12	Jun 12, 2012 04:00	Jun 13, 2012 18:00	2.08E-02	3.86E-03	1.55±0.39	1.49±0.34	1.46±0.60
13	Aug 21, 2012 20:00	Aug 23, 2012 11:10	1.69E-02	1.27E-02	2.71±0.33	2.95±0.30	3.09±0.46
14	Apr 18, 2013 16:00	Apr 19, 2013 14:19	5.27E-03	2.37E-03	3.60±0.43	2.84±0.42	3.09±0.46
15	Jul 17, 2013 00:00	Jul 22, 2013 16:00	1.08E-02	4.36E-04	4.08±0.24	4.56±0.38	
16	Sep 24, 2013 08:00	Sep 25, 2013 12:00	5.21E-03	3.88E-04	4.05±0.74		
17	Oct 24, 2013 10:00	Oct 26, 2013 02:25	3.91E-03	6.26E-04	3.97±0.47	3.67±0.53	
18	Apr 28, 2014 16:47	Apr 30, 2014 19:05	1.47E-02	2.76E-02	2.06±0.67	1.85±0.34	2.11±0.59
19	May 06, 2014 02:37	May 07, 2014 02:00	1.20E-02	1.53E-02	3.06±0.35	2.53±0.29	2.82±0.51
20	Jun 03, 2014 07:27	Jun 05, 2014 00:00	1.29E-02	6.44E-04	3.45±0.41	3.19±0.19	2.72±0.76

Table 4.1: A list of SIR events, O/ ^4He & Fe/ ^4He ratios calculated during the enhancement of ^4He fluxes

, and spectral indices of ^4He , O, & Fe calculated during the flux enhancement intervals associated with these SIR events. The event no 12 is marked differently as nearly identical spectral indices are observed in ^4He , Fe and O during this event, which has not been observed for other events

and 12 are shown in Figure 4.1 The start and end times of these SIR events are enlisted in the columns 2 and 3 of Table 4.1. O/ ^4He and Fe/ ^4He ratios are calculated for the energy range of 0.14–1.09 MeV n^{-1} during the intervals of enhanced ^4He . These ratios are mentioned in columns 4 and 5 of Table 4.1. Once the events are identified, the duration of flux enhancements for ^4He , O, and Fe are marked. Subsequently, the spectral indices are calculated from the differential directional flux vs. energy spectra. The results obtained from this exercise are discussed in the next section.

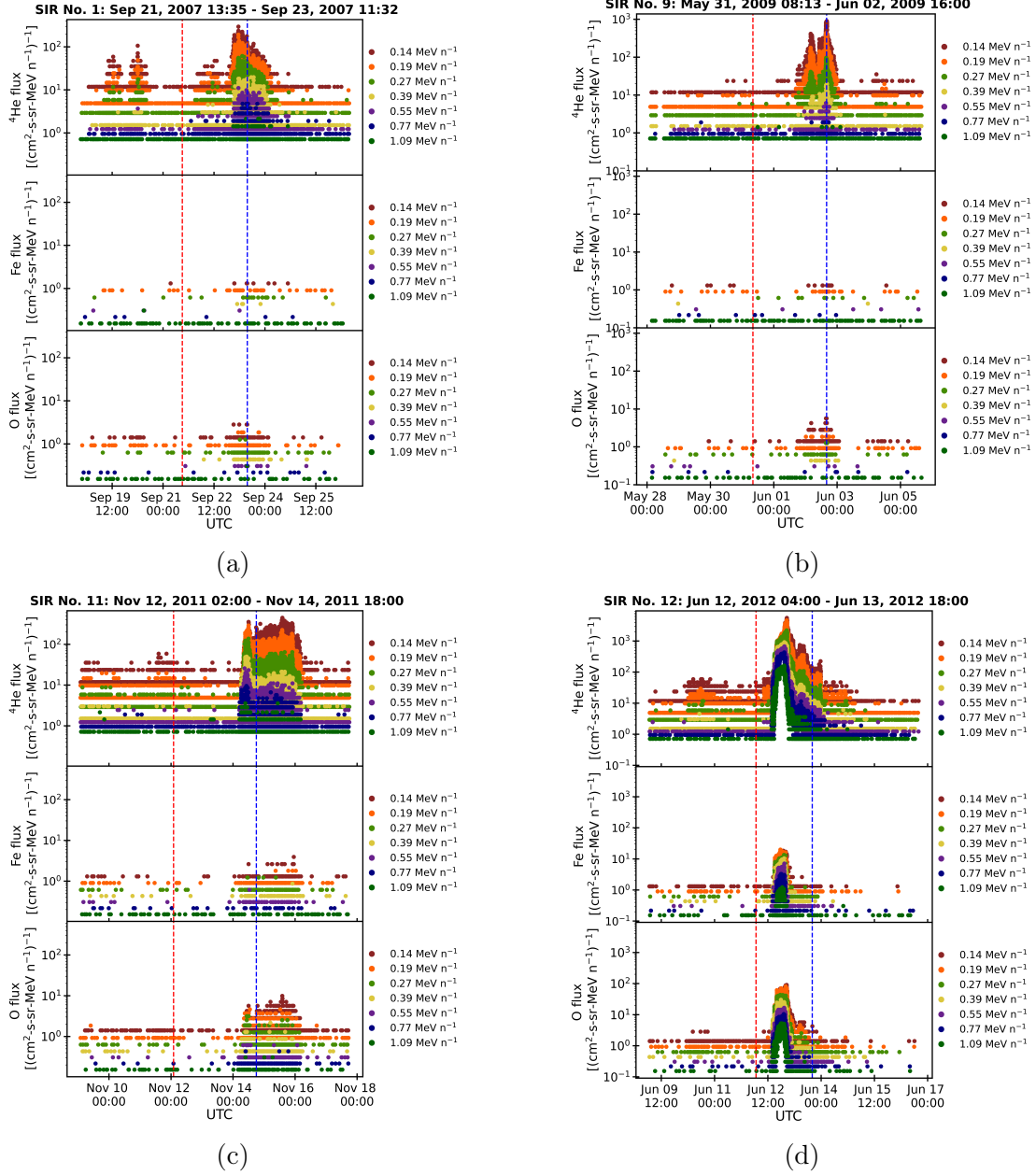


Figure 4.1: Variations in ${}^4\text{He}$, Fe, and O fluxes at different energy channels during (a) SIR 1, (b) SIR 9, (c) SIR 11, and (d) SIR 12. The red (blue) vertical dashed lines indicate the start (end) times of these SIR events. The energy channels are written at the right of each panel. The duration of these events are also mentioned at the top of each sub-figure.

4.4 Spectral analysis

The power law nature of differential directional flux vs energy spectra of suprathermal particles is well known. Although the underlying process of particle acceleration is difficult to uncover, similar spectral indices of different species may be indicative of similar acceleration mechanism. Figure 4.2 shows the spectra of ^4He during the flux enhancements in all the 20 SIR events. The spectral indices and corresponding margin of errors (MoEs) are tabulated in the column 6 of Table 4.1. It can be seen that ^4He spectral indices vary between 1.55 and 4.08. Figure 4.3 and Figure 4.4 present the spectra of O and Fe respectively in 16 and 9 SIR events when fluxes of these two elements increased. Table 4.1 includes the spectral indices of O and Fe as well. The spectral indices of O vary in the range 1.49–4.56. The range of Fe spectral indices is 1.46–4.04. Note that O and Fe spectra are sometimes best fitted up to 0.77 MeV n^{-1} . From the 6th, 7th, and 8th columns of Table 4.1 one can see that the spectral indices of ^4He , O, and Fe are different even for a particular SIR event. However, SIR 12 is an exception because these three elements exhibit almost identical spectra indices (close to 1.5) corresponding to this particular SIR. The flux enhancements of ^4He , O, and Fe in SIR 12 are also distinct from that in other SIR events. An impulsive increase and gradual decay in the fluxes of these elements can be seen. Therefore, SIR 12 draws attention by virtue of its disparate flux variations and almost identical spectral indices for three elements with diverse first ionization potential (FIP) and m/q . The reason for such observations is explored in this chapter. In addition to the above-mentioned 20 SIR events observed by STEREO-A, Spectral indices of these three elements (i.e., ^4He , O, and Fe) during two SIR events observed by STEREO-B are also studied. Actually, SIR 1 and 2 (Table 4.1) are also observed by STEREO-B before STEREO-A in the IP medium. A list of SIR events observed by both the STEREO satellites is available at https://stereo-ssc.nascom.nasa.gov/data/ins_data/impact/level3/. The relative positions of STEREO-A and STEREO-B with respect to the Earth at times very close to the 2 SIR events are shown in Figure 4.5 (a) and (b). Figure 4.5 (a) shows the positions of STEREO-A, The Earth, and STEREO-B on

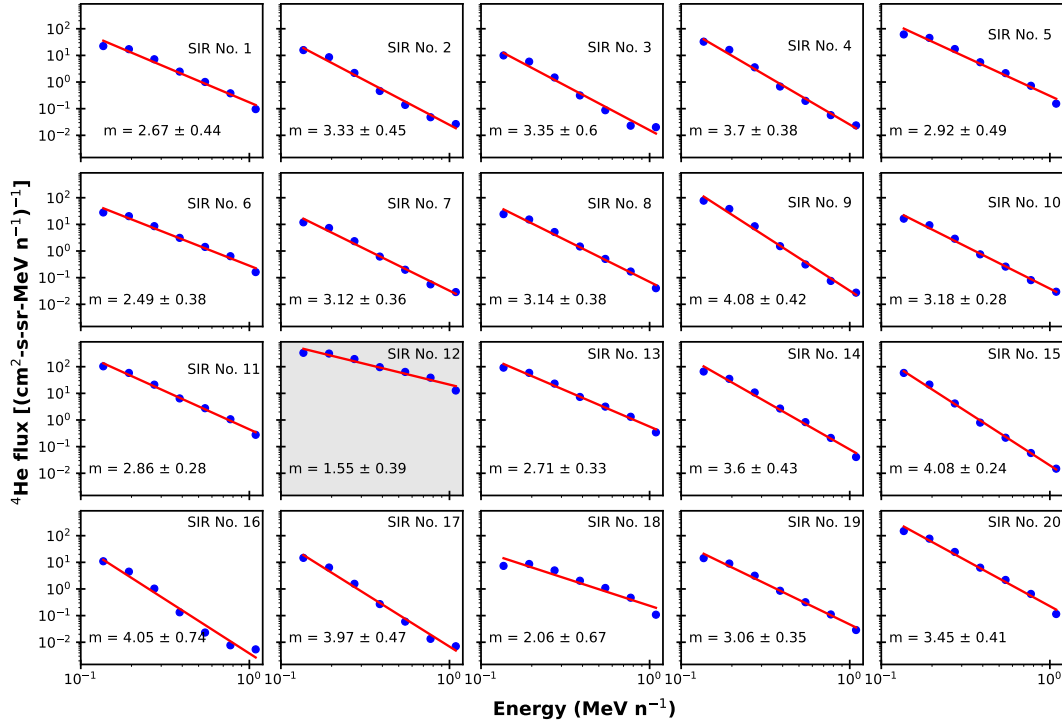


Figure 4.2: The graphs illustrate the contrast between the differential directional flux and energy spectra of ^4He during flux enhancements associated with SIRs 1–20. Each graph corresponds to a specific SIR event, as indicated in the upper right corner. The spectral indices (m) and corresponding MoEs within the 95% confidence bounds are provided in the bottom left corner of each graph. Notably, the spectral indices of ^4He range from 1.55 to 4.08. SIR 12 is highlighted with a gray background because the spectral index of 1.55 is the lowest among all spectral indices.

September 20, 2007. Note that STEREO-B and STEREO-A observed the SIR-1 on September 19 at 18:15 UTC and September 21 at 13:35 UTC respectively. On the other hand, positions of these two satellites and the Earth on October 24, 2007 are shown in Figure 4.5 (b). SIR-2 was observed by STEREO-B on October 24 at 11:20 UTC and by STEREO-A on October 25 at 18:04 UTC.

Figure 4.6 (a) and (e) show the variations of ^4He fluxes associated with SIR 1 observed by STEREO-A and STEREO-B, respectively. The corresponding spectra during flux enhancements are shown in panels (b) and (f) of Figure 4.6. The spectral indices for STEREO-A (2.67) and STEREO-B (2.69) match very well. Figures 4.6 (c) and (g) show ^4He flux variations during SIR- 2 as observed by

4.4. SPECTRAL ANALYSIS

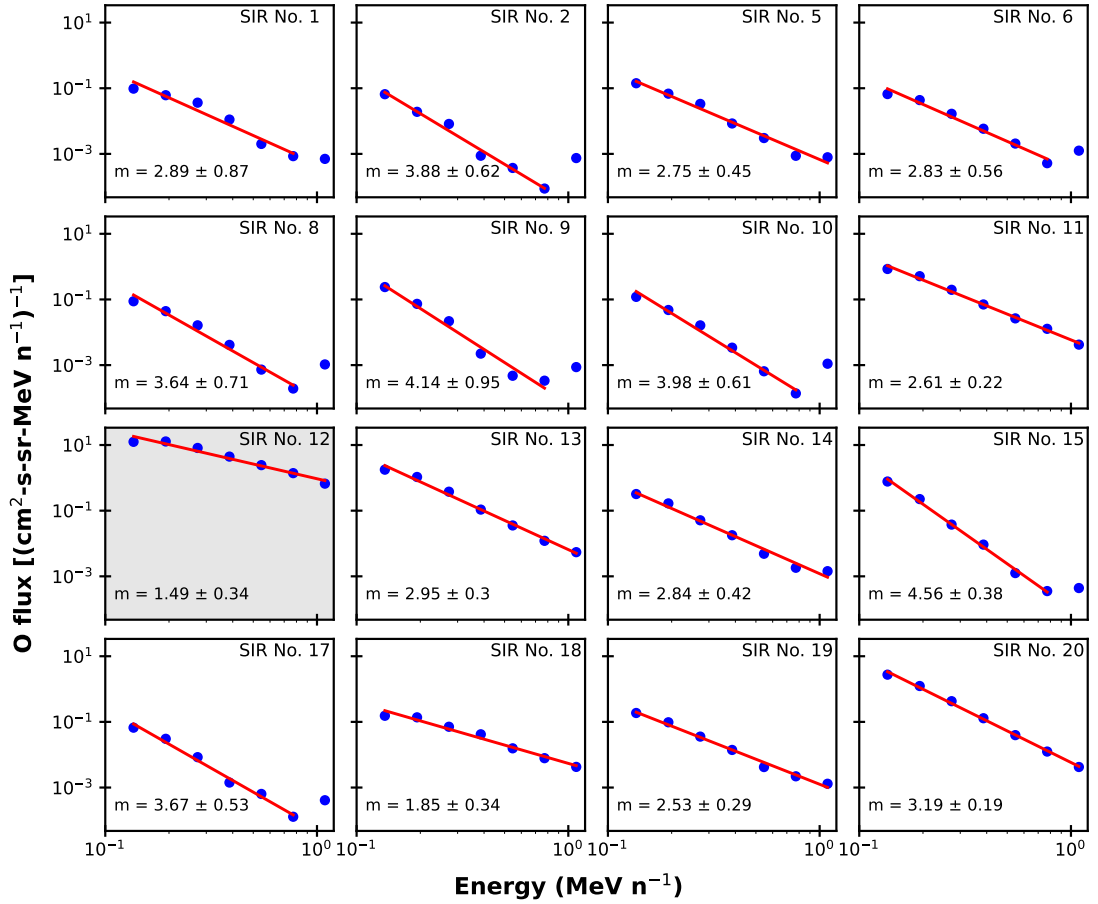


Figure 4.3: The figures depict the O spectra during enhancements within the SIR events specified in the upper right corner of each panel. Spectral indices (m) and their MoEs are indicated in the bottom left corner of all panels. Note that spectral indices for O range from 1.49 to 4.56. As in Figure 4.2, SIR 12 is highlighted with a gray background due to its noticeably lower spectral index of 1.49 compared to the other events.

STEREO-A and STEREO-B, respectively. The corresponding spectra during the increase of ^4He fluxes are plotted in Figure 4.6 (d) and (h). The spectral indices are 3.33 (STEREO-A) and 2.94 (STEREO-B). Although spectral indices different by at least 0.5 is considered significant in the present study, this exercise shows that spectral index of SIR associated ^4He may match or slightly vary as well even if observed by two different spacecrafts in the close vicinity. This aspect will be discussed in the next section.

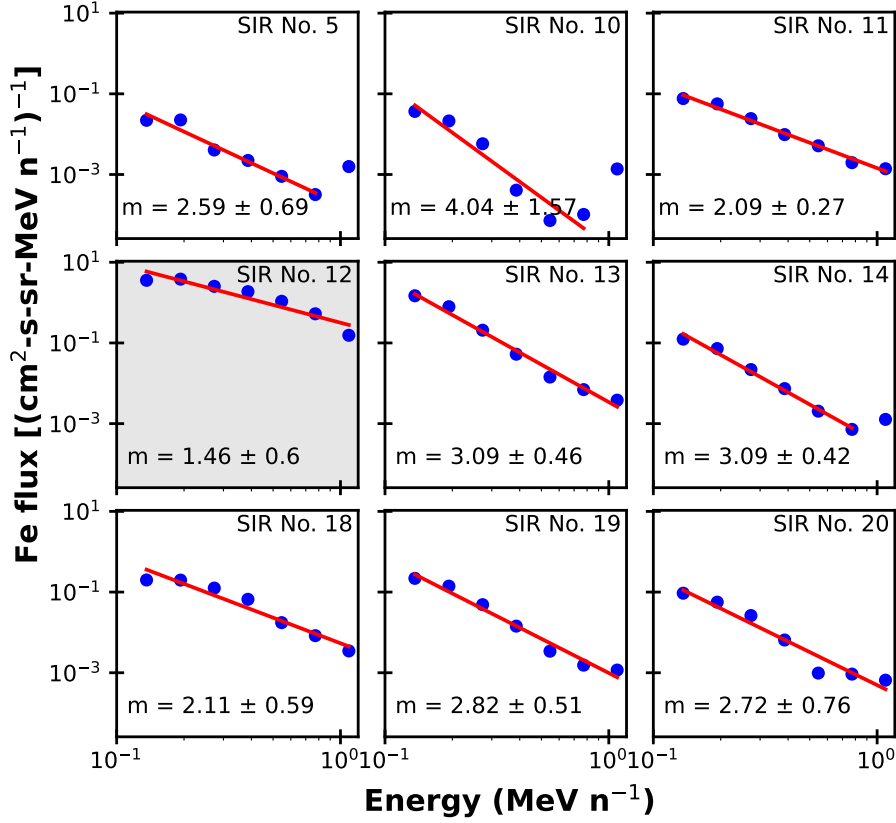


Figure 4.4: The figure shows Fe spectra during enhancements due to the SIR events specified in the upper right corner of each panel. Spectral indices (m) and their MoEs are indicated in the bottom left corner of all panels. Note that spectral indices for Fe range from 1.46 to 4.04. As in Figure 4.2 and 4.3, SIR 12 is highlighted with a gray background due to its noticeably lower spectral index of 1.46 compared to the other events.

4.5 Discussions and conclusions

This study reveals that during an SIR event, the fluxes of various suprathermal elements, such as ^4He , O, and Fe, with comparable energies per nucleon (velocities), may not exhibit enhancement. One potential explanation for this phenomenon could be the absence of initial seed populations in the IP medium that undergo acceleration or deceleration, eventually contributing to the suprathermal pool of particles. It is also possible that the intensity of seed populations was below the instrument's sensitivity threshold. It can be seen from columns 4 and 5 of Table 4.1 that O/ ^4He and Fe/ ^4He ratios vary at least one order of magnitude and

4.5. DISCUSSIONS AND CONCLUSIONS

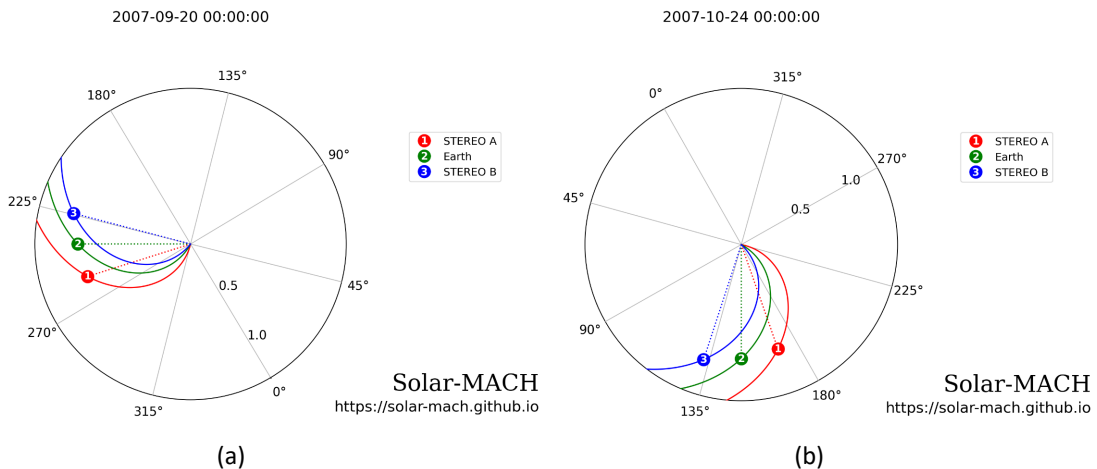


Figure 4.5: The diagrams illustrate the relative positions of (1) STEREO-A (red), (2) the Earth (green), and (3) STEREO-B (blue) at two specific times: (a) on September 20, 2007, at 00:00 hours, and (b) on October 24, 2007, at 00:00 hours. The solid colored lines represent Parker spirals connecting these objects, calculated assuming a solar wind speed of 400 km/s. This visualization was generated using Solar-MACH software (Gieseler et al., 2023) [URL: <https://solar-mach.streamlit.app/?embedded=true>].

two orders of magnitude, respectively. While in 18 SIR events $O/{}^4\text{He} > \text{Fe}/{}^4\text{He}$, there are 2 events (SIR-18 and SIR-19) when the $O/{}^4\text{He} < \text{Fe}/{}^4\text{He}$. Therefore, it seems unlikely that the absence of enhanced O or Fe fluxes in some of the SIR events is due to instrument sensitivity as in that case, the above two exceptions would not have occurred. Another possible factor could be the effectiveness of the mechanism responsible for generating suprathermal ions within the IP medium. Ebert et al. (2012) demonstrated a correlation between the peak intensity of $< 0.8 \text{ MeV n}^{-1} {}^4\text{He}$ ions and local magnetic compression ratios (M) at 1 AU, even without reverse shocks. Similarly, Desai et al. (1998) established a link between the strength of local compression ratios and the intensity of $\sim 1 \text{ MeV}$ protons at 5 AU. Thus, it seems that the strength of local compression ratios significantly influences the variations in intensity observed in $< 1 \text{ MeV n}^{-1}$ suprathermal particles. Nevertheless, the studies mentioned do not provide clarity on the specific threshold of compression ratio strength necessary to elevate suprathermal fluxes above the background level.

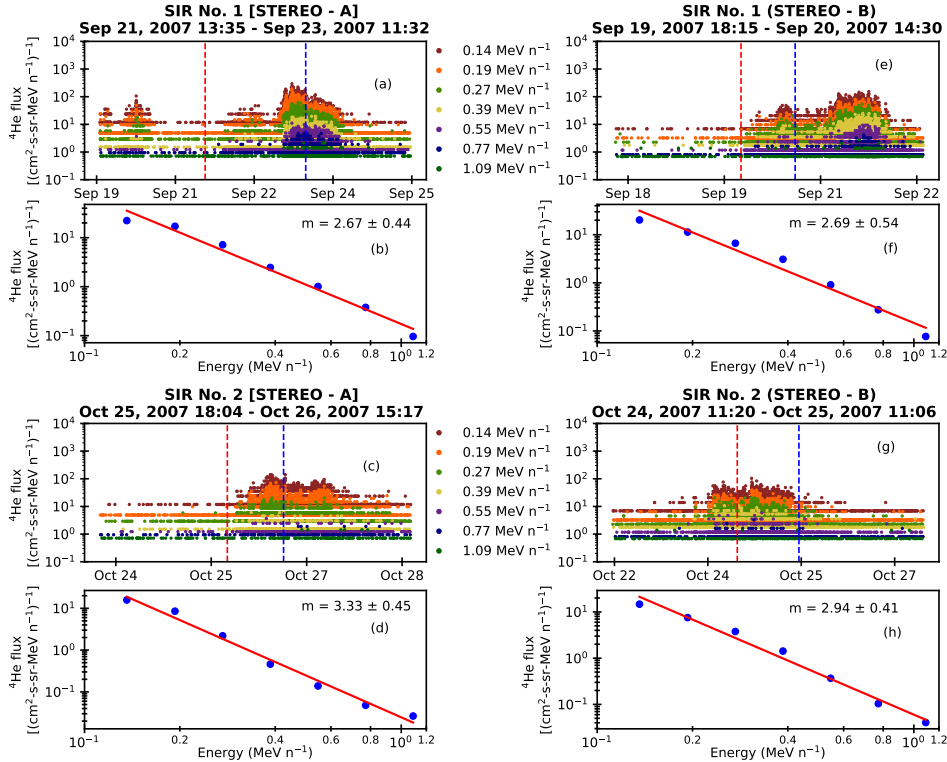


Figure 4.6: The temporal variations of ${}^4\text{He}$ fluxes at various energies, as noted between panels (a) and (c) for measurements by STEREO-A, and panels (e) and (g) for measurements by STEREO-B, correspond to two pairs of SIR events (SIR–1 observed by both STEREO-A and STEREO-B, and SIR–2 observed likewise). These spacecraft were in close proximity during these observations. The spectra of ${}^4\text{He}$ during the enhanced periods linked with SIR–1 (for both STEREO-A and STEREO-B) and SIR–2 (again, for both spacecraft) are displayed in panels (b) and (f) and panels (d) and (h), respectively, along with the spectral indices (m) and their corresponding MoEs.

The spectral analysis of ${}^4\text{He}$, O, and Fe fluxes reveals considerable variability in the spectral indices across different shock-less SIR events, with indices ranging from 1.55 to 4.08 for ${}^4\text{He}$, 1.49 to 4.56 for O, and 1.46 to 4.04 for Fe. Similar ranges of spectral indices have been reported by [Mason et al. \(2008b\)](#) and [Allen et al. \(2021\)](#) for CIR-associated ${}^4\text{He}$ within the energy range of 0.16–0.91 MeV n^{-1} , measured by the Ultra-Low Energy Isotope Spectrometer (ULEIS) on board the Advanced Composition Explorer (ACE) and the Suprathermal Ion Spectrograph (SIS) on board the Solar Orbiter. Some of the events studied by [Mason et al. \(2008b\)](#) involve shocks, but even in the absence of well-defined shocks at 1

4.5. DISCUSSIONS AND CONCLUSIONS

AU, particle acceleration can occur in gradual compressing regions associated with SIR/CIRs (Giacalone et al., 2002). Filwett et al. (2019) also observed variations in spectral indices of suprathermal particles across different SIR events. Notably, suprathermal heavy ions (such as O and Fe) associated with IP shocks also exhibit spectral index variations ranging from 1.00 to 4.00 in the energy range of 0.1–0.5 MeV n^{-1} (Desai et al., 2004). Hence, wide variations in spectral indices of suprathermal particles below 1 MeV n^{-1} appear to be a common characteristic of stochastically accelerated particles.

To examine the spatial variability in the spectral index of suprathermal particles linked with SIR events, the ^4He spectra from two specific SIR events (designated as SIRs 1 and 2 in Table 4.1) are contrasted. These events were initially detected by STEREO-B and subsequently by STEREO-A when the satellites were in close proximity (approximately 84 Gm) to each other. Despite their proximity, the satellites recorded differences in solar wind parameters across both events, including variations in magnetic field, maximum proton density, and extreme solar wind speeds. Notably, in the first SIR event observed initially by STEREO-B and then by STEREO-A, the spectral indices of ^4He were nearly identical (2.67 for STEREO-A and 2.69 for STEREO-B). Conversely, in the second SIR event, there were differences in the spectral indices for ^4He observed by STEREO-B and STEREO-A (2.94 for STEREO-B and 3.33 for STEREO-A). Further investigation revealed that the second SIR event observed by STEREO-B followed an interplanetary coronal mass ejection (ICME), whereas STEREO-A did not detect any ICME during that time. This observation suggests that the spectral index of suprathermal particles associated with SIRs may vary when the suprathermal particle population comprises particles from multiple sources. This idea finds support in the work of Schwadron et al. (2010), who proposed that the time-averaged spectra of particles are essentially a combination of various distribution functions associated with different solar wind conditions, such as temperature and density. In essence, because SIRs gather residual particles from different events (for instance, particles from an ICME in the second SIR event observed by STEREO-B)

across various regions of the IP medium throughout their evolution, it is plausible that multiple processes influence the modulation of suprathermal particle spectra.

It is notable from Table 4.1 that there are variations in the spectral indices for different elements across 19 SIR events, with the exception of SIR 12. Earlier studies have also documented the presence of nonuniform spectral indices for different elements within a particular SIR event (Filwett et al., 2019). Mason et al. (2008b) previously reported a strong correlation between the spectral indices of ^4He and O within the energy range of 0.16–0.91 MeV n^{-1} , noting that the average spectral index of O is approximately 1.03 times that of ^4He . However, this investigation reveals a different scenario. It is observed that in 50% of the SIR events where enhancements in O fluxes are observed (as indicated in Columns 4 and 5 of Table 4.1), the spectra of ^4He are actually harder. Furthermore, the spectral index of Fe does not align with the spectral index of other elements either. Considering the FIP, where O (~ 13.6 eV) lies between Fe (~ 7.9 eV) and ^4He (~ 24.6 eV), and the differences in m/q among these elements, it appears that the source and generation mechanisms responsible for producing the suprathermal particles associated with most shock-less SIR events at 1 AU might be influenced by both the FIP and m/q values. While FIP of elements is one of the primary factors that controls the original abundances of different elements closer to the Sun, the m/q of elements can affect the abundance in the IP medium. Therefore, these two factors appear to produce a difference in behaviors of ^4He , O, and Fe for most of the cases.

According to these arguments, SIR-12 appears as an exceptional and distinctive case. Despite having different values for and m/q , the suprathermal ^4He , O, and Fe exhibit nearly identical spectral indices (close to 1.5) within SIR 12. In a series of papers, Fisk and Gloeckler (2006, 2008, 2014) proposed that compressional turbulences could accelerate particles when, in a steady state, these particles do equal work on the turbulences. The source of free energy in this process stems from pressure variations in the core particles. This free energy then flows upward in energy through suprathermal tails, exhibiting a power-law index of 1.5 (Fisk and Gloeckler, 2006). However, this scenario evidently does not hold true for

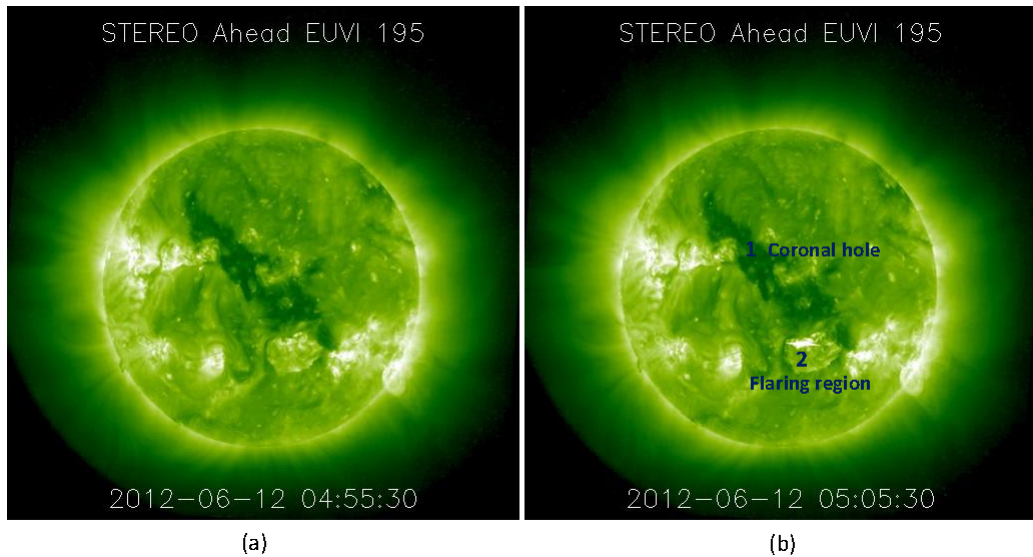


Figure 4.7: These images are captured by SECCHI instrument (e.g., [Wülser et al., 2004](#)) on board STEREO-A in 19.5 nm on June 12, 2012 at (a) 04:55:30 UTC and (b) 05:05:30 UTC. A massive coronal hole and a flaring region are marked by ‘1’ and ‘2’, respectively in panel (b). The location of the flare region, as mentioned in [Chertok et al. \(2015\)](#), is S15W126.

suprathermal particles associated with other SIR events examined in this study. [Mason et al. \(2008b\)](#) and [Filwett et al. \(2019\)](#) did not observe any clustering of spectral indices around 1.5. Notably, the pump mechanism proposed by [Fisk and Gloeckler \(2008\)](#), which they suggested accounts for the 1.5 spectral index, is only applicable to the quiet solar wind, devoid of shocks or large-scale compression regions. Given that a spectral index very close to 1.5 is observed in the ^4He , O, and Fe spectra associated with only one SIR event (SIR-12), the involvement of the pump mechanism can be discarded in this case. In the subsequent section, alternative explanations for the occurrence of the 1.5 spectral index across different species are explored.

To investigate SIR 12, Figure 4.7 is presented, which displays images of the solar corona in 19.5 nm (extreme ultraviolet) light captured by the Sun-Earth Connection Coronal and Heliospheric Investigation (SECCHI) instrument aboard STEREO-A on June 12, 2012, at approximately (a) 04:55 UT and (b) 05:05 UT. From Figure 4.7, it is evident that a sizable coronal hole was present during this time, extending from the northeast to the southwest mid-latitudes of the Sun and

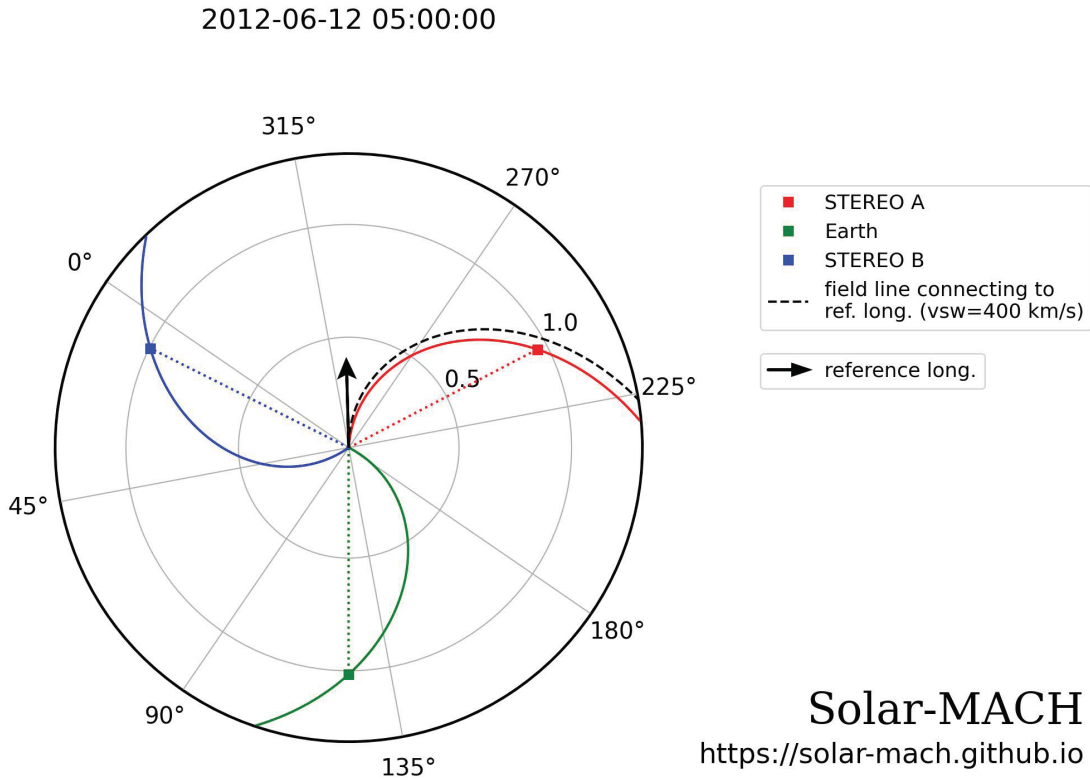


Figure 4.8: On June 12, 2012, at 05:00 UT, the positions of STEREO-A (red), Earth (green), and STEREO-B (blue) are shown. Solid colored spirals, based on a solar wind speed of 400 km/s, connect these objects to the Sun. A solid arrow indicates the location and direction of the solar flare referenced in Figure 4.7. Additionally, a dashed black spiral represents the magnetic field line originating from the flare location. This figure suggests that there is a possibility of STEREO-A being magnetically connected to the flaring region during the passage of SIR 12. It is noted that at this time, the Carrington longitudes of Earth and STEREO-A were 127.2 and 244.6, respectively.

encompassing the equatorial region. Figure 4.8 depicts the positions of STEREO-A, the Earth, and STEREO-B around the same time. At this juncture, the Carrington longitudes of the Earth and STEREO-A were 127.2 and 244.6, respectively. Consequently, this coronal hole was not visible from either the Earth or STEREO-B. It is possible that SIR 12, which commenced on June 12, 2012, at 04:00 UT, was triggered by the fast solar wind stream emanating from this extensive coronal hole. Interestingly, the SECCHI images also reveal the onset of a flare at 05:05 UT. The flaring region was situated at the edge of this coronal hole (denoted by "2" in Figure 4.7). Chertok et al. (2015) identified this flare event as an M4.6 class flare

4.5. DISCUSSIONS AND CONCLUSIONS

by analyzing the length of the blooming streak associated with it. As depicted in Figure 4.8, the magnetic field line connecting the flare location (S15W126, according to Chertok et al., 2015) closely aligns with STEREO-A. Therefore, it is likely that the sharp enhancements in suprathermal ^4He , O, and Fe fluxes are associated with an impulsive solar energetic particle (ISEP) event associated with the solar flare, as illustrated in Figure 4.7.

Mason et al. (2000, 2002) demonstrated, through data analysis from the ULEIS and Solar Isotope Spectrometer (SIS) instruments aboard ACE spacecraft, that a specific category of ^3He -rich ISEP events displays power-law behavior in the heavy ion spectra (e.g., ^3He , ^4He , O, and Fe) within the energy range of 0.1–1.0 MeV n^{-1} . In their study, Mason et al. (2002) highlighted an ISEP event observed by ACE on September 9, 1998, where ions with energies below 1.5 MeV n^{-1} , including ^3He , ^4He , O, and Fe, exhibited comparable variations in their spectra. The spectral indices fell within the range of 1.15–1.38. While the association of these ISEP events with solar flares appears promising for yielding similar spectral indices, conflicting evidence exists in the literature. The typical time difference between the onset of a solar flare (as measured by GOES X-ray fluxes) and the detection of an ISEP event near Earth is approximately 1 hour, as noted by Papaioannou et al. (2023). However, in the case of SIR-12, this interval extends to about 9 hours. Additionally, even in certain ISEP events, the simultaneous enhancement of various energy channels does not always occur as expected, as highlighted by Mason et al. (2000). This indicates that the increase in particles, such as ^4He , at higher energies (e.g., 1 MeV n^{-1}), may commence earlier than for particles at lower energies (e.g., 0.5 MeV n^{-1}). Assuming a typical Parker-spiral path length of 1.2 AU between the flaring region depicted in Figure 4.7 and the location of STEREO-A, the expected time delay between a 0.5 MeV n^{-1} and a 1 MeV n^{-1} particle regardless of the specific particle type, given the energy unit normalization by mass number is calculated to be over an hour. However, in the case of the ^4He flux enhancements corresponding to energies of 0.55 MeV n^{-1} and 1.09 MeV n^{-1} in SIR-12, no significant time delay is observed. Consequently, it appears unlikely

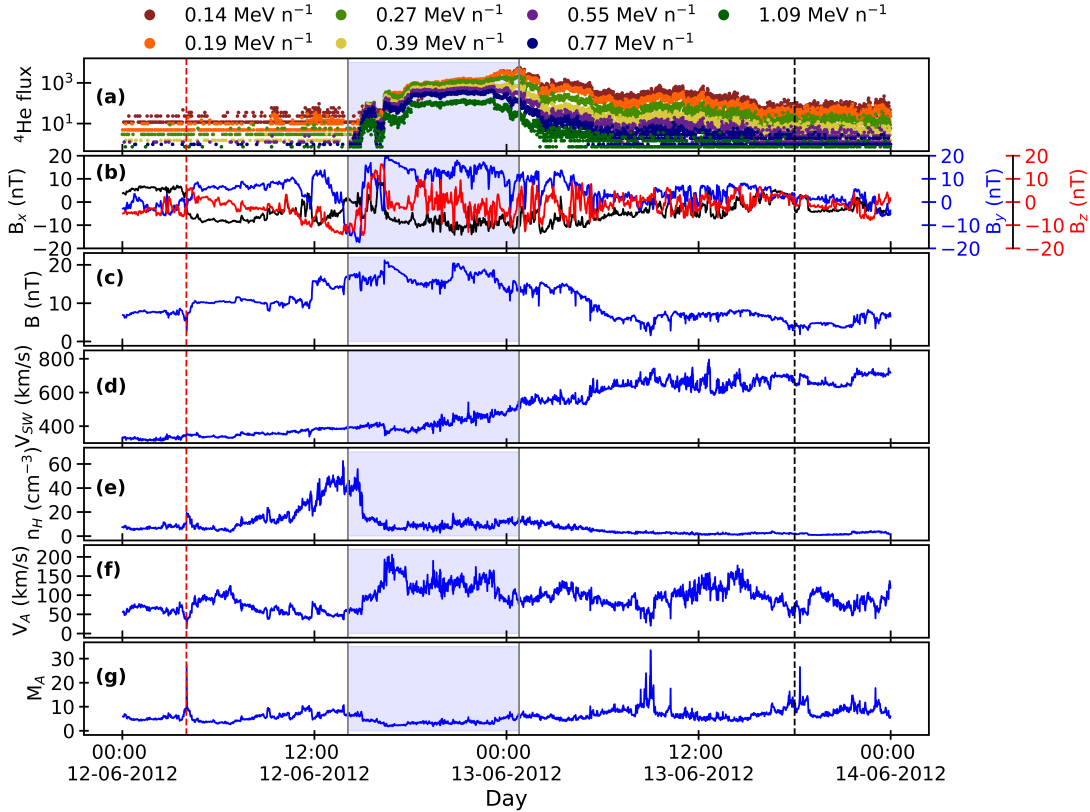


Figure 4.9: Panel (a) shows the variation in ${}^4\text{He}$ fluxes at different energy channels (mentioned at the top of the figure) in SIR 12. Panels (b)–(e) depict respectively the components of IMF (B_x , B_y , and B_z) in the Radial Tangential Normal (RTN) coordinate system, total magnetic field (B), solar wind velocity (V_{sw}), and proton density (n_H). The variations in the Alfvén speed (V_A) during SIR 12 is plotted in panel (f). Panel (g) shows the fluctuations in the Alfvénic Mach number (M_A). The interval between the start of the ${}^4\text{He}$ flux enhancement and the time of the peak 0.14 MeV n^{-1} flux is shaded.

that these flux enhancements directly originate from the flaring region. Another process within the IP medium may be at play, resulting in an insignificant time delay and the consistent spectral index observed across three different elements with varying FIP and m/q .

In this context, it is proposed that a more fitting mechanism to explain this event could be the acceleration of particles through the merging and contraction of small-scale magnetic islands (SMIs), as discussed by Drake et al. (2006a,b), Cargill et al. (2006), , Bian and Kontar (2013), Zank et al. (2014), Khabarova et al. (2015a), Le Roux et al. (2015), and others. These SMIs can form in the

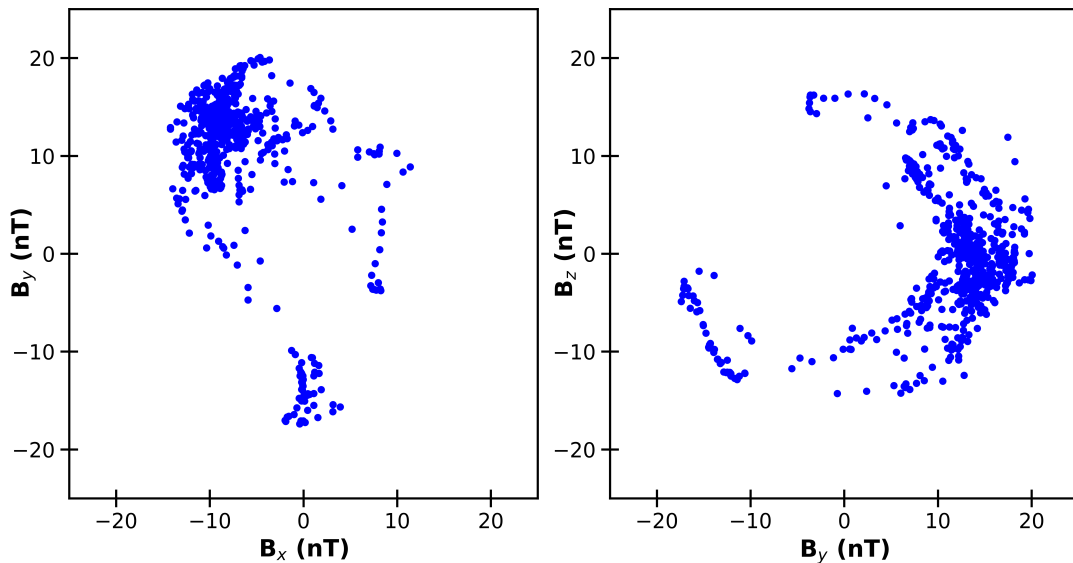


Figure 4.10: Hodograms of the IMF (a) B_x – B_y and (b) B_y – B_z during the shaded interval, as shown in Figure 4.9. The rotation in the magnetic field components establishes the existence of magnetic islands during this interval.

vicinity of the heliospheric current sheet (Bemporad, 2008; Cartwright and Moldwin, 2008; Khabarova et al., 2015a,b, 2016 etc.) due to various active processes in the solar corona (such as solar flares, CMEs) or instabilities within the current sheets (Eastwood et al., 2002; Drake et al., 2006a). Typically, the length scale of these SMIs ranges from 10^6 to 10^7 kilometers (Khabarova et al., 2015a). Zank et al. (2014) demonstrated analytically that particles accelerated by the merging and contraction of magnetic islands exhibit power-law behavior, with the spectral indices dependent on the Alfvénic Mach (M_A) number, which is independent of the m/q of the particles. At 1 AU, a specific case of this theory (with $M_A = 7$) predicts a velocity distribution spectrum that follows a V^{-5} dependence (where V represents particle speed), equivalent to a differential directional flux spectrum of approximately $E^{-1.5}$ (where E is the energy of the particle). To evaluate the applicability of Zank et al.’s theory to our observations, particularly concerning the 1.5 spectral indices, Figures 4.9 and 4.10 are presented. Figure 4.9 depicts (a) ^4He fluxes across different energy channels, (b) the components (B_x , B_y , and B_z) of the IMF in the RTN coordinate system, (c) the magnitude of the magnetic field (B), (d) the bulk solar wind speed (V_{SW}), (e) the proton number density

(n_H), (f) the Alfvén speed (V_A), and (g) the Alfvénic Mach number (M_A) during SIR-12. Figure 4.9 (g) illustrates that M_A fluctuates within the range of 5–10 several hours before the onset of ^4He flux enhancements, aligning with Zank et al. (2014)’s hypothesis. More importantly, the presence of magnetic islands is corroborated by hodograms (e.g., Khabarova et al., 2015a) displayed in Figures 4.10, where rotation within the IMF inside the magnetic islands (as indicated by the shaded interval in Figure 4.9) is evident. To estimate the typical length scale (l), Eq. 2 from Khabarova et al. (2015b) is used, which states $l = r \times (B/B_0)^{1/2}$ km (where r is distance in AU, $B = B(r)$ is the magnetic field, and $B_0=10,000$ nT is the minimum coronal magnetic field). With a typical value of $B = 15$ nT inside the shaded region in Figure 4.9, $l \simeq 6 \times 10^6$ km is the calculated value of length scale of SMIs at 1 AU. Hodograms corresponding to other SIR events have been checked. A few events other than SIR-12 showed indication of rotation of magnetic field components. However, the very fact that the spectral indices of these elements are different in those cases suggests that processes other than merging/contraction of SMIs might also be operational.

At this point, it is important to discuss the origin of SMIs in IP medium. Generally, dynamical processes associated with magnetic reconnection and turbulence can lead to the production of magnetic islands (Greco et al., 2010; Markidis et al., 2013). It may be noted that Susino et al. (2013), Eriksson et al. (2014) suggested, which was supported by Khabarova et al. (2015a), that these SMIs near the heliospheric current sheet in the solar wind are likely to be formed due to magnetic reconnection occurring anywhere from the solar corona to a distance of several AU. Therefore, the origin of these SMIs may be debated but the acceleration of the particles in this case appears to be local (coming from the same source without significant dispersion) in nature. The spectral index of the particles corresponding to SIR 12 is around 1.5, which is also consistent with the corresponding spectral index associated with the acceleration of particles due to magnetic reconnection (e.g., Gordovskyy et al., 2010). This provides an additional clue to the origin of the energetic particles during SIR 12.

4.6. KEY FINDINGS

Another possibility of detecting the almost identical spectral indices could be related to the unmodulated propagation of different ion species from the source location to the observer. In the reconnection site, due to direct electric field, particles may be accelerated. In this context, the Dreicer electric field is a critical electric field above which electrons in a collisional plasma can be accelerated to become runaway electrons. It can be estimated by the following formula (Connor and Hastie, 1975)

$$E_d = \frac{1}{4\pi\epsilon_0} \frac{ne^3 \ln(\Lambda)}{m_e v_{T_e}^2}$$

where e is the electronic charge, m_e is the mass of electron, n is the electron density, $\ln(\Lambda)$ is the Coulomb logarithm (equals to 10), and v_{T_e} is the electron thermal speed. Accelerated electrons experience a drift $\frac{E_d \times B}{B^2}$, which is independent of charge and mass. This electric field is not applicable for the ions which the present work is concerned with.

Hence, it seems that the almost identical spectral indices (nearly 1.5) observed for ^4He , O, and Fe linked with SIR-12 stem from the localized acceleration of these particles by SMIs. This localized particle acceleration also supports the minimal modulation, indicated by the absence of significant changes in spectral indices, observed in these particles prior to their detection by STEREO-A. These findings further support the characteristics of the source process.

4.6 Key findings

The salient outcomes of this chapter can be summarized into the following points.

1. All SIR events do not generally enhance heavy ion (like O and Fe) fluxes at 1 AU. The possible reasons include low seed population densities, less efficient acceleration mechanism framework etc.
2. SIR-associated suprathermal particles display wide variations in spectral indices. This variation is prominent in case of different elements. It appears to be consistent with stochastic nature of acceleration mechanism and IP modulation of these particles depending on FIP and m/q of species.

3. Sometimes, suprathermal particles may be accelerated near the spacecraft at 1 AU by merger and contraction of small-scale magnetic islands. Spectral indices of different elements accelerated by this mechanism may be identical.

Chapter 5

Suprathermal particles upstream of the Earth's bow shock

Excerpt

Energetic upstream ions propagating towards the Sun from the Earth's bow shock have been observed in the past. In this chapter, the relationship between solar wind suprathermal and upstream ions has been investigated by analyzing fluxes of H, ^4He , and CNO obtained from multidirectional in-situ measurements at the first Lagrange point (L1) of the Sun-Earth system during 2012–2014. In this work, a total of 49 upstream events have been selected by comparing the flux enhancements of the upstream ions with the solar wind suprathermal ions. It is found that the suprathermal ions with energies less than 300 keV are observed at the L1 point during the upstream events suggesting an energy cut-off that exists for these events. This points towards the efficiency of the terrestrial bow shock in generating the upstream ions. Interestingly, spectra of upstream ions soften systematically as compared to the spectra of their solar wind counterpart. The degree of spectral softening increases with decreasing mass-to-charge ratio of the species. Since during most of the events the interplanetary magnetic field (IMF) was radial, it is argued that cross-field diffusion of upstream ions gives rise to the modulation (spectral softening) of upstream ions, which is dependent on the mass-to-charge ratio of species. This work indicates towards a systematic change in solar wind suprathermal ions after interaction with the bow shock. In addition,

this work gives a hint for possible source of heavy ions (CNO) during the upstream events.

5.1 Introduction

Origin and characteristics of energetic ions (< 1 MeV) upstream of the Earth's bow-shock has been studied for the past few decades (e.g. [Asbridge et al., 1968](#); [Sarris et al., 1976](#); [Scholer et al., 1979](#); [Paschmann et al., 1980](#); [Desai et al., 2000](#); [Meziane et al., 2002](#); [Kronberg et al., 2011](#) etc.). These upstream events are generally characterized by short durations (~ 1 -2 hours), steeply falling spectra ($j \sim E^{-2}$ to E^{-6} , ([Anagnostopoulos et al., 1998](#)), field aligned sunward anisotropies ([Mitchell and Roelof, 1983](#); [Müller-Mellin et al., 2008b](#); [Desai et al., 2008](#) etc.). These events are observed in higher numbers associated with corotating interaction regions (CIRs) (e.g., [Desai et al., 2000](#)), intense geomagnetic activity ([Anagnostopoulos et al., 1998](#)). Despite a number of studies, there exists significant uncertainty about the origin of these upstream ions. There are broadly two schools of thought regarding the origin of these upstream particles – (i) these ions are accelerated by the Earth's bow shock ([Lee, 1982](#); [Trattner et al., 2003](#)) and (ii) these are generated in the Earth's magnetosphere ([Sheldon et al., 2003](#); [Anagnostopoulos et al., 2005](#); [Chen et al., 2005](#)) and diffuse upstream of the bow shock.

There are different types of ions present in the upstream region of the Earth's bow shock. Specularly reflected ions are the least energetic (with energies of few keV) among all the suprathermal and energetic ions that are observed immediate upstream and downstream of the quasi-perpendicular (shock normal angle, $\theta_{Bn} > 45^\circ$) bow shock. These ions are energized by the solar wind electric field ([Gosling et al., 1982](#)) and are confined to within one gyro-radius upstream from the shock ([Gosling and Robson, 1985](#)). A relatively more energetic ($< \sim 10$ keV) field aligned proton beams are thought to be produced either by reflection from the shock or by the leakage of hot proton populations from the magnetosheath into the upstream region ([Schwartz and Burgess, 1984](#)). Diffuse ions, on the other hand, can extend up to 200 keV per charge and show almost isotropic distribution in the spacecraft

frame (Scholer et al., 1979, 1981). Large-amplitude hydromagnetic waves are always observed in association with these diffuse ions Paschmann et al. (1979).

It is to be noted that Both ions and electrons are reflected from the Earth's bow shock due to various reasons like (i) magnetic mirroring, (ii) interaction with low frequency waves, (iii) interaction with electric field and (iv) due to cross-shock potential. According to test particle simulation, dynamics of particles in the upstream of the Earth's bow shock is divided into three kinds: specular reflection (Broll et al., 2018), multiple traversal, and multiple bounce. The specular reflection of protons is mainly due to a cross-field potential, in the Hoffman-Teller frame of reference, formed by plasma pressure gradient, magnetic pressure gradient and different gyrations of ions and electrons (Broll et al., 2018). Ions with energy less than this electrostatic potential are reflected back upstream. Particles with sufficiently larger pitch angles can be reflected from the bow shock due to combined effects of magnetic mirroring and pitch angle scattering (Burgess, 2007). Particles may also be lost due to wave-particle interactions and pitch angle scattering and leave the magnetic field. In that case, loss-cone will depend on the IMF strength. Energetic particles upstream of the bow shock are observed to show loss-cone shaped distribution (e.g., Seki et al., 2009).

One of the interesting observations regarding upstream ion events is that these ions are observed at wide spatial distances starting from the vicinity of the bow-shock (Ipavich et al., 1981; Meziane et al., 2002) to up to $1750R_E$ (Desai et al., 2008; Kronberg et al., 2011) upstream of it. Paschmann et al. (1980) proposed a theory in which solar wind particles are reflected by the Earth's bow shock and the energy gained by these particles is a function of IMF, solar wind velocity, and the local shock normal. Interestingly, Dwyer et al. (2000) reported that there is more than 50% chance that two spacecraft located at $\sim 70 R_E$ apart can also observe upstream events simultaneously. These authors remarked that the size of the source regions of these simultaneously observed upstream events are larger than the spatial size of the bow shock. While most of these studies indicated a magnetic connection between the spacecraft and the bow shock to be essential for

observing upstream events, [Haggerty et al. \(2000\)](#) has reported upstream events that were observed with transverse magnetic field configuration ahead of the bow shock. Results by [Desai et al. \(2008\)](#) show that upstream events can be observed simultaneously by two spacecraft even if they are separated by $800 R_E$ both radially and laterally. These authors suggested that one of the possible sources of these events is large amplitude Alfvén waves with spatial scales of the order of 0.03 AU.

Upstream ion distributions in the vicinity of the bow shock and far upstream are very different ([Scholer et al., 1981](#)). It is possible that highly anisotropic energetic particles far-upstream of the bow shock are originally the leaked diffuse ions that travelled mostly scatter-free to long distances ([Scholer et al., 1981](#); [Mitchell and Roelof, 1983](#)). However, the particle fluxes decay exponentially with increasing distance from the bow shock ([Ipavich et al., 1981](#); [Trattner et al., 1994](#); [Kis et al., 2004](#)). These studies essentially show that the e-folding distance in that case depends on the energy of the particles indicating energy dependent escape of particles from the bow shock ([Desai et al., 2008](#)). Therefore, how the properties of ions with different masses are modulated during the transport from the bow shock to interplanetary (IP) medium remains unclear till date.

One way to address this issue is to explore any systematic relationship that may or may not exist between the solar wind suprathermal ions (propagating away from the Sun) and the upstream ions (propagating towards the Sun) reaching the L1 orbit. Since there are evidences of the solar wind ion populations to be scattered by the Earth's bow shock, upstream ions should carry the signatures of bow shock modulation. Therefore, a comparative study between suprathermal particles during upstream events at L1 and the original solar wind suprathermal particles that crossed L1 earlier might capture these effects. It can be conjectured that this approach may lead to two scenarios about upstream ions. One possible scenario may be systematic modulation (changes in the spectral slope of upstream ions in different events vary systematically) indicating dominance of bow shock related effects and the second scenario may be random modulations of spectral

5.2. DATA USED AND INSTRUMENTATION

slopes indicating multiple processes/sources in action that includes bow shock as well. Keeping this objective in mind, by using the observations from the Wind spacecraft, spectra of suprathermal H, CNO, and ^4He propagating towards the Sun and towards the Earth are compared. The analyses bring out a mass-dependent systematic softening in the spectra of sunward propagating suprathermal ions over the suprathermal ions propagating toward the Earth.

5.2 Data used and instrumentation

H, ^4He , and CNO fluxes analyzed in this work are obtained from the two telescopes (T1 and T2) of STEP instrument of EPACT investigation [Von Rosenvinge et al. \(1995\)](#) on board the Wind spacecraft. The measurement technique of STEP has already been discussed in Chapter 2. It is to be mentioned here that T1 and T2 of the STEP instrument are oriented at $\pm 26^\circ$, respectively with respect to the ecliptic plane (equivalently, 116° and 64° , respectively with respect to the spacecraft's spin axis, which is along $-Z$ direction in the Geocentric Solar Ecliptic (GSE) coordinate system. T1 and T2 scan the IP medium just above and below the ecliptic plane in eight azimuthal sectors of 45° each (see [Desai et al., 2000](#) for a schematic of the scan planes and sector information). This configuration is useful to analyze and compare suprathermal particles that come from both the ‘‘Sun sector’’ (i.e., Sun-looking sector) (by combining data of sector 1, 2, and 3 of STEP telescopes) and the ‘‘bow shock sector’’ (bow-shock-looking sector) (by combining data from sector 5, 6, and 7 of the STEP telescopes).

Event No.	Start time	End time	Flux ratio ($F_{BS/SS}$)		
			H @ 140 keV/n	^4He @ 60 keV/n	CNO @ 60 keV/n
1	2012 Jan 06 06:59	2012 Jan 06 07:53	3.94	10.67	–
2	2012 Jan 16 16:59	2012 Jan 16 18:03	15.12	28.23	0.60
3	2012 Jan 23 06:21	2012 Jan 23 07:59	0.97	1.15	0.92
4	2012 Feb 02 10:17	2012 Feb 02 11:32	0.78	0.84	0.95
5	2012 Feb 17 07:11	2012 Feb 17 08:48	7.79	11.49	2.06
6	2012 Apr 27 09:43	2012 Apr 27 10:26	6.71	5.50	4.33

CHAPTER 5. UPSTREAM ENERGETIC IONS

7	2012 May 20 00:29	2012 May 20 01:34	0.70	0.64	0.61
8	2012 May 23 14:06	2012 May 23 16:27	2.26	1.87	1.66
9	2012 Jul 07 09:56	2012 Jul 07 11:16	1.92	5.39	0.98
10	2012 Aug 01 01:34	2012 Aug 01 01:57	1.85	3.95	3.92
11	2012 Aug 20 07:06	2012 Aug 20 08:00	6.96	14.90	6.57
12	2012 Aug 21 04:48	2012 Aug 21 06:05	0.73	3.15	1.00
13	2012 Aug 27 04:39	2012 Aug 27 05:12	10.20	29.00	–
14	2012 Sep 05 17:03	2012 Sep 05 17:56	1.58	1.96	0.79
15	2012 Sep 20 16:57	2012 Sep 20 17:50	5.62	3.80	5.83
16	2012 Oct 11 12:12	2012 Oct 11 13:16	2.01	3.66	1.43
17	2012 Oct 14 04:16	2012 Oct 14 04:59	7.58	11.30	–
18	2012 Nov 26 20:42	2012 Nov 26 21:58	1.25	1.59	1.37
19	2013 Jan 08 02:34	2013 Jan 08 04:03	1.08	3.34	1.00
20	2013 Jan 27 13:58	2013 Jan 27 15:23	1.88	1.60	0.72
21	2013 Jan 27 20:48	2013 Jan 27 22:14	4.06	7.94	2.79
22	2013 Mar 13 06:25	2013 Mar 13 07:08	1.57	7.49	–
23	2013 Mar 28 00:44	2013 Mar 28 01:37	9.94	39.52	–
24	2013 May 05 05:56	2013 May 05 06:47	1.89	4.49	–
25	2013 Jun 03 23:32	2013 Jun 04 01:20	2.51	3.73	1.25
26	2013 Jun 04 10:45	2013 Jun 04 12:34	3.75	4.32	–
27	2013 Jun 21 02:06	2013 Jun 21 03:11	2.64	3.16	1.85
28	2013 Jun 21 04:17	2013 Jun 21 04:59	2.31	3.85	1.67
29	2013 Jun 30 08:54	2013 Jun 30 09:38	0.86	0.86	0.44
30	2013 Jul 18 23:23	2013 Jul 19 00:27	2.20	3.29	1.87
31	2013 Aug 22 09:55	2013 Aug 22 11:21	2.16	1.66	0.72
32	2013 Oct 16 21:20	2013 Oct 16 22:46	1.50	2.25	0.76
33	2013 Nov 10 10:54	2013 Nov 10 12:52	2.16	3.35	2.52
34	2013 Nov 10 17:56	2013 Nov 10 19:22	2.71	3.22	1.07
35	2013 Nov 17 18:22	2013 Nov 17 19:37	3.70	11.57	1.71
36	2013 Dec 08 21:47	2013 Dec 09 01:46	1.72	1.56	1.08
37	2013 Dec 31 14:51	2013 Dec 31 15:25	1.21	2.90	0.53
38	2014 Jan 03 11:46	2014 Jan 03 12:40	1.10	1.43	0.75
39	2014 Jan 04 01:34	2014 Jan 04 03:00	1.43	4.93	0.89
40	2014 Jan 04 03:13	2014 Jan 04 03:57	6.54	13.51	8.26
41	2014 Mar 06 15:27	2014 Mar 06 16:21	2.29	6.07	1.51
42	2014 Apr 04 12:46	2014 Apr 04 13:42	2.15	3.95	4.07
43	2014 May 04 15:26	2014 May 04 16:20	2.35	4.85	0.53
44	2014 Jun 19 15:13	2014 Jun 19 18:16	3.45	7.52	1.00
45	2014 Aug 04 14:11	2014 Aug 04 14:44	3.79	13.75	0.64
46	2014 Oct 20 19:54	2014 Oct 20 20:49	2.40	2.35	1.85
47	2014 Dec 08 04:37	2014 Dec 08 05:40	1.14	1.71	1.31
48	2014 Dec 08 20:47	2014 Dec 08 22:58	1.49	2.07	1.43

5.3. SELECTION OF UPSTREAM EVENTS AND METHOD

49	2014 Dec 09 02:12	2014 Dec 09 03:41	5.41	7.91	7.87
----	-------------------	-------------------	------	------	------

Table 5.1: List of start (column 2) and end (column 3) times of upstream events. Note that in all the events, either T1 or T2, or both have recorded enhancement in either H (@ ~ 140 keV) flux or ^4He (@ ~ 60 keV) flux or both the fluxes. These events are selected on the basis of T2 measurements only. Flux ratios ($F_{BS/SS}$, defined as the ratio between the ion fluence at a particular energy observed in the bow shock sector during an event and the ion fluence observed in the “Sun sector” during the same event) of H, ^4He , and CNO during the chosen upstream events are mentioned in columns 4, 5, and 6, respectively.

5.3 Selection of upstream events and method

49 upstream events are selected based on enhancements in the H (at 0.14 MeV [in T2]), ^4He (at 0.06 MeV n^{-1} [in T2]) observed in the “bow shock sector” during 2012–2014. An event is identified based on the enhancement in at least one of these two elements in the “bow shock sector” when compared to the “Sun sector” at the same time. Fluxes observed in the “Sun sector” of the detector units need not necessarily show any enhancement during these intervals. The start and end times of these events are selected based on visual inspections. The start and end times of the events are enlisted respectively in columns 2 and 3 of Table 5.1. 15 and 34 events among the 49 events listed in Table 5.1 are chosen based on the increments in H and ^4He , respectively. It is observed that the ion fluxes measured by T2 are higher than the fluxes measured by T1 most of the time. The flux variations observed by T2 are given preferences while choosing these events. It is observed that not all the three elements exhibit enhancements during all the events mentioned here. Enhancements in multiple elements are also observed in many events. Flux ratios ($F_{BS/SS}$, defined as the ratio between ion fluence at a particular energy observed in the bow shock sector during an event and ion fluence observed in the “Sun sector” during the same event) of H, ^4He , and CNO are calculated during these events and are tabulated in columns 4, 5, and 6, respectively. Note that $F_{BS/SS}$ does not capture the relative enhancement of fluxes in the “bow shock sector” with respect to the “Sun sector” during an event. Instead, it gives an idea

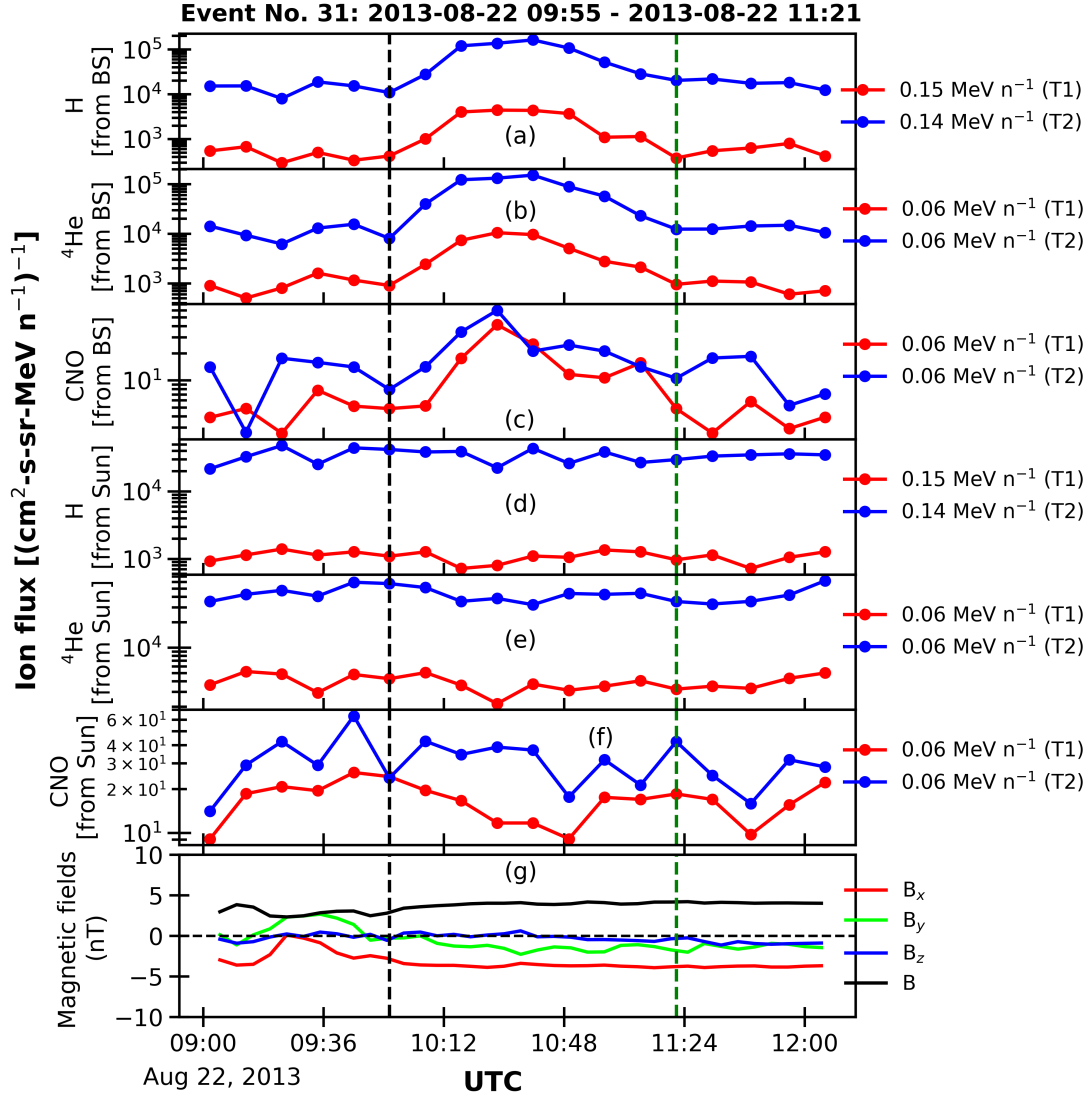


Figure 5.1: Flux variations during the upstream event 31 as listed in Table 5.1. Panel (a), (b), and (c) show respectively H, CNO, and ${}^4\text{He}$ fluxes measured by T1 (blue) and T2 (red) from the bow shock direction. The energy values are mentioned in the right side of each panel. H, CNO, and ${}^4\text{He}$ fluxes coming from the “Sun sector” are shown in panel (d), (e), and (f), respectively. Interestingly, T2 reports greater fluxes than that measured by T1 in most of the events. The start and end times of the event are marked by vertical black and green dashed line, respectively. As mentioned in Table 5.1, this event is chosen based on variation in ${}^4\text{He}$ (at 0.06 MeV n^{-1}) flux measured by T2. Panel (g) shows the components of IMF (red: B_x , green: B_y , and blue: B_z) and total magnetic field, B (black) in the GSE coordinate system.

of the relative fluence of different ions observed in both sectors.

Figure 5.1 captures a typical event in which temporal variations of H, ${}^4\text{He}$,

5.3. SELECTION OF UPSTREAM EVENTS AND METHOD

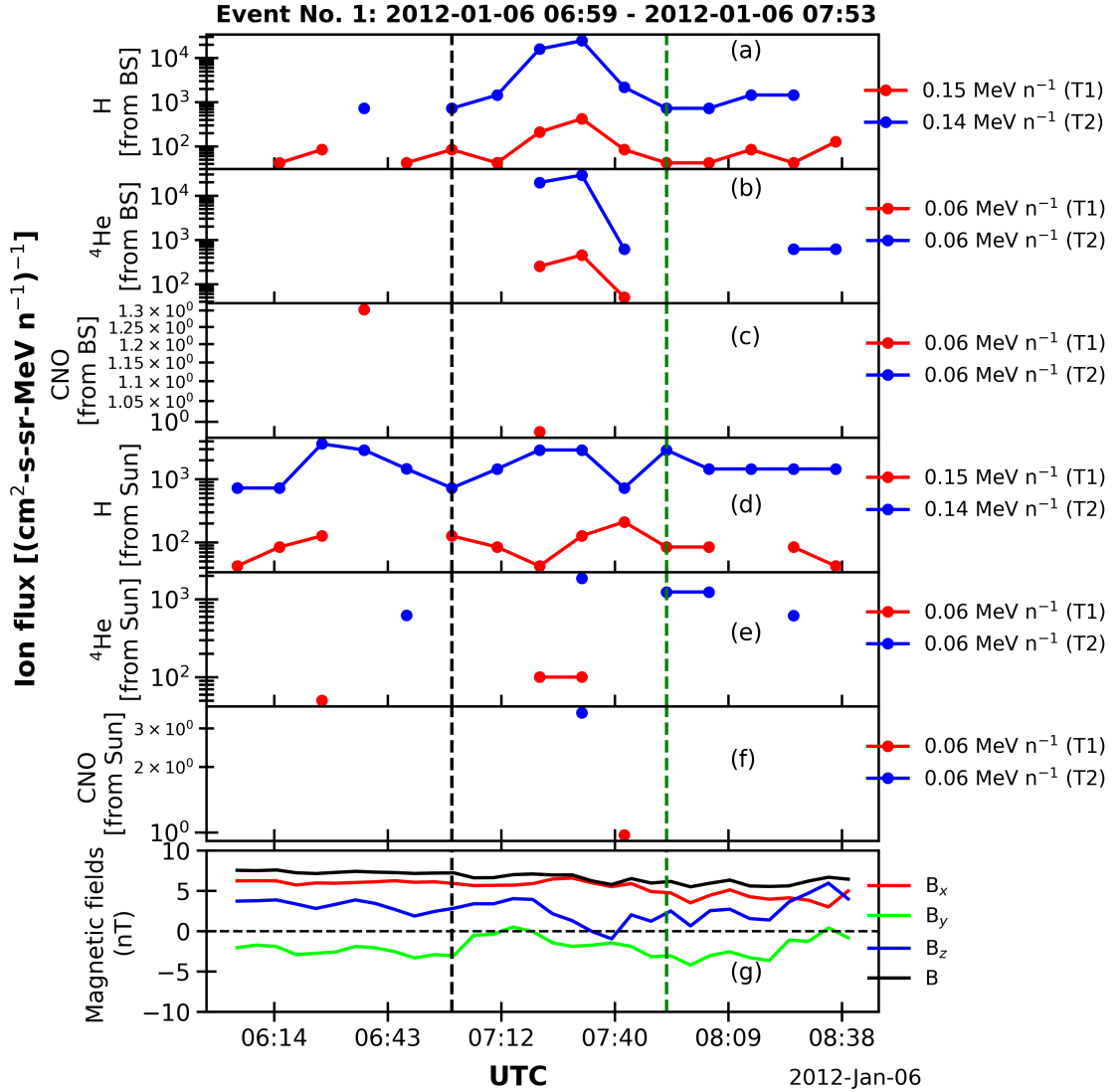


Figure 5.2: Flux variations during the upstream event 1 as listed in Table 5.1. The figure description is same as Figure 5.1. Here, no enhancement is observed in CNO fluxes.

and CNO fluxes from the “bow shock sector” and the “Sun sector” corresponding to upstream event 31 in Table 5.1 are shown. The top three panels (a, b, and c) clearly show enhancements in H, ^4He , and CNO fluxes during the event (interval between the black and green vertical dashed lines) above the background. The next three panels (e, f, and g) show flux variations in the “Sun sector” of the telescopes. Components of IMF in geocentric solar ecliptic (GSE) coordinate system during the event are shown in panel (g) of Figure 5.1. It is seen that the IMF connecting

the spacecraft and the nose of the bow shock is nearly radial and lies in the ecliptic plane during the event. Figure 5.2 is an example in which CNO fluxes are not observed by both the T1 and T2 STEP telescopes.

Once the upstream events are selected, the spectral indices of all the three elements are calculated if there is enhancement in at least three consecutive energy channels. The results obtained from this analysis are discussed in the following section.

5.4 Results

This section presents a comparison between the spectral indices of H, ^4He , and CNO observed in the “Sun sector” and the “bow shock sector” during the selected upstream events. In order to do so, it is assumed that the Sun is the major source of particles and the “bow shock sector” of T1 and T2 observes the particles scattered/reflected by the bow-shock. It should be acknowledged that there is possibility of mixing up of particles observed at L1 from different sources. Considering the path of a particle (say, H) to be a straight line between the position of Wind and the bow-shock nose with a path length of $200 R_E$, the travel-time of a proton with kinetic energy E from the spacecraft location to the bow shock nose and back can be calculated. For $E=60$ keV, this travel-time appears to be around 25 minutes. Therefore, according to the previous assumption, particles detected in the “Sun sector” of the detector units at any point of time are expected to be detected by the “bow shock sector” of the detector units on an average 30 minutes later. In Figure 5.3, the spectra of H, ^4He , and CNO observed at the “Sun sector” 30 minutes before the upstream event 31 and “bow shock sector” during the event by T1 and T2 telescopes are shown. While calculating the spectral indices from the “Sun sector”, ion fluxes are averaged over the same duration as those of the upstream events. From the spectral indices mentioned in Figure 5.3 it is found that spectra observed in the “bow shock sector” seem to be softer than that observed in the “Sun sector” of T1 and T2. This aspect is further illustrated in Figure 3 where spectral indices of H, ^4He , and CNO observed at the “bow shock

5.4. RESULTS

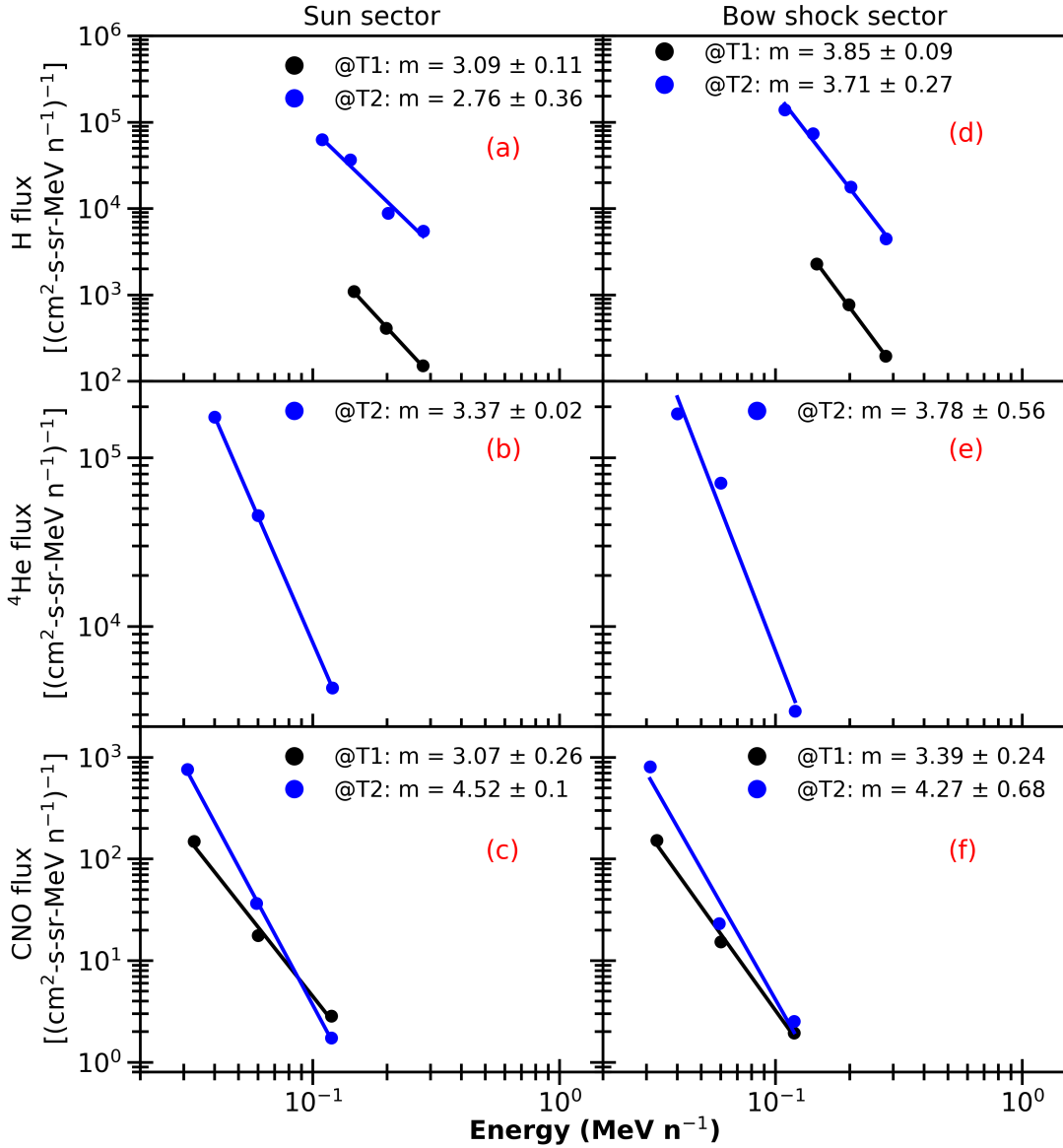


Figure 5.3: Spectra of H, ^4He , and CNO during upstream event No. 31 observed by T1 (black) and T2 (blue) in the “Sun sector” are shown in panel (a), (b), and (c), respectively. The corresponding spectra for the “bow shock sector” are shown in panel (d), (e), and (f). The spectral indices and standard errors (SEs) are mentioned in the lower left corner of the panels.

sector” are plotted against those observed at the “Sun sector” of T1 and T2. The 45° black dashed line in each panel of Figure 5.4 indicates equal spectral indices in both the sectors. From panel (a) and (b) of Figure 5.4 it can be seen that spectral indices of H in the “bow shock sector” are most of the times above the line of equal spectral indices (systematic softening) in T1 and T2, respectively. Interestingly,

spectral indices of CNO (panel ‘e’ and ‘f’) observed in both T1 and T2 in the “bow shock sector” go almost hand in hand (no softening) with the spectral indices observed in the “Sun sector”. It can be seen from panel (d) of Figure 5.4 that the softening in ^4He spectra observed in the “bow sector” is intermediate between H (softest among the three elements) and CNO (least soft). This mass-dependent hardening effect is more prominent in case of T2. In order to evaluate the origin of the upstream ions (^4He and CNO), $^4\text{He}/\text{H}$ and CNO/H between the Sun sector and the bow shock sector are compared in Figure 5.5. This figure shows that the correlation between $(\text{CNO}/\text{H})_{\text{Sunsector}}$ and $(\text{CNO}/\text{H})_{\text{bowshocksector}}$ (see panel ‘b’, $R^2=0.55$) is better than the corresponding correlation between $(^4\text{He}/\text{H})_{\text{Sunsector}}$ and $(^4\text{He}/\text{H})_{\text{bowshocksector}}$ (see panel ‘a’, $R^2=0.18$). The implications of these observations are discussed in the following section.

5.5 Discussions and conclusions

The durations of these upstream events discussed in the previous section vary in the range of 0.5–3.5 hours, which is consistent with the existing literature (e.g., Desai et al., 2000). The degree of enhancements in H, ^4He , and CNO fluxes differ and vary from event to event, which is clear from Table 5.1. CNO fluxes show enhancements in fewer events as compared to H or ^4He fluxes. This may be due to the lack of suprathermal CNO fluxes above the instrument threshold level.

In the present work, upstream events exhibit steeply falling spectra with spectral indices in the range of 2–6. This is consistent with earlier results (Anagnostopoulos et al., 1998; Desai et al., 2000 etc.). Further, it is seen that in 80% of the upstream events observed by T2, the enhancement in H fluxes is limited to < 300 keV per nucleon. The corresponding percentages for < 300 keV per nucleon cut-off for CNO and ^4He are 100% and 93%, respectively. Therefore, it appears that there is an energy cut-off of the upstream events observed in the “bow shock sector”. Meziane et al. (2002) showed by statistical study of upstream events that in the absence of pre-existing population of energetic ions (> 50 keV), ion energy spectrum is limited to 200–300 keV. It is to be noted that the Hillas criterion

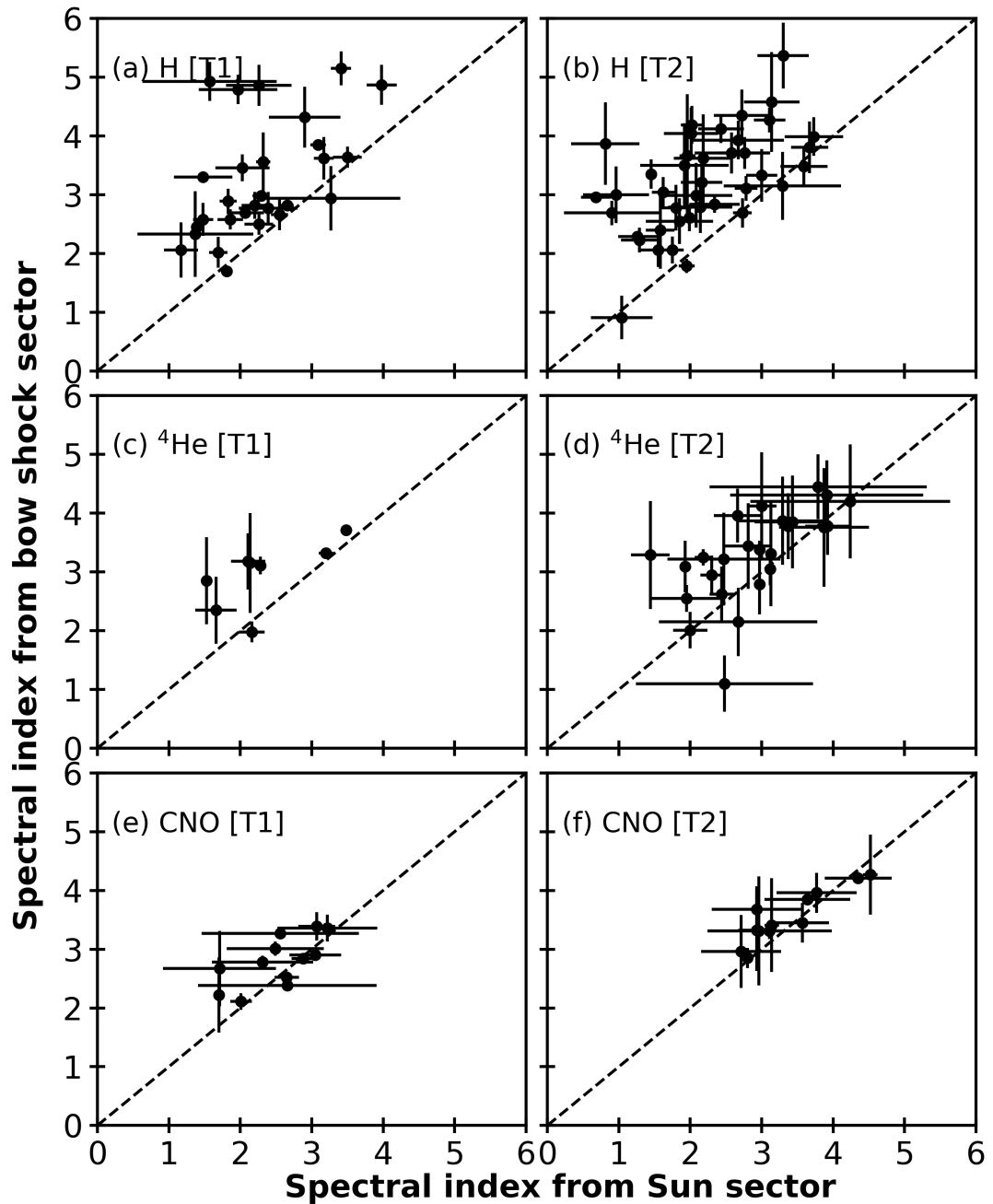


Figure 5.4: Comparisons of spectral indices of H [(a) T1, (b) T2]; ^4He [(c) T1, (d) T2], and CNO [(e) T1, (f) T2] observed from the “Sun sector” and “bow shock sector” of the telescopes. The black 45° dashed line in each panel represents the line of equal spectral indices.

puts an upper limit on the energy gained by a charged particle accelerated at an acceleration site. Conventionally, this criterion estimates the maximum energy of cosmic rays to identify the sources of such high energetic particles. According to

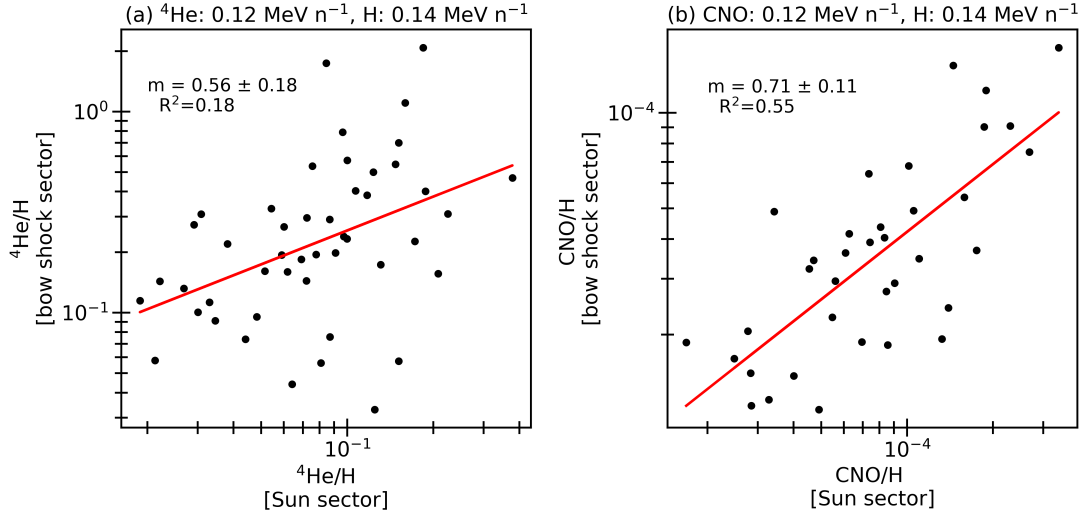


Figure 5.5: (a) Comparisons between the ${}^4\text{He}/\text{H}$ ratios observed at the Sun sector 30 minutes earlier than the start of upstream events (duration being same as that of the upstream events) and ${}^4\text{He}/\text{H}$ ratios during the upstream events. All fluxes are measured by T2 telescope. The ratio is calculated for nearly equal energy channels of ${}^4\text{He}$ and H. The energy channels are mentioned at the top of the panel. The red line shows the linear regression fit. The corresponding fit parameters (slope, m and goodness of fit, R^2) are mentioned in the panel. (b) Same as panel (a), but for CNO/H.

Hillas condition, as long as a charged particle, with charge q and energy ε , remains at the acceleration region and the Larmor radius ($R_L = \varepsilon/qB$) of the particle is smaller than the size of the accelerator (R), it will gain energy. Therefore, the maximum energy gained by the particle before it escapes the acceleration site is (following [Bustamante et al., 2010](#))

$$\varepsilon_{max} = qBR$$

An enhancement in H fluxes is observed below 300 keV for 80% of the upstream events studied in this chapter. Going along the line of Hillas criterion, this upper limit in energy corresponds to the accelerator size $R = 12 \times 10^9$ km (taking B at the bow shock = 25 nT) which is ~ 80 AU. Therefore, the size of the Earth's bow shock has to be very large to produce 300 keV protons. This shows that the upper limit in the energy of upstream suprathermal particles cannot be explained

5.5. DISCUSSIONS AND CONCLUSIONS

in terms of the Hillas criterion.

It is verified that at least 42 out of 49 upstream events analyzed in this study neither do follow an interplanetary coronal mass ejections (ICMEs) nor associated with high-speed solar wind stream, which are considered as sources of energetic particles in the solar wind. In such cases, [Meziane et al. \(2002\)](#) did not find any dependence of the energy spectrum on shock geometry. Turbulent quasi-parallel bow shock can accelerate particles up to ~ 300 keV almost isotropically ([Lin et al., 1974](#); [Greenstadt et al., 1980](#)). [Ellison and Moebius \(1987\)](#) showed that the fraction of solar wind energy flux imparted to the high-energy ion flux (the injected particles) falls off very rapidly with energy. This limits the ion acceleration up to very high energy. Diffused ions are the most energetic among all types of upstream ions discussed in the introduction section. Therefore, an energy cut-off at 300 keV n^{-1} suggests that the observed upstream events are essentially diffused ions accelerated by the first order Fermi acceleration at the quasi-parallel bow shock and propagated to the orbit of the Wind spacecraft.

It can be seen from [Figure 5.4](#) that the spectral indices of H observed in the “bow shock sector” of both T1 and T2 are more scattered above the line of equal spectral indices and towards the lower side of the spectral indices. This suggests a systematic softening of the H spectra observed in the “bow shock sector”. This is an interesting insight that has come out of this investigation. Another interesting result that comes out of this investigation is that the difference between spectral indices for both the sectors decreases with increase in the mass of the species ($\text{H} > {}^4\text{He} > \text{CNO}$). In fact, [Figure 5.4](#) reveals that spectral softening decreases with increasing mass of the elements. This mass-dependent modulation in spectra of energetic particles observed upstream of the bow shock at L1 point is a new result. [Sarris et al. \(1978\)](#) hinted towards rigidity-dependent escape of protons from the magnetosphere and subsequent acceleration of these particles to explain harder proton spectra outside the magnetosphere than spectra observed inside the magnetosphere. In this study, a mass-dependent modulation in particle spectra during upstream events at L1 point is observed. Since the observed upstream ions

appear to be the diffused ions, the proposition of Sarris et al. does not seem to explain our observations. Instead, it may be possible that the softening of particle spectra is due to mass-dependent modulation of the ions during the course of their transport from the bow shock to the spacecraft. One of the reasons for such modulation could be cross-field diffusion of these upstream ions. An estimate of the cross-field diffusion due to resonant scattering can be written as follows (Jokipii, 1987)

$$\frac{\kappa_{\perp}}{\kappa_{\parallel}} = \frac{1}{1 + (\lambda_{\parallel}/r_g)^2} \quad (5.1)$$

where κ_{\parallel} and κ_{\perp} are the coefficients for diffusion parallel and perpendicular to the magnetic field, λ_{\parallel} is the parallel mean free path and r_g is ion gyroradius, which depends on the mass-to-charge ratio (m/q) of ion species. r_g increases with increasing m/q , so does $\frac{\kappa_{\perp}}{\kappa_{\parallel}}$. This will lead to greater mixing of upstream ions with the solar wind suprathermal ions. Therefore, the points mostly lie along the line of equal spectral indices between the Sun sector and bow shock sector for CNO as m/q is higher and there is enhanced mixing between solar wind and upstream ions due to enhanced perpendicular diffusion. On the contrary, in case of H, the cross-field diffusion is less, which allows the upstream ions reach the L1 point in a focused manner. Since bow shock softens the solar wind spectra, the points mostly lie above the line of equal spectral indices. The behavior of ${}^4\text{He}$ seems to be intermediate between H and CNO. This suggests that cross-field diffusion may play an important role during the propagation of upstream ions from bow shock to the L1 point. Cross-field diffusion also supports observation of upstream events in places far apart laterally consistent with earlier observations (Dwyer et al., 2000; Desai et al., 2008 etc.). Not only in upstream events, Dalal et al. (2022) have shown the modulation of quiet-time suprathermal particles depending on m/q of elements. Therefore, it appears that upstream ions do get modulated depending on the m/q of the species.

Although systematic softening of spectra is observed as far as the upstream ions are concerned with respect to solar wind, the possibility of mixing up of suprathermal particles coming from multiple sources like diffused ions from the

magnetosphere, bow shock accelerated particles, particles accelerated by reverse shocks of stream interaction regions (SIRs) formed beyond the Earth’s orbit, pick up ions etc. cannot be ruled out. Figure 5.5 seems to give an idea about the sources of the upstream ions. The good correlation between CNO/H from the “Sun sector” and the “bow shock sector” probably suggests that upstream CNO reaching L1 are mostly of solar wind origin. On the contrary, poor correlation between ^4He from the “Sun sector” and the “bow shock sector” suggests that ^4He fluxes reaching at L1 get mixed up with suprathermal populations coming from other sources. Detailed investigations are needed to understand this aspect.

It is observed that IMF was near radial (see panel ‘g’ of Figure 5.1 for an example) during 67% of the events analyzed here. This is consistent with earlier studies (e.g., Desai et al., 2000). Radial magnetic field is indicative of connection between the L1 point and the magnetosphere of the Earth (Haggerty et al., 2000). It is possible that these upstream ions propagated along the magnetic field in all the events. This proposition appears to be valid because the typical width of magnetic flux tubes linked to the Earth in case of impulsive solar energetic particle (ISEP) events is $\sim 4.7 \times 10^6$ km ($\sim 750 R_E$) (Mazur et al., 2000; Giacalone et al., 2000). The spatial scale length in which IP shocks accelerate particles is $\sim 2.97 \times 10^6$ km ($\sim 460 R_E$) (Neugebauer et al., 2006). Therefore, large-scale magnetic flux tubes seem to be very common in the heliosphere. The present investigation essentially supports the observation of upstream events originated from a small source region and thereafter propagating along magnetic flux tubes having larger spatial scale sizes.

5.6 key findings

1. An energy cut-off of around 300 keV per nucleon seems to occur for the upstream ions.
2. Systematic hardening of ion spectra with increasing m/q during upstream events observed at the L1 point. Cross-field diffusion may be the possible

cause.

3. Solar wind CNO fluxes as major source of upstream CNO ions.

Chapter 6

Contrasting impacts of two CMEs on the terrestrial magnetosphere measured by STEPS/ASPEX during the earth-bound orbits of Aditya-L1

Excerpt

Geomagnetic storms with varying intensities are often observed during the passages of interplanetary coronal mass ejections (ICMEs). Interplanetary (IP) shocks associated with ICMEs accelerate energetic particles (e.g., gradual solar energetic particles, GSEPs), which can harm space assets. Although there have been reports in the past regarding the access of high energetic (> 10 MeV) solar energetic particles (SEPs) into the magnetosphere, studies regarding the effect of low energetic (< 2 MeV) SEPs and suprathermal ions on the magnetospheric energetic particle environment are sparse. In this chapter, by using the first observations from the SupraThermal and Energetic Particle Spectrometer (STEPS), a subsystem of the Aditya Solar wind Particle EXperiment (ASPEX) payload on board the Aditya-L1 spacecraft of India, the effects of a “stealthy” and a typical ICME on the magnetospheric energetic particle environment have been assessed. This study reveals, for the first time, that although “stealth” CMEs can create geomagnetic impact as strong as typical CMEs, ions with energies < 2 MeV associated with “stealth” CMEs do not change the energetic particle environment in the Earth’s

magnetosheath and magnetosphere significantly. On the other hand, ions with energies < 2 MeV associated with ICMEs having speeds > 500 km/s can directly affect the magnetospheric energetic particle environment if the SEP spectra are hard enough at L1. This study is important in assessing the impacts of ICMEs on the space-assets inside the Earth's magnetosphere.

6.1 Introduction

The solar wind continuously interacts with the Earth's magnetosphere and a bow shock is created ahead of the terrestrial magnetosphere. The magnetosheath region in between the bow shock and the magnetopause boundary is always filled with energetic ions (Anderson et al., 1965; Meng and Anderson, 1970, 1975; West Jr and Buck, 1976; Daly et al., 1979; Sibeck et al., 1987). Among the sources of these particles are the magnetosphere (Haskell, 1969; Hones Jr et al., 1972), cosmic rays, solar wind particles accelerated in both the bow shock (West Jr and Buck, 1976; Asbridge et al., 1978) and the magnetotail (Fan et al., 1975, 1976), and solar wind particles accelerated at the dayside magnetopause during merging of magnetic fields (Axford, 1976; Richter et al., 1979; Cohen et al., 2016). The study of these energetic ions is important because of their adverse effects on the space assets. For example, decrease in power outputs of the uncovered solar cells due to exposure of these cells to low energy (< 1 MeV) proton fluxes was reported by Statler and Curtin (1971). Astrophysical and cosmological observations are hampered if these protons enter inside the X-ray telescope (Fioretti et al., 2016). O'Dell et al. (2000) also reported damage of the front-illuminated charge-coupled devices (CCDs) in the advanced CCD imaging spectrometer (ACIS) on board the Chandra X-ray Observatory by 100-300 keV protons.

Solar wind particles can enter the terrestrial magnetosphere through magnetic reconnection and Kelvin-Helmholtz instability Kronberg et al. (2011). Energetic ions (> 0.1 MeV) can infiltrate into the magnetosphere through two regions: (i) through near equatorial dayside magnetopause and (ii) through the regions of magnetopause intersected by open field lines (Tverskoi et al., 1973; Kalegaev et al.,

2018). According to [Richard et al. \(2002\)](#), protons with energies less than 10 MeV can enter the magnetosphere along open field lines and more energetic particles can directly penetrate the dayside magnetopause. Significant changes in the magnetospheric energetic particle environment takes place during geomagnetic storms caused due to passage of ICMEs when solar energetic particles (SEPs) are observed at lower latitudes of the Earth than under quiet conditions ([Flückiger et al., 1990](#); [Kudela et al., 2008](#); [Kalegaev et al., 2018](#)). Access of > 5 MeV protons to the geosynchronous Earth orbit (GEO) was reported in many past studies ([Filwett et al., 2020](#); [Kalegaev et al., 2018](#); [Paulikas and Blake, 1969](#) etc.). The fluctuations in the magnetic field outside the GEO govern the entry of 5–21 MeV protons in the GEO ([Paulikas and Blake, 1969](#)). The access of > 1 MeV protons to altitudes below the GEO is observed to correlate with Dst, AE, and dynamic pressure ([Ivanova et al., 1985](#)). The importance of the orientation of the interplanetary magnetic field (IMF) was studied by [Richard et al. \(2002\)](#). It is found that southward IMF conditions are more favorable for SEP injection into the magnetosphere. However, how the low energy part of SEPs (with energies in the range 0.1–2 MeV) associated with different ICMEs enter the magnetosphere and affect the particle population there are not clear till date.

For example, a fairly good percentage of earth-bound CMEs are “stealth” CMEs (e.g., [Ma et al., 2010](#); [Wang et al., 2011](#); [Kilpua et al., 2014](#); [O’Kane et al., 2019](#) etc.), which do not have distinct eruptive signatures in the low solar corona. This type of CMEs generally have speeds < 500 km/s ([D’Huys et al., 2014](#)). Sources of “stealth” CMEs could be quiet Sun ([Ma et al., 2010](#)) and regions close to open magnetic field ([Nitta and Mulligan, 2017](#)). According to [Howard and Harrison \(2013\)](#), stealth CMEs are less energetic events and might originate from streamer blowouts. These authors suggest that the nomenclature (“stealth”) is possibly due to limitations in instrumentation. It still remains an open issue if there is any difference between typical CMEs and “stealth” CMEs. However, despite having low speeds, “stealth” CMEs cause geomagnetic disturbances (e.g., [Zhang et al., 2007](#); [Nitta and Mulligan, 2017](#)). While there are some studies regarding the geo-

magnetic impacts of stealth CMEs, the impact of SEPs associated with “stealth” CMEs on the Earth’s magnetospheric particle environment has not been studied explicitly. This is a very important issue from the perspective of the assessment of the impacts of transient events like ICMEs on space assets.

Quite serendipitously, the first observations made by SupraThermal and Energetic Particle Spectrometer (STEPS), a subsystem of the Aditya Solar wind Particle EXperiment (ASPEX) payload on board the Aditya-L1 (AL1) mission of Indian Space Research Organization (ISRO) that was launched on September 2, 2023, provided a set of observations to address this important issue. The relevant details of the ASPEX payload and its subsystems can be found in [Goyal et al. \(2018\)](#), [Janardhan et al. \(2017\)](#), [Tripathi et al. \(2022\)](#). It is to be noted that AL1 accomplished a number of earth-bound orbits before it started cruising towards the halo orbit around the L1 point. This trans-L1 or cruise phase started on September 19, 2023. After the third earth-bound maneuver on September 10, AL1 traversed thrice around the Earth in an orbit of dimension $296 \text{ km} \times 71767 \text{ km}$ (distances from the surface of the Earth) before the fourth earth-bound maneuver on September 15. It accomplished another two revolutions around the Earth before the trans-L1 phase on September 19 started. Some detector units of STEPS [specifically, Parker Spiral (PS) and North Pointing (NP) units] were turned on during these earth-bound phases when the altitude of AL1 was beyond 52000 km (approximately beyond the outer radiation belt). These were the first sensors that were switched on in this mission. This brought an opportunity to sample suprathermal particles from the Earth’s magnetosphere, magnetosheath, and solar wind regions from two mutually perpendicular directions during three ICME events, which hit the Earth during the observation period (September 11 – 19, 2023). Interestingly, one ICME was “stealthy” in nature. This study brings out contrasting impacts of the “stealthy” and a typical ICME on the energetic particle environments of magnetosheath and magnetosphere regions though geomagnetically they affect similarly. The results are described in the next section.

6.2 Data used and instrumentation

The details of the data used in this chapter have already been discussed in Chapter 2.

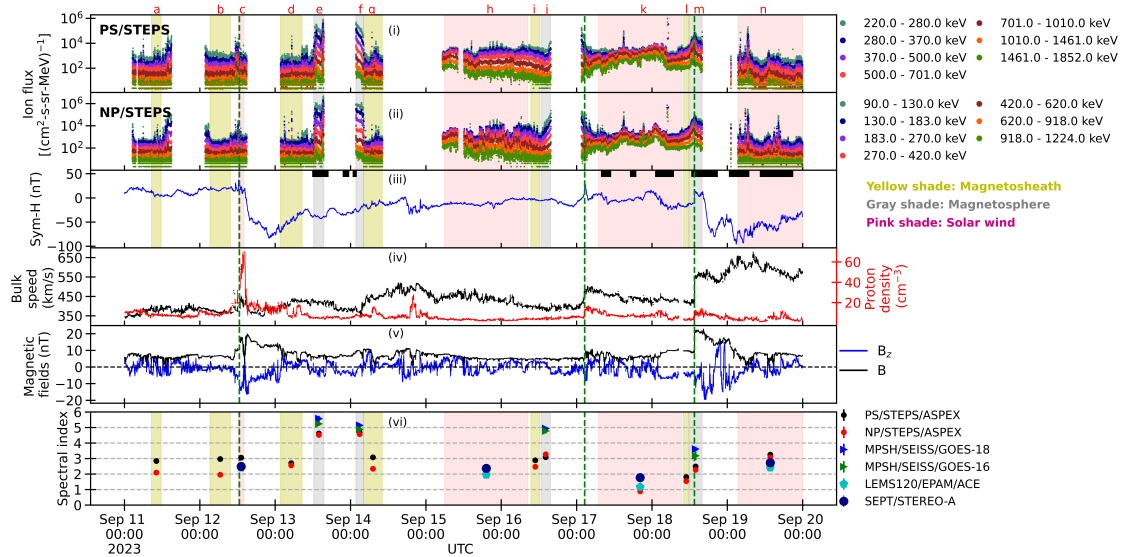


Figure 6.1: Panels (i) and (ii) present the ion fluxes at different energy channels as measured by PS and NP units, respectively, of the STEPS/ASPEX. The energy channels are mentioned at the right side of these panels. Variations in the Sym-H are shown in panel (iii). The black horizontal bars in panel (iii) represent the intervals when fluctuations in westward auroral electrojet index (AL) went below -500 nT. Solar wind bulk speed (black) and proton density (red) are plotted in panel (iv). Panel (v) shows the variations in Z-component (north-south component in GSE coordinate) in the IMF B_z (blue) and magnitude of IMF total field B (black). The green vertical dashed lines represent arrival of three ICMEs at L1 point. Based on the empirical model calculations described in Eq. 2 and Eq. 3, several intervals are selected when AL1 was inside the magnetosphere (gray shaded intervals), magnetosheath (yellow shaded regions), and in the IP medium (pink shaded regions). The spectral indices of ions (PS, NP, LEMS120, and SEPT) and protons (MPSH-16, 18) are shown for these intervals in panel (vi). Different symbols mentioned in the right side of panel (vi) represent different instruments.

6.3 Observations

Panels (i) and (ii) of Figure 6.1 show the ion flux variations during September 11–19, 2023 as measured respectively by the PS and NP detector units of STEPS.

The gaps in the variations are when the STEPS units were switched off. Sym-H and other solar wind parameters like bulk speed, proton density, magnetic field in the geocentric solar ecliptic (GSE) coordinate system are shown in panels (iii) – (v). The black horizontal bars in this panel denote the intervals when real time westward auroral electrojet index (AL, available at <https://wdc.kugi.kyoto-u.ac.jp/wdc/Sec3.html>) went below -500 nT, which is indicative of possible substorm related activities in the night side magnetotail.

As mentioned earlier, the earth-bound orbits of AL1 are highly elliptical and therefore, STEPS samples ion fluxes from solar wind/IP medium, magnetosheath, and inside the magnetopause boundary. The position of bow shock nose are available in the NASA GSFC CDAWeb (<https://cdaweb.gsfc.nasa.gov/index.html>). However, the magnetopause nose distance (L_{mp}) is calculated using the formula given below (Kivelson and Russell, 1995),

$$L_{mp} = 107.4(n_{sw}u_{sw}^2)^{-\frac{1}{6}} \quad (6.1)$$

where n_{sw} and u_{sw} are the proton number density and solar wind bulk speed. Once the standoff distance of the magnetopause is obtained, the magnetopause boundary is calculated Shue et al. (1997),

$$r = r_0 \left(\frac{2}{1 + \cos\theta} \right)^\alpha \quad (6.2)$$

where r_0 and α are the standoff distance and the flaring angle, respectively. This model is useful to get any idea of the location of AL1 with respect to the magnetopause boundary. The shape of the magnetopause in the night side is determined by α . For $\alpha = 0.5$, the magnetopause boundary behaves asymptotically. The magnetopause is closed for $\alpha < 0.5$ and it expands with increasing distance from the Earth for $\alpha > 0.5$. For the present study, $\alpha = 0.7$ is used to obtain a magnetopause boundary which is expanding in the night side. Since we are using STEPS data when AL1 was in the dayside (and not in the magnetotail), this choice of α does not affect the results derived from this investigation. The L_{MP} values are fed

6.3. OBSERVATIONS

as r_0 in Eq. 6.2. Along with the magnetopause surface, an estimate of the bow shock surface is also required. The shape of the bow shock surface is described by similar expression as in Eq. 6.2 (from Chao et al., 2002),

$$r = r_0 \left(\frac{1 + \varepsilon}{1 + \varepsilon \cos \theta} \right)^\alpha \quad (6.3)$$

where ε is an eccentricity factor and α is the tail flaring parameter. We calculate the bow shock nose distance from the position coordinates in GSE coordinate system and feed these values in Eq. 6.3. According to Chao et al. (2002), $\varepsilon = 1.029$. In this case, $\alpha = 1.2$ is chosen. It is to be noted that the bow shock and magnetopause are considered symmetric in both the Y and Z directions in the GSE coordinate system.

Depending on the positions of AL1, several intervals shown by differently shaded regions in Figure 6.1 are selected. During the intervals marked by ‘a’, ‘b’, ‘d’, ‘g’, ‘i’, and ‘l’ (yellow shaded intervals in Figure 6.1), AL1 was inside the magnetosheath region according to the models presented in Eq. 6.2 and Eq. 6.3. It was inside the magnetopause boundary (within magnetosphere) during the intervals ‘e’, ‘f’, ‘j’, and ‘m’ (gray shaded regions). The pink shaded intervals (i.e., ‘c’, ‘h’, ‘k’, and ‘n’) are the intervals when AL1 was in the IP medium (i.e. measuring solar wind suprathermal ions). Figure 6.2 (a) and (b) show the position of AL1 (marked by red dot in each panel) during these intervals in both the XY and XZ planes in GSE coordinate system. The magnetopause (depicted by blue solid curves) and bow shock (depicted by dashed magenta curves) boundaries are calculated using Eq. 6.2 and Eq. 6.3, respectively. Spectral indices of ions measured by PS and NP units during each of these intervals are shown in panel (vi) of Figure 6.1. Proton spectral indices (in the energy range 0.08–1.9 MeV) derived based on the measurements by Magnetospheric Particle Sensor for High energy (MPSH) on board Geostationary Operational Environmental Satellites (GOES)-16 and GOES-18 along with those derived based on the measurements by the STEPS/ASPEX during the intervals ‘e’, ‘f’, ‘j’, and ‘m’ are shown in panel (vi). Spectral indices of ions derived based on the measurements by the Low-Energy

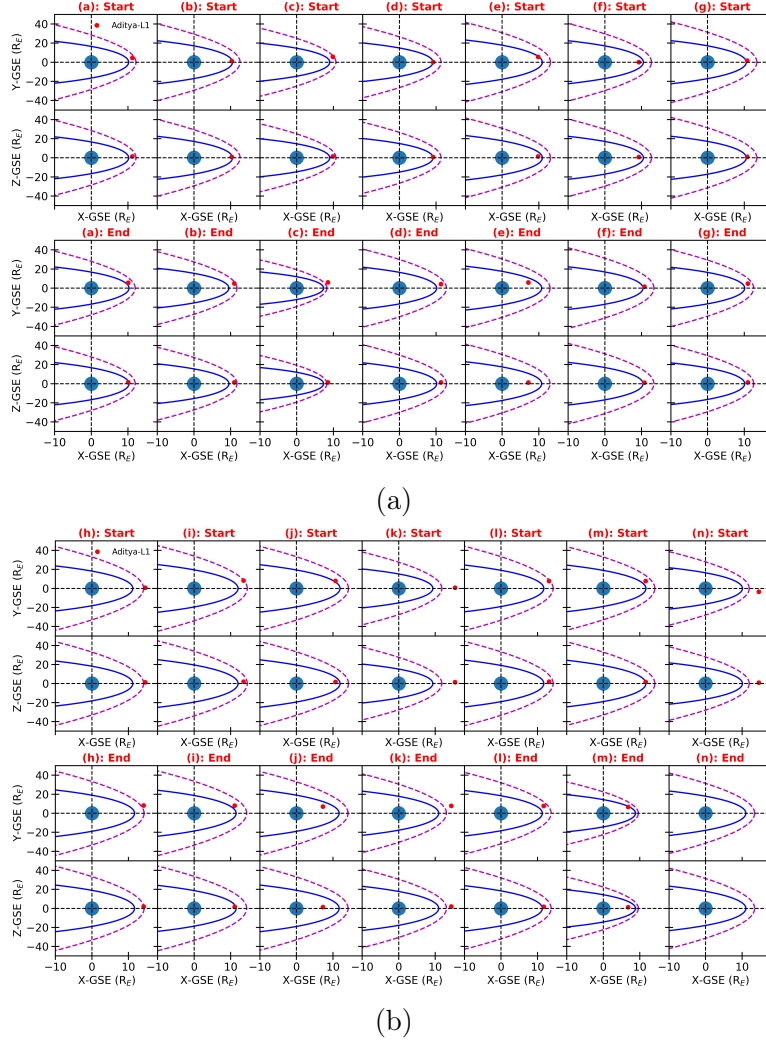


Figure 6.2: Position of AL1 (red dot) with respect to the bow shock (magenta dashed curve) and the magnetopause (blue solid curve) boundaries at the start and end times of the intervals (a) ‘a’-‘g’ and (b) ‘h’-‘n’ as mentioned in Figure 6.1. These boundaries are calculated using Eq. 6.2 and Eq.6.3. Both (a) and (b) consist of 7×4 panels. The first rows of both (a) and (b) show the positions of AL1 in the XY plane in the GSE coordinate system at the start of different intervals. The positions of AL1 in the XZ plane at the start of the intervals are shown in the second rows of (a) and (b). The third and fourth rows describe the positions of AL1 in the XY and XZ planes, respectively, at the end of the intervals. Sometimes, due to unavailability of solar wind parameter data just at the start and end times of the intervals, the boundaries correspond to closest times of the start and end of the intervals (vertically stacked) are drawn. The blue circle in each of the panels represents the Earth, which is at the center of the GSE coordinate system.

6.3. OBSERVATIONS

Magnetic Spectrometer (LEMS120, [Gold et al., 1998](#)), which is one of the two magnetic telescopes of the Electron Proton and Alpha Monitor (EPAM, [Gold et al., 1998](#)) and oriented 120° with the spin axis of the Advanced Composition Explorer (ACE, [Stone et al., 1998c](#)) satellite and the Solar Electron Proton Telescope (SEPT, [Müller-Mellin et al., 2008a](#)) on board the Solar-Terrestrial Relations Observatory Ahead (STEREO-A, [Kaiser et al., 2008](#)) are also calculated during the intervals when AL1 was in the IP medium and presented in panel (vi) of Figure 6.1.

The green vertical dashed lines represent the arrivals of three ICMEs at the Earth. The ICMEs on September 17 (ICME-2) and 18 (ICME-3) are enlisted in the Richardson and Cane’s list of ICMEs ([https://izw1.caltech.edu/ACE/ASC/DATA/level3/icmetable2.htm#\(c\)](https://izw1.caltech.edu/ACE/ASC/DATA/level3/icmetable2.htm#(c))) at 1 AU. In this paper, only the effects of ICMEs on September 12 (ICME-1) and ICME-3 are discussed because these two ICMEs caused geomagnetic storms in the Earth’s magnetosphere. Interestingly, minimum Dst for reached ~ -84 nT and ~ -98 nT corresponding to the geomagnetic storms caused by ICME-1 and ICME-3, respectively. This can be noted from panel (iii) of Figure 6.1. The nature of ICME-1 is debatable. This was “unexpected” and “stealthy” according to <https://spaceweather.com/>. In addition, it is not included in the Richardson and Cane catalogue as well. The main differences between these two ICMEs are seen in proton density, pressure, and bulk solar wind speed. Proton density in the ICME-1 goes very high (> 60 per cm^3) and so as the pressure (not shown here and can be verified from <https://cdaweb.gsfc.nasa.gov/index.html>). Due to the high solar wind pressure, the bow shock and the magnetosphere were compressed and AL1 went outside the bow shock boundary for some time (see interval ‘c’ in Figure 6.1 and panel ‘c’ in Figure 6.2). On the other hand, solar wind bulk speed, magnetic field, and proton density show signatures of shock arrival (clear jump in those parameters) associated with the ICME-3. The details of these intervals and spectral indices are mentioned in Table 1 where yellow, grey and pink shades are used to mark magnetosheath, magnetosphere and solar wind similar to Figure 6.1. At this juncture, it is important to note the orientations

Interval	Start time	End time	Spectral index					
			PS STEPS	NP STEPS	MPSH GOES-16	MPSH GOES-18	EPAM ACE	SEPT STEREO-A
a	2023-09-11 08:38	2023-09-11 11:42	2.84 ± 0.09	2.1 ± 0.05				
b	2023-09-12 03:15	2023-09-12 09:45	2.97 ± 0.08	1.96 ± 0.08				
c	2023-09-12 12:15	2023-09-12 14:05	3.06 ± 0.05	2.49 ± 0.03			2.41 ± 0.07	2.49 ± 0.03
d	2023-09-13 01:40	2023-09-13 08:35	2.7 ± 0.09	2.56 ± 0.14				
e	2023-09-13 12:18	2023-09-13 15:31	4.62 ± 0.05	4.53 ± 0.07	5.24 ± 0.14	5.57 ± 0.19		
f	2023-09-14 01:43	2023-09-14 04:07	4.68 ± 0.1	4.57 ± 0.07	4.88 ± 0.3	5.14 ± 0.1		
g	2023-09-14 04:10	2023-09-14 10:08	3.08 ± 0.05	2.34 ± 0.06				
h	2023-09-15 06:00	2023-09-16 08:30	2.16 ± 0.14	1.89 ± 0.18			1.95 ± 0.2	2.37 ± 0.09
i	2023-09-16 09:25	2023-09-16 12:15	2.89 ± 0.11	2.47 ± 0.1				
j	2023-09-16 12:40	2023-09-16 15:40	3.09 ± 0.06	3.28 ± 0.05	4.78 ± 0.16	4.93 ± 0.07		
k	2023-09-17 07:00	2023-09-18 09:30	1.18 ± 0.13	0.89 ± 0.07			1.17 ± 0.15	1.77 ± 0.06
l	2023-09-18 10:05	2023-09-18 11:45	1.81 ± 0.16	1.55 ± 0.17				
m	2023-09-18 11:50	2023-09-18 16:00	2.49 ± 0.14	2.28 ± 0.18	3.18 ± 0.28	3.61 ± 0.14		
n	2023-09-19 03:25	2023-09-19 23:59	3.25 ± 0.13	3.08 ± 0.1			2.41 ± 0.05	2.73 ± 0.03

Table 6.1: List of start and end times of different intervals and spectral indices as shown in Figure 6.1.

of PS and NP telescopes. Although PS and NP are meant for looking along the Parker spiral and the ecliptic north, respectively, their orientations were different during the earth-bound phases. Actually, AL1 was rotated by 90° most of the times in such a way that NP looked along the +Y-axis of the GSE coordinate system. Figure 6.3 gives an overview of the orientations of these two sensors during ICME-1 (from the start of interval ‘b’ to the end of interval ‘c’) and during ICME-3 (from the start of interval ‘k’ to the end of interval ‘m’). It is clear from the figure that during ICME-1 and ICME-3, orientations of PS and NP detector units were similar. In the next part of this section, variations of spectral indices of suprathermal particles during the above-mentioned intervals (‘a’-‘n’) are presented. It is to be noted that while calculating these spectral indices, ion fluxes measured by PS and NP sensors are averaged over the whole duration of the intervals regardless of the orientations of these sensors. It is well known that fluxes of energetic ions associated with an ICME start enhancing well before the arrival of the ICME shock at the measurement location. From Table 6.1, it can be noted that during intervals ‘a’ and ‘b’, PS unit recorded ions with spectral indices 2.84 and 2.97, respectively, in the magnetosheath region. On the other hand, the spectral indices observed by NP unit during these two interval are 2.1 and 1.96, respectively. ICME-1 was recorded at L1 point on at 12:37 UT on September 12. After the ICME hit, a sudden compression in the bow shock and

6.3. OBSERVATIONS

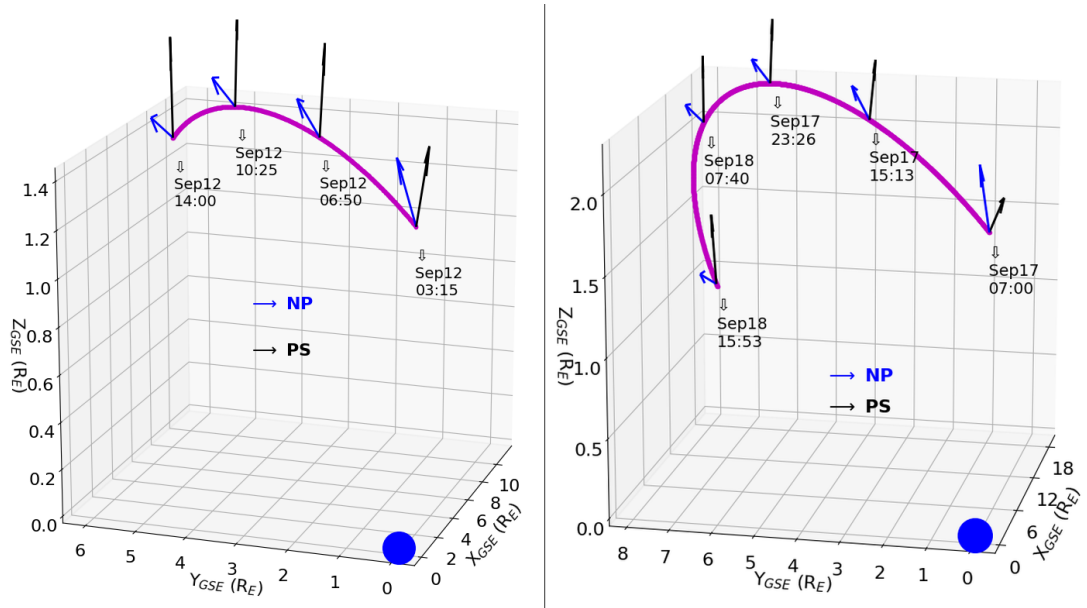


Figure 6.3: Orientations of PS (black arrow) and NP (blue arrow) during intervals ‘b’-‘c’ (left, corresponding to ICME-1) and ‘k’-‘m’ (right, corresponding to ICME-3) with respect to the GSE coordinate system. The +X-axis in this coordinate system is looking at the Sun. The trajectory of AL1 is marked by magenta dots. The Earth’s location is shown by big blue solid circle. The date and times corresponding to each arrow is also mentioned.

the magnetopause was observed for a very short period (interval ‘c’) according to the models in Eq. 6.2, 6.3 and panel ‘c’ in Figure 6.2. Consequently, AL1 tasted the solar wind for the first time. Ion spectral indices observed by PS, NP, LEMS120, and SEPT during this interval are 3.06, 2.49, 2.41, and 2.49, respectively. PS and NP detectors sampled energetic ions in the magnetosheath region during interval ‘d’ with spectral indices 2.7 and 2.56, respectively. AL1 entered inside the magnetopause boundary roughly at the start of interval ‘e’. Softer spectra are observed by both the PS and NP units during this interval, the spectral indices being 4.62 and 4.53, respectively. Energetic protons (in the energy range 0.08–1.9 MeV) observed by MPSH-16, 18 in the geosynchronous orbits also show softer spectra during this interval and the corresponding spectral indices are 5.24 and 5.57, respectively. Magnetospheric ions are also observed by STEPS during the interval ‘f’. This time, the spectral indices measured by PS, NP, MPSH-16 (MPSH on board GOES-16), and MPSH-18 (MPSH on board GOES-

18) are 4.68, 4.57, 4.88, and 5.14, respectively. Ions in the magnetosheath during interval ‘g’ show spectral indices of 3.08 and 2.34 as observed by PS and NP units, respectively. It is to be noted from panel (iii) of Figure 6.1 that the AL values went below -500 nT during interval ‘e’ and ‘f’ (marked by black thick horizontal lines). This indicates the occurrence of possible substorm in the nightside magnetosphere and it has been verified that the increase and decrease in the flux levels during intervals ‘e’ and ‘f’ coincide with the enhancement and decrease in the AL indices. Solar wind suprathermal ions are measured by STEPS units as well as by LEMS120 and SEPT during interval ‘h’. The spectral indices vary in the range 1.89–2.37. STEPS again measured suprathermal ions from the magnetosheath region during interval ‘i’. The spectral indices of ions observed by PS and NP units are 2.89 and 2.47, respectively, during this interval. STEPS units recorded comparatively softer spectra of magnetospheric ions with spectral indices 3.09 (PS) and 3.28 (NP) in the interval ‘j’. The spectral indices of protons in the geosynchronous orbits are 4.78 (MPSH-16) and 4.93 (MPSH-18). In-situ signatures of ICME-2 was recorded at L1 at 02:34 UT on September 17. Interestingly, AL1 sampled suprathermal particles from solar wind and magnetosheath before the arrival of IP shock associated with ICME-3 on September 18, 13:31 UT at the L1. It can be seen from panel (vi) of Figure 6.1 and Table 6.1 that a much harder spectra were detected by PS, NP, LEMS120, and SEPT during the interval ‘k’. The spectral indices are calculated to be 1.18, 0.89, 1.17, and 1.77, respectively. Comparatively harder ion spectra were observed by STEPS detector units also in the magnetosheath region during the interval ‘l’. The effect of ICME-3 persisted in the magnetosphere even during the interval ‘m’. The spectral indices of ions as measured by PS and NP are 2.49 and 2.28, respectively during this interval. MPSH-16 and MPSH-18 recorded proton spectra with spectral indices 3.18 and 3.61, respectively. There is a possibility of substorm related particle enhancement in the magnetosphere during interval ‘m’. However, the comparatively smaller spectral indices clearly show that low energy SEPs associated with ICME-3 penetrated the magnetopause boundary and made the proton and ion spectra harder. During the interval marked by ‘n’, spectral

6.3. OBSERVATIONS

indices of solar wind suprathermal particles as observed by PS, NP, LEMS120, and SEPT are 3.25, 3.08, 2.41, and 2.73, respectively.

To summarize, ICME-1 does not alter the spectral indices in the magnetosphere (compare intervals ‘b’ and ‘d’) while ICME-2 hardens the spectra in the magnetosphere (compare intervals ‘l’- ‘n’ with special attention to intervals ‘k’ and ‘l’). Another important observation that came out is the significant softening of spectra during ‘e’ and ‘f’ when substorms occurred as indicated by the variations in the AL indices. It can be seen from Figure 6.1 and Table 6.1 that

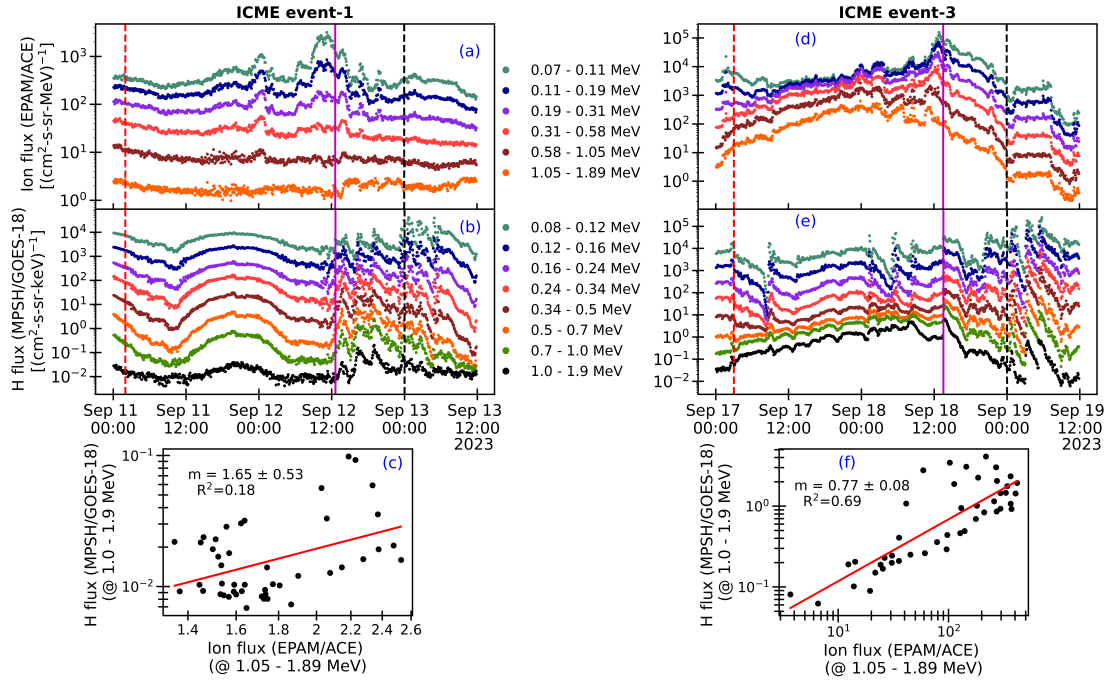


Figure 6.4: Panel (a) shows the temporal variations of ion fluxes at different energy channels as observed by LEMS120 corresponding to ICME-1. The magenta colored vertical solid line marks the arrival of shock/bow wave associated with the ICME at L1 point. Variations in proton fluxes measured by MPSH-18 corresponding to the ICME are plotted in panel (b). Panel (c) shows the correlation between ion fluxes (with energies 1.05–1.89 MeV) measured by LEMS120 and proton fluxes (with energies 1.0–1.9 MeV) measured by MPSH-18 during the interval bounded by the red and black vertical dashed lines. The red line is the linear regression line. The slope of fitted line and the R^2 values are mentioned. Panels (d), (e), and (f) represent the similar variations as (a), (b), and (c), respectively, but corresponding to ICME-3.

although both ICME-1 and ICME-3 caused almost similar impact on the geomag-

netic field, their impact on the energetic particle environment of magnetosphere and magnetosheath region are contrasting in nature. While ICME-1 (“stealthy”) does not alter the energetic particle environment in the magnetosphere (spectral index remains nearly the same), ICME-2 does the opposite (hardens the spectra). Figure 6.4 is presented to garner further support for this observation. Figure 6.1 (a) and (d) show the temporal variations of ion fluxes obtained from LEMS120 during ICME-1 and ICME-3, respectively. The corresponding proton fluxes obtained from MPSH-18 are plotted in panel (b) and (e), respectively. It can be seen from panel (c) that the correlation between the hourly averaged ion fluxes in the energy range 1.05–1.89 MeV observed by LEMS120 and hourly averaged proton fluxes in the energy range 1.0–1.9 MeV observed by MPSH-18 is negligible. On the other hand, there is a relatively stronger correlation between > 1 MeV ion fluxes measured by LEMS120 and > 1 MeV proton fluxes measured by MPSH-18 (panel (f)). This suggests direct impact of energetic ions associated with ICME-3 on the magnetospheric proton fluxes. The implications of these observations are discussed in the next section.

6.4 Discussions and conclusions

It can be seen from the above section that almost similar intensity geomagnetic storms occurred due to ICME-1 and ICME-3. However, hardening in spectra of ions (see Figure 6.1) corresponding to the IP medium (change in spectral index from ~ 2 to ~ 1.17), magnetosheath (change in spectral index from ~ 3 to ~ 1.8), and magnetosphere (change in spectral index from > 5 to ~ 2.5) is observed only in the case of the latter ICME, which appears to be a typical ICME with clear shock signatures like jumps in solar wind bulk speed, magnetic field. However, the proton density remains low in ICME-3. On the other hand, a large enhancement in the proton density is observed in ICME-1. Harder spectra due to ICME-3 in the geosynchronous orbit are also observed by GOES satellites. The direct impact of the SEPs associated with this event is confirmed by Figure 6.4 (f) where a very good correlation ($R^2=0.69$) between the 1.05–1.89 MeV ion flux observed at L1

6.4. DISCUSSIONS AND CONCLUSIONS

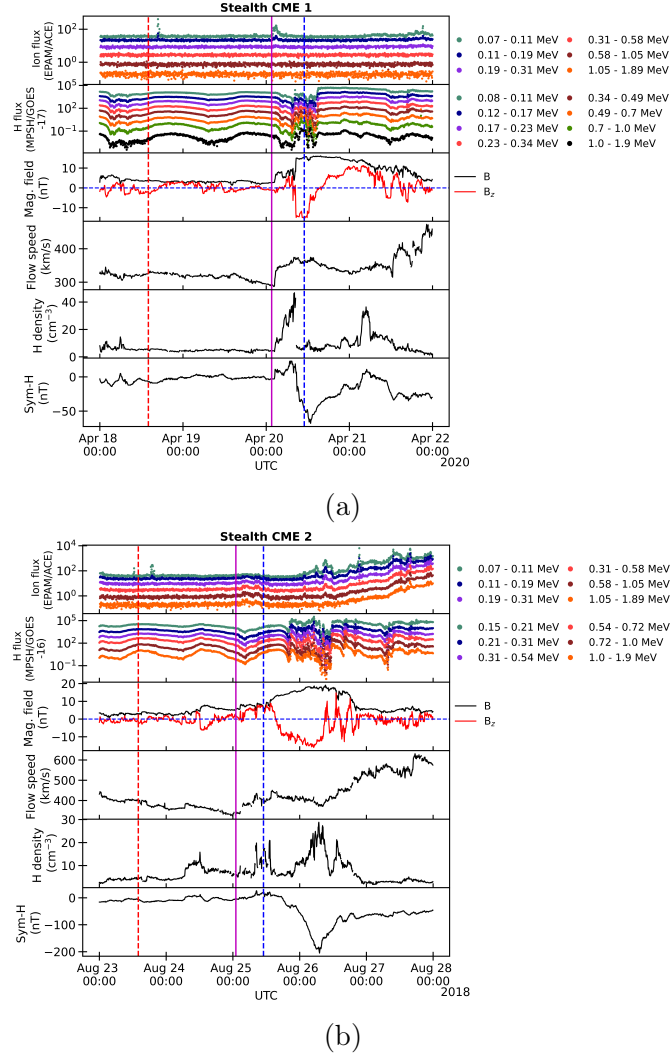
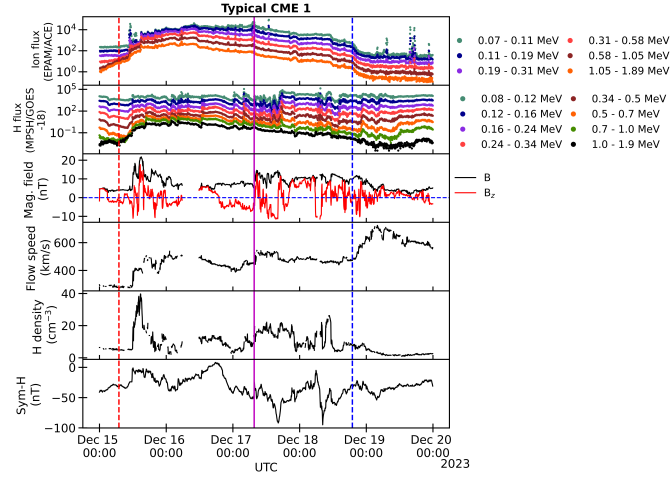


Figure 6.5: (a) From top to bottom: ion fluxes measured by LEMS120 at different energy channels, proton fluxes measured by MPSH/GOES-17 (MPSH-17) at various energy channels, total (black) and z-component (red) of the IMF, solar wind flow speed, proton density, and Sym-H corresponding to Stealth CME 1 (taken from O’Kane et al., 2021). The arrival of the shock front is marked by magenta colored vertical solid line. Ion and proton fluxes during the interval between the red and blue vertical dashed lines are used to calculate correlation coefficient as shown in Figure 6.7 (a). (b) From top to bottom: same as Figure 6.5 (a) except for proton flux measured by MPSH-16 corresponding to Stealth CME 2. This event is taken from Nitta et al. (2021). The correlation between IP ion flux and magnetospheric proton flux is shown in Figure 6.7 (b).

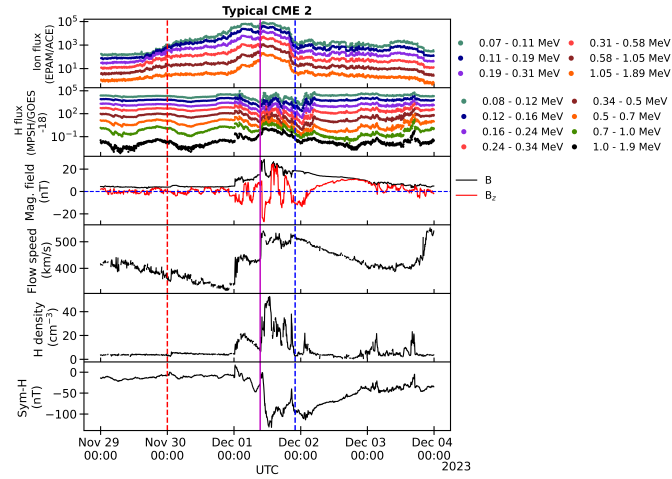
point by LEMS120 and 1.0–1.9 MeV protons observed by MPSH is shown. On the contrary, poor correlation ($R^2=0.18$) between the LEMS120 ion flux and MPSH proton flux suggests little effects of SEPs associated with the “stealthy” ICME-1 on the magnetospheric energetic particles. Now, the question remains whether this is the case for all the “stealth” CMEs. In order to answer this question, suprathermal particles associated with two “stealth” CMEs (Stealth CME 1 is taken from [O’Kane et al., 2021](#) and details of Stealth CME 2 can be found in [Nitta et al., 2021](#)) and two typical ICMEs (from Richardson and Cane catalogue) as measured by LEMS120 are compared with proton fluxes measured at geosynchronous orbit. Figure 6.5 (a) and (b) show the temporal variations of proton fluxes in the geosynchronous orbit, Sym-H, ion fluxes and solar wind parameters measured at the L1 point corresponding to Stealth CME 1 and Stealth CME 2, respectively. Figure 6.6 (a) and (b) show the corresponding variations during Typical CME 1 and Typical CME 2, respectively. The correlations between ion fluxes measured by LEMS120 and proton fluxes measured by GOES satellites during the two “stealth” CMEs and two typical CMEs are described in Figure 6.7. It can be noted from Figure 6.7 (a) and (b) that there is very little correlation between the SEPs (in the energy range of 1.05–1.89 MeV) associated with these “stealth” CMEs and proton fluxes (1.0–1.9 MeV) measured at geosynchronous orbits. On the other hand, Figure 6.7 (c) and (d) show very good correlations between SEP fluxes associated with typical CMEs and protons in the geosynchronous orbit. An interesting similarity between the Stealth CME 1 and Stealth CME 2 is that solar wind speed is < 400 km/s at the beginning of both the events (see Figure 5). The solar wind speed during the “stealthy” ICME-1 (Figure 1) also is < 450 km/s. On the contrary, solar wind speed is observed to be > 500 km/s at the onset of both the typical CME events. This condition is very much similar to ICME-3 studied in this work. Therefore, it appears that the local speed (or in other words, the strength of the shock) of ICMEs is an important factor that controls the impact of SEPs on the magnetospheric energetic particle environment.

The geomagnetic impact of “stealth” CMEs has been known for quite some

6.4. DISCUSSIONS AND CONCLUSIONS



(a)



(b)

Figure 6.6: (a) From top to bottom: ion fluxes measured by LEMS120 at different energy channels, proton fluxes measured by MPSH-18 at various energy channels, total (black) and z-component (red) of the IMF, solar wind flow speed, proton density, and Sym-H corresponding to Typical CME 1 (taken from Richardson and Cane catalogue). The arrival of the shock front is marked by magenta vertical solid line. Ion and proton fluxes during the interval between the red and blue vertical dashed lines are used to calculate correlation coefficient as shown in Figure 6.7 (c). (b) Same sequence is followed as in Figure 6.6 (a). The corresponding correlation is shown in Figure 6.7 (d).

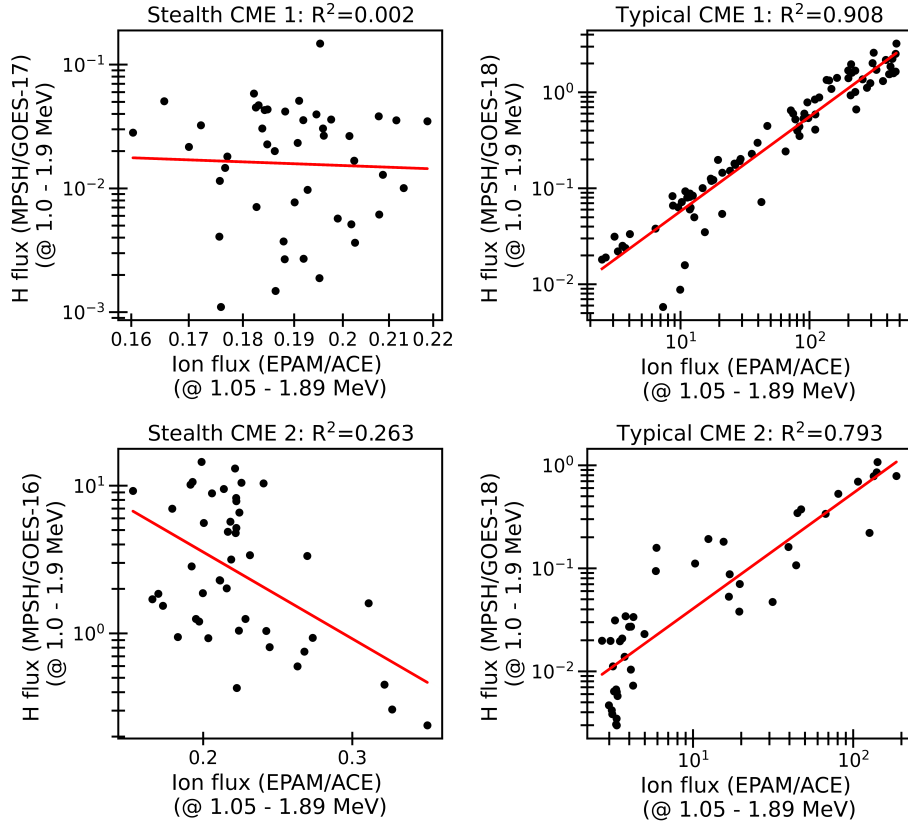


Figure 6.7: (a) Comparison between 1.05–1.89 MeV ion flux measured by LEMS120 and 1.0–1.9 MeV proton flux measured by MPSH-17 during the interval bounded by red and blue vertical dashed lines corresponding to Stealth CME 1 in Figure 6.5 (a). The R^2 value is mentioned at the top of the panel. (b) Comparison between 1.05–1.89 MeV ion flux measured by LEMS120 and 1.0–1.9 MeV proton flux measured by MPSH-16 during the interval bounded by red and blue vertical dashed lines corresponding to Stealth CME 2 in Figure 6.5 (b). The R^2 value is mentioned at the top of the panel. (c) Comparison between 1.05–1.89 MeV ion flux measured by LEMS120 and 1.0–1.9 MeV proton flux measured by MPSH-18 during the interval bounded by red and blue vertical dashed lines corresponding to Typical CME 1 in Figure 6.6 (a). The R^2 value is mentioned at the top of the panel. (d) Comparison between 1.05–1.89 MeV ion flux measured by LEMS120 and 1.0–1.9 MeV proton flux measured by MPSH-18 during the interval bounded by red and blue vertical dashed lines corresponding to Typical CME 2 in Figure 6.6 (b). The R^2 value is mentioned at the top of the panel.

time. However, the contrasting impact of < 2 MeV SEPs associated with a “stealthy” and a typical ICME on the magnetospheric particle environment is being reported for the first time in this work based on the earth-bound orbits of AL1. This study indicates that low energy SEPs with harder spectra (and as-

sociated with ICMEs with speed > 500 km/s) at L1 are likely to penetrate the magnetopause boundary and condition the magnetospheric energetic particle environment. On the contrary, “stealth” CMEs, having speeds < 450 km/s on most of the occasions, do not affect the energetic particle environment of the magnetosphere. Attempts are being made to strengthen this inference by evaluating a greater number of stealth and typical CMEs. Nevertheless, it is clear that this study is important in assessing the impact of ICME associated energetic particles on the terrestrial magnetosphere by simply evaluating the hardness of the particle spectra at the L1 point.

6.5 Key findings

1. Based on ASPEX payload on-board Aditya-L1 mission of India as well as other satellite and ground based observations, it is shown that stealth CMEs and typical shock CMEs can cause magnetic perturbations of equivalent strengths but their impact on the energetic particle environment on the magnetosphere can be entirely different.
2. SEPs or energetic ions with energies less than 2 MeV associated with stealth CMEs are, in general, are not effective in modulating magnetospheric energetic particle environment. This is because of low velocity and low shock strength of stealth CMEs.
3. SEPs or energetic ions with energies less than 2 MeV associated with typical CMEs with speed > 500 km/s affect the magnetospheric energetic particle environment if the spectral indices are harder at the L1 point.

Chapter 7

Summary and Future works

7.1 Summary

Suprathermal particles/ions (with energies $\sim 0.01\text{--}1.0\text{ MeV n}^{-1}$) are important to study for both scientific and technical reasons. These particles can directly affect the space assets (or indirectly by providing seeds for solar energetic particles). While this aspect raises technological concerns, the lack of understanding of the origin and energization processes of these particles make them scientifically critical. This thesis provides a detailed understanding of the generation and modulation of suprathermal ions during quiet IP conditions, passage of SIRs, and upstream of the terrestrial bow shock. It also discusses the impacts of SEPs associated with different types of ICME on the magnetospheric particle environment.

One of the objectives of this thesis is to understand the factors that contribute to the consistent presence of suprathermal particles in the IP medium even in the absence of transient events like ICMEs, SIR/CIRs, solar flares, etc. (i.e., during quiet times). This objective is achieved by comparing the differential directional fluxes of H, ^3He , ^4He , C, O, and Fe with sunspot number during solar cycles 23 and 24. It is observed that quiet-time suprathermal particles vary with the solar activity cycle (sunspot number cycle). However, in some cases, a time delay (lag) between the flux variation and sunspot number variation is observed. A lag in the quiet-time suprathermal ion fluxes is indicative of heliospheric modulation of suprathermal particles. This modulation is observed to depend on the m/q of different ion species, as ^4He and Fe behaved differently in terms of lag and

spectral indices in solar cycle 24, while C and O behave similarly in both solar cycles. SIR/CIRs are thought to play a vital role in modulating suprathermal particles in the interplanetary medium.

Therefore, as an obvious choice, SIR-associated suprathermal particles are studied in the next work. It is observed that SIR-associated suprathermal particles do not show a systematic dependence on the m/q of the species. On most of the occasions, large variations in the spectral indices are observed regardless of the type of events. This indicates that possibly multiple processes are involved in the acceleration of suprathermal particles. An observational evidence of acceleration of suprathermal particles by merger and/or contraction of small-scale magnetic islands during the passage of an SIR in the IP medium is also shown. This is indicative of the local acceleration of suprathermal particles in the interplanetary medium.

The characteristics of back-streaming suprathermal ions from the Earth's bow shock are investigated next. A direct comparison between suprathermal particles arriving at the L1 point from the direction of the Sun and from the direction of the Earth's bow shock is done in this work. In case of upstream events, modulation dependent on the m/q ratio in the suprathermal particles is prominent. This time, cross-field diffusion of different species appears to create the difference between light (H) and heavy (CNO) suprathermal species.

Another important aspect of the thesis is the first observations made by STEPS/ASPEX on board the Aditya-L1 satellite during its earth-bound phases. Contrasting impacts of suprathermal and low energy SEPs (< 2 MeV) associated with a typical ICME and an ICME corresponding to a "stealthy" CME on the dayside terrestrial magnetospheric energetic particle environment is shown.

This thesis highlights the importance of multi-point, multidirectional, species-separated measurements of suprathermal and energetic particles to decouple different processes regarding the energization of these particles. In addition, physics-based modeling is required to understand some of the aspects concerning the acceleration of suprathermal particles and SEPs.

7.2 Future works

This thesis explores the behaviors of suprathermal particles in different IP conditions. A number of factors governing the generation and modulation of these particles in the IP medium has been identified. The coupling between multiple sources and processes on the suprathermal ion pool has come out from the studies. Therefore, a single point measurement is not sufficient to understand the energization of these particles. There is a need of multi-point measurements to sample suprathermal particles from different parts of ICMEs, SIRs etc. The observations are to be coupled with physics-based models to get a comprehensive understanding of the acceleration mechanisms. It has been observed that energetic phenomena (like flare) can potentially affect the suprathermal ion populations in the IP medium. Therefore, remote sensing observations of the Sun are also helpful to identify source processes.

There are still many unknowns regarding the origin, acceleration, and fates of suprathermal particles. Some immediate scientific questions that surfaced during the course of this thesis are listed below:

1. The validity of “quiet” periods as far as suprathermal particles are concerned can be evaluated further.
2. It is observed that SIR-associated suprathermal particles exhibit softer spectra than during quiet times on many occasions. It is not yet clear under what conditions it is possible, particularly when there is an active acceleration framework (e.g., compression region) is present.
3. During the last phase of this thesis, the strongest geomagnetic storm in the past 20 years occurred on May 10, 2024. The implications of this storm on the suprathermal particle populations in the IP medium (at L1 point to be precise) needs to be investigated by using directional measurements from STEPS/ASPEX.
4. The energization processes of SEPs from the suprathermal particles can be better understood with the help of modeling and observations.

5. Suprathermal particles are frequently observed to enhance during the passage of ICMEs. This thesis does not include such investigation. Therefore, this study can be taken up in the near future.
6. Selective enhancements in heavy ion fluxes (Fe, O, CNO etc.) are observed during SIR events, upstream events. Although the detection limitation is argued to be one of the major reasons for such observations, a comprehensive understanding is needed in this regard.
7. The sources of suprathermal particles in the upstream events has been debated for past few decades. There is a need to delineate the solar wind and magnetospheric origin of these particles.
8. This thesis does not include the characteristics and acceleration of suprathermal electrons. This can be investigated for quiet/SIR/ICME events in future by using multi-point observations.
9. Modeling on the energization of suprathermal particles, connection of these particles with SEPs, transport of these particles in the interplanetary medium can be one of the potential future studies that can be taken up.
10. The association of energetic particles with the solar sources can be taken up using multi-vantage point observations and modeling.

Bibliography

- Aharonian, F., Akhperjanian, A., Bazer-Bachi, A., Beilicke, M., Benbow, W., Berge, D., Bernlöhr, K., Boisson, C., Bolz, O., Borrel, V., et al., 2011. Primary particle acceleration above 100 tev in the shell-type supernova remnant rx j1713. 7- 3946 with deep hess observations (corrigendum). *Astronomy & Astrophysics* 531, C1. doi:<https://doi.org/10.1051/0004-6361/20066381e>.
- Alfvén, H., 1941. On the solar corona. *Arkiv för matematik, astronomi och fysik* 27, 1–23.
- Allen, R., Mason, G., Ho, G., Rodríguez-Pacheco, J., Wimmer-Schweingruber, R., Andrews, G., Berger, L., Boden, S., Cernuda, I., Lara, F.E., et al., 2020. Suprathermal particles from corotating interaction regions during the first perihelion pass of solar orbiter. *Astronomy & Astrophysics* doi:<https://doi.org/10.1051/0004-6361/202039870>.
- Allen, R.C., Ho, G.C., Mason, G.M., 2019. Suprathermal ion abundance variations in corotating interaction regions over two solar cycles. *The Astrophysical Journal Letters* 883, L10. doi:[10.3847/2041-8213/ab3f2f](https://doi.org/10.3847/2041-8213/ab3f2f).
- Allen, R.C., Mason, G.M., Ho, G.C., Rodriguez-Pacheco, J., Wimmer-Schweingruber, R.F., Andrews, G., Berger, L., Boden, S., Cernuda, I., Lara, F.E., et al., 2021. Suprathermal particles from corotating interaction regions during the first perihelion pass of solar orbiter. *Astronomy & Astrophysics* 656, L2. doi:<https://doi.org/10.1051/0004-6361/202039870>.
- Anagnostopoulos, G., Efthymiadis, D., Sarris, E., Krimigis, S., 2005. Evidence and features of magnetospheric particle leakage on days 30–36, 1995: Wind, geotail, and imp 8 observations compared. *Journal of Geophysical Research: Space Physics* 110. doi:<https://doi.org/10.1029/2004JA010827>.
- Anagnostopoulos, G., Rigas, A., Sarris, E., Krimigis, S., 1998. Characteristics of upstream energetic ($e \geq 50$ kev) ion events during intense geomagnetic activity. *Journal of Geophysical Research: Space Physics* 103, 9521–9533. doi:<https://doi.org/10.1029/97JA02925>.
- Anderson, K., Harris, H., Paoli, R., 1965. Energetic electron fluxes in and beyond the earth's outer magnetosphere. *Journal of Geophysical Research* 70, 1039–1050. doi:<https://doi.org/10.1029/JZ070i005p01039>.

- Antecki, T., Schlickeiser, R., Zhang, M., 2013. Stochastic acceleration of suprathermal particles under pressure balance conditions. *The Astrophysical Journal* 764, 89. doi:[10.1088/0004-637X/764/1/89](https://doi.org/10.1088/0004-637X/764/1/89).
- Aptekar, R., Frederiks, D., Golenetskii, S., Ilynskii, V., Mazets, E., Panov, V., Sokolova, Z., Terekhov, M., Sheshin, L., Cline, T., et al., 1995. Konus-w gamma-ray burst experiment for the ggs wind spacecraft. *Space Science Reviews* 71, 265–272. doi:[10.1007/BF00751332](https://doi.org/10.1007/BF00751332).
- Armstrong, T.P., Pesses, M.E., Decker, R.B., 1985. Shock Drift Acceleration. American Geophysical Union (AGU). pp. 271–285. URL: <https://agupubs.onlinelibrary.wiley.com/doi/abs/10.1029/GM035p0271>, doi:<https://doi.org/10.1029/GM035p0271>, arXiv:<https://agupubs.onlinelibrary.wiley.com/doi/pdf/10.1029/GM035p0271>.
- Asbridge, J., Bame, S., Gosling, J., Paschmann, G., Sckopke, N., 1978. Energetic plasma ions within the earth's magnetosheath. *Geophysical Research Letters* 5, 953–955. doi:<https://doi.org/10.1029/GL005i011p00953>.
- Asbridge, J., Bame, S., Strong, I., 1968. Outward flow of protons from the earth's bow shock. *Journal of Geophysical Research* 73, 5777–5782. doi:<https://doi.org/10.1029/JA073i017p05777>.
- Axford, W., 1976. Flow of mass and energy in the solar system. *Physics of Solar Planetary Environments*, edited by DJ Williams , 270.
- Bame, S.J., Asbridge, J., Felthouser, H., Hones, E., Strong, I., 1967. Characteristics of the plasma sheet in the earth's magnetotail. *Journal of Geophysical Research* 72, 113–129. doi:<https://doi.org/10.1029/JZ072i001p00113>.
- Baral, R., Adhikari, B., Calabia, A., Shah, M., Mishra, R.K., Silwal, A., Bohara, S., Manandhar, R., del Peral, L., Frías, M.D.R., 2023. Spectral features of forrush decreases during geomagnetic storms. *Journal of Atmospheric and Solar-Terrestrial Physics* 242, 105981. doi:<https://doi.org/10.1016/j.jastp.2022.105981>.
- Barnes, C., Simpson, J., 1976. Evidence for interplanetary acceleration of nucleons in corotating interaction regions. *Astrophysical Journal*, vol. 210, Dec. 1, 1976, pt. 2, p. L91-L96. 210, L91–L96. doi:[10.1086/182311](https://doi.org/10.1086/182311).
- Belcher, J., Davis Jr, L., 1971. Large-amplitude alfvén waves in the interplanetary medium, 2. *Journal of Geophysical Research* 76, 3534–3563. doi:<https://doi.org/10.1029/JA076i016p03534>.
- Bell, A., 1978. The acceleration of cosmic rays in shock fronts–i. *Monthly Notices of the Royal Astronomical Society* 182, 147–156. doi:<https://doi.org/10.1093/mnras/182.2.147>.
- Bemporad, A., 2008. Spectroscopic detection of turbulence in post-cme current sheets. *The Astrophysical Journal* 689, 572. doi:[10.1086/592377](https://doi.org/10.1086/592377).

BIBLIOGRAPHY

- Bian, N.H., Kontar, E.P., 2013. Stochastic acceleration by multi-island contraction during turbulent magnetic reconnection. *Physical review letters* 110, 151101. doi:<https://doi.org/10.1103/PhysRevLett.110.151101>.
- Blandford, R.D., Ostriker, J.P., 1978. Particle acceleration by astrophysical shocks. *Astrophysical Journal, Part 2-Letters to the Editor*, vol. 221, Apr. 1, 1978, p. L29-L32. 221, L29-L32. doi:[10.1086/182658](https://doi.org/10.1086/182658).
- Bougeret, J.L., Goetz, K., Kaiser, M., Bale, S., Kellogg, P., Maksimovic, M., Monge, N., Monson, S., Astier, P., Davy, S., et al., 2008. S/waves: The radio and plasma wave investigation on the stereo mission. *Space Science Reviews* 136, 487–528. doi:[10.1007/s11214-007-9298-8](https://doi.org/10.1007/s11214-007-9298-8).
- Bougeret, J.L., Kaiser, M.L., Kellogg, P.J., Manning, R., Goetz, K., Monson, S., Monge, N., Friel, L., Meetre, C., Perche, C., et al., 1995. Waves: The radio and plasma wave investigation on the wind spacecraft. *Space Science Reviews* 71, 231–263. doi:<https://doi.org/10.1007/BF00751331>.
- Broll, J.M., Fuselier, S., Trattner, K., Schwartz, S., Burch, J., Giles, B., Anderson, B., 2018. Mms observation of shock-reflected he++ at earth's quasi-perpendicular bow shock. *Geophysical Research Letters* 45, 49–55.
- Bryant, D., Cline, T., Desai, U., McDonald, F.B., 1965. Continual acceleration of solar protons in the mev range. *Physical Review Letters* 14, 481. doi:<https://doi.org/10.1103/PhysRevLett.14.481>.
- Bučík, R., Mall, U., Korth, A., Mason, G., 2009. On acceleration of < 1 mev/n he ions in the corotating compression regions near 1 au: Stereo observations, in: *Annales Geophysicae*, Copernicus GmbH. pp. 3677–3690. doi:<https://doi.org/10.5194/angeo-27-3677-2009,2009>.
- Bučík, R., Mall, U., Korth, A., Mason, G., 2011. Stereo observations of the energetic ions in tilted corotating interaction regions. *Journal of Geophysical Research: Space Physics* 116. doi:<https://doi.org/10.1029/2010JA016311>.
- Burgess, D., 2007. Particle acceleration at the earth's bow shock, in: *The high energy solar corona: waves, eruptions, particles*. Springer, pp. 161–191.
- Bustamante, M., Jez, P., Monroy Montañez, J., Carrillo Montoya, G., Romeo, G., Padilla Cabal, F., Duarte Chavez, J., Saldaña-Salazar, U., Pino Rozas, M., Velasquez, M., et al., 2010. High-energy cosmic-ray acceleration .
- Cane, H.V., Erickson, W., Prestage, N., 2002. Solar flares, type iii radio bursts, coronal mass ejections, and energetic particles. *Journal of Geophysical Research: Space Physics* 107, SSH-14. doi:<https://doi.org/10.1029/2001JA000320>.
- Cargill, P.J., Vlahos, L., Turkmani, R., Galsgaard, K., Isliker, H., 2006. Particle acceleration in a three-dimensional model of reconnecting coronal magnetic fields. *Solar Dynamics and Its Effects on the Heliosphere and Earth* 124, 249–259. doi:https://doi.org/10.1007/978-0-387-69532-7_17.

- Cartwright, M., Moldwin, M., 2008. Comparison of small-scale flux rope magnetic properties to large-scale magnetic clouds: Evidence for reconnection across the hcs? *Journal of Geophysical Research: Space Physics* 113. doi:<https://doi.org/10.1029/2008JA013389>.
- Chao, J., Wu, D., Lin, C.H., Yang, Y.H., Wang, X., Kessel, M., Chen, S., Lepping, R., 2002. Models for the size and shape of the earth's magnetopause and bow shock, in: *COSPAR colloquia series*, Elsevier. pp. 127–135. doi:[https://doi.org/10.1016/S0964-2749\(02\)80212-8](https://doi.org/10.1016/S0964-2749(02)80212-8).
- Chen, J., Fritz, T.A., Sheldon, R.B., 2005. Multiple spacecraft observations of energetic ions during a high solar wind pressure event. *Journal of Geophysical Research: Space Physics* 110. doi:<https://doi.org/10.1029/2005JA011043>.
- Chertok, I., Belov, A., Grechnev, V., 2015. A simple way to estimate the soft x-ray class of far-side solar flares observed with stereo/euvi. *Solar Physics* 290, 1947–1961. doi:<https://doi.org/10.1007/s11207-015-0738-4>.
- Chottoo, K., Schwadron, N., Mason, G., Zurbuchen, T., Gloeckler, G., Posner, A., Fisk, L., Galvin, A., Hamilton, D., Collier, M., 2000. The suprathermal seed population for corotating interaction region ions at 1 au deduced from composition and spectra of h⁺, he⁺⁺, and he⁺ observed on wind. *Journal of Geophysical Research: Space Physics* 105, 23107–23122. doi:<https://doi.org/10.1029/1998JA000015>.
- Christon, S., Mitchell, D., Williams, D., Frank, L., Huang, C., Eastman, T., 1988. Energy spectra of plasma sheet ions and electrons from ~ 50 eV/e to ~ 1 MeV during plasma temperature transitions. *Journal of Geophysical Research: Space Physics* 93, 2562–2572. doi:<https://doi.org/10.1029/JA093iA04p02562>.
- Christon, S., Simpson, J., 1979. Separation of corotating nucleon fluxes from solar flare fluxes by radial gradients and nuclear composition. *Astrophysical Journal, Part 2-Letters to the Editor*, vol. 227, Jan. 1, 1979, p. L49–L53. 227, L49–L53. doi:<https://doi.org/10.1086/182865>.
- Christon, S.P., 1981. On the origin of the MeV energy nucleon flux associated with CIRs. *Journal of Geophysical Research: Space Physics* 86, 8852–8868. doi:<https://doi.org/10.1029/JA086iA11p08852>.
- Cohen, C., Mewaldt, R., Leske, R., Cummings, A., Stone, E., Wiedenbeck, M., Christian, E., Von Rosenvinge, T., 1999. New observations of heavy-ion-rich solar particle events from ACE. *Geophysical Research Letters* 26, 2697–2700. doi:<https://doi.org/10.1029/1999GL900560>.
- Cohen, I., Mauk, B., Anderson, B., Westlake, J., Sibeck, D.G., Giles, B.L., Pollock, C., Turner, D., Fennell, J., Blake, J., et al., 2016. Observations of energetic particle escape at the magnetopause: Early results from the MMS energetic ion spectrometer (EIS). *Geophysical Research Letters* 43, 5960–5968. doi:<https://doi.org/10.1002/2016GL068689>.

BIBLIOGRAPHY

- Connor, J., Hastie, R., 1975. Relativistic limitations on runaway electrons. *Nuclear fusion* 15, 415.
- Dalal, B., Chakrabarty, D., Srivastava, N., 2022. Differential behaviors of suprathermal 4He and Fe populations in the interplanetary medium during solar cycle 24. *The Astrophysical Journal* 938, 26. doi:[10.3847/1538-4357/ac88d8](https://doi.org/10.3847/1538-4357/ac88d8).
- Daly, P., Keppler, E., Williams, D., 1979. Ion and electron layers at the magnetopause: ISEE-2. *Magnetospheric Boundary Layers* 148, 137–141.
- Dayeh, M., Desai, M., Mason, G., Ebert, R., Farahat, A., 2017. Origin and properties of quiet-time 0.11–1.28 MeV nucleon⁻¹ heavy-ion population near 1 au. *The Astrophysical Journal* 835, 155. doi:[10.3847/1538-4357/835/2/155](https://doi.org/10.3847/1538-4357/835/2/155).
- Dayeh, M.A., Desai, M.I., Dwyer, J.R., Rassoul, H.K., Mason, G.M., Mazur, J.E., 2009. Composition and spectral properties of the 1 au quiet-time suprathermal ion population during solar cycle 23. *The Astrophysical Journal* 693, 1588–1600. URL: <https://doi.org/10.1088/0004-637x/693/2/1588>, doi:[10.1088/0004-637x/693/2/1588](https://doi.org/10.1088/0004-637x/693/2/1588).
- Desai, M., Dayeh, M., Mason, G., 2009. Origin of suprathermal ions near 1 au. *Proc. of the 31st ICRC* 61.
- Desai, M., Giacalone, J., 2016. Large gradual solar energetic particle events. *Living Reviews in Solar Physics* 13, 3. doi:<https://doi.org/10.1007/s41116-016-0002-5>.
- Desai, M., Marsden, R., Sanderson, T., Balogh, A., Forsyth, R., Gosling, J., 1998. Particle acceleration at corotating interaction regions in the three-dimensional heliosphere. *Journal of Geophysical Research: Space Physics* 103, 2003–2014. doi:<https://doi.org/10.1029/97JA02529>.
- Desai, M., Mason, G., Dwyer, J., Mazur, J., Von Rosenvinge, T., Lepping, R., 2000. Characteristics of energetic (≥ 30 keV/nucleon) ions observed by the Wind/STEP instrument upstream of the Earth's bow shock. *Journal of Geophysical Research: Space Physics* 105, 61–78. doi:<https://doi.org/10.1029/1999JA900406>.
- Desai, M., Mason, G., Müller-Mellin, R., Korth, A., Mall, U., Dwyer, J., von Rosenvinge, T., 2008. The spatial distribution of upstream ion events from the Earth's bow shock measured by ACE, Wind, and STEREO. *Journal of Geophysical Research: Space Physics* 113. doi:<https://doi.org/10.1029/2007JA012909>.
- Desai, M.I., Mason, G.M., Dwyer, J.R., Mazur, J.E., Gold, R.E., Krimigis, S.M., Smith, C.W., Skoug, R.M., 2003. Evidence for a suprathermal seed population of heavy ions accelerated by interplanetary shocks near 1 au. *The Astrophysical Journal* 588, 1149. doi:[10.1086/374310](https://doi.org/10.1086/374310).

- Desai, M.I., Mason, G.M., Wiedenbeck, M.E., Cohen, C., Mazur, J.E., Dwyer, J.R., Gold, R.E., Krimigis, S.M., Hu, Q., Smith, C.W., et al., 2004. Spectral properties of heavy ions associated with the passage of interplanetary shocks at 1 au. *The Astrophysical Journal* 611, 1156. doi:[10.1086/422211](https://doi.org/10.1086/422211).
- D’Huys, E., Seaton, D., Poedts, S., Berghmans, D., 2014. Observational characteristics of coronal mass ejections without low-coronal signatures. *The Astrophysical Journal* 795, 49. doi:[10.1088/0004-637X/795/1/49](https://doi.org/10.1088/0004-637X/795/1/49).
- Diehl, R., Kallenbach, R., Parizot, E., Von Steiger, R., 2001. The astrophysics of galactic cosmic rays. *Space science reviews* 99, 3–11. doi:[10.1023/A:1013882424934](https://doi.org/10.1023/A:1013882424934).
- Drake, J., Swisdak, M., Che, H., Shay, M., 2006a. Electron acceleration from contracting magnetic islands during reconnection. *Nature* 443, 553–556. doi:<https://doi.org/10.1038/nature05116>.
- Drake, J., Swisdak, M., Fermo, R., 2012. The power-law spectra of energetic particles during multi-island magnetic reconnection. *The Astrophysical Journal Letters* 763, L5. doi:[10.1088/2041-8205/763/1/L5](https://doi.org/10.1088/2041-8205/763/1/L5).
- Drake, J., Swisdak, M., Schoeffler, K., Rogers, B., Kobayashi, S., 2006b. Formation of secondary islands during magnetic reconnection. *Geophysical research letters* 33. doi:<https://doi.org/10.1029/2006GL025957>.
- Drake, J.F., Cassak, P., Shay, M., Swisdak, M., Quataert, E., 2009. A magnetic reconnection mechanism for ion acceleration and abundance enhancements in impulsive flares. *The Astrophysical Journal Letters* 700, L16. doi:[10.1088/0004-637X/700/1/L16](https://doi.org/10.1088/0004-637X/700/1/L16).
- Drury, L.O., 1983. An introduction to the theory of diffusive shock acceleration of energetic particles in tenuous plasmas. *Reports on Progress in Physics* 46, 973.
- Dwyer, J., Mason, G., Desai, M., Mazur, J., von Rosenvinge, T., 2000. The spatial size of ion events measured far upstream of the earth’s bow shock by ace/uleis and wind/step. *Geophysical research letters* 27, 65–68. doi:<https://doi.org/10.1029/1999GL003670>.
- Eastwood, J., Balogh, A., Dunlop, M., Smith, C., 2002. Cluster observations of the heliospheric current sheet and an associated magnetic flux rope and comparisons with ace. *Journal of Geophysical Research: Space Physics* 107, SSH–9. doi:<https://doi.org/10.1029/2001JA009158>.
- Ebert, R., Dayeh, M., Desai, M., Mason, G., 2012. Corotating interaction region associated suprathermal helium ion enhancements at 1 au: Evidence for local acceleration at the compression region trailing edge. *The Astrophysical Journal* 749, 73. doi:[10.1088/0004-637X/749/1/73](https://doi.org/10.1088/0004-637X/749/1/73).

BIBLIOGRAPHY

- Ellison, D.C., Moebius, E., 1987. Diffusive shock acceleration-comparison of a unified shock model to bow shock observations. *Astrophysical Journal, Part 1* (ISSN 0004-637X), vol. 318, July 1, 1987, p. 474-484. NASA-supported research. 318, 474–484. doi:[10.1086/165384](https://doi.org/10.1086/165384).
- Eriksson, S., Newman, D., Lapenta, G., Angelopoulos, V., 2014. On the signatures of magnetic islands and multiple x-lines in the solar wind as observed by artemis and wind. *Plasma Physics and Controlled Fusion* 56, 064008.
- Fan, C., Gloeckler, G., Hovestadt, D., 1975. Energy spectra and charge states of h, he, and heavy ions observed in the earth's magnetosheath and magnetotail. *Physical Review Letters* 34, 495. doi:<https://doi.org/10.1103/PhysRevLett.34.495>.
- Fan, C., Hovestadt, D., Gloeckler, G., 1976. Low-energy heavy-ion observations on the imp 7 satellite, in: *The Scientific Satellite Programme during the International Magnetospheric Study: Proceedings of the 10th ESLAB Symposium, Held at Vienna, Austria, 10–13 June 1975*, Springer. pp. 187–197. doi:https://doi.org/10.1007/978-94-010-1892-0_12.
- Feldman, U., Widing, K., 2002. A review of the first ionization potential effect on elemental abundances in the solar corona and in flares. *Physics of Plasmas* 9, 629–635. doi:<https://doi.org/10.1063/1.1435000>.
- Fermi, E., 1949. On the origin of the cosmic radiation. *Physical review* 75, 1169. doi:<https://doi.org/10.1103/PhysRev.75.1169>.
- Filwett, R., Desai, M., Dayeh, M., Broiles, T., 2017. Source population and acceleration location of suprathermal heavy ions in corotating interaction regions. *The Astrophysical Journal* 838, 23. doi:[10.3847/1538-4357/aa5ca9](https://doi.org/10.3847/1538-4357/aa5ca9).
- Filwett, R., Desai, M., Ebert, R., Dayeh, M., 2019. Spectral properties and abundances of suprathermal heavy ions in compression regions near 1 au. *The Astrophysical Journal* 876, 88. doi:[10.3847/1538-4357/ab12cf](https://doi.org/10.3847/1538-4357/ab12cf).
- Filwett, R.J., Jaynes, A.N., Baker, D.N., Kanekal, S.G., Kress, B., Blake, J.B., 2020. Solar energetic proton access to the near-equatorial inner magnetosphere. *Journal of Geophysical Research: Space Physics* 125, e2019JA027584. doi:<https://doi.org/10.1029/2019JA027584>.
- Fioretti, V., Bulgarelli, A., Malaguti, G., Spiga, D., Tiengo, A., 2016. Monte carlo simulations of soft proton flares: testing the physics with xmm-newton, in: *Space Telescopes and Instrumentation 2016: Ultraviolet to Gamma Ray*, SPIE. pp. 1991–2004. doi:[10.1117/12.2232537](https://doi.org/10.1117/12.2232537).
- Fisk, L., Gloeckler, G., 2006. The common spectrum for accelerated ions in the quiet-time solar wind. *The Astrophysical Journal Letters* 640, L79. doi:[10.1086/503293](https://doi.org/10.1086/503293).

- Fisk, L., Gloeckler, G., 2008. Acceleration of suprathermal tails in the solar wind. *The Astrophysical Journal* 686, 1466. doi:[10.1086/591543](https://doi.org/10.1086/591543).
- Fisk, L., Gloeckler, G., 2014. The case for a common spectrum of particles accelerated in the heliosphere: Observations and theory. *Journal of Geophysical Research: Space Physics* 119, 8733–8749. doi:<https://doi.org/10.1002/2014JA020426>.
- Fisk, L., Kozlovsky, B., Ramaty, R., 1974. An interpretation of the observed oxygen and nitrogen enhancements in low-energy cosmic rays. *Astrophysical Journal*, vol. 190, p. L35 190, L35. doi:[10.1086/181498](https://doi.org/10.1086/181498).
- Fisk, L., Lee, M., 1980. Shock acceleration of energetic particles in corotating interaction regions in the solar wind. *The Astrophysical Journal* 237, 620–626. doi:[10.1086/157907](https://doi.org/10.1086/157907).
- Fisk, L.A., 1976. The acceleration of energetic particles in the interplanetary medium by transit time damping. *Journal of Geophysical Research (1896-1977)* 81, 4633–4640. URL: <https://agupubs.onlinelibrary.wiley.com/doi/abs/10.1029/JA081i025p04633>, doi:<https://doi.org/10.1029/JA081i025p04633>, arXiv:<https://agupubs.onlinelibrary.wiley.com/doi/pdf/10.1029/JA081i025p04633>.
- Fisk, L.A., Gloeckler, G., 2007. Thermodynamic constraints on stochastic acceleration in compressional turbulence. *Proceedings of the National Academy of Sciences* 104, 5749–5754. doi:<https://doi.org/10.1073/pnas.0700881104>.
- Flückiger, E., Smart, D., Shea, M., 1990. Determining the strength of the ring and the magnetopause currents during the initial phase of a geomagnetic storm using cosmic ray data. *Journal of Geophysical Research: Space Physics* 95, 1113–1118. doi:[10.1029/JA095iA02p01113](https://doi.org/10.1029/JA095iA02p01113).
- Formisano, V., Moreno, G., Palmiotto, F., Hedgecock, P., 1973. Solar wind interaction with the earth's magnetic field: 1. magnetosheath. *Journal of Geophysical Research* 78, 3714–3730. doi:<https://doi.org/10.1029/JA078i019p03714>.
- Frisch, P., 1996. Lism structure—fragmented superbubble shell? *Space Science Reviews* 78, 213–222. doi:<https://doi.org/10.1007/BF00170807>.
- Fu, S., Zhang, X., Zhao, L., Li, Y., 2021. Variations of the galactic cosmic rays in the recent solar cycles. *The Astrophysical Journal Supplement Series* 254, 37. doi:[10.3847/1538-4365/abf936](https://doi.org/10.3847/1538-4365/abf936).
- Galvin, A.B., Kistler, L.M., Popecki, M.A., Farrugia, C.J., Simunac, K.D., Ellis, L., Möbius, E., Lee, M.A., Boehm, M., Carroll, J., et al., 2008. The plasma and suprathermal ion composition (plastic) investigation on the stereo observatories. *The STEREO Mission*, 437–486doi:<https://doi.org/10.1007/s11214-007-9296-x>.

BIBLIOGRAPHY

- Ghosh, A., Chatterjee, S., Khan, A.R., Tripathi, D., Ramaprakash, A., Banerjee, D., Chordia, P., Gandorfer, A.M., Krivova, N., Nandy, D., et al., 2016. The solar ultraviolet imaging telescope onboard aditya-11, in: Space Telescopes and Instrumentation 2016: Ultraviolet to Gamma Ray, SPIE. pp. 10–20. doi:[10.1117/12.2232266](https://doi.org/10.1117/12.2232266).
- Giacalone, J., Drake, J., Jokipii, J., 2012. The acceleration mechanism of anomalous cosmic rays. *Space science reviews* 173, 283–307. doi:<https://doi.org/10.1007/s11214-012-9915-z>.
- Giacalone, J., Jokipii, J., Mazur, J., 2000. Small-scale gradients and large-scale diffusion of charged particles in the heliospheric magnetic field. *The Astrophysical Journal* 532, L75. doi:[10.1088/0004-637X/780/1/16](https://doi.org/10.1088/0004-637X/780/1/16).
- Giacalone, J., Jokipii, J.R., Kota, J., 2002. Particle acceleration in solar wind compression regions. *The Astrophysical Journal* 573, 845–850. URL: <https://doi.org/10.1086/340660>, doi:[10.1086/340660](https://doi.org/10.1086/340660).
- Gloeckler, G., 2003. Ubiquitous suprathermal tails on the solar wind and pickup ion distributions, in: AIP Conference Proceedings, American Institute of Physics. pp. 583–588. doi:<https://doi.org/10.1063/1.1618663>.
- Gloeckler, G., Balsiger, H., Bürgi, A., Bochsler, P., Fisk, L.A., Galvin, A.B., Geiss, J., Gliem, F., Hamilton, D., Holzer, T., et al., 1995a. The solar wind and suprathermal ion composition investigation on the wind spacecraft. *Space Science Reviews* 71, 79–124. doi:<https://doi.org/10.1007/BF00751327>.
- Gloeckler, G., Cain, J., Ipavich, F., Tums, E., Bedini, P., Fisk, L., Zurbuchen, T., Bochsler, P., Fischer, J., Wimmer-Schweingruber, R., et al., 1998. Investigation of the composition of solar and interstellar matter using solar wind and pickup ion measurements with swics and swims on the ace spacecraft. *The advanced composition explorer mission* , 497–539doi:[10.1023/A:1005036131689](https://doi.org/10.1023/A:1005036131689).
- Gloeckler, G., Geiss, J., Balsiger, H., Bedini, P., Cain, J., Fischer, J., Fisk, L., Galvin, A., Gliem, F., Hamilton, D., et al., 1992. The solar wind ion composition spectrometer. *Astronomy and Astrophysics Supplement Series* (ISSN 0365-0138), vol. 92, no. 2, Jan. 1992, p. 267–289. 92, 267–289. doi:[1992A&AS...92..267G](https://doi.org/10.1051/aa:1992267).
- Gloeckler, G., Hamilton, D., 1987. Ampte ion composition results. *Physica Scripta* 1987, 73. doi:[10.1088/0031-8949/1987/T18/009](https://doi.org/10.1088/0031-8949/1987/T18/009).
- Gloeckler, G., Roelof, E., Ogilvie, K., Berdichevsky, D., 1995b. Proton phase space densities ($0.5 \text{ eV} < e < p < 5 \text{ MeV}$) at midlatitudes from ulysses swics/hi-scale measurements. *Space Science Reviews* 72, 321–326.
- Gold, R., Krimigis, S., Hawkins, S., Haggerty, D., Lohr, D., Fiore, E., Armstrong, T., Holland, G., Lanzerotti, L., 1998. Electron, proton, and alpha monitor on the advanced composition explorer spacecraft. *The Advanced Composition Explorer Mission* , 541–562doi:<https://doi.org/10.1023/A:1005088115759>.

- Gopalswamy, N., Akiyama, S., Yashiro, S., Xie, H., Mäkelä, P., Michalek, G., 2014. Anomalous expansion of coronal mass ejections during solar cycle 24 and its space weather implications. *Geophysical Research Letters* 41, 2673–2680. doi:<https://doi.org/10.1002/2014GL059858>.
- Gordovskyy, M., Browning, P., Vekstein, G., 2010. Particle acceleration in a transient magnetic reconnection event. *Astronomy & Astrophysics* 519, A21.
- Gosling, J., Asbridge, J., Bame, S.J., Feldman, W., Zwickl, R., Paschmann, G., Sckopke, N., Hynds, R., 1981. Interplanetary ions during an energetic storm particle event: The distribution function from solar wind thermal energies to 1.6 mev. *Journal of Geophysical Research: Space Physics* 86, 547–554. doi:<https://doi.org/10.1029/JA086iA02p00547>.
- Gosling, J., Robson, A., 1985. Ion reflection, gyration, and dissipation at supercritical shocks. *Collisionless shocks in the heliosphere: Reviews of current research* 35, 141–152. doi:<https://doi.org/10.1029/GM035p0141>.
- Gosling, J., Thomsen, M., Bame, S., Feldman, W., Paschmann, G., Sckopke, N., 1982. Evidence for specularly reflected ions upstream from the quasi-parallel bow shock. *Geophysical Research Letters* 9, 1333–1336. doi:<https://doi.org/10.1029/GL009i012p01333>.
- Gouveia Dal Pino, E.M.d., Lazarian, A., 2005. Production of the large scale superluminal ejections of the microquasar grs 1915+ 105 by violent magnetic reconnection. *Astronomy and Astrophysics* , 845–853doi:[10.1051/0004-6361:20042590](https://doi.org/10.1051/0004-6361:20042590).
- Goyal, S., Kumar, P., Janardhan, P., Vadawale, S., Sarkar, A., Shanmugam, M., Subramanian, K., Bapat, B., Chakrabarty, D., Adhyaru, P., et al., 2018. Aditya solarwind particle experiment (aspeX) onboard the aditya-l1 mission. *Planetary and Space Science* 163, 42–55. doi:<https://doi.org/10.1016/j.pss.2018.04.008>.
- Greco, A., Servidio, S., Matthaeus, W., Dmitruk, P., 2010. Intermittent structures and magnetic discontinuities on small scales in mhd simulations and solar wind. *Planetary and Space Science* 58, 1895–1899. doi:<https://doi.org/10.1016/j.pss.2010.08.019>.
- Greenstadt, E., Russell, C., Hoppe, M., 1980. Magnetic field orientation and suprathermal ion streams in the earth's foreshock. *Journal of Geophysical Research: Space Physics* 85, 3473–3479.
- Haggerty, D., Roelof, E., Smith, C., Ness, N., Tokar, R., Skoug, R., 2000. Interplanetary magnetic field connection to the l1 lagrangian orbit during upstream energetic ion events. *Journal of Geophysical Research: Space Physics* 105, 25123–25131.

BIBLIOGRAPHY

- Haskell, G., 1969. Anisotropic fluxes of energetic particles in the outer magnetosphere. *Journal of Geophysical Research* 74, 1740–1748. doi:<https://doi.org/10.1029/JA074i007p01740>.
- Hilchenbach, M., Grünwaldt, H., Kallenbach, R., Klecker, B., Kucharek, H., Ipavich, F., Galvin, A., 1999. Observation of suprathermal helium at 1 au: Charge states in cirs, in: *AIP Conference Proceedings*, American Institute of Physics. pp. 605–608. doi:<https://doi.org/10.1063/1.58812>.
- Hillas, A., 2006. The cosmic-ray knee and ensuing spectrum seen as a consequence of bell's self-magnetized snr shock acceleration process, in: *Journal of Physics: Conference Series*, IOP Publishing. p. 168. doi:[10.1088/1742-6596/47/1/021](https://doi.org/10.1088/1742-6596/47/1/021).
- Hones Jr, E., Akasofu, S.I., Bame, S., Singer, S., 1972. Outflow of plasma from the magnetotail into the magnetosheath. *Journal of Geophysical Research* 77, 6688–6695. doi:<https://doi.org/10.1029/JA077i034p06688>.
- Howard, R.A., Moses, J., Vourlidas, A., Newmark, J., Socker, D.G., Plunkett, S.P., Korendyke, C.M., Cook, J., Hurley, A., Davila, J., et al., 2008. Sun earth connection coronal and heliospheric investigation (secchi). *Space Science Reviews* 136, 67–115. doi:<https://doi.org/10.1007/s11214-008-9341-4>.
- Howard, T.A., Harrison, R.A., 2013. Stealth coronal mass ejections: A perspective. *Solar Physics* 285, 269–280. doi:<https://doi.org/10.1007/s11207-012-0217-0>.
- Ipavich, F., Galvin, A., Gloeckler, G., Scholer, M., Hovestadt, D., 1981. A statistical survey of ions observed upstream of the earth's bow shock: Energy spectra, composition, and spatial variation. *Journal of Geophysical Research: Space Physics* 86, 4337–4342. doi:<https://doi.org/10.1029/JA086iA06p04337>.
- Ivanova, T., Kuznetsov, S., Sosnovets, E.N., Tverskaia, L., 1985. Dynamics of the low-latitude boundary of penetration of low-energy solar protons into the magnetosphere. *Geomagnetism and Aeronomy* 25, 7–12.
- Janardhan, P., Fujiki, K., Ingale, M., Bisoi, S.K., Rout, D., 2018. Solar cycle 24: An unusual polar field reversal. *Astronomy & Astrophysics* 618, A148. doi:<https://doi.org/10.1051/0004-6361/201832981>.
- Janardhan, P., Vadawale, S., Bapat, B., Subramanian, K., Chakrabarty, D., Kumar, P., Sarkar, A., Srivastava, N., Thampi, R.S., Yadav, V.K., et al., 2017. Probing the heliosphere using in situ payloads on-board aditya-l1. *Current Science* , 620–624.
- Jokipii, J., 1982. Particle drift, diffusion, and acceleration at shocks. *Astrophysical Journal*, Part 1, vol. 255, Apr. 15, 1982, p. 716-720. 255, 716–720. doi:[10.1086/159870](https://doi.org/10.1086/159870).

- Jokipii, J., 1987. Rate of energy gain and maximum energy in diffusive shock acceleration. *Astrophysical Journal, Part 1* (ISSN 0004-637X), vol. 313, Feb. 15, 1987, p. 842-846. doi:[10.1086/165022](https://doi.org/10.1086/165022).
- Kaiser, M.L., Kucera, T., Davila, J., St Cyr, O., Guhathakurta, M., Christian, E., 2008. The stereo mission: An introduction. *Space Science Reviews* 136, 5–16. doi:https://doi.org/10.1007/978-0-387-09649-0_2.
- Kalegaev, V.V., Vlasova, N.A., Nazarkov, I.S., Melkova, S.A., 2018. Magnetospheric access for solar protons during the january 2005 sep event. *Journal of Space Weather and Space Climate* 8, A55. doi:<https://doi.org/10.1051/swsc/2018040>.
- Kasper, J.C., Stevens, M.L., Lazarus, A.J., Steinberg, J.T., Ogilvie, K.W., 2007. Solar wind helium abundance as a function of speed and heliographic latitude: Variation through a solar cycle. *The Astrophysical Journal* 660, 901. doi:[10.1086/510842](https://doi.org/10.1086/510842).
- Kecskemety, K., Zeldovich, M., LOGACHEV, Y., 2011. Relative abundances of quiet-time suprathermal ions at 1 au, in: *Proc. of 32th Int. Cosmic Ray Conference, Beijing*. doi:[10.7529/ICRC2011/V11/0397](https://doi.org/10.7529/ICRC2011/V11/0397).
- Khabarova, O., Zank, G., Li, G., Le Roux, J., Webb, G., Dosch, A., Malandraki, O., 2015a. Small-scale magnetic islands in the solar wind and their role in particle acceleration. i. dynamics of magnetic islands near the heliospheric current sheet. *The Astrophysical Journal* 808, 181. doi:[10.1088/0004-637X/808/2/181](https://doi.org/10.1088/0004-637X/808/2/181).
- Khabarova, O.V., Zank, G.P., Li, G., Malandraki, O.E., le Roux, J.A., Webb, G.M., 2016. Small-scale magnetic islands in the solar wind and their role in particle acceleration. ii. particle energization inside magnetically confined cavities. *The Astrophysical Journal* 827, 122. doi:[10.1088/0004-637X/808/2/181](https://doi.org/10.1088/0004-637X/808/2/181).
- Khabarova, O.V., Zank, G.P., Li, G., le Roux, J.A., Webb, G.M., Malandraki, O.E., Zharkova, V.V., 2015b. Dynamical small-scale magnetic islands as a source of local acceleration of particles in the solar wind, in: *Journal of Physics: Conference Series*, IOP Publishing. p. 012033. doi:[10.1088/1742-6596/642/1/012033](https://doi.org/10.1088/1742-6596/642/1/012033).
- Kilpua, E., Mierla, M., Zhukov, A., Rodriguez, L., Vourlidas, A., Wood, B., 2014. Solar sources of interplanetary coronal mass ejections during the solar cycle 23/24 minimum. *Solar Physics* 289, 3773–3797. doi:<https://doi.org/10.1007/s11207-014-0552-4>.
- Kis, A., Scholer, M., Klecker, B., Möbius, E., Lucek, E., Rème, H., Bosqued, J., Kistler, L., Kucharek, H., 2004. Multi-spacecraft observations of diffuse ions upstream of earth's bow shock. *Geophysical research letters* 31. doi:<https://doi.org/10.1029/2004GL020759>.

BIBLIOGRAPHY

- Kivelson, M.G., Russell, C.T. (Eds.), 1995. Introduction to Space Physics. Cambridge University Press, Cambridge, UK. University of California, Los Angeles.
- Klecker, B., Hovestadt, D., Scholer, M., Gloeckler, G., Ipavich, F., Fan, C., Fisk, L., 1984. Direct determination of the ionic charge distribution of helium and iron in he-3-rich solar energetic particle events. *Astrophysical Journal, Part 1* (ISSN 0004-637X), vol. 281, June 1, 1984, p. 458-462. Sponsorship: Bundesministerium für Forschung und Technologie. 281, 458–462. doi:[10.1086/162117](https://doi.org/10.1086/162117).
- Kletzing, C., Scudder, J., Dors, E., Curto, C., 2003. Auroral source region: Plasma properties of the high-latitude plasma sheet. *Journal of Geophysical Research: Space Physics* 108. doi:[10.1029/2002JA009678](https://doi.org/10.1029/2002JA009678), 2003.
- Knoll, G.F., 2010. Radiation detection and measurement. John Wiley & Sons.
- Kowal, G., Dal Pino, E.d.G., Lazarian, A., 2011. Magnetohydrodynamic simulations of reconnection and particle acceleration: three-dimensional effects. *The Astrophysical Journal* 735, 102. doi:[10.1088/0004-637X/735/2/102](https://doi.org/10.1088/0004-637X/735/2/102).
- Kowal, G., de Gouveia Dal Pino, E.M., Lazarian, A., 2012. Particle acceleration in turbulence and weakly stochastic reconnection. *Physical Review Letters* 108, 241102. doi:[10.1103/PhysRevLett.108.241102](https://doi.org/10.1103/PhysRevLett.108.241102).
- Kronberg, E., Bučík, R., Haaland, S., Klecker, B., Keika, K., Desai, M., Daly, P., Yamauchi, M., Gómez-Herrero, R., Lui, A., 2011. On the origin of the energetic ion events measured upstream of the earth's bow shock by stereo, cluster, and geotail. *Journal of Geophysical Research: Space Physics* 116. doi:<https://doi.org/10.1029/2010JA015561>.
- Krymskii, G., 1977. A regular mechanism for the acceleration of charged particles on the front of a shock wave, in: *Akademiia Nauk SSSR Doklady*, pp. 1306–1308.
- Kucharek, H., Möbius, E., Li, W., Farrugia, C.J., Popecki, M.A., Galvin, A.B., Klecker, B., Hilchenbach, M., Bochsler, P., 2003. On the source and acceleration of energetic he⁺: A long-term observation with ace/sepica. *Journal of Geophysical Research: Space Physics* 108. doi:<https://doi.org/10.1029/2003JA009938>.
- Kudela, K., Bučík, R., Bobik, P., 2008. On transmissivity of low energy cosmic rays in disturbed magnetosphere. *Advances in Space Research* 42, 1300–1306. doi:[10.1016/j.asr.2007.09.033](https://doi.org/10.1016/j.asr.2007.09.033).
- Kunow, H., Witte, M., Wibberenz, G., Hempe, H., Mueller-Mellin, R., Green, G., Fuckner, J., et al., 1976. Cosmic ray measurements on board helios 1 from december 1974 to september 1975: Quiet time spectra, radial gradients, and solar events. *Journal of Geophysics* 42, 615–631.
- Laming, J.M., 2015. The fip and inverse fip effects in solar and stellar coronae. *Living Reviews in Solar Physics* 12, 1–76.

- Lazar, M., Schlickeiser, R., Poedts, S., 2012. Suprathermal particle populations in the solar wind and corona. *Exploring the Solar Wind*, 241doi:[10.5772/39281](https://doi.org/10.5772/39281).
- Le Roux, J., Zank, G., Webb, G., Khabarova, O., 2015. A kinetic transport theory for particle acceleration and transport in regions of multiple contracting and reconnecting inertial-scale flux ropes. *The Astrophysical Journal* 801, 112. doi:[10.1088/0004-637X/801/2/112](https://doi.org/10.1088/0004-637X/801/2/112).
- Lee, M.A., 1982. Coupled hydromagnetic wave excitation and ion acceleration upstream of the earth's bow shock. *Journal of Geophysical Research: Space Physics* 87, 5063–5080. doi:<https://doi.org/10.1029/JA087iA07p05063>.
- Lepping, R., Acuña, M., Burlaga, L., Farrell, W., Slavin, J., Schatten, K., Mariani, F., Ness, N., Neubauer, F., Whang, Y., et al., 1995. The wind magnetic field investigation. *Space Science Reviews* 71, 207–229. doi:<https://doi.org/10.1007/BF00751330>.
- Li, G., Lee, M.A., 2015. Scatter-dominated interplanetary transport of solar energetic particles in large gradual events and the formation of double power-law differential fluence spectra of ground-level events during solar cycle 23. *The Astrophysical Journal* 810, 82. doi:[10.1088/0004-637X/810/1/82](https://doi.org/10.1088/0004-637X/810/1/82).
- Lin, R., Anderson, K., Ashford, S., Carlson, C., Curtis, D., Ergun, R., Larson, D., McFadden, J., McCarthy, M., Parks, G., et al., 1995. A three-dimensional plasma and energetic particle investigation for the wind spacecraft. *Space Science Reviews* 71, 125–153. doi:<https://doi.org/10.1007/BF00751328>.
- Lin, R.P., Meng, C.I., Anderson, K.A., 1974. 30-to 100-keV protons upstream from the earth's bow shock. *Journal of Geophysical Research* 79, 489–498. doi:<https://doi.org/10.1029/JA079i004p00489>.
- Luhmann, J., Curtis, D., Schroeder, P., McCauley, J., Lin, R., Larson, D., Bale, S., Sauvaud, J.A., Aoustin, C., Mewaldt, R., et al., 2008. Stereo impact investigation goals, measurements, and data products overview, in: *The STEREO Mission*. Springer, pp. 117–184. doi:https://doi.org/10.1007/978-0-387-09649-0_6.
- Luhn, A., Klecker, B., Hovestadt, D., Gloeckler, G., Ipavich, F., Scholer, M., Fan, C., Fisk, L., 1984. Ionic charge states of n, ne, mg, si and s in solar energetic particle events. *Advances in Space Research* 4, 161–164. doi:[https://doi.org/10.1016/0273-1177\(84\)90307-7](https://doi.org/10.1016/0273-1177(84)90307-7).
- Luhn, A., Klecker, B., Hovestadt, D., Möbius, E., 1987. The mean ionic charge of silicon in he-3-rich solar flares. *Astrophysical Journal, Part 1 (ISSN 0004-637X)*, vol. 317, June 15, 1987, p. 951-955. 317, 951–955. doi:[10.1086/165343](https://doi.org/10.1086/165343).
- Ma, S., Attrill, G., Golub, L., Lin, J., 2010. Statistical study of coronal mass ejections with and without distinct low coronal signatures. *The Astrophysical Journal* 722, 289. doi:[10.1088/0004-637X/722/1/289](https://doi.org/10.1088/0004-637X/722/1/289).

BIBLIOGRAPHY

- Machol, J.L., Eparvier, F.G., Viereck, R.A., Woodraska, D.L., Snow, M., Thiemann, E., Woods, T.N., McClintock, W.E., Mueller, S., Eden Jr, T.D., et al., 2020. Goes-r series solar x-ray and ultraviolet irradiance, in: The GOES-R Series. Elsevier, pp. 233–242. doi:<https://doi.org/10.1016/B978-0-12-814327-8.00019-6>.
- Maksimovic, M., Pierrard, V., Riley, P., 1997. Ulysses electron distributions fitted with kappa functions. *Geophysical research letters* 24, 1151–1154. doi:<https://doi.org/10.1029/97GL00992>.
- Markidis, S., Henri, P., Lapenta, G., Divin, A., Goldman, M., Newman, D., Laure, E., 2013. Kinetic simulations of plasmoid chain dynamics. *Physics of Plasmas* 20.
- Marshall, F., Stone, E., 1978. Characteristics of sunward flowing proton and alpha particle fluxes of moderate intensity. *Journal of Geophysical Research: Space Physics* 83, 3289–3298. doi:<https://doi.org/10.1029/JA083iA07p03289>.
- Mason, G., 2000. Composition and energy spectra of ions accelerated in corotating interaction regions, in: *AIP Conference Proceedings*, American Institute of Physics. pp. 234–241. doi:<https://doi.org/10.1063/1.1324318>.
- Mason, G., Desai, M., Li, G., 2012. Solar cycle abundance variations in corotating interaction regions: Evidence for a suprathermal ion seed population. *The Astrophysical Journal Letters* 748, L31. doi:[10.1088/2041-8205/748/2/L31](https://doi.org/10.1088/2041-8205/748/2/L31).
- Mason, G., Dwyer, J., Mazur, J., 2000. New properties of 3He-rich solar flares deduced from low-energy particle spectra. *The Astrophysical Journal* 545, L157. doi:[10.1086/317886](https://doi.org/10.1086/317886).
- Mason, G., Gloeckler, G., 2012. Power law distributions of suprathermal ions in the quiet solar wind. *Space science reviews* 172, 241–251. doi:<https://doi.org/10.1007/s11214-010-9741-0>.
- Mason, G., Gold, R., Krimigis, S., Mazur, J., Andrews, G., Daley, K., Dwyer, J., Heurman, K., James, T., Kennedy, M., et al., 1998. The ultra-low-energy isotope spectrometer (uleis) for the ace spacecraft. *The Advanced Composition Explorer Mission* , 409–448doi:https://doi.org/10.1007/978-94-011-4762-0_16.
- Mason, G., Korth, A., Walpole, P., Desai, M.v., Von Roseninge, T., Shuman, S., 2008a. The suprathermal ion telescope (sit) for the impact/sep investigation. *Space science reviews* 136, 257–284. doi:<https://doi.org/10.1007/s11214-006-9087-9>.
- Mason, G., Mazur, J., Dwyer, J., Reames, D., Von Roseninge, T., 1997. New spectral and abundance features of interplanetary heavy ions in corotating interaction regions. *The Astrophysical Journal Letters* 486, L149. doi:[10.1086/310845](https://doi.org/10.1086/310845).

- Mason, G., Von Steiger, R., Decker, R., Desai, M., Dwyer, J., Fisk, L., Gloeckler, G., Gosling, J., Hilchenbach, M., Kallenbach, R., et al., 1999. Origin, injection, and acceleration of cir particles: Observations. Corotating Interaction Regions , 327–367doi:https://doi.org/10.1007/978-94-017-1179-1_16.
- Mason, G.M., Leske, R.A., Desai, M.I., Cohen, C., Dwyer, J.R., Mazur, J.E., Mewaldt, R.A., Gold, R.E., Krimigis, S.M., 2008b. Abundances and energy spectra of corotating interaction region heavy ions observed during solar cycle 23. *The Astrophysical Journal* 678, 1458. doi:[10.1086/533524](https://doi.org/10.1086/533524).
- Mason, G.M., Wiedenbeck, M.E., Miller, J.A., Mazur, J.E., Christian, E.R., Cohen, C., Cummings, A.C., Dwyer, J.R., Gold, R.E., Krimigis, S.M., et al., 2002. Spectral properties of he and heavy ions in 3he-rich solar flares. *The Astrophysical Journal* 574, 1039. doi:[10.1086/341112](https://doi.org/10.1086/341112).
- Mazur, J., Mason, G., Dwyer, J., Giacalone, J., Jokipii, J., Stone, E., 2000. Interplanetary magnetic field line mixing deduced from impulsive solar flare particles. *The Astrophysical Journal* 532, L79. doi:[10.1086/312561](https://doi.org/10.1086/312561).
- Mazur, J., Mason, G., Mewaldt, R., 2002. Charge states of energetic particles from corotating interaction regions as constraints on their source. *The Astrophysical Journal* 566, 555. doi:<https://doi.org/10.1086/337989>.
- McComas, D., Bame, S., Barker, P., Feldman, W., Phillips, J., Riley, P., Griffee, J., 1998. Solar wind electron proton alpha monitor (swepam) for the advanced composition explorer. *The advanced composition explorer mission* , 563–612doi:<https://doi.org/10.1023/A:1005040232597>.
- McDonald, F., Teegarden, B., Trainor, J., Vonrosenvinge, T., Webber, W., 1976. The interplanetary acceleration of energetic nucleons. *The Astrophysical Journal Letters* , L149–L154doi:[10.1086/182040](https://doi.org/10.1086/182040).
- McHugh, M.L., 2008. Standard error: meaning and interpretation. *Biochemia Medica* 18, 7–13.
- Meng, C., Anderson, K., 1970. A layer of energetic electrons (> 40 kev) near the magnetopause. *Journal of Geophysical Research* 75, 1827–1836. doi:<https://doi.org/10.1029/JA075i010p01827>.
- Meng, C.I., Anderson, K., 1975. Characteristics of the magnetopause energetic electron layer. *Journal of Geophysical Research* 80, 4237–4243. doi:<https://doi.org/10.1029/JA080i031p04237>.
- Mewaldt, R., Cohen, C., Mason, G., Haggerty, D., Desai, M., 2007. Long-term fluences of solar energetic particles from h to fe. *The Composition of Matter* , 323–328.
- Mewaldt, R., Cohen, C., Mason, G., von Roseninge, T., Li, G., Smith, C.W., Vourlidis, A., 2015. An Investigation of the Causes of Solar-Cycle Variations in

BIBLIOGRAPHY

- SEP Fluences and Composition, in: 34th International Cosmic Ray Conference (ICRC2015), p. 30. doi:[10.22323/1.236.0030](https://doi.org/10.22323/1.236.0030).
- Mewaldt, R., Stone, E., Vogt, R., 1978. The radial diffusion coefficient of 1.3-23 mev protons in recurrent proton streams. *Geophysical Research Letters* 5, 965–968. doi:<https://doi.org/10.1029/GL005i011p00965>.
- Meziane, K., Hull, A., Hamza, A., Lin, R., 2002. On the bow shock θ bn dependence of upstream 70 kev to 2 mev ion fluxes. *Journal of Geophysical Research: Space Physics* 107, SSH-4. doi:[10.1029/2001JA005012](https://doi.org/10.1029/2001JA005012).
- Mingalev, O., Khabarova, O., Malova, K.V., Mingalev, I., Kislov, R., Mel'nik, M., Setsko, P., Zelenyi, L., Zank, G., 2019. Modeling of proton acceleration in a magnetic island inside the ripple of the heliospheric current sheet. *Solar System Research* 53, 30–55. doi:[10.1134/S0038094619010064](https://doi.org/10.1134/S0038094619010064).
- Mitchell, D., Roelof, E., 1983. Dependence of 50-kev upstream ion events at imp 7& 8 upon magnetic field bow shock geometry. *Journal of Geophysical Research: Space Physics* 88, 5623–5634. doi:[10.1029/JA088iA07p05623](https://doi.org/10.1029/JA088iA07p05623).
- Möbius, E., Kistler, L., Popecki, M., Crocker, K., Granoff, M., Turco, S., Anderson, A., Demain, P., Distelbrink, J., Dors, I., et al., 1998. The solar energetic particle ionic charge analyzer (sepica) and the data processing unit (s3dpu) for swics, swims and sepica. *The Advanced Composition Explorer Mission* , 449–495doi:<https://doi.org/10.1023/A:1005084014850>.
- Möbius, E., Morris, D., Popecki, M., Klecker, B., Kistler, L., Galvin, A., 2002. Charge states of energetic (≈ 0.5 mev/n) ions in corotating interaction regions at 1 au and implications on source populations. *Geophysical research letters* 29, 1–4. doi:<https://doi.org/10.1029/2001GL013410>.
- Müller-Mellin, R., Böttcher, S., Falenski, J., Rode, E., Duvet, L., Sanderson, T., Butler, B., Johlander, B., Smit, H., 2008a. The solar electron and proton telescope for the stereo mission. *The STEREO Mission* , 363–389doi:<https://doi.org/10.1007/s11214-007-9204-4>.
- Müller-Mellin, R., Gomez-Herrero, R., Böttcher, S., Klassen, A., Heber, B., Wimmer-Schweingruber, R., Duvet, L., Sanderson, T., 2008b. Upstream events and recurrent cir-accelerated particle events observed by stereo/sept. *Proc. of the 30th ICRC*, edited by: Caballero , 371–374.
- Ness, N.F., 1970. Magnetometers for space research. *Space Science Reviews* 11, 459–554. doi:[Magnetometersforspaceresearch](https://doi.org/10.1007/978-94-007-0000-0_11).
- Neugebauer, M., Giacalone, J., Chollet, E., Lario, D., 2006. Variability of low-energy ion flux profiles on interplanetary shock fronts. *Journal of Geophysical Research: Space Physics* 111. doi:<https://doi.org/10.1029/2006JA011832>.

- Nitta, N.V., Mulligan, T., 2017. Earth-affecting coronal mass ejections without obvious low coronal signatures. *Solar Physics* 292, 1–26. doi:<https://doi.org/10.1007/s11207-017-1147-7>.
- Nitta, N.V., Mulligan, T., Kilpua, E.K., Lynch, B.J., Mierla, M., O’Kane, J., Pagano, P., Palmerio, E., Pomoell, J., Richardson, I.G., et al., 2021. Understanding the origins of problem geomagnetic storms associated with “stealth” coronal mass ejections. *Space Science Reviews* 217, 82. doi:<https://doi.org/10.1007/s11214-021-00857-0>.
- O’Dell, S.L., Bautz, M.W., Blackwell Jr, W.C., Butt, Y.M., Cameron, R.A., Elsner, R.F., Gussenhoven, M.S., Kolodziejczak, J.J., Minow, J.I., Suggs, R.M., et al., 2000. Radiation environment of the chandra x-ray observatory, in: *X-ray and gamma-ray instrumentation for astronomy XI*, SPIE. pp. 99–110. doi:[10.1117/12.409104](https://doi.org/10.1117/12.409104).
- Ogilvie, K., Chornay, D., Fritzenreiter, R., Hunsaker, F., Keller, J., Lobell, J., Miller, G., Scudder, J., Sittler, E., Torbert, R., et al., 1995. Swe, a comprehensive plasma instrument for the wind spacecraft. *Space Science Reviews* 71, 55–77. doi:<https://doi.org/10.1007/BF00751326>.
- Oka, M., Phan, T.D., Krucker, S., Fujimoto, M., Shinohara, I., 2010. Electron acceleration by multi-island coalescence. *The Astrophysical Journal* 714, 915. doi:[10.1088/0004-637X/714/1/915](https://doi.org/10.1088/0004-637X/714/1/915).
- Owens, A., Baker, R., Cline, T., Gehrels, N., Jermakian, J., Nolan, T., Ramaty, R., Seifert, H., Shephard, D., Smith, G., et al., 1995. A high-resolution geospectrometer for gamma-ray burst astronomy. *Space Science Reviews* 71, 273–296. doi:<https://doi.org/10.1007/BF00751333>.
- O’Kane, J., Green, L., Long, D.M., Reid, H., 2019. Stealth coronal mass ejections from active regions. *The Astrophysical Journal* 882, 85. doi:[10.3847/1538-4357/ab371b](https://doi.org/10.3847/1538-4357/ab371b).
- O’Kane, J., Green, L.M., Davies, E.E., Möstl, C., Hinterreiter, J., von Forstner, J.L.F., Weiss, A.J., Long, D.M., Amerstorfer, T., 2021. Solar origins of a strong stealth cme detected by solar orbiter. *Astronomy & Astrophysics* 656, L6. doi:<https://doi.org/10.1051/0004-6361/202140622>.
- Papaioannou, A., Herbst, K., Ramm, T., Cliver, E.W., Lario, D., Veronig, A.M., 2023. Revisiting empirical solar energetic particle scaling relations-i. solar flares. *Astronomy & Astrophysics* 671, A66. doi:<https://doi.org/10.1051/0004-6361/202243407>.
- Parker, E., 1965. Dynamical theory of the solar wind. *Space Science Reviews* 4, 666–708. doi:[10.1007/BF00216273](https://doi.org/10.1007/BF00216273).
- Paschmann, G., Scopke, N., Asbridge, J., Bame, S., Gosling, J., 1980. Energization of solar wind ions by reflection from the earth’s bow shock. *Journal*

BIBLIOGRAPHY

- of Geophysical Research: Space Physics 85, 4689–4693. doi:<https://doi.org/10.1029/JA085iA09p04689>.
- Paschmann, G., Sckopke, N., Bame, S., Asbridge, J., Gosling, J., Russell, C., Greenstadt, E., 1979. Association of low-frequency waves with suprathermal ions in the upstream solar wind. *Geophysical Research Letters* 6, 209–212. doi:<https://doi.org/10.1029/GL006i003p00209>.
- Paulikas, G., Blake, J., 1969. Penetration of solar protons to synchronous altitude. *Journal of Geophysical Research* 74, 2161–2168. doi:[10.1029/JA074i009p02161](https://doi.org/10.1029/JA074i009p02161).
- Pesses, M.E., Jokipii, J.R., Eichler, D., 1981. Cosmic ray drift, shock wave acceleration, and the anomalous component of cosmic rays. *The Astrophysical Journal Letters* 246, L85–L88. doi:[10.1086/183559](https://doi.org/10.1086/183559).
- Pierrard, V., Lazar, M., 2010. Kappa distributions: Theory and applications in space plasmas. *Solar physics* 267, 153–174. doi:<https://doi.org/10.1007/s11207-010-9640-2>.
- Pierrard, V., Lemaire, J., 1996. Fitting the ae-8 energy spectra with two maxwellian functions. *Radiation measurements* 26, 333–337.
- Prasad, B.R., Banerjee, D., Singh, J., Nagabhushana, S., Kumar, A., Kamath, P., Kathiravan, S., Venkata, S., Rajkumar, N., Natarajan, V., et al., 2017. Visible emission line coronagraph on aditya-l1. *Current Science* , 613–615doi:<https://www.jstor.org/stable/26293898>.
- Rahmanifard, F., de Wet, W., Schwadron, N., Owens, M.J., Jordan, A., Wilson, J., Joyce, C., Spence, H., Smith, C., Townsend, L., 2020. Galactic cosmic radiation in the interplanetary space through a modern secular minimum. *Space Weather* 18, e2019SW002428. doi:<https://doi.org/10.1029/2019SW002428>.
- Ramachandran, K.M., Tsokos, C.P., 2021. Chapter 5 - statistical estimation, in: Ramachandran, K.M., Tsokos, C.P. (Eds.), *Mathematical Statistics with Applications in R (Third Edition)*. third edition ed.. Academic Press, pp. 179–251. URL: <https://www.sciencedirect.com/science/article/pii/B9780128178157000051>, doi:<https://doi.org/10.1016/B978-0-12-817815-7.00005-1>.
- Reames, D.V., 1999a. Particle acceleration at the sun and in the heliosphere. *Space Science Reviews* 90, 413–491. doi:<https://doi.org/10.1023/A:1005105831781>.
- Reames, D.V., 1999b. Quiet-time spectra and abundances of energetic particles during the 1996 solar minimum. *The Astrophysical Journal* 518, 473. doi:[10.1086/307255](https://doi.org/10.1086/307255).
- Reames, D.V., 2013. The two sources of solar energetic particles. *Space Science Reviews* 175, 53–92.

- Reames, D.V., 2018a. Abundances, ionization states, temperatures, and fip in solar energetic particles. *Space Science Reviews* 214, 61. doi:<https://doi.org/10.1007/s11214-018-0495-4>.
- Reames, D.V., 2018b. The “fip effect” and the origins of solar energetic particles and of the solar wind. *Solar Physics* 293, 1–9. doi:<https://doi.org/10.1007/s11207-018-1267-8>.
- Reames, D.V., 2020. Four distinct pathways to the element abundances in solar energetic particles. *Space Science Reviews* 216, 20. doi:<https://doi.org/10.1007/s11214-020-0643-5>.
- Richard, R., El-Alaoui, M., Ashour-Abdalla, M., Walker, R., 2002. Interplanetary magnetic field control of the entry of solar energetic particles into the magnetosphere. *Journal of Geophysical Research: Space Physics* 107, SSH–7. doi:[doi:10.1029/2001JA000099](https://doi.org/10.1029/2001JA000099).
- Richardson, I., 1985. Anisotropy of > 35 keV ions in corotating particle events at 1 au. *Planetary and space science* 33, 147–157. doi:[https://doi.org/10.1016/0032-0633\(85\)90125-4](https://doi.org/10.1016/0032-0633(85)90125-4).
- Richardson, I., Barbier, L., Reames, D., Von Roseninge, T., 1993. Corotating mev/amu ion enhancements at ≥ 1 au from 1978 to 1986. *Journal of Geophysical Research: Space Physics* 98, 13–32. doi:<https://doi.org/10.1029/92JA01837>.
- Richardson, I.G., 2018. Solar wind stream interaction regions throughout the heliosphere. *Living reviews in solar physics* 15, 1–95. doi:<https://doi.org/10.1007/s41116-017-0011-z>.
- Richter, A., Keppler, E., Axford, W., Denskat, K., 1979. Dynamics of low-energy electrons (≥ 17 keV) and ions (≥ 80 keV) in the vicinity of the low-latitude, duskside magnetopause: Helios 1 and 2 observations. *Journal of Geophysical Research: Space Physics* 84, 1453–1463.
- Sanderson, T., Marsden, R., Wenzel, K.P., Balogh, A., Forsyth, R., Goldstein, B., 1994. Ulysses high-latitude observations of ions accelerated by co-rotating interaction regions. *Geophysical research letters* 21, 1113–1116. doi:[doi:10.1029/94GL01062](https://doi.org/10.1029/94GL01062).
- Sankarasubramanian, K., Ramadevi, M., Bug, M., Umapathy, C., Seetha, S., Sreekumar, P., et al., 2011. Solexs-a low-energy x-ray spectrometer for solar coronal studies. arXiv preprint arXiv:1111.5820 .
- Sankarasubramanian, K., Sudhakar, M., Nandi, A., Ramadevi, M., Adoni, A.A., Kushwaha, A., Agarwal, A., Dey, A., Joshi, B., Singh, B., et al., 2017. X-ray spectrometers on-board aditya-l1 for solar flare studies .

BIBLIOGRAPHY

- Sarris, E., Krimigis, S., Armstrong, T., 1976. Observations of magnetospheric bursts of high-energy protons and electrons at $\sim 35 r_e$ with imp 7. *Journal of Geophysical Research* 81, 2341–2355. doi:<https://doi.org/10.1029/JA081i013p02341>.
- Sarris, E., Krimigis, S., Bostrom, C., Armstrong, T., 1978. Simultaneous multi-spacecraft observations of energetic proton bursts inside and outside the magnetosphere. *Journal of Geophysical Research: Space Physics* 83, 4289–4305. doi:<https://doi.org/10.1029/JA083iA09p04289>.
- Scholer, M., Gloeckler, G., Ipavich, F., Hovestadt, D., Klecker, B., 1979. Pitch angle distributions of energetic protons near the earth's bow shock. *Geophysical Research Letters* 6, 707–710. doi:<https://doi.org/10.1029/GL006i009p00707>.
- Scholer, M., Hovestadt, D., Ipavich, F., Gloeckler, G., 1981. Simultaneous observations of energetic protons close to the bow shock and far upstream. *Journal of Geophysics Zeitschrift Geophysik* 49, 186–191.
- Schwadron, N., Fisk, L., Gloeckler, G., 1996. Statistical acceleration of interstellar pick-up ions in co-rotating interaction regions. *Geophysical research letters* 23, 2871–2874. doi:<https://doi.org/10.1029/96GL02833>.
- Schwadron, N.A., Dayeh, M., Desai, M., Fahr, H., Jokipii, J., Lee, M.A., 2010. Superposition of stochastic processes and the resulting particle distributions. *The Astrophysical Journal* 713, 1386. doi:[10.1088/0004-637X/713/2/1386](https://doi.org/10.1088/0004-637X/713/2/1386).
- Schwartz, S.J., Burgess, D., 1984. On the theoretical/observational comparison of field-aligned ion beams in the earth's foreshock. *Journal of Geophysical Research: Space Physics* 89, 2381–2384. doi:<https://doi.org/10.1029/JA089iA04p02381>.
- Schwartz, S.J., Owen, C.J., Burgess, D., 2004. *Astrophysical plasmas*. Astronomy Unit, Queen Mary, University of London , 11–45.
- Seetha, S., Megala, S., 2017. Aditya-11 mission. *Current Science* , 610–612.
- Seki, Y., Nishino, M., Fujimoto, M., Miyashita, Y., Keika, K., Hasegawa, H., Okabe, K., Kasaba, Y., Terasawa, T., Yamamoto, T., et al., 2009. Observations of loss cone-shaped back streaming energetic protons upstream of the earth's bow shock. *Journal of Geophysical Research: Space Physics* 114.
- Sheldon, R., Chen, J., Fritz, T., 2003. Comment on “origins of energetic ions in the cusp” by kj trattner et al. *Journal of Geophysical Research: Space Physics* 108. doi:<https://doi.org/10.1029/2002JA009575>.
- Shue, J.H., Chao, J., Fu, H., Russell, C., Song, P., Khurana, K., Singer, H., 1997. A new functional form to study the solar wind control of the magnetopause size and shape. *Journal of Geophysical Research: Space Physics* 102, 9497–9511. doi:<https://doi.org/10.1029/97JA00196>.

- Sibeck, D., McEntire, R., Lui, A., Lopez, R., Krimigis, S., Decker, R., Zanetti, L., Potemra, T., 1987. Energetic magnetospheric ions at the dayside magnetopause: Leakage or merging? *Journal of Geophysical Research: Space Physics* 92, 12097–12114. doi:<https://doi.org/10.1029/JA092iA11p12097>.
- Smith, C.W., L'Heureux, J., Ness, N.F., Acuna, M.H., Burlaga, L.F., Scheifele, J., 1998. The ace magnetic fields experiment. The advanced composition explorer mission , 613–632doi:<https://doi.org/10.1023/A:1005092216668>.
- Statler, R.L., Curtin, D.J., 1971. Radiation damage in silicon solar cells from low-energy protons. *IEEE Transactions on Electron Devices* 18, 412–417. doi:[10.1109/TNS.2002.805359](https://doi.org/10.1109/TNS.2002.805359).
- Stone, E.C., Cohen, C., Cook, W., Cummings, A., Gauld, B., Kecman, B., Leske, R., Mewaldt, R., Thayer, M., Dougherty, B., et al., 1998a. The cosmic-ray isotope spectrometer for the advanced composition explorer. The Advanced Composition Explorer Mission , 285–356doi:<https://doi.org/10.1023/A:1005075813033>.
- Stone, E.C., Cohen, C., Cook, W., Cummings, A., Gauld, B., Kecman, B., Leske, R., Mewaldt, R., Thayer, M., Dougherty, B., et al., 1998b. The solar isotope spectrometer for the advanced composition explorer. The Advanced Composition Explorer Mission , 357–408doi:<https://doi.org/10.1023/A:1005027929871>.
- Stone, E.C., Frandsen, A., Mewaldt, R., Christian, E., Margolies, D., Ormes, J., Snow, F., 1998c. The advanced composition explorer. *Space Science Reviews* 86, 1–22. doi:<https://doi.org/10.1023/A:1005082526237>.
- Susino, R., Bemporad, A., Krucker, S., 2013. Plasma heating in a post eruption current sheet: a case study based on ultraviolet, soft, and hard x-ray data. *The Astrophysical Journal* 777, 93.
- Tan, L., Mason, G., Klecker, B., Hovestadt, D., 1989. Seed population for about 1 mev per nucleon heavy ions accelerated by interplanetary shocks. *Astrophysical Journal, Part 1 (ISSN 0004-637X)*, vol. 345, Oct. 1, 1989, p. 572-583. 345, 572–583. doi:[10.1086/167931](https://doi.org/10.1086/167931).
- Tanur, J.M., 2011. Margin of error, in: *International Encyclopedia of Statistical Science*. Springer, pp. 765–765.
- Tibshirani, R.J., Efron, B., 1993. An introduction to the bootstrap. *Monographs on statistics and applied probability* 57, 1–436. doi:<https://doi.org/10.1201/9780429246593>.
- Torsti, J., Kocharov, L., Laivola, J., Lehtinen, N., Kaiser, M., Reiner, M., 2002. Solar particle event with exceptionally high ^3He enhancement in the energy range up to 50 mev nucleon $^{-1}$. *The Astrophysical Journal* 573, L59. doi:[10.1086/341936](https://doi.org/10.1086/341936).

BIBLIOGRAPHY

- Trattner, K., Fuselier, S., Peterson, W., Chang, S.W., Friedel, R., Aellig, M., 2003. Reply to comment on “origins of energetic ions in the cusp” by r. sheldon, j. chen, and ta fritz. *Journal of Geophysical Research: Space Physics* 108. doi:<https://doi.org/10.1029/2002JA009781>.
- Trattner, K., Möbius, E., Scholer, M., Klecker, B., Hilchenbach, M., Lühr, H., 1994. Statistical analysis of diffuse ion events upstream of the earth’s bow shock. *Journal of Geophysical Research: Space Physics* 99, 13389–13400. doi:[10.1029/94JA00576](https://doi.org/10.1029/94JA00576).
- Tripathi, D., Chakrabarty, D., Nandi, A., Prasad, B.R., Ramaprakash, A., Shaji, N., Sankarasubramanian, K., Thampi, R.S., Yadav, V., 2022. The aditya-l1 mission of isro. *Proceedings of the International Astronomical Union* 18, 17–27. doi:[10.1017/S1743921323001230](https://doi.org/10.1017/S1743921323001230).
- Tsurutani, B., Lin, R., 1985. Acceleration of > 47 keV ions and > 2 keV electrons by interplanetary shocks at 1 au. *Journal of Geophysical Research: Space Physics* 90, 1–11. doi:<https://doi.org/10.1029/JA090iA01p00001>.
- Tverskoi, B., Derchieva, L., Ivanova, T., Koval’skaya, I.Y., Panasyuk, M., Sosnovets, E., Tverskaya, L., Tel’tsov, M., Kocharova, G., Dergacheva, V., 1973. Solar cosmic ray penetration into the earth’s magnetosphere. V Leningrad International Seminar .
- Van Hollebeke, M., McDonald, F., Trainor, J.v., Von Roseninge, T., 1978. The radial variation of corotating energetic particle streams in the inner and outer solar system. *Journal of Geophysical Research: Space Physics* 83, 4723–4731. doi:<https://doi.org/10.1029/JA083iA10p04723>.
- Vanhollebeke, M., McDonald, F., Trainor, J., Vonroseninge, T., 1979. Corotating energetic particle and fast plasma streams in the inner and outer solar system: radial dependence and energy spectra, in: *Solar Wind 4 Conf. Lecture Notes in Physics*.
- Vasyliunas, V.M., 1968. A survey of low-energy electrons in the evening sector of the magnetosphere with ogo 1 and ogo 3. *Journal of Geophysical Research* 73, 2839–2884. doi:<https://doi.org/10.1029/JA073i009p02839>.
- Verscharen, D., Klein, K.G., Maruca, B.A., 2019. The multi-scale nature of the solar wind. *Living Reviews in Solar Physics* 16, 5.
- Vocks, C., Mann, G., 2003. Generation of suprathermal electrons by resonant wave-particle interaction in the solar corona and wind. *The Astrophysical Journal* 593, 1134. doi:[10.1086/376682](https://doi.org/10.1086/376682).
- Von Roseninge, T., Barbier, L., Karsch, J., Liberman, R., Madden, M., Nolan, T., Reames, D., Ryan, L., Singh, S., Trexel, H., et al., 1995. The energetic particles: acceleration, composition, and transport (epact) investigation on the wind spacecraft. *Space Science Reviews* 71, 155–206. doi:<https://doi.org/10.1007/BF00751329>.

- Wang, Y., Chen, C., Gui, B., Shen, C., Ye, P., Wang, S., 2011. Statistical study of coronal mass ejection source locations: Understanding cmes viewed in coronagraphs. *Journal of Geophysical Research: Space Physics* 116. doi:<https://doi.org/10.1029/2010JA016101>.
- West Jr, H.I., Buck, R.M., 1976. Observations of > 100 -keV protons in the earth's magnetosheath. *Journal of Geophysical Research* 81, 569–584. doi:<https://doi.org/10.1029/JA081i004p00569>.
- Wiedenbeck, M., Christian, E., Cohen, C., Cummings, A., Leske, R., Mewaldt, R., Slocum, P., Stone, E., von Rosenvinge, T., 2000. Enhanced abundances of ^3He in large solar energetic particle events, in: *AIP Conference Proceedings*, American Institute of Physics. pp. 107–110. doi:<https://doi.org/10.1063/1.1324290>.
- Wilcox, J.M., Ness, N.F., 1965. Quasi-stationary corotating structure in the interplanetary medium. *Journal of Geophysical Research* 70, 5793–5805. doi:<https://doi.org/10.1029/JZ070i023p05793>.
- Wüest, M., Evans, D.S., von Steiger, R., 2007. Calibration of particle instruments in space physics. International Space Science Institute.
- Wülser, J.P., Lemen, J.R., Tarbell, T.D., Wolfson, C.J., Cannon, J.C., Carpenter, B.A., Duncan, D.W., Gradwohl, G.S., Meyer, S.B., Moore, A.S., et al., 2004. Euvi: the stereo-secchi extreme ultraviolet imager, in: *Telescopes and instrumentation for solar astrophysics*, SPIE. pp. 111–122. doi:<https://doi.org/10.1117/12.506877>.
- Xiao, F., Shen, C., Wang, Y., Zheng, H., Wang, S., 2008. Energetic electron distributions fitted with a relativistic kappa-type function at geosynchronous orbit. *Journal of Geophysical Research: Space Physics* 113. doi:[10.1029/2007JA012903](https://doi.org/10.1029/2007JA012903), 2008.
- Yadav, V.K., Srivastava, N., Ghosh, S., Srikar, P., Subhalakshmi, K., 2018. Science objectives of the magnetic field experiment onboard aditya-l1 spacecraft. *Advances in Space Research* 61, 749–758. doi:<https://doi.org/10.1016/j.asr.2017.11.008>.
- Zank, G.I., Le Roux, J., Webb, G., Dosch, A., Khabarova, O., 2014. Particle acceleration via reconnection processes in the supersonic solar wind. *The Astrophysical Journal* 797, 28. doi:[10.1088/0004-637X/797/1/28](https://doi.org/10.1088/0004-637X/797/1/28).
- Zhang, J., Richardson, I., Webb, D., Gopalswamy, N., Huttunen, E., Kasper, J., Nitta, N., Poomvises, W., Thompson, B., Wu, C.C., et al., 2007. Solar and interplanetary sources of major geomagnetic storms ($\text{dst} \leq -100$ nt) during 1996–2005. *Journal of Geophysical Research: Space Physics* 112. doi:<https://doi.org/10.1029/2007JA012321>.
- Zhang, M., Lee, M., 2013. Stochastic acceleration of energetic particles in the heliosphere. *Space Science Reviews* 176, 133–146.

BIBLIOGRAPHY

- Zhao, L., Zhang, M., Rassoul, H.K., 2016. Double power laws in the event-integrated solar energetic particle spectrum. *The Astrophysical Journal* 821, 62. doi:[10.3847/0004-637X/821/1/62](https://doi.org/10.3847/0004-637X/821/1/62).
- Zhao, L., Zhang, M., Rassoul, H.K., 2017. The effects of interplanetary transport in the event-intergrated solar energetic particle spectra. *The Astrophysical Journal* 836, 31. doi:[10.3847/1538-4357/836/1/31](https://doi.org/10.3847/1538-4357/836/1/31).
- Zwickl, R., Doggett, K., Sahm, S., Barrett, W., Grubb, R., Detman, T., Raben, V., Smith, C., Riley, P., Gold, R., et al., 1998. The noaa real-time solar-wind (rtsw) system using ace data. *The advanced composition explorer mission* , 633–648doi:<https://doi.org/10.1023/A:1005044300738>.
- Zwickl, R., Roelof, E., 1981. Interplanetary propagation of < 1 -mev protons in nonimpulsive energetic particle events. *Journal of Geophysical Research: Space Physics* 86, 5449–5471. doi:<https://doi.org/10.1029/JA086iA07p05449>.

List of Publications

Publications included in the thesis

1. **Dalal, B.**, Chakrabarty, D., Srivastava, N., “Differential behaviors of suprathermal ^4He and Fe populations in the interplanetary medium during solar cycle 24”, 2022, The Astrophysical Journal, 938, 26 (doi: <https://doi.org/10.3847/1538-4357/ac88d8>)
2. **Dalal, B.**, Chakrabarty, D., Srivastava, N., Sarkar, A., “Suprathermal population associated with stream interaction regions observed by STEREO-A: New insights”, 2024, The Astrophysical Journal, 960, 16 (doi: <https://doi.org/10.3847/1538-4357/ad08c6>)
3. **Dalal, B.**, Chakrabarty, D., Cohen, C. M. S., and Srivastava, N., “Investigation on upstream ion events from L1 point observation: New Insights" (to be communicated shortly)
4. Evidence of contrasting impact of two CMEs on the terrestrial magnetosphere measured by STEPS/ASPEX during the earth-bound orbits of Aditya-L1: First observations (to be communicated shortly)

List of Publications

Presentations in national or international conferences or workshops or schools

Contributory

- **Dalal, B.**, Chakrabarty, D., Srivastava, N., Sarkar, A., “Suprathermal particles associated with stream interaction regions: STEREO-A observations”, presented in National Space Science Symposium (NSSS-2024) held at Goa University, Goa, India during February 26 - March 1, 2024 [**Mode: In person oral presentation**]
- **Dalal, B.**, Chakrabarty, D., Srivastava, N., Sarkar, A., “Study of origin and acceleration of suprathermal and energetic particles using Aditya-L1 data”, presented in the 42nd Meeting of the Astronomical Society of India (ASI-2024) held at Indian Institute of Science, Bengaluru, India during January 31 - February 4, 2024 [**Mode: In person poster presentation**]
- **Dalal, B.**, Chakrabarty, D., Srivastava, N., Sarkar, A., “Properties of suprathermal ⁴He, O, and Fe population in stream interaction regions observed by STEREO-A - Insights”, presented in AGU Fall Meeting - 2023 [**Mode: Online oral presentation**]
- **Dalal, B.**, “Space weather studies using Aditya-L1 and DISHA missions: An energetic particle perspective”, presented in the 2nd Indian Space Weather Conference (ISWC-2) held at Physical Research Laboratory, Ahmedabad, India during October 19 - 20, 2023 [**Mode: In person oral presentation**]
- **Dalal, B.**, Chakrabarty, D., and Srivastava, N., “Behaviors of suprathermal particles in quiet times and during stream interaction regions”, presented in Heliophysics Summer School (HSS-2023) held in Boulder, Colorado, USA during August 7 - 11, 2023 [**Mode: In person poster presentation**]
- **Dalal, B.**, Chakrabarty, D., and Srivastava, N., “Suprathermal particles associated with stream interaction regions: connection with solar energetic

particles”, presented in USO-PRL Solar Physics Workshop (USPW-2023) held at Udaipur Solar Observatory, Udaipur, India during April 3 - 5, 2023

[**Mode: In person poster presentation**]

- **Dalal, B.**, Chakrabarty, D., Srivastava, N., “Variations in the suprathermal populations in the solar wind during solar cycles 23 and 24”, presented in 15th quadrennial Solar-Terrestrial Physics Symposium (STP-15) held during February 21 - 25, 2022 [**Mode: Online oral presentation**]
- **Dalal, B.**, Chakrabarty, D., Srivastava, N., “Comparison of suprathermal particles between the last two solar cycles: Insights”, presented in National Space Science Symposium, 2022 (NSSS-2022) held during January 31 - February 04, 2022 [**Mode: Online poster presentation**]
- **Dalal, B.**, Chakrabarty, D., Srivastava, N., “Investigation on solar cycle dependence of interplanetary suprathermal populations”, presented in the 1st Indian Space Weather Conference, 2022 (ISWC-1) held during January 11 - 12, 2022 [**Mode: Online recorded talk**]

Invited

- “Investigations on energetic particles in the solar wind using ASPEX measurements” in Aditya-L1 Science Support Cell Workshop (ALSSC-1) held in Aryabhata Research Institute of Observational Sciences (ARIES), Nainital, India during June 27 - July 06, 2022 [**Mode: In person oral presentation**]

Publications attached with the thesis

1. **Dalal, B.**, Chakrabarty, D., Srivastava, N., “Differential behaviors of suprathermal ^4He and Fe populations in the interplanetary medium during solar cycle 24”, 2022, The Astrophysical Journal, 938, 26 (doi: <https://doi.org/10.3847/1538-4357/ac88d8>)
2. **Dalal, B.**, Chakrabarty, D., Srivastava, N., Sarkar, A., “Suprathermal population associated with stream interaction regions observed by STEREO-A: New insights”, 2024, The Astrophysical Journal, 960, 16 (doi: <https://doi.org/10.3847/1538-4357/ad08c6>)



Differential Behaviors of Suprathermal ^4He and Fe Populations in the Interplanetary Medium during Solar Cycle 24

Bijoy Dalal^{1,2}, D. Chakrabarty¹, and N. Srivastava³¹ Physical Research Laboratory, Ahmedabad—380009, India; bijoydalal.at@gmail.com² Indian Institute of Technology Gandhinagar, Gandhinagar—382055, India³ Udaipur Solar Observatory, Physical Research Laboratory, Udaipur—313001, India

Received 2021 December 24; revised 2022 July 26; accepted 2022 August 9; published 2022 October 11

Abstract

Investigations on the solar cycle variation of the properties of suprathermal populations (H and other heavy ions like ^4He , ^3He , C, O, and Fe) in the solar wind are sparse and hence poorly understood. In the present investigation, solar cycle variations of “quiet” time suprathermal elements are investigated using $< \sim 1 \text{ MeV n}^{-1}$ particle flux data obtained from the Ultra-Low Energy Isotope Spectrometer on board the Advanced Composition Explorer satellite during solar cycles 23 and 24. The analysis reveals that helium (^4He) shows zero or positive lags with respect to sunspot numbers in solar cycle 23 while it shows zero or negative lag in solar cycle 24. On the contrary, although iron (Fe) shows a zero or positive lag in cycle 23 similar to ^4He , it shows only a zero lag in cycle 24 and no negative lag is seen. Further, significant differences in the spectral indices are seen between ^4He and Fe in cycle 24 compared to cycle 23. These results suggest that generation mechanisms responsible for suprathermal ^4He and Fe underwent changes in cycle 24 and these mechanisms are probably dependent on the first ionization potential and mass-to-charge ratio. This proposition gets credence from the fact that changes in the lags and spectral slopes for C and O are not significantly different in cycles 23 and 24.

Unified Astronomy Thesaurus concepts: [Solar energetic particles \(1491\)](#); [Corotating streams \(314\)](#); [Solar wind \(1534\)](#); [Solar coronal mass ejections \(310\)](#)

1. Introduction

Suprathermal particles with energies from $\sim 10 \text{ KeV}$ per nucleon (keV n^{-1}) to $\sim 1 \text{ MeV}$ per nucleon (MeV n^{-1}) are thought to act as seed populations for further acceleration by interplanetary (IP) shocks associated with solar eruptive events like coronal mass ejections (CMEs) (Gosling et al. 1981; Desai et al. 2003, 2004 etc.) and corotating interaction regions (CIRs) (e.g., Fisk & Lee 1980; Chotoo et al. 2000; Allen et al. 2019). The two most widely known acceleration mechanisms, namely first-order Fermi acceleration (or diffusive shock acceleration) (Krymskii 1977; Bell 1978 etc.) and the second-order Fermi acceleration (Fermi 1949), necessitate the initial presence of suprathermal particles in the acceleration framework. Energetic protons as well as heavy ions from ^4He to Fe and beyond constitute the suprathermal ion pool in the IP medium. Compositional abundance studies reveal that possible sources of the suprathermal ion pool include solar wind ions (Desai et al. 2003), particles associated with previously occurred transient events (Fisk & Lee 1980; Giacalone et al. 2002 etc.), and interstellar pick-up ions (Allen et al. 2019). In general, a dominant contribution from pick-up ions in the suprathermal populations is observed beyond 1 au (Fisk 1976). Suprathermal particles exhibit a power-law distribution, also known as a “quiet” time tail, when the velocity distribution function (differential directional flux) is plotted against velocity (energy). Often, a spectral index of -5 (-1.5) (Fisk & Gloeckler 2006, 2007) has been reported in the past regardless of the species considered. In this work, the spectral index of the differential flux versus energy convention (-1.5) is chosen.

There have been a few reports in the past (e.g., Gloeckler 2003; Mason et al. 2012; Dayeh et al. 2017) that showed that this spectral index deviates substantially from the -1.5 value. The reasons for significant variations in the spectral index is a topic that is still poorly understood. Further, it is also not abundantly clear why different elements in the suprathermal ion pool should follow a similar spectral index (Fisk & Gloeckler 2006; Mason et al. 2008). These issues are important and need critical attention as they might throw light on the generation of the suprathermal ion population in the IP medium. Enhancements of suprathermal protons and other heavy ions in CIRs within and beyond 1 au have been reported by many authors (Mason et al. 1997; Chotoo et al. 2000; Mason et al. 2008, 2012; Bučik et al. 2009; Ebert et al. 2012; Filwett et al. 2017; Yu et al. 2018; Allen et al. 2019, 2020; etc.). As a possible source of energization of suprathermal particles associated with CIRs, many have suggested diffusive shock acceleration by forward and reverse shocks bounding the compression region of a CIR (e.g., Palmer & Gosling 1978; Fisk & Lee 1980). Fisk & Lee (1980) proposed a model in which particles accelerated by shock fronts can be decelerated to lower energies by the effect of adiabatic expansion and associated cooling in the IP medium. However, the spectral rollover predicted by this model below 0.5 MeV n^{-1} could not be observed (Mason et al. 1997). The gradual compression region bounded by the shock pair associated with a CIR is also considered as an effective source of acceleration under suitable conditions (Mason 2000; Giacalone et al. 2002), although the shock pairs might not be adequately formed within 1 au on many occasions. Nevertheless, the presence of suprathermal populations in the IP medium in the absence of such compression regions and shock structures makes it difficult to comprehend the acceleration processes involved. Further, there are also evidences that “quiet” time suprathermal particles depend on solar activity. By

studying the relative abundances of “quiet” time suprathermal ions at 1 au, Kecskemety et al. (2011) found out that during solar cycle minima, the suprathermal Fe/O ratio resembles the corresponding ratio in the solar wind. These results were supported later on by Dayeh et al. (2017), in which the solar cycle dependence of suprathermal C/O, Fe/O, and $^3\text{He}/^4\text{He}$ with very strong correlations with the yearly averaged sunspot number (SSN) were reported. They argued that suprathermal particles are transported from remote places during “quiet” times and are accelerated locally. Regardless of the acceleration process involved, it is expected that during the course of transport of suprathermal particles through the IP medium, the particles may show a systematic time delay with solar activity proxies (for example, SSN) and this may provide important clues for understanding the source of these particle populations. Although indicated in a few earlier works (e.g., Mason et al. 2012; Allen et al. 2019) detailed investigations on these time delays are sparse. Further, comparison of these time delays and spectral indices for various elements for multiple solar cycles may lead to new insights related to the role of solar/IP processes for the generation of these particles. Keeping these issues in mind, the suprathermal particle flux data from the Ultra-Low Energy Isotope Spectrometer (ULEIS) (Mason et al. 1998) on board the Advanced Composition Explorer (ACE) (Stone et al. 1998) for solar cycles 23 and 24 (henceforth, SC23 and SC24, respectively) have been extensively analysed and the results are presented in the present work. The results reveal important differences between SC23 and SC24 as far as the above aspects are concerned.

2. Data Set

ACE is a spin-stabilized spacecraft revolving around Lagrangian point L1 of the Sun–Earth system in a halo orbit. In this work, one-hour-integrated differential directional flux (level 2) data corresponding to different energy channels for H, ^4He , ^3He , O, C, and Fe from 1998 March 1 to 2020 August 31 obtained by ULEIS on board ACE are used. ULEIS is a time of flight mass spectrometer, which measures the time of flight (τ) and deposited energy (E) of isotopes with $Z = 2\text{--}28$. Using the measured τ and corrected energy (see Mason et al. 1998 for details), the mass (M) of the isotope is determined. The uncertainties in the energy measurements of ULEIS may affect mass separation near the low-energy threshold in the presence of significant noise (see Mason et al. 1998 and references cited therein). This problem is particularly relevant for ^3He and ^4He . Nevertheless, we have avoided using low-energy ($<100\text{ keV n}^{-1}$) channels for all the elements in our investigation. The data set spans almost 22 yr covering SC23 and SC24 and is available at <https://cdaweb.gsfc.nasa.gov/index.html>. A list of CIR events, identified based on the measurements at the L1 point and reported by Allen et al. (2019), is also used to remove the concomitant enhancements in the suprathermal flux associated with CIR events. In addition, as stated in the next section, we also remove any other transient event that causes enhancements in the suprathermal flux. We have termed these events as “non-CIR” transient events. This step leads to a time series corresponding to “quiet” time. Here “quiet” is put inside the inverted commas as we will argue later that in either case—whether it is exhaustive removal of the transient events or removal of transient events based on a cut off flux level—the propagation of the suprathermal flux from the transient events (CIRs, interplanetary coronal mass

ejections (ICMEs)) into the “quiet” time suprathermal ion pool cannot be completely eliminated in presence of a significant lag with the SSN. We will come back to this point later on in more detail. The daily averaged SSN data are available at <http://www.sidc.be/silso/datafiles>.

3. Selection of Quiet Periods, Sensitivity Analyses, and Validation

As indicated in the previous section, the data set used in the present work pertains to periods devoid of transient events (e.g., CIR and any other non-CIR events) that cause enhancements in the suprathermal flux. From the entire data set spanning over 22 yr, it is noted that transient CIR or non-CIR events take flux levels much higher than the background flux level encountered at other times. Therefore, these transient flux variations are apparently easy to remove by choosing a threshold flux level (e.g., Kecskemety et al. 2011). However, in the present work, we do not initially choose any cut off flux level as a reference level to remove transient events. Rather, we remove the flux variations associated with these transient variations in totality (from base flux level to peak flux level) so that the propagation of the peak flux into the “quiet” time flux is minimized significantly. It is possible that some minor transient injections will remain in the time series even after doing this. Therefore, we also perform detailed sensitivity analyses and cross check critically to show that the results obtained through present analysis procedure (no cut off level, removal of transient events) remains nearly unchanged with those obtained with four different cut off flux levels (much lower than the peak levels of the transient injection events from base to peak levels). Note, at least two of these cut off levels are below the lowest flux level encountered during solar minima (between SC23 and SC24) in the original time series. We also subject these to sensitivity analyses for different averaging windows (in days). These detailed sensitivity analyses with different cut off levels and averaging windows are provided as supplementary Figures A1–A12. It is found that the correlation coefficients and the lags, thus derived, between the suprathermal fluxes for each element (at different energy channels) and the SSN remain nearly invariant for different choices of cut off levels and averaging windows. Therefore, we will not discuss this point subsequently in this paper.

We now come back to the methodology adopted in this work. This aspect is illustrated in Figure 1. Figures 1(a) and 1(b) show the variations in the proton fluxes for the original and “quiet” (after removal of the transient events from base to peak) data set, respectively, from 2007 June 2 to August 3. Different colors correspond to different energy channels. The mean of the upper and lower limits of each energy channel is taken to represent (legend) the corresponding energy channel. During the representative interval shown in Figure 1, there was one CIR event (according to Allen et al. 2019), the start and end times of which are marked in red and blue vertical dashed lines, respectively. The other transient events are termed as “non-CIR transient events” and no attempt is made here to characterize those events. Figures 1(c) and 1(d) respectively show the original and corresponding “quiet” time fluxes of ^4He at various energy channels during the same time interval as that of H. It is to be noted that durations of transient events removed from the time series of ^4He may be different from those removed from the H time series. This is because of the fact that the enhancement and depletion of different elements at the

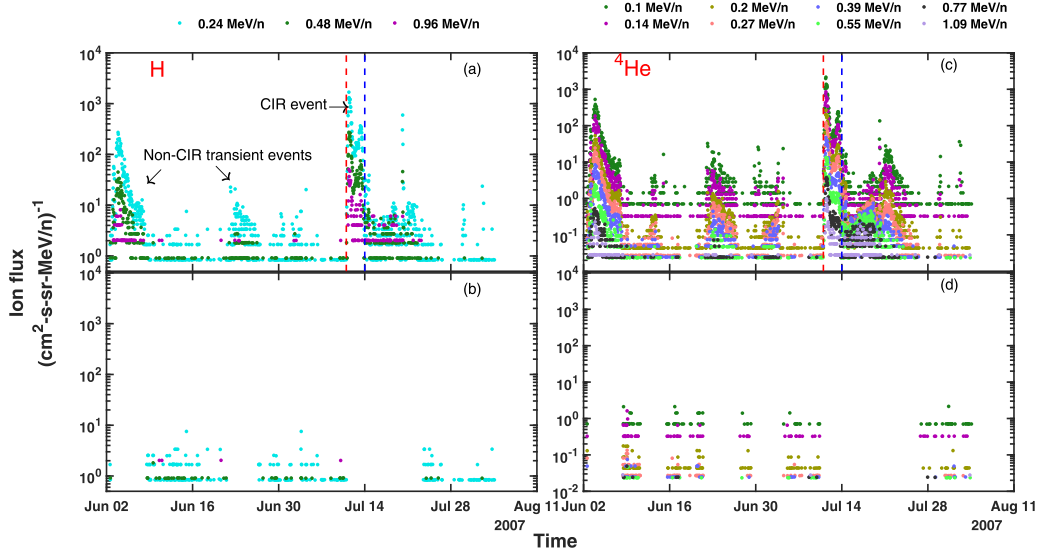


Figure 1. The left column shows the proton flux data (a) before and (b) after the removal of the transient events. The dashed vertical lines indicate the start (red) and end (blue) times of the CIR event during this period as observed by ULEIS/ACE. The non-CIR transient events are indicated by arrows in (a). Different energy channels are represented by the mean of the lower and upper energy limits and are shown by colored dots. The right column shows the ^4He flux variation before (c) and after (d) the removal of transient events similar to what has been done for the proton channels.

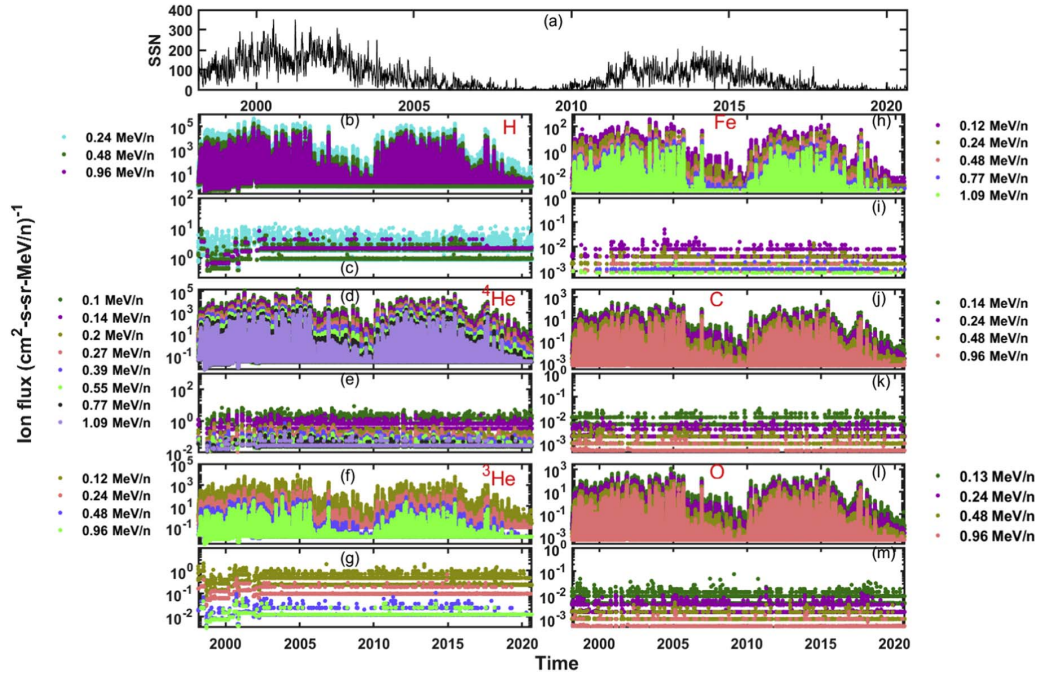


Figure 2. Original vis-à-vis modified (after removal of the transient events) variations of the fluxes of different elements for the entire period (1998–2020) along with the SSN data used in this paper (panel (a)). Subplots (b), (d), (f), (h), (j), and (l) show the original flux variations of H, ^4He , ^3He , Fe, C, and O, respectively. The modified (“quiet”) fluxes of the elements in the similar order are plotted in subplots (c), (e), (g), (i), (k), and (m). Legends for the different energy channels of an element are marked by colored dots and are appropriately placed at the left and right of the plots.

measurement location are not simultaneous in many cases (Reames 2018). Considering this important aspect, we have removed the transient events for each element manually. The complete exclusion of the transient events for the whole duration of the data set for each element under consideration is shown in Figure 2. The daily averaged SSN data are shown in

Figure 2(a). Please note that detailed correlation analyses of this SSN time series are performed with the elemental flux time series using different averaging windows. These aspects are discussed in Figures 3–5 and in Figures A1–A12. In Figure 2, subplots (b), (d), (f), (h), (j), and (l) show the temporal variations of the suprathermal H, ^4He , ^3He , Fe, C, and O fluxes,

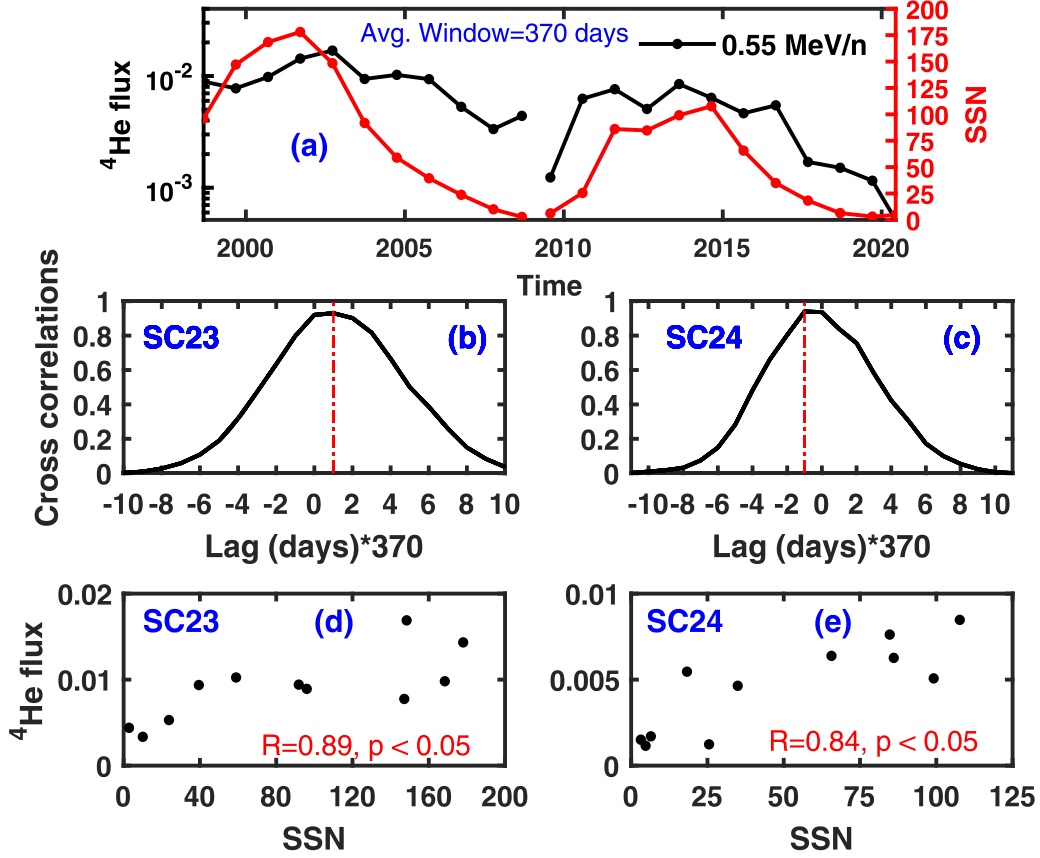


Figure 3. Panel (a) shows typical variations of the 370 day averaged ^4He flux (black) corresponding to 0.55 MeV n^{-1} (mentioned at the right corner) and SSN (red). Variations of the normalized cross-correlation coefficients between the ^4He flux and SSN with respect to the lags (in multiples of 370 days) for SC23 and SC24 are shown in subplots (b) and (c), respectively. The scatter plots in subplots (d) and (e) represent variations of the averaged and adjusted ^4He fluxes with respect to the SSN in SC23 and SC24, respectively (see the text for details). Pearson’s correlation coefficient (R) between flux and SSN and corresponding p values are mentioned at the bottom of panels (d) and (e).

respectively. The corresponding “quiet” time fluxes are shown in subplots (c), (e), (g), (i), (k), and (m) respectively. The mean values (up to two decimal place) of each energy channel for H, ^4He , and ^3He are mentioned at the top left of Figure 2 using colored dots as legends. The same is done for Fe, C, and O, as mentioned at the top right of the figure.

It is to be noted at this point that all the subplots of Figure 2 are significantly compressed in time as these contain data spanning over 22 yr. Although there is apparent bunching of spikes in some of the “quiet” time series plots (for example, in (i)) giving an impression of flux changes associated with transient events, it is verified that those spikes are formed due to temporal compression of the plot and constituent data points that are temporarily far apart from each other. Another important point to be noted here is that the resultant “quiet” flux variations for all the elements lie below conspicuous threshold levels that emerge out automatically for each element. The “quiet” time particle flux data obtained through this method are then analysed further and the results are discussed in subsequent sections.

4. Results

4.1. Correlation Coefficients and Lags with the Variations in the SSN in SC23 and SC24

Correlations between the “quiet” suprathermal fluxes and SSN during SC23 and SC24 are investigated in this section. Fluxes of different particles at different energy channels and SSN have been subjected to averaging over 240 days to 400 days in steps of 10 days. In each such step, the maximum cross-correlation coefficient and corresponding lag between the flux and SSN is determined. In order to get an idea about the significance of these correlations, we use these lags, apply them to the time series data, and calculate the Pearson’s correlation coefficients (CCs) and corresponding p values (probability of acceptance of the null hypothesis that these correlations are occurring by chance) between the lagged fluxes and SSN. The method adopted in this work to compute CCs and lags is depicted in Figure 3. Figure 3(a) shows typical variations of the 370 day averaged ^4He flux with energy 0.55 MeV n^{-1} and SSN for SC23 and SC24. In each case, the SSN variation is subjected to positive and negative lags with respect to the flux variation to maximize the cross-correlation coefficient. The results obtained by this method for SC23 and SC24 are shown in Figures 3(b) and 3(c), respectively. The lags corresponding

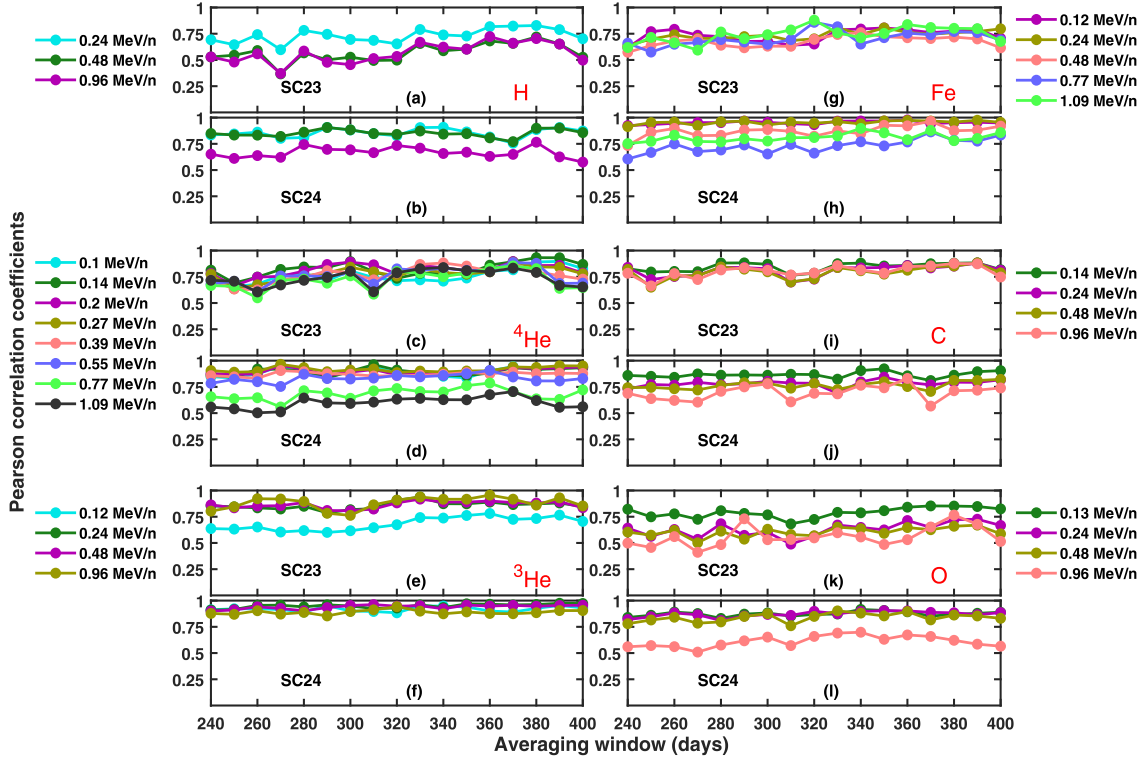


Figure 4. Variations of Pearson’s CC between the lagged fluxes and SSN with respect to the averaging window. Panels (a), (c), (e), (g), (i), and (k) show the variations of CC for H, ^4He , ^3He , Fe, C, and O, respectively during SC23. Panels (b), (d), (f), (h), (j), and (l) represent the same for SC24. Energy channels corresponding to H, ^4He , and ^3He are written on the left side of the left column of the figure. The same corresponding to Fe, C, and O are mentioned on the right of the right column of the figure.

to the maximum cross-correlation coefficients (marked by vertical red dotted–dashed lines) are considered as the lags of interest. A positive lag value indicates that the flux variation lags the SSN variation. On the other hand, a negative lag reveals that the flux variation leads the SSN variation, which essentially means that the increase in flux has started earlier than the increase in SSN. The above two scenarios are clear from Figures 3(b) and 3(c), respectively. It can be seen that the 370 day averaged ^4He flux lags the SSN variation in SC23 by 370 days and leads it in SC24 by the same number of days. Once the lag is noted, the flux variation is adjusted for the lag, and then Pearson’s CC and the corresponding p value are estimated. Figures 3(d) and 3(e) show Pearson’s CCs and p values for SC23 and SC24, respectively. Note, in both the cases Pearson’s CC (R) is higher than 0.8 and the p values are <0.05 , which indicate that these high correlations are real.

Figure 4 shows the variations of Pearson’s CCs with respect to the averaging window during SC23 and SC24 for various elements. Every vertical pair of subplots in this figure corresponds to the variations of Pearson’s CCs of an element in SC23 and SC24. It can be seen from Figure 4 that the CC values corresponding to any particular energy channel of any element do not vary significantly depending on the averaging windows. In most of the cases it is observed that $p < 0.05$.

Variations of the lags corresponding to each point in Figure 4 are shown in Figure 5. Some interesting outcomes from this figure are discussed in the following part of this section. “Quiet” time suprathermal H at L1 point does not show any noticeable time delay with respect to the SSN variation in

SC23. The time lags are inconsistent in SC24 as positive, zero, and negative lags are observed in different energy channels of H. Interestingly, although ^4He shows zero and positive lags in SC23, zero and negative lags are observed on some occasions in SC24.

^3He flux variation does not lag the SSN variation in both SC23 and SC24 except for at 0.96 MeV n^{-1} energy channel when negative lags are seen in SC24 for some averaging periods. While zero or positive lags are observed for the Fe fluxes in SC23, predominantly zero lags are there in SC24. C and O show mostly zero lags in both solar cycles.

4.2. Variations in the Spectral Index of Different Elements at Different Phases of SC23 and SC24

In order to evaluate the variabilities of the spectral indices of different suprathermal elements during the different phases of SC23 and SC24, seven phases are identified from the SSN data spanning from 1998 March to 2020 August. The duration of each phase is two years. These phases are: (1) maximum of SC23 (from 1999 November 11 to 2001 November 11), (2) descending phase of SC23 (from 2003 July 15 to 2005 July 15), (3) minimum of SC23–24 (from 2007 July 05 to 2009 July 05), (4) ascending phase of SC24 (from 2009 September 24 to 2011 September 24), (5) maximum of SC24 (from 2012 April 20 to 2014 April 20), (6) descending phase of SC24 (from 2015 July 8 to 2017 July 8), and (7) minimum of SC24–25 (from 2018 August 31 to 2020 August 31). “Quiet” time suprathermal ion fluxes of each element are then averaged over each phase

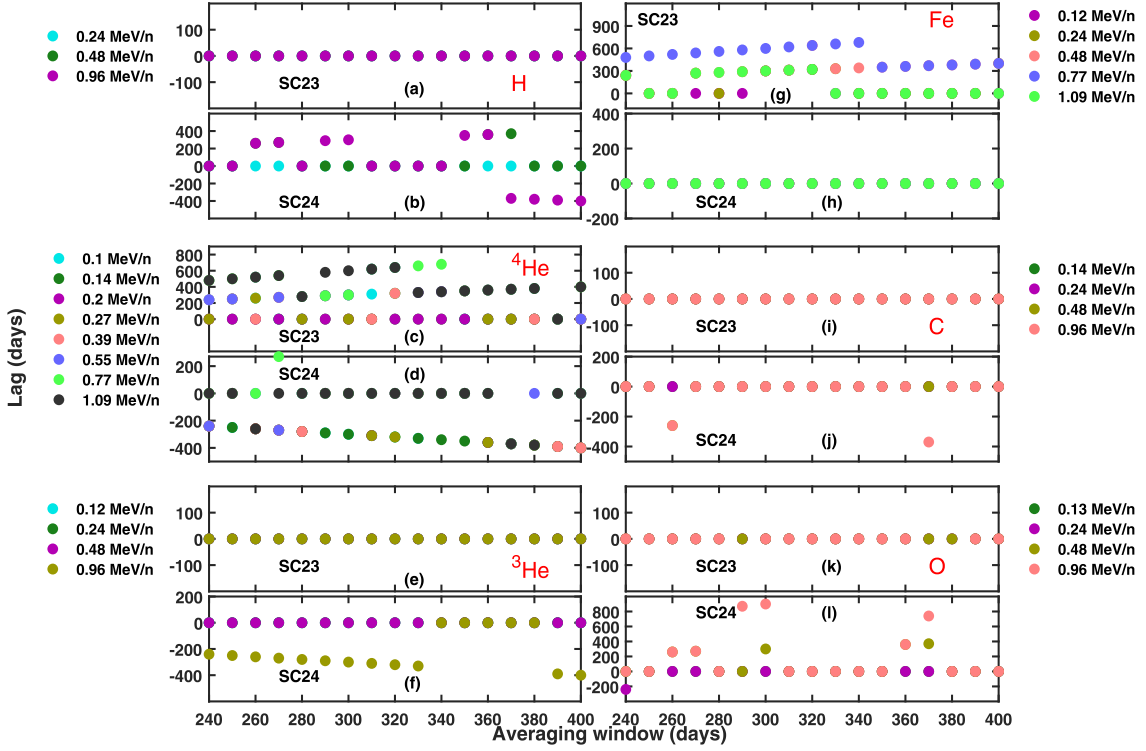


Figure 5. Variations of the lags between the averaged fluxes and SSN with respect to the averaging window. Panels (a), (c), (e), (g), (i), and (k) show the variations of the lags for H, ^4He , ^3He , Fe, C, and O, respectively, during SC23. Panels (b), (d), (f), (h), (j), and (l) represent the same during SC24. Energy channels corresponding to H, ^4He , and ^3He are written on the left side of the left column of the figure. The same corresponding to Fe, C, and O are mentioned on the right of the right column of the figure.

and plotted against the corresponding energies (represented by colored dots), as shown in Figure 6. Each subplot in Figure 6 corresponds to the spectra of an element mentioned at the right upper corner of each subplot. Lines with seven different colors are the least-squares fitted lines corresponding to the seven phases of solar cycles as mentioned earlier. The spectral indices denoted by m_i (where $i = 1, 2, 3, 4, 5, 6,$ and 7) are the estimated mean slopes of the fitted lines corresponding to different phases. The margin of errors (MoE; which sets a lower and upper bound on the estimated value corresponding to a specified confidence level) within 95% confidence bounds in estimating the mean slopes are also mentioned here. It is to be noted that the MoE depends on the variability of the data points, sample size, and confidence level (e.g., Agresti & Coull 1998). Bootstrap sampling (Efron & Tibshirani 1993) is a useful method to calculate the confidence intervals and MoE of an estimated (fitted) parameter like the spectral index.

Figure 7 summarizes the results shown in Figure 6. It shows the variations of the spectral indices of (a) H, (b) ^3He , (c) C and O, and (d) ^4He and Fe with different phases of the solar cycles as mentioned above. The MoEs are also shown. Note, the y-axis scales are made different for each subplot in Figure 7 to provide better visualization.

Figure 7(a) shows the variations in the mean spectral indices for suprathermal H at different phases of the solar cycles. The mean spectral index is found to vary from 1.51 (mean m_2) to 1.88 (mean m_5) except for that at the minimum of SC24–25 when it changes to 2.2 (mean m_7). It can be seen that the spectral index changed significantly during the minimum of

SC24–25. However, since the variabilities of the fluxes are large and the number of data points is only three (corresponding to the three energy channels), the MoE is relatively large. This argument is justified as Bootstrap sampling depends on the number of original data points and the more the data points, the better is the normal approximation used in Wald’s method (see, for example, Agresti & Coull 1998). Therefore, a larger sample size and smaller variability of the sample data lead to a smaller MoE.

Figure 7(b) shows the corresponding variations of the spectral indices of ^3He similar to what is shown in Figure 7(a). It is noted that the m_i of ^3He vary from 2.35 (mean m_1) to 2.64 (mean m_7). The MoEs are also quite high (except for the MoEs of the mean m_1 (0.69) and mean m_6 (0.80)). Comparative variations of the spectral indices of C and O (Figure 7(c)) reveal that these two elements go almost hand in hand over all the phases of the solar cycles, with the largest difference between the mean m_i appearing to occur during the minimum of SC23–24. This is in contrast to ^4He and Fe wherein the largest difference between the spectral slopes seems to occur during the minimum of SC24–25. The spectral indices (from m_1 to m_5) of ^4He and Fe vary almost hand in hand between the maximum of SC23 and the maximum of SC24. However, during the descending phase of SC24, m_6 of ^4He reaches a minimum value (1.72) and in the next phase, the index m_7 of ^4He changes abruptly to a maximum value (2.50). Such abrupt changes are not seen in case of Fe during the minimum of SC24–25.

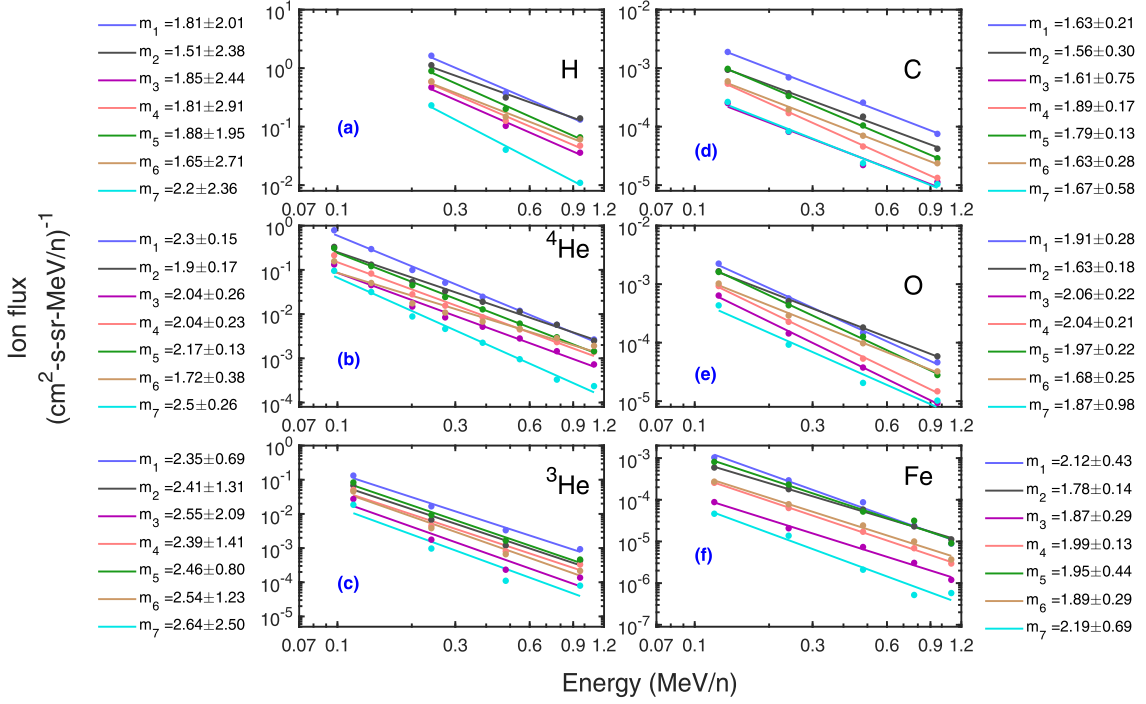


Figure 6. Plots of two year “quiet” time averaged differential directional flux vs. energy for the six elements under consideration. The spectral slopes (m_i) of the fitted lines for different phases of SC23 and SC24 are also shown in different colors. The MoEs of the spectral index estimations within 95% confidence bounds are written on the left for H, ^4He , and ^3He and on the right for C, O, and Fe.

5. Discussion

Variations of “quiet” time suprathermal heavy ion ratios (C/O, Fe/O, and $^3\text{He}/^4\text{He}$) with solar activity were reported in the past (e.g., Dayeh et al. 2009; Kecskemety et al. 2011; Dayeh et al. 2017; etc.). It was also suggested that these ratios exhibit a solar energetic particle (SEP)-like signature during solar maximum and a CIR/solar wind-like signature during solar minimum. Therefore, the contribution from SEP and CIR events to the suprathermal ion pool in the IP medium during solar maximum and minimum, respectively, have been indicated in the past. Our investigation explicitly brings out not only the solar activity dependence (based on significant CCs) but also the time delays between the SSN and “quiet” time suprathermal fluxes. Therefore, our results augment and consolidate the earlier results (e.g., Dayeh et al. 2017) on the solar activity dependence of suprathermal particles in the IP medium. It appears that as the occurrence of SEP (both impulsive and gradual events) and CIR events vary with solar activity, so does the suprathermal population in the IP medium. The most striking point in this context emerges when we see conspicuous lags on many occasions despite the removal of transient events. This strongly suggests that the so-called “quiet” time suprathermal population in the IP medium may possibly be composed of leftover particles from previous solar and IP transient events. Therefore, the “quiet” time population of suprathermal population may not be truly “quiet” (even after the removal of the transient events).

This investigation, for the first time, shows that there exists negative lags between the suprathermal ^4He fluxes and SSN in SC24. This essentially means that suprathermal ^4He flux levels started rising in the IP medium before the SSN started rising

during SC24. This indicates toward source processes that dominate during the minimum phase of the solar cycle. Since CIRs are the major source of energetic particles in the IP medium during the minimum of solar cycles, the negative lags of suprathermal ^4He during the minimum of SC23–24 probably indicate the production of these suprathermal particles from CIR events in the IP medium. The deep minimum of SC23–34 provides an ideal background condition for this. This argument is supported by the negative lags observed in the 0.96 MeV n^{-1} ^3He flux in SC24. It is known that impulsive flare events contribute to the energetic ^3He population in the IP medium (e.g., Mason et al. 2002). Therefore, a negative lag in the ^3He fluxes may additionally suggest the role of remnant flare particles that were accelerated by CIR events during the minimum of the solar cycle and contributed to the suprathermal ion pool.

Mason et al. (2012) used ACE/ULEIS data from 1998 to 2011 and found that CIR event-averaged suprathermal Fe/O lagged behind SSN in SC23 but became more in phase in SC24. The results of Mason et al. (2012) also got extended and supported by the work of Allen et al. (2019) wherein similar behavior for the CIR averaged suprathermal Fe/O (in the energy range of $0.32\text{--}0.45 \text{ MeV n}^{-1}$) was brought out using ACE/ULEIS data from both SC23 and 24 (1998–2018). Interestingly, the present results that deal with “quiet” time suprathermal populations show consistency with the results obtained by both Mason et al. (2012) and Allen et al. (2019) as far as the difference in lags of the suprathermal Fe is concerned within both cycles. This result also indicates the contribution of CIR-associated particles in the “quiet” time suprathermal particle population.

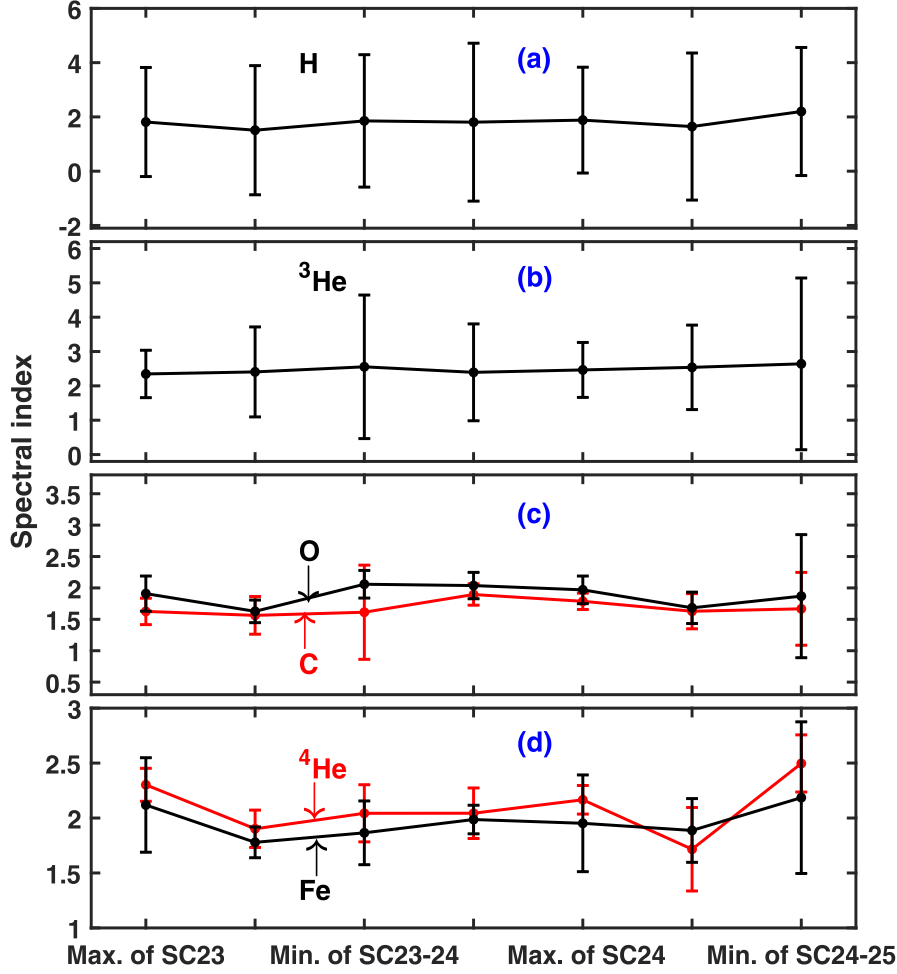


Figure 7. Variations of spectral indices of (a) H and (b) ³He and comparative variations of (c) C (red) and O (black) and (d) ⁴He (red) and Fe (black) with respect to the different phases of the solar cycles starting from the maximum of SC23 up to the minimum of SC24–25. The MoEs corresponding to the 95% confidence interval, in estimating the spectral indices as shown in Figure 6, are set as error bars.

Drastic changes in the spectral index of ⁴He occur after the maximum of SC24. In the descending phase of SC24, the mean spectral index (m_6) of ⁴He reaches its minimum value at 1.72. In the next phase, the index ($m_7 = 2.50$) is the highest among all the phases. The change is greater than any of the MoEs for ⁴He. On the other hand, the spectral indices of Fe vary quite smoothly and reach a maximum in the minimum of SC24–25. These variations in the spectral indices of ⁴He and Fe suggest that there were some differences in the production and (or) processing of these two suprathermal elements in the IP medium. Earlier, we have noted different lags of these two elements in SC23 and SC24. Therefore, it is clear that as far as the generation and processing of suprathermal ⁴He and Fe are concerned, there exist significant differences in SC24. In fact, SC24 is special in many ways. One such specialty is that SC24 is the weakest solar cycle in the last century and succeeds an extended minimum. Janardhan et al. (2018) also reported unusual polar field reversal in the Sun. Therefore, it is natural to assume that the differential behavior of suprathermal ⁴He and Fe in SC24 may be associated with changes in the Sun itself. However, the lags and spectral index variations of C and O

look similar in both solar cycles. This contradiction leads us to think about the preferential processing of suprathermal particles in the IP medium. The acceleration of suprathermal population in the IP medium has also been suggested to depend on the mass-to-charge ratio (M/q) (e.g., Drake et al. 2009; Zhao et al. 2017; Reames 2018) and first ionization potential (FIP) effects (e.g., Feldman & Widing 2002). Owing to the significant M/q and FIP differences, it is possible that the processing of ⁴He and Fe in the IP medium were affected in SC24. This argument gets credence from the fact that C and O have similar FIP and M/q values. Hence, no differential changes are noticed in the lags and spectral indices of C and O in SC23 and SC24. Therefore, the present investigation suggests a sensitive dependence of the generation of a suprathermal population in the IP medium on FIP and M/q . In the context of SC24 being different, a few other results are also relevant here. Mewaldt et al. (2015) revealed that the fluence of SEP particles were conspicuously lower during the initial phase of SC24 and this reduction is attributed to two factors—a lower interplanetary magnetic field (IMF) in the IP medium and depletion in the seed population (suprathermal particles). While a reduced IMF

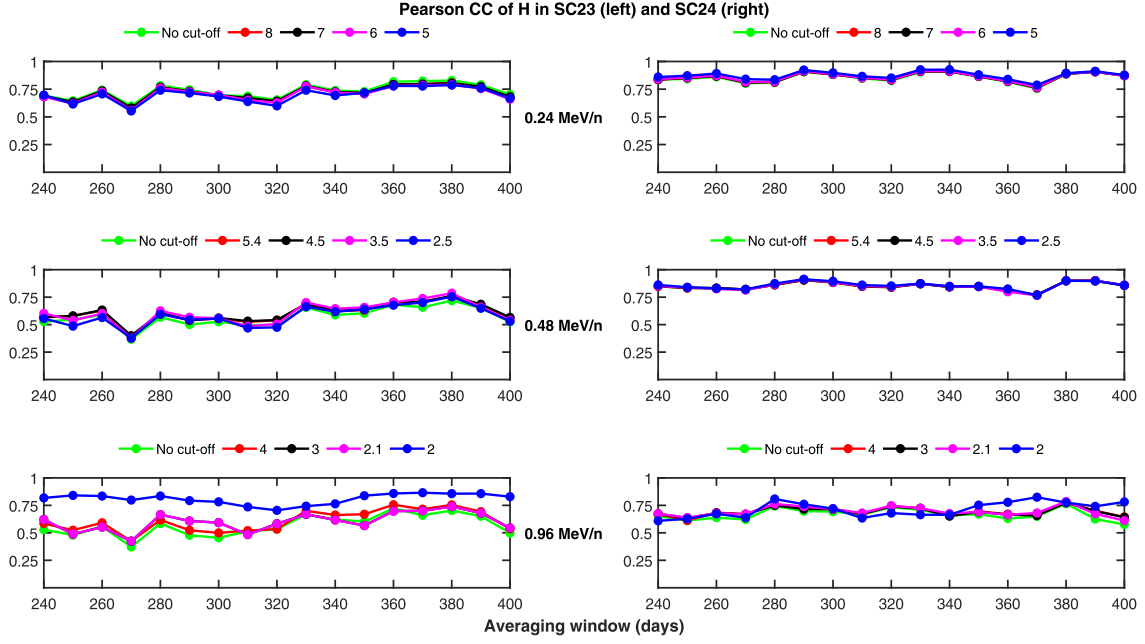


Figure A1. Variations of Pearson's CC between the averaged and shifted H fluxes at different energies (written in the middle column) and the averaged SSN with respect to the averaging window during SC23 (left) and SC24 (right) are shown. The fluxes are shifted based on the calculated lags with respect to the SSN variation. The green dots are Pearson's CCs when there is no cutoff on the fluxes (as shown in Figure 3 in the main text). The red, black, pink, and blue dots represent Pearson's CCs obtained in the similar way after putting cutoffs on the fluxes. The threshold values of the fluxes in units of particles/(cm²-s-r-MeV/n) are written above each subplot.

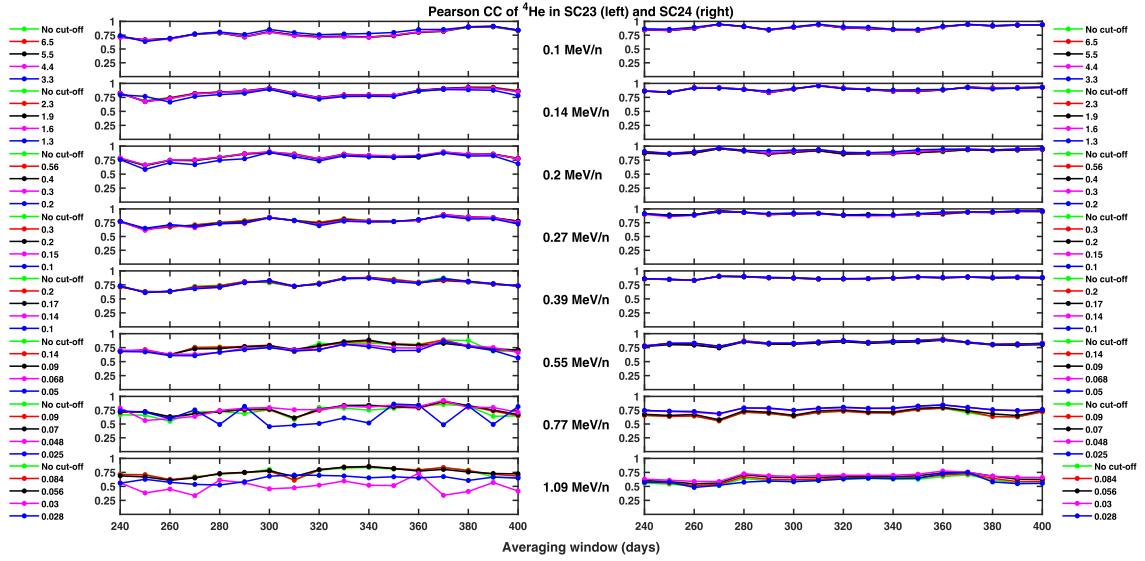


Figure A2. Variations of Pearson's CC between the averaged and shifted ⁴He fluxes at different energies (written in the middle column) and the averaged SSN with respect to the averaging window during SC23 (left) and SC24 (right) are shown. The fluxes are shifted based on the calculated lags with respect to the SSN variation. The green dots are Pearson's CCs when there is no cutoff on the fluxes (as shown in Figure 3 in the main text). The red, black, pink, and blue dots represent Pearson's CCs obtained in the similar way after putting cutoffs on the fluxes. Threshold values of the fluxes in units of particles/(cm²-s-r-MeV/n) are written on the left and right of each pair of subplots corresponding to SC23 and SC24, respectively.

reduces the efficiency of acceleration leading to an underpopulation in the SEP energy domain (e.g., Gopalswamy et al. 2014; Mewaldt et al. 2015; Allen et al. 2019), lower densities of the seed population may limit the maximum energies that particles can be accelerated to by Alfvén waves through wave-

particle interaction at the shock front (e.g., Li & Lee 2015). Another possibility is the changes in the spectral slopes through variations in the pick-up ion populations in the IP medium.

The relative importance of the acceleration and deceleration processes in the changes of suprathermal ⁴He that we see

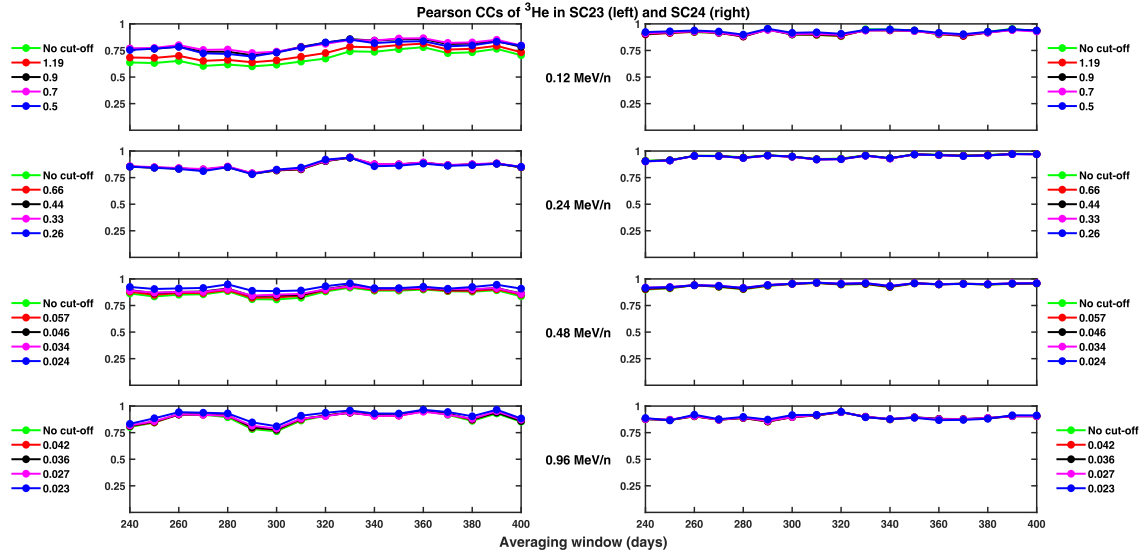


Figure A3. Similar to Figure A2 but for ${}^3\text{He}$.

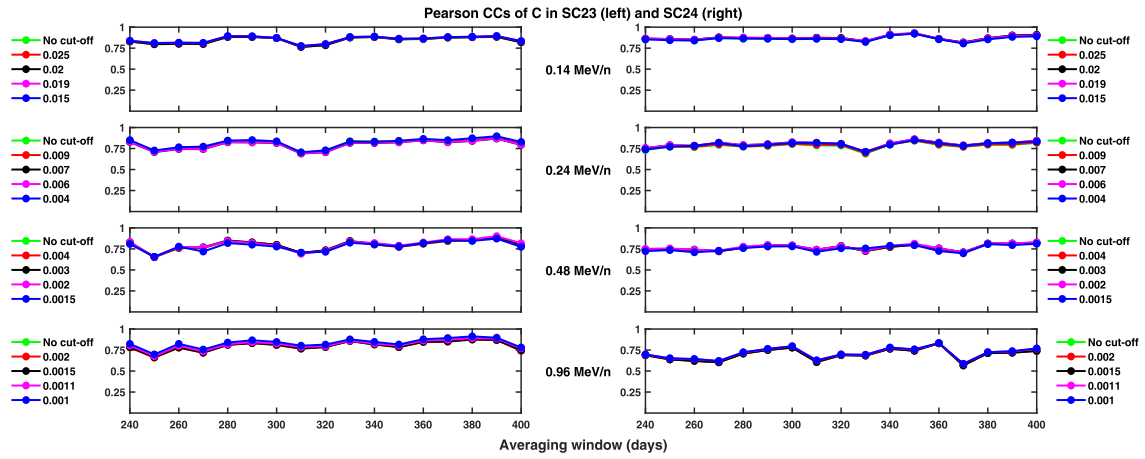


Figure A4. Similar to Figure A3 but for C.

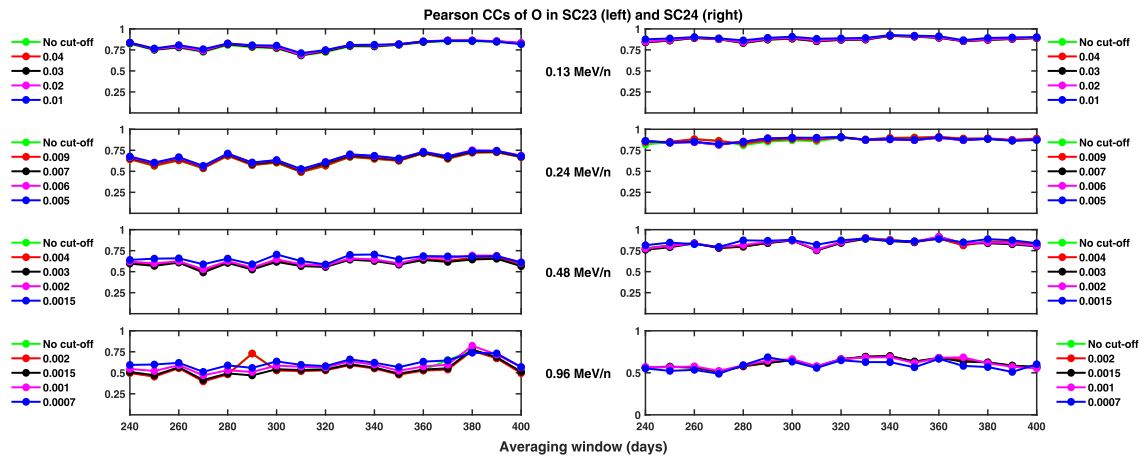


Figure A5. Similar to Figure A4 but for O.

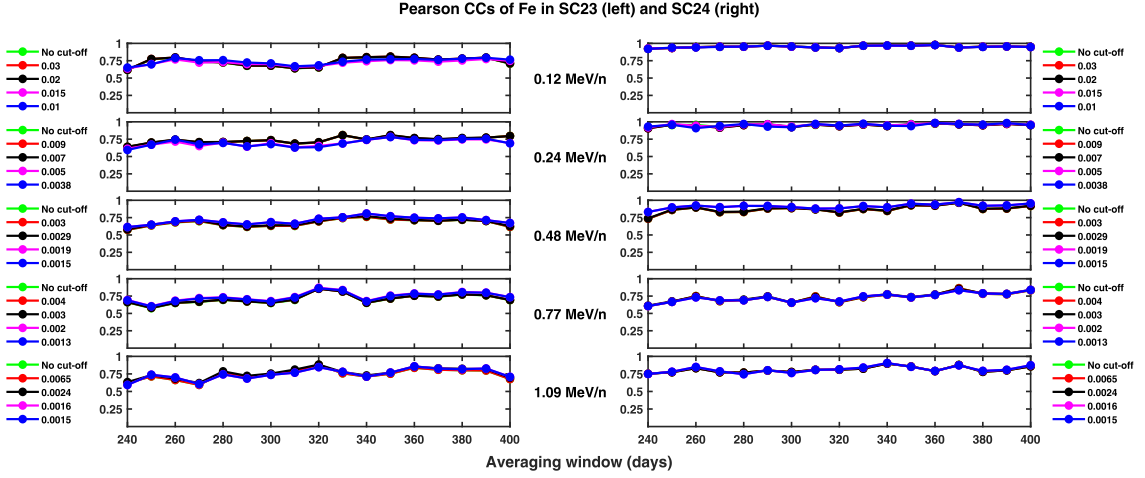


Figure A6. Similar to Figure A5 but for Fe.

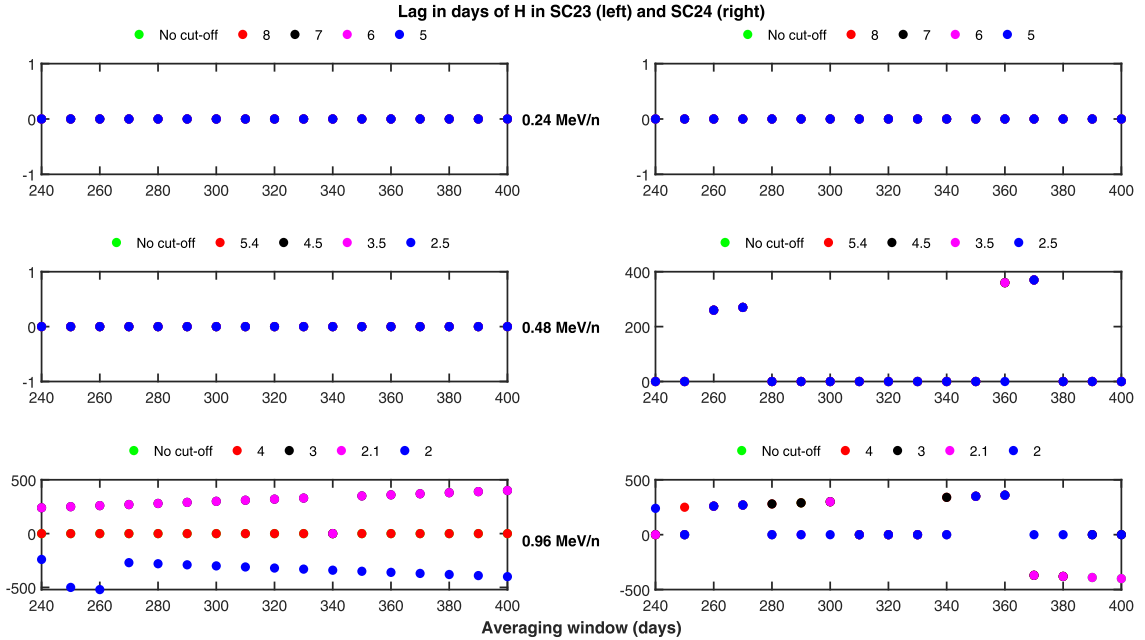


Figure A7. Variations of the lag between the averaged and shifted H fluxes at different energies (mentioned in between the subplots) and the averaged SSN with respect to the averaging window during SC23 (left) and SC24 (right) are shown. The fluxes are shifted based on the calculated lags with respect to the SSN variation. The green dots are the lags when there is no cutoff on the fluxes (as shown in Figure 4 in the main text). The red, black, pink, and blue dots represent Pearson's CCs obtained in the similar way after putting cutoffs on the fluxes. The threshold values of the fluxes in units of particles/cm²-s-sr-MeV/n are written above each subplot.

during the minimum of SC24–25 also deserves attention at this stage. Dayeh et al. (2017) discussed that suprathermal tails are either generated due to (1) continuous acceleration of the seed populations in the IP medium (e.g., Fisk & Gloeckler 2006, 2008, 2014; Zank et al. 2014 etc.) or due to (2) deceleration of energetic particles from solar and IP events (e.g., Fisk & Lee 1980; Giacalone et al. 2002 etc.). Earlier studies have suggested that the lower-energy part of the CIR- (or stream interface region, SIR)-associated suprathermal populations gets affected primarily by local acceleration processes (e.g., Schwadron et al. 1996; Giacalone et al. 2002; Ebert et al. 2012; Filwett et al. 2017, 2019; Allen et al.

2020, 2021) while the higher-energy part gets affected by shock acceleration occurring far away (e.g., Ebert et al. 2012; Filwett et al. 2019). Therefore, the importance of acceleration, whether local or shock-induced, is undeniable in the observed changes that are reported in the present investigation. Schwadron et al. (2010) theorized that variable superpositions of stochastic processes (distribution functions represented by exponential and Gaussian functions) could give rise to a power-law distribution function with an exponent of -5 ($f \propto v^{-5}$) (or -1.5 in differential intensity w.r.t. the energy approach). This work essentially suggests that variable acceleration and heating processes may be in operation in the IP medium for the

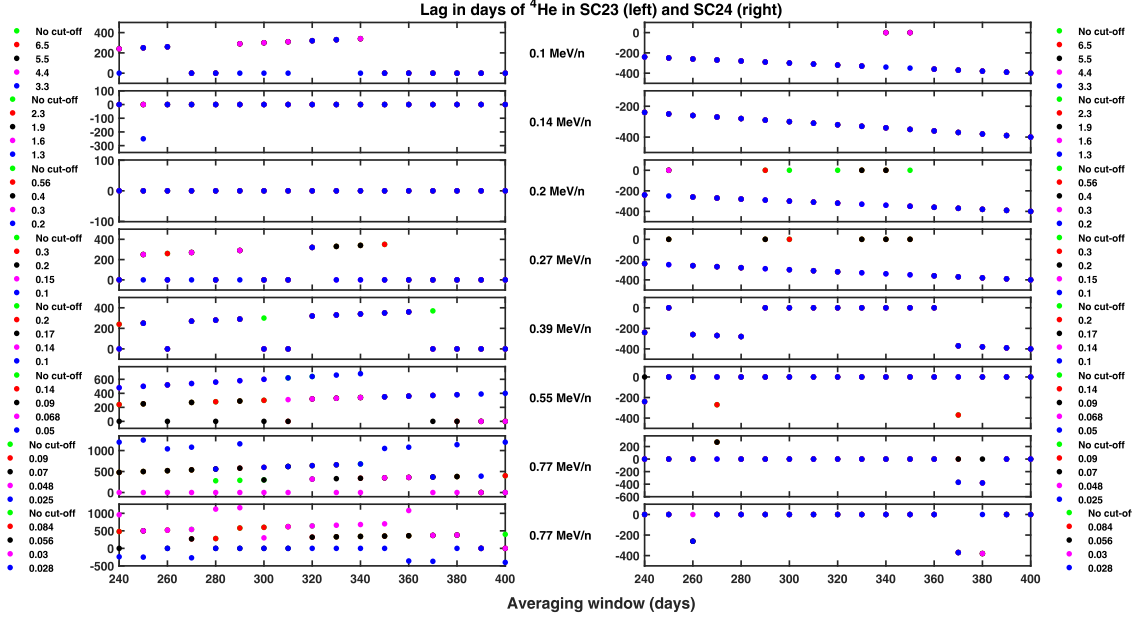


Figure A8. Similar as Figure A7 but for ^4He . Also, the legends are shown adjacent to the subplots.

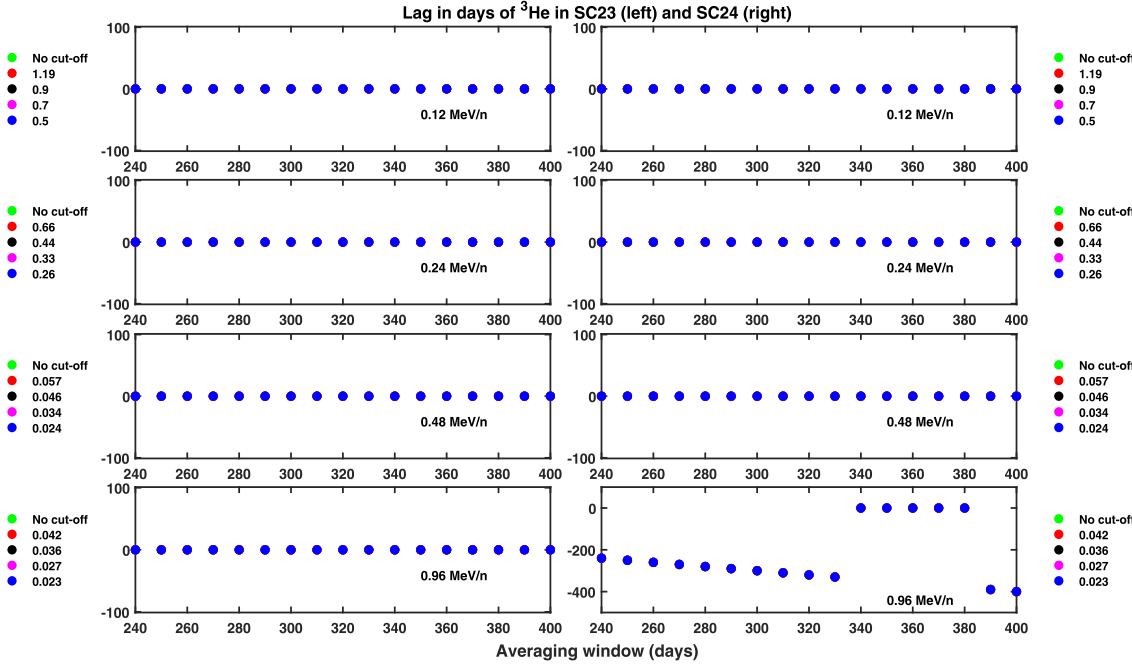


Figure A9. Similar as Figure A8 but for ^3He . Energy channels are mentioned inside the subplots.

generation of suprathermal particles. Anteck *et al.* (2013) adopted stochastic acceleration under a pressure balance condition—the timescale of acceleration is in balance with the timescale of adiabatic cooling in the solar wind as an effective means of producing a -1.5 spectral index. On the other hand, the possible role of deceleration processes for the observed changes in the suprathermal ^4He particles during the minimum of SC24–25 cannot be ruled out also. This is because the particles that are accelerated at the distant shock fronts can

be thrown back into the inner heliosphere leading to increased scattering and magnetic cooling processes. This may result in modulations in the intensity and spectral index (e.g., Fisk & Lee 1980; Mason *et al.* 1999; Zhao *et al.* 2016; Allen *et al.* 2021). Most importantly, particles accelerated through previous transient events, while speeding through the IP medium, experience adiabatic expansion of the solar wind resulting in the deceleration of these particles. As a consequence, the energetic particles slow down and enter into the suprathermal

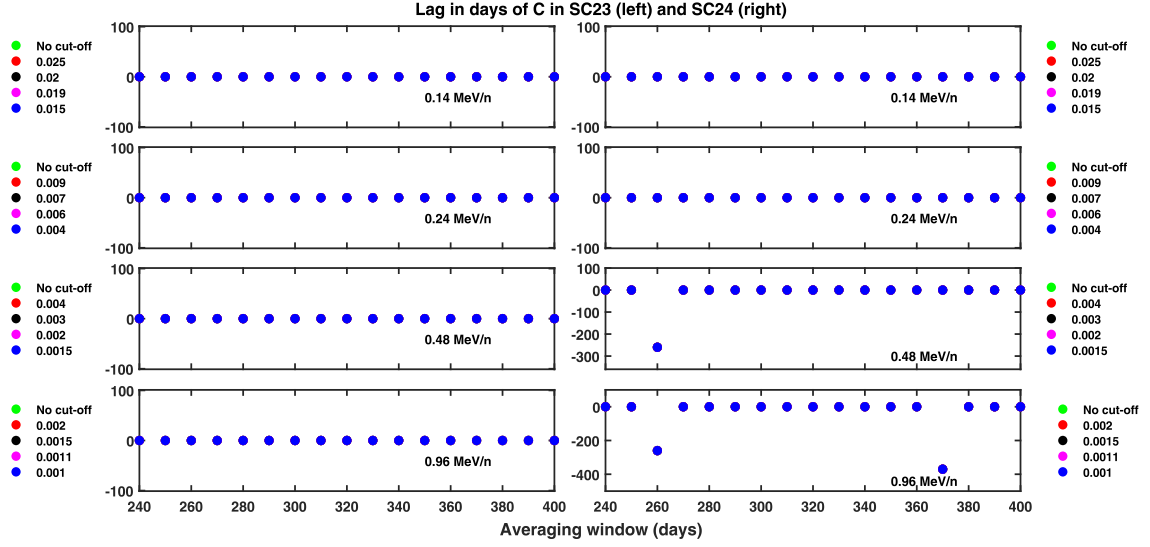


Figure A10. Similar as Figure A9 but for C.

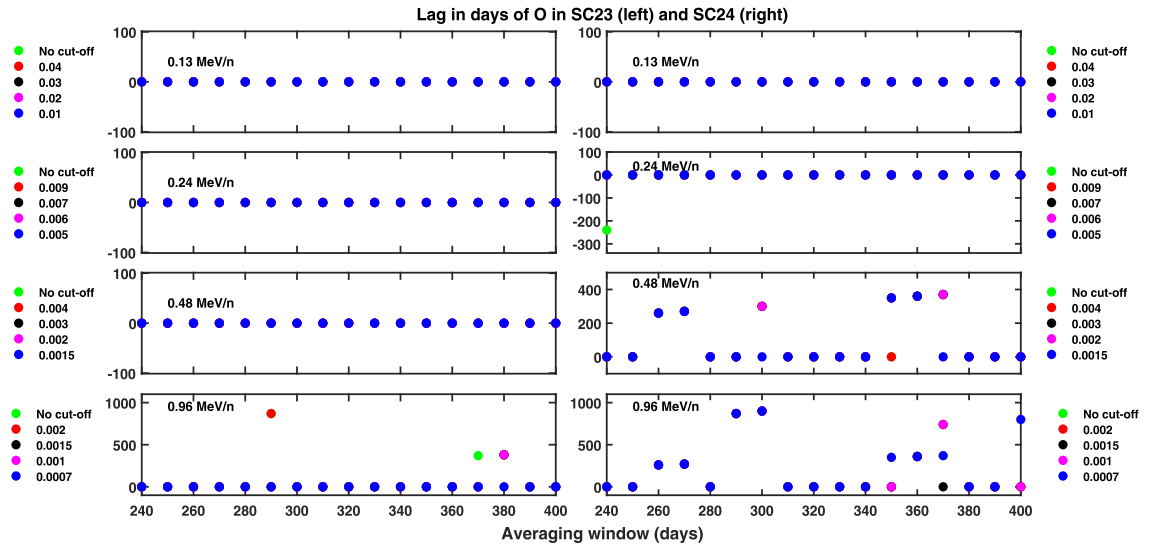


Figure A11. Similar as Figure A10 but for O.

pool. According to Fisk & Lee (1980), this type of particle is expected to show a rollover below $\sim 0.5 \text{ MeV n}^{-1}$ in the spectra. However, no such rollover is observed by Mason et al. (1997). We also do not see such a rollover feature in the present investigation. Nevertheless, although difficult to comment, the relative role of deceleration processes on the significant changes in the spectral slope of ^4He during SC24–25 cannot be ruled out. It seems, therefore, reasonable to argue that variable contributions of acceleration and deceleration or distribution functions may lead to variations in the spectral indices with varying solar activity. These processes might have undergone changes in the minimum of SC24–25 so as to cause changes in the spectral indices as far as heavier ions like Fe and ^4He are concerned. These aspects need more critical attention in the future, and the multidirectional suprathermal particle measurements on board India’s forthcoming Aditya-L1 mission

(Goyal et al. 2018) may throw important light on some of these issues.

6. Summary

In this work, by analysing 22 yr of flux variations of suprathermal H, ^3He , ^4He , C, O, and Fe measured by the ACE spacecraft from the first Lagrangian point of the Sun–Earth system, we show that these particles follow a solar cycle variation with varying lags or time delays. These time delays are shown to vary with energy and element. It is inferred that the suprathermal population in the IP medium during “quiet” times is not free from particles originating from earlier transient events. Further, this investigation, for the first time, reveals that suprathermal Fe and ^4He show discernible changes in lags and spectral slopes in SC24. It is hypothesized that these changes in lags and spectral slopes may result from acceleration/

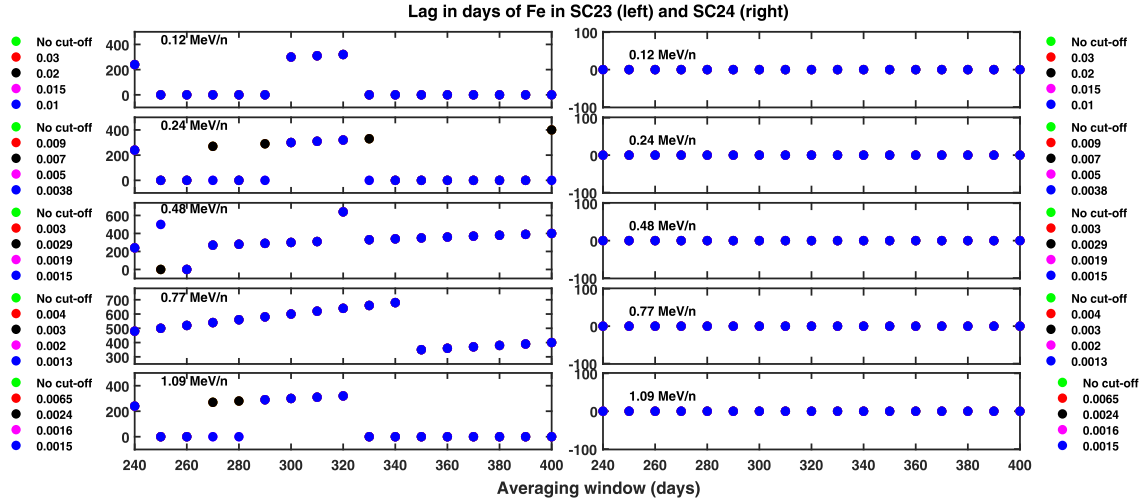


Figure A12. Similar as Figure A11 but for Fe.

deceleration processes that depend on the mass-to-charge ratio and FIP. This suggestion gets credence from the behavior of C and O wherein no such differential changes are noticed. Further investigations are needed to understand the underlying physical processes that are responsible for the differential changes in the suprathermal helium and iron in the IP medium in SC24.

We are grateful to the Principal Investigator and all the members of the ULEIS team for constructing the ULEIS instrument and thereafter, generating and managing the data set used in this work. We also thank WDC-SILSO, Royal Observatory of Belgium, Brussels for the daily estimated SSN data used in this paper. We express our sincere gratitude to the Department of Space, Government of India for supporting this work.

Data Sources: The suprathermal particle flux data used in this paper are available at <https://cdaweb.gsfc.nasa.gov/index.html>. The daily estimated SSN data can be downloaded from <http://www.sidc.be/silso/datafiles>.

Appendix

Rigorous sensitivity tests to validate the results regarding lags of suprathermal particles with respect to SSN variation are performed. These plots reveal how the correlation between the “quiet” suprathermal fluxes and SSN varies depending on the flux thresholds. Four sets of flux thresholds have been selected at random in decreasing order for each energy channel of each element. We have repeated the same exercise depicted in the main text to calculate the lags and Pearson’s CCs between SSNs and fluxes with the above mentioned cutoffs. The results of the same are shown in Figures A1–A12. Figures A1–A6 show the variations in Pearson’s CC for H, ^4He , ^3He , C, O, and Fe, respectively. It can be seen from Figure A1 to Figure A6 that irrespective of the thresholds, the flux and Pearson’s CC do not change significantly if we compare these values with the CCs calculated by only removing transient events. Not only the CCs, but also the time delays between the fluxes and SSN also do not change depending on the flux baselines (see Figures A7–A12). These give direct credence to the

methodology adopted here for generating quiet time data by removing the transient events.

ORCID iDs

Bijoy Dalal <https://orcid.org/0000-0001-8993-9118>

D. Chakrabarty <https://orcid.org/0000-0003-2693-5325>

N. Srivastava <https://orcid.org/0000-0002-0452-5838>

References

- Agresti, A., & Coull, B. A. 1998, *Am. Stat.*, 52, 119
 Allen, R., Ho, G., Jian, L., et al. 2021, *A&A*, 650, A25
 Allen, R., Mason, G., Ho, G., et al. 2020, *A&A*, 656, L2
 Allen, R. C., Ho, G. C., & Mason, G. M. 2019, *ApJL*, 883, L10
 Anteecki, T., Schlickeiser, R., & Zhang, M. 2013, *ApJ*, 764, 89
 Bell, A. R. 1978, *MNRAS*, 182, 147
 Bučik, R., Mall, U., Korth, A., & Mason, G. 2009, *AnGeo*, 27, 3677
 Chotoo, K., Schwadron, N. A., Mason, G. M., et al. 2000, *JGRA*, 105, 23107
 Dayeh, M. A., Desai, M. I., Dwyer, J. R., et al. 2009, *ApJ*, 693, 1588
 Dayeh, M. A., Desai, M. I., Mason, G. M., Ebert, R. W., & Farahat, A. 2017, *ApJ*, 835, 155
 Desai, M. I., Mason, G. M., Dwyer, J. R., et al. 2003, *ApJ*, 588, 1149
 Desai, M. I., Mason, G. M., Wiedenbeck, M. E., et al. 2004, *ApJ*, 611, 1156
 Drake, J. F., Cassak, P. A., Shay, M. A., Swisdak, M., & Quataert, E. 2009, *ApJL*, 700, L16
 Ebert, R. W., Dayeh, M. A., Desai, M. I., & Mason, G. M. 2012, *ApJ*, 749, 73
 Efron, B., & Tibshirani, R. J. 1993, *An Introduction to the Bootstrap: Monographs on Statistics and Applied Probability 57* (New York: Chapman and Hall)
 Feldman, U., & Widing, K. G. 2002, *PhPI*, 9, 629
 Fermi, E. N. R. I. C. O. 1949, *PhRv*, 75, 1169
 Filwett, R. J., Desai, M. I., Dayeh, M. A., & Broiles, T. W. 2017, *ApJ*, 838, 23
 Filwett, R. J., Desai, M. I., Ebert, R. W., & Dayeh, M. A. 2019, *ApJ*, 876, 88
 Fisk, L. A. 1976, *JGR*, 81, 4633
 Fisk, L. A., & Gloeckler, G. 2006, *ApJL*, 640, L79
 Fisk, L. A., & Gloeckler, G. 2007, *PNAS*, 104, 5749
 Fisk, L. A., & Gloeckler, G. 2008, *ApJ*, 686, 1466
 Fisk, L. A., & Gloeckler, G. 2014, *JGRA*, 119, 8733
 Fisk, L. A., & Lee, M. A. 1980, *ApJ*, 237, 620
 Giacalone, J., Jokipii, J. R., & Kota, J. 2002, *ApJ*, 573, 845
 Gloeckler, G. 2003, in *AIP Conf. Proc.* 679, *Solar Wind Ten: Proc. of the Tenth International Solar Wind Conference*, ed. M. Velli, R. Bruno, & F. Malara (Melville, NY: AIP), 583
 Gopalswamy, N., Akiyama, S., Yashiro, S., et al. 2014, *GeoRL*, 41, 2673
 Gosling, J. T., Asbridge, J. R., Bame, S. J., et al. 1981, *JGRA*, 86, 547
 Goyal, S. K., Kumar, P., Janardhan, P., et al. 2018, *P&SS*, 163, 42

- Janardhan, P., Fujiki, K., Ingale, M., Bisoi, S. K., & Rout, D. 2018, [A&A](#), **618**, [A148](#)
- Kecskemeti, K., Zeldovich, M., & Logachev, Y. 2011, *ICRC*, 11, 115
- Krymskii, G. 1977, *DoSSR*, **234**, [1306](#)
- Li, G., & Lee, M. A. 2015, [ApJ](#), **810**, [82](#)
- Mason, G. 2000, in *AIP Conf. Proc.* 528, *Acceleration and Transport of Energetic Particles Observed in the Heliosphere: ACE 2000 Symp.*, ed. R. A. Mewaldt et al. (Melville, NY: AIP), [234](#)
- Mason, G., Steiger, Von, Decker, R., et al. 1999, *SSRv*, **89**, 327
- Mason, G. M., Desai, M. I., & Li, G. 2012, [ApJL](#), **748**, [L31](#)
- Mason, G. M., Gold, R. E., Krimigis, S. M., et al. 1998, *SSRv*, **86**, 409
- Mason, G. M., Leske, R. A., Desai, M. I., et al. 2008, [ApJ](#), **678**, [1458](#)
- Mason, G. M., Mazur, J. E., Dwyer, J. R., Reames, D. V., & von Rosenvinge, T. T. 1997, [ApJL](#), **486**, [L149](#)
- Mason, G. M., Wiedenbeck, M. E., Miller, J. A., et al. 2002, [ApJ](#), **574**, [1039](#)
- Mewaldt, R., Cohen, C., Mason, G., et al. 2015, *ICRC (The Hague)*, 34, 30
- Palmer, I. D., & Gosling, J. T. 1978, *JGRA*, **83**, [2037](#)
- Reames, D. V. 2018, *SoPh*, **293**, [1](#)
- Schwadron, N. A., Dayeh, M. A., Desai, M., et al. 2010, [ApJ](#), **713**, [1386](#)
- Schwadron, N. A., Fisk, L. A., & Gloeckler, G. 1996, *GeoRL*, **23**, [2871](#)
- Stone, E. C., Frandsen, A. M., Mewaldt, R. A., et al. 1998, *SSRv*, **86**, [1](#)
- Yu, J., Berger, L., Drews, C., Wimmer-Schweingruber, R., & Taut, A. 2018, [A&A](#), **615**, [A126](#)
- Zank, G. P., le Roux, J. A., Webb, G. M., Dosch, A., & Khabarova, O. 2014, [ApJ](#), **797**, [28](#)
- Zhao, L., Zhang, M., & Rassoul, H. K. 2016, [ApJ](#), **821**, [62](#)
- Zhao, L., Zhang, M., & Rassoul, H. K. 2017, [ApJ](#), **836**, [31](#)



Suprathermal Population Associated with Stream Interaction Regions Observed by STEREO-A: New Insights

Bijoy Dalal^{1,2} , Dibyendu Chakrabarty¹ , Nandita Srivastava³ , and Aveek Sarkar¹ ¹Physical Research Laboratory, Ahmedabad—380009, India²Indian Institute of Technology Gandhinagar, Gandhinagar—382055, India³Udaipur Solar Observatory, Physical Research Laboratory, Udaipur—313001, India

Received 2023 September 19; revised 2023 October 25; accepted 2023 October 25; published 2023 December 19

Abstract

Stream interaction regions (SIRs) are often thought to be responsible for the generation of suprathermal population in the interplanetary medium. Even though the source is the same, wide variations in the spectral indices of suprathermal populations are observed at 1 au during SIRs. This poses a significant uncertainty in understanding the generation of suprathermal ion populations by SIRs and indicates an interplay of multiple source mechanisms. By analyzing variations in suprathermal ⁴He, O, and Fe for 20 SIR events recorded by STEREO-A during 2007–2014, we find that the spectral indices of these elements vary in the range of 2.06–4.08, 1.85–4.56, and 2.11–4.04 for 19 events. However, in one special case, all three suprathermal elements show nearly identical (~1.5) spectral indices. We describe possible mechanisms that might cause significant variations in the spectral indices of suprathermal particles. More importantly, we show the possible role of merging and/or contraction of small-scale magnetic islands near 1 au in producing nearly identical spectral indices for three different elements with different first ionization potentials and mass-to-charge ratios. The occurrence of these magnetic islands near 1 au also supports the minimal modulation in the spectral indices of these particles. We also suggest that a possible solar flare may have played a role in generating these magnetic islands near the heliospheric current sheet.

Unified Astronomy Thesaurus concepts: Solar wind (1534); Interplanetary shocks (829); Corotating streams (314); Solar energetic particles (1491); Solar flares (1496)

1. Introduction

Suprathermal particles with energies in the range 0.01–1.0 MeV per nucleon (hence, MeV n⁻¹), often characterized by power-law distributions, are ubiquitous in the heliosphere (Gloeckler 2003). The power-law index (spectral index) has been suggested to be ~1.5 in general due to stochastic acceleration in compressional turbulences during quiet times when the differential directional flux is plotted against the energy of the particles (Gloeckler 2003; Fisk & Gloeckler 2006, 2007, 2008, 2014, etc.) The generation of suprathermal particles in the interplanetary (IP) medium has been one of the most debated topics for several decades. Stream interaction regions (SIRs) are considered the main source of suprathermal and energetic particles in the IP medium (Tsurutani et al. 1982; Mason et al. 2012; Richardson 2018; Allen et al. 2019, 2021, etc.). SIRs form when faster solar wind streams from coronal holes interact with preceding slower streams originating from coronal streamers (Belcher & Davis 1971; Richardson 2018). Coronal holes and the fast solar wind emanating from them sometimes persist for several solar rotations (the Carrington rotation is ~27 days). This causes the compressed interaction regions to corotate with the Sun for more than one solar rotation. These structures are then called corotating interaction regions (CIRs; Gosling et al. 1981). The spectral indices of SIR/CIR-associated suprathermal ⁴He calculated over an energy 0.1–1 MeV n⁻¹ observed at 1 au may vary in the range 1.3–5 (Mason et al. 2008b; Allen et al. 2021). Mason et al. (2008b) found that the spectral indices of CIR-associated ⁴He and O in the energy range 0.16–0.91 MeV n⁻¹ are correlated and similar.

However, the slopes of Fe spectra are found to be different from those of ⁴He and O. This raises the question whether the acceleration of SIR/CIR-associated suprathermal ions depends on the first-ionization potential (FIP) and mass-to-charge ratio (m/q) of the species. In a recent paper, Dalal et al. (2022) have shown that the modulation of quiet-time suprathermal particles in the IP medium depends on the FIP and m/q of elements. In particular, elements with a contrasting FIP and m/q (e.g., ⁴He and Fe) behave differently during quiet times in solar cycle 24 as compared with cycle 23, while species with a similar FIP and m/q (e.g., C and O) are modulated similarly in both the solar cycles.

One theory related to particle acceleration in SIR/CIRs is that suprathermal and energetic particles are generated in forward and reverse shocks associated with the leading and trailing edges of SIRs, respectively (Fisk & Lee 1980). However, these shocks may or may not form at 1 au (Richardson 2018), and suprathermal particles may intensify during the passage of shock-less SIR/CIR events as well (Giacalone et al. 2002; Mason et al. 2008b; Bučik et al. 2009; Ebert et al. 2012; Allen et al. 2019; Filwett et al. 2019; Allen et al. 2021, etc.). We note that shock-less events do not exclude shock-accelerated particles at the satellite location. As discussed by Fisk & Lee (1980), the contribution from suprathermal particles generated by a reverse shock beyond 1 au may cause enhancements in the suprathermal fluxes at 1 au.

In the present work, we select the events wherein the signatures of shocks are not identified at the satellite location. It is also to be noted that not only shocks, but also the gradual compression regions have been suggested (Giacalone et al. 2002) to play an important role in the generation of suprathermal population in the IP medium. While the role of shocks in particle acceleration is well accepted, the role of

 Original content from this work may be used under the terms of the [Creative Commons Attribution 4.0 licence](https://creativecommons.org/licenses/by/4.0/). Any further distribution of this work must maintain attribution to the author(s) and the title of the work, journal citation and DOI.

Table 1
List of SIR Events and Spectral Indices of ${}^4\text{He}$, O, and Fe Corresponding to These Events

SIR No.	Start Time	End Time	Spectral Index		
			${}^4\text{He}$	O	Fe
1	2007 September 21 13:35	2007 September 23 11:32	2.67 ± 0.44	2.89 ± 0.87	
2	2007 October 25 18:04	2007 October 26 15:17	3.33 ± 0.45	3.88 ± 0.62	
3	2007 November 13 18:00	2007 November 16 03:30	3.35 ± 0.60		
4	2007 December 11 18:00	2007 December 13 04:10	3.70 ± 0.38		
5	2008 February 11 00:00	2008 February 13 04:40	2.92 ± 0.49	2.75 ± 0.45	2.59 ± 0.69
6	2008 February 29 16:00	2008 March 3 03:15	2.49 ± 0.38	2.83 ± 0.56	
7	2008 June 16 06:00	2008 June 17 18:36	3.12 ± 0.36		
8	2008 August 7 18:10	2008 August 12 00:00	3.14 ± 0.38	3.64 ± 0.71	
9	2009 May 31 08:13	2009 June 2 16:00	4.08 ± 0.42	4.14 ± 0.95	
10	2011 January 12 12:03	2011 January 14 08:00	3.18 ± 0.28	3.98 ± 0.61	4.04 ± 1.57
11	2011 November 12 02:00	2011 November 14 18:00	2.86 ± 0.28	2.61 ± 0.22	2.09 ± 0.27
12	2012 June 12 04:00	2012 June 13 18:00	1.55 ± 0.39	1.49 ± 0.34	1.46 ± 0.60
13	2012 August 21 20:00	2012 August 23 11:10	2.71 ± 0.33	2.95 ± 0.30	3.09 ± 0.46
14	2013 April 18 16:00	2013 April 19 14:19	3.60 ± 0.43	2.84 ± 0.42	3.09 ± 0.46
15	2013 July 17 00:00	2013 July 22 16:00	4.08 ± 0.24	4.56 ± 0.38	
16	2013 September 24 08:00	2013 September 25 12:00	4.05 ± 0.74		
17	2013 October 24 10:00	2013 October 26 02:25	3.97 ± 0.47	3.67 ± 0.53	
18	2014 April 28 16:47	2014 April 30 19:05	2.06 ± 0.67	1.85 ± 0.34	2.11 ± 0.59
19	2014 May 6 02:37	2014 May 7 02:00	3.06 ± 0.35	2.53 ± 0.29	2.82 ± 0.51
20	2014 June 3 07:27	2014 June 5 00:00	3.45 ± 0.41	3.19 ± 0.19	2.72 ± 0.76

gradual compression regions in generating suprathermal pool has not received enough attention. Further, if well-defined shock structures are detected by the spacecraft, they might dominate the suprathermal flux enhancements at the satellite location. Therefore, in order to ensure that we do not disregard the contribution of the suprathermal population generated from other processes such as the gradual compression regions, the so-called shock-less events are chosen. After selecting these events, we focus on the evaluation of the spectra of elements with a different FIP and m/q . In this work, we therefore estimate the spectral indices of ${}^4\text{He}$, O, and Fe with energies 0.14–1.09 MeV n^{-1} associated with 20 shock-less SIR events observed by the Solar Terrestrial Relations Observatory–Ahead (STEREO-A). We note significant variations in the spectral indices across the SIR events and elements similar to quiet-time conditions (e.g., Dalal et al. 2022). The possible physical processes that might contribute to this spectral index variability during SIR events are discussed. Interestingly, we also find one particular SIR event in which these three elements exhibit nearly identical spectral indices. We investigate this particular SIR event in detail and argue that the enhancement in the suprathermal population during this event is a consequence of merging and/or contraction of a small-scale magnetic island near the spacecraft. The following section discusses the data used in this work. In the subsequent section, we present our results. The discussions and conclusions follow the results section. We summarize the results in the last section.

2. Data Used

The SIR events used in this work were observed by STEREO-A during 2007–2014 and are available at <https://stereo-dev.epss.ucla.edu/media/SIRs.pdf>. The start, end, and approximate passage times of the stream interface structure are determined based on criteria discussed in Jian et al. (2006, 2013, 2019). Suprathermal ${}^4\text{He}$, O, and Fe fluxes with energies <1 MeV n^{-1} obtained from the Suprathermal Ion

Telescope (SIT; Mason et al. 2008a) during and close to these events are used. The SIT is a time-of-flight mass spectrometer with a mass resolution (σ_m/m) of 0.1 in the 0.1–1 MeV n^{-1} energy range. This mass resolution is high enough to distinguish ${}^3\text{He}$ and ${}^4\text{He}$ in the energy range of interest (see Mason et al. 2008a for details). Suprathermal particle flux data for ${}^4\text{He}$, O, and Fe can be found at <https://cdaweb.gsfc.nasa.gov/index.html>. These elements have a different FIP and m/q . It is also checked whether any IP shock was observed by STEREO-A at the time of the event. The list of IP shocks observed by STEREO-A is available at <http://www.ipshocks.fi/database>. The solar wind proton density and bulk speed data are obtained from the Plasma and Suprathermal Ion Composition (PLASTIC) instrument (Galvin et al. 2008) on board STEREO-A. The components of the interplanetary magnetic field (IMF) in the radial-tangential-normal (RTN) coordinate system are measured by the fluxgate magnetometer (Acuña et al. 2008), which is a subsystem of the In-situ Measurements of Particles and CME Transients (IMPACT) investigation (Luhmann et al. 2008) on board STEREO-A. These data are also available at <https://cdaweb.gsfc.nasa.gov/index.html>. The event-selection criteria adopted in this work are discussed in the next section.

3. Selection of Events

From all the SIR events listed in the above link (<https://stereo-dev.epss.ucla.edu/media/SIRs.pdf>), we have selected 20 SIR events during 2007–2014 when there were noticeable enhancements in the suprathermal ${}^4\text{He}$. These events are denoted SIR 1–20 and are listed in Table 1. As discussed earlier, these are shock-less SIR events. It is noted that not every SIR event is associated with enhancements in the O and Fe fluxes. Sixteen events are observed when the O fluxes show small or moderate enhancements, and nine events are seen when the Fe fluxes show enhancements. Figure 1 shows the typical temporal variations of the ${}^4\text{He}$, Fe, and O fluxes at

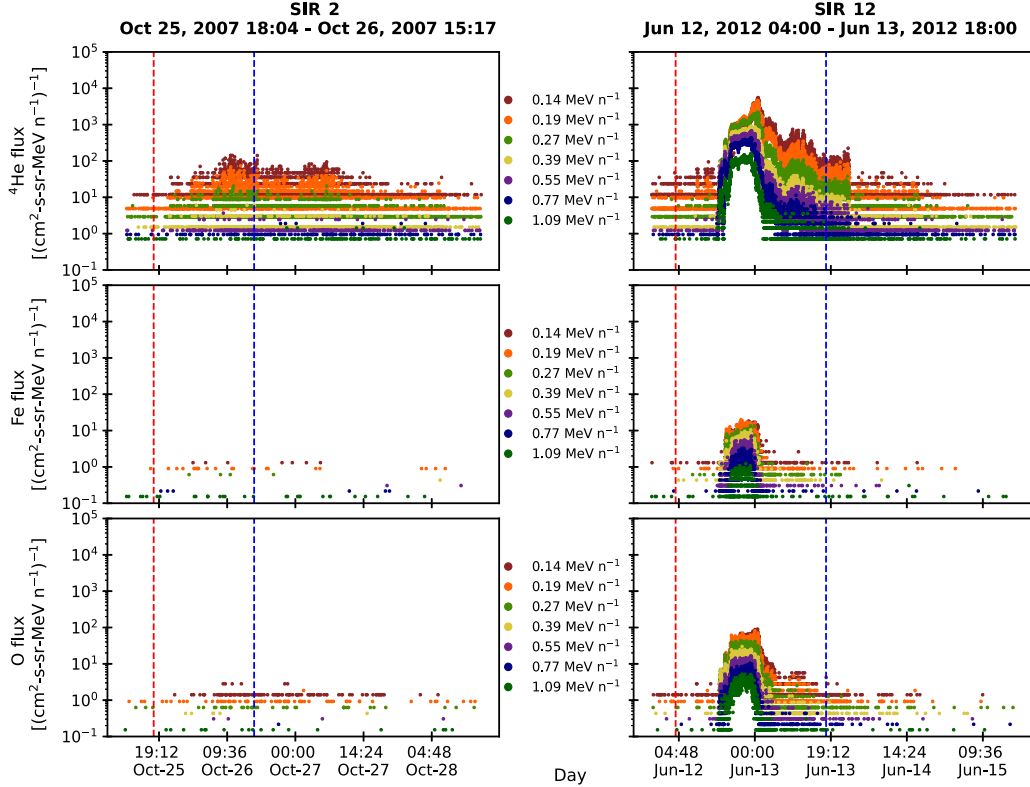


Figure 1. Temporal variations of suprathermal ${}^4\text{He}$ (top row), Fe (middle row), and O (bottom row) fluxes at different energy channels associated with two typical SIR events: SIR 2 (left) and SIR 12 (right). Table 1 provides the details on the date and time of arrival of these SIRs at the location of STEREO-A. The start and end times of these events (determined by the characteristic changes in the solar wind parameters associated with SIR/CIR) are shown by the vertical dashed red and blue lines. The intervals of these events are written in the titles of the left and right column of the figure. The energy channels are mentioned in between the columns.

different energy channels corresponding to SIR 2 and SIR 12. One can easily see that ${}^4\text{He}$ fluxes have increased noticeably above the background (level before and after the enhancement) in connection with SIR 2. The enhancement in Fe fluxes is negligible, and averaged O fluxes have negligible increment. On the other hand, large enhancements in all the three elements are observed in association with SIR 12. The second and third columns of Table 1 enlist the start and end times of the 20 SIR events observed by STEREO-A.

4. Results: Spectral Analysis

As is known, suprathermal ions ($<1 \text{ MeV n}^{-1}$) at 1 au exhibit a power law in the differential flux versus energy spectra. In the present investigation, we use the spectral indices associated with these power laws as representative of the processes that generate the suprathermal particles corresponding to the SIR events. The spectra of ${}^4\text{He}$ during the enhanced flux level corresponding to SIRs 1–20 are shown in Figure 2. The spectral indices and associated margin of errors (MoEs) within the 95% confidence bounds are listed in the fourth column of Table 1. Dalal et al. (2022) have rigorously used MoEs as error bars in their estimated spectral indices of quiet suprathermal particles, and for a detailed discussion, we refer to Agresti & Coull (1998) as well as Dalal et al. (2022). One can see from Figure 2 and Table 1 that the spectral indices of suprathermal ${}^4\text{He}$ lie between 1.55 and 4.08 for these events.

Figures 3 and 4 show the spectra of O and Fe, respectively, corresponding to the SIR events for which we see enhancements in these elements. Their spectral indices are also listed in Table 1. It is noted that O and Fe spectra are sometimes best fit up to 0.77 MeV n^{-1} , as shown in Figures 3 and 4. The spectral indices of O and Fe vary from 1.49 to 4.56 and from 1.46 to 4.04, respectively. Although the spectral indices for ${}^4\text{He}$, O, and Fe are different from those of other SIR events in general, they are almost equal for SIR 12 and are very close to 1.5 (1.55, 1.49, and 1.46, respectively). This is consistent with the fact that the nature of the flux variations of all three elements in SIR 12 (shown in the right panel of Figure 1) are different (an impulsive increase followed by a gradual decay in the flux) from the nature of the flux variations during other SIR events.

In addition to the 20 SIR events observed by STEREO-A, we also calculate the spectral indices for suprathermal ${}^4\text{He}$ associated with 2 SIR events observed by STEREO-B. Interestingly, SIRs 1 and 2 (see Table 1) were observed by STEREO-B before they were observed by STEREO-A (a list of SIR events observed by both the STEREO spacecraft is available at https://stereo-ssc.nascom.nasa.gov/data/ins_data/impact/level3/). Figures 5(a) and 5(b) show the positions of STEREO-A and STEREO-B with respect to the Earth on 2007 September 20 and 2007 October 24, respectively. Figures 6(a) and (e) show ${}^4\text{He}$ flux variations corresponding to SIR 1 (STEREO-A; started on 2007 September 21, 13:37) and SIR 1 (STEREO-B; started on 2007 September 19, 18:15), respectively. The corresponding ${}^4\text{He}$

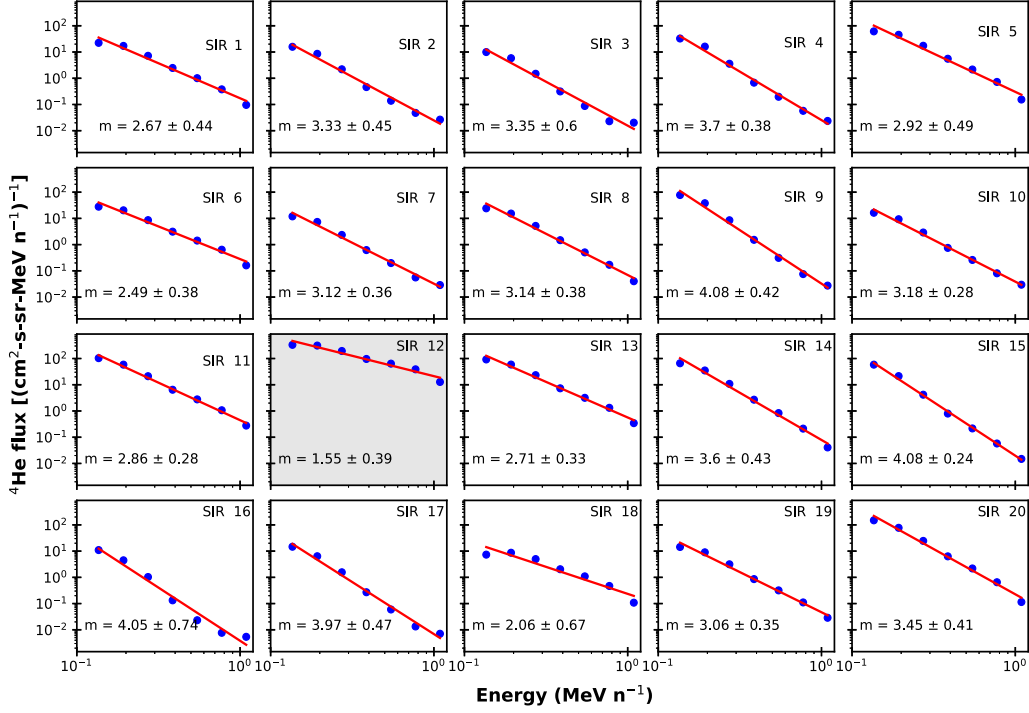


Figure 2. Differential directional flux vs. energy spectra of ${}^4\text{He}$ during flux enhancements associated with SIRs 1–20. Each panel corresponds to the SIR event written in the upper right corner of the panel. The spectral indices (m) along with the MoEs within the 95% confidence bounds as errors are written in the bottom left corner of each panel. It is noted that the spectral indices of ${}^4\text{He}$ vary from 1.55 to 4.08. SIR 12 is overplotted on a gray background because the spectral index for this event is 1.55 and is distinctly lower than in the remaining events.

spectra are shown in Figures 6(b) and (f). The spectral indices for ${}^4\text{He}$ observed by STEREO-A and STEREO-B are 2.67 and 2.69, respectively. Figures 6(c) and (g) show ${}^4\text{He}$ flux variations during another pair of SIR events observed by STEREO-A and STEREO-B. This time, the spectral indices are 3.33 and 2.94 as observed by STEREO-A and STEREO-B, respectively. This exercise shows that the spectral index of SIR-associated ${}^4\text{He}$ observed by closely spaced spacecraft may also vary. We discuss all these aspects in the next section.

5. Discussions and Conclusions

In this work, it is shown that the fluxes of all suprathermal elements (e.g., ${}^4\text{He}$, O, and Fe) with similar energies per nucleon may not be enhanced during an SIR event. One of the probable reasons for this could be the lack of seed populations in the IP medium that are subjected to acceleration (or deceleration) and eventually become part of the suprathermal pool of particles. Another possibility may be linked to the efficacy of the generation mechanism of suprathermal ions in the IP medium. Ebert et al. (2012) showed that the peak intensity of the $<0.8 \text{ MeV n}^{-1}$ ${}^4\text{He}$ population is correlated with the local magnetic compression ratios (M , defined as the ratio of the downstream and upstream magnetic fields) at 1 au even in the absence of reverse shocks. The correlation between the local compression ratio strength and $\sim 1 \text{ MeV n}^{-1}$ proton intensities at 5 au was established by Desai et al. (1998). Therefore, it appears that the local compression ratio strength plays an important role in shaping the intensity variations of the $<1 \text{ MeV n}^{-1}$ suprathermal particles. However, the critical value of the compression ratio strength required to raise

suprathermal fluxes above the background level is not clear from these studies.

It is brought out from the spectral analysis of the ${}^4\text{He}$, O, and Fe fluxes that there are wide variations in the spectral indices of these elements in different shock-less SIR events. The spectral indices lie in the range 1.55–4.08 and 1.49–4.56 and from 1.46–4.04 for ${}^4\text{He}$, O, and Fe, respectively. Mason et al. (2008b) and Allen et al. (2021) also reported spectral indices in a similar range in the energy range $0.16\text{--}0.91 \text{ MeV n}^{-1}$ for CIR-associated ${}^4\text{He}$ measured by the Ultra-Low Energy Isotope Spectrometer (ULEIS) on board the Advanced Composition Explorer (ACE) and the Suprathermal Ion Spectrograph (SIS) on board Solar Orbiter. Some of the SIR/CIR events investigated in Mason et al. (2008b) are associated with shocks. Even though there are no well-formed shocks at 1 au, the acceleration of particles is still possible in gradual compression regions associated with SIR/CIRs (Giacalone et al. 2002). Filwett et al. (2019) also reported variations in the spectral indices of suprathermal particles in different SIR events. It is worth noting that suprathermal heavy ions (e.g., O and Fe) associated with IP shocks also show spectral indices that vary from 1.00 to 4.00 (Desai et al. 2004) in the energy range of $0.1\text{--}0.5 \text{ MeV n}^{-1}$. Therefore, wide variations in the spectral indices of suprathermal particles below 1 MeV n^{-1} seem to be a common feature in case of stochastically accelerated particles.

In order to check the spatial variation in the spectral index of suprathermal particles associated with SIR events, we compare the spectra of ${}^4\text{He}$ corresponding to two SIR events (SIRs 1 and 2 in Table 1) that were observed first by STEREO-B and then by STEREO-A when these satellites were very close (around

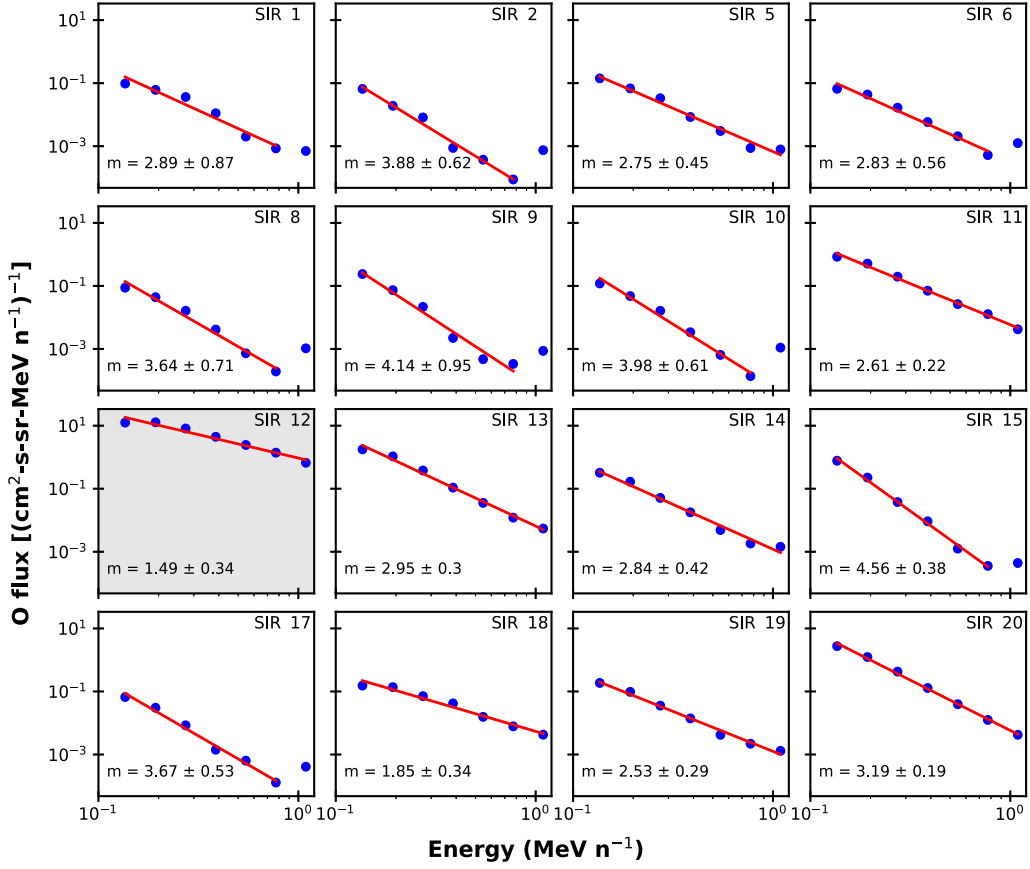


Figure 3. Spectra of O during the enhancements in the SIR events mentioned in the upper right corner of each panel. The spectral indices (m) and MoEs are written in the bottom left corner of all the boxes. The spectral indices here vary from 1.49 to 4.56. Similar to Figure 2, SIR 12 is overplotted on gray background because the spectral index is 1.49 in this event, which is distinctly lower than in the remaining events.

84 Gm) to each other. Despite the proximity of STEREO-A and STEREO-B, these satellites recorded differences in solar wind parameters (e.g., in the magnetic field, the maximum proton density, and in the extreme solar wind speeds across the SIRs) in both events. Interestingly, we find that in the first SIR event that was first observed by STEREO-B and then by STEREO-A, the spectral indices of ^4He are almost equal (STEREO-A: 2.67 and STEREO-B: 2.69). On the other hand, the spectral indices for ^4He observed by STEREO-B and STEREO-A differ (STEREO-A: 3.33 and STEREO-B: 2.94) for the second SIR event. By further investigation, we find that the second SIR event observed by STEREO-B (Figure 6) followed an interplanetary coronal mass ejection (ICME; the list of ICMEs can be found at https://stereo-ssc.nascom.nasa.gov/data/ins_data/impact/level3/), while STEREO-A did not observe any ICME. This suggests that the spectral index of suprathermal particles associated with SIRs may differ if the suprathermal particle population contains particles from more than one source. This hypothesis is supported by Schwadron et al. (2010), who argued that the time-averaged spectra of particles are essentially a superposition of many distribution functions related to different solar wind conditions, such as temperature and density. In other words, because SIRs acquire remnant particles from different events (e.g., particles from an ICME in the second SIR event observed by STEREO-B) from different

parts of the IP medium, during the course of their evolution, it is possible that many processes are at play in modulating suprathermal particle spectra.

It is to be noted from Table 1 that we see differences in the spectral indices for different elements corresponding to 19 SIR events, except for SIR 12. Nonuniform spectral indices for different elements corresponding to a particular SIR event have been reported earlier (Filwett et al. 2019). Mason et al. (2008b) reported that the ^4He and O spectral indices in the energy range 0.16–0.91 MeV n^{-1} are extremely well correlated and that the average spectral index of O is 1.03 times that of ^4He . However, this is not the case in our investigation. We find that the spectra of ^4He are harder in 50% of the SIR events when we see enhancements in the O fluxes (see Columns 4 and 5 of Table 1). The spectral index of Fe does not match the spectral index of other elements either. In terms of the FIP, O (~ 13.6 eV) lies in between Fe (~ 7.9 eV) and ^4He (~ 24.6 eV). These elements also differ in m/q . Therefore, it appears that the source and generation mechanisms involved in producing the suprathermal particles associated with most of the shock-less SIR events at 1 au might be dependent on the FIP and m/q values.

According to these arguments, SIR 12 stands out as an anomalous and special case. Even though it has a different FIP and m/q , the suprathermal ^4He , O, and Fe exhibit a nearly identical spectral index (close to 1.5) in SIR 12. In a series of

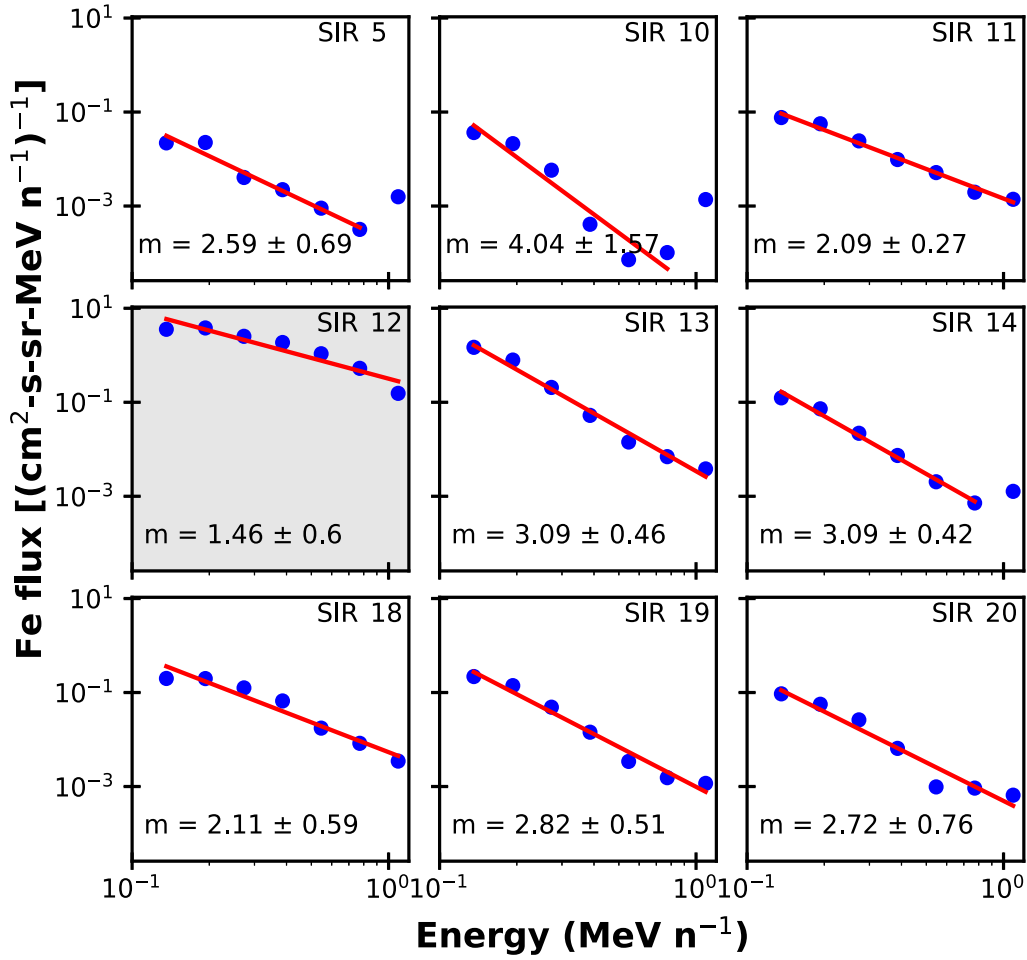


Figure 4. Spectra of Fe during the enhancements in the SIR events mentioned in the upper right corner of each panel. The spectral indices (m) and MoEs are written in the bottom left corner of all the boxes. In the case of Fe, the spectral indices vary from 1.46 to 4.04. Similar to Figures 2 and 3, SIR 12 is also overplotted on gray background to highlight the distinctly lower spectral index (1.46) as compared to the remaining events.

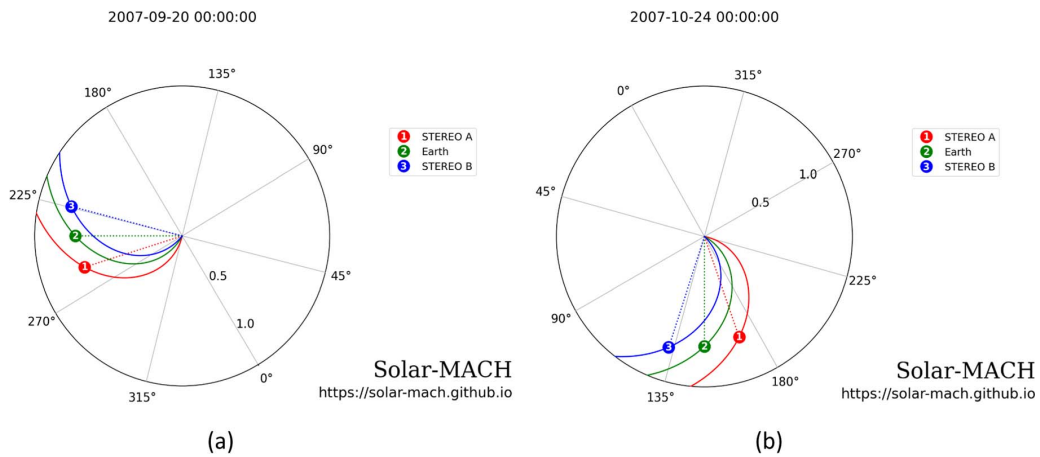


Figure 5. Relative positions of (1) STEREO-A (red), (2) the Earth (green), and (3) STEREO-B (blue) on (a) 2007 September 20 at 00:00 hour and (b) 2007 October 24 at 00:00 hour. The solid colored lines are Parker spirals connecting these objects and are calculated based on a solar wind speed of 400 km s^{-1} . This figure is generated using Solar-MACH software (Gieseler et al. 2023) based on the inputs provided [URL: <https://solar-mach.streamlit.app/?embedded=true>].

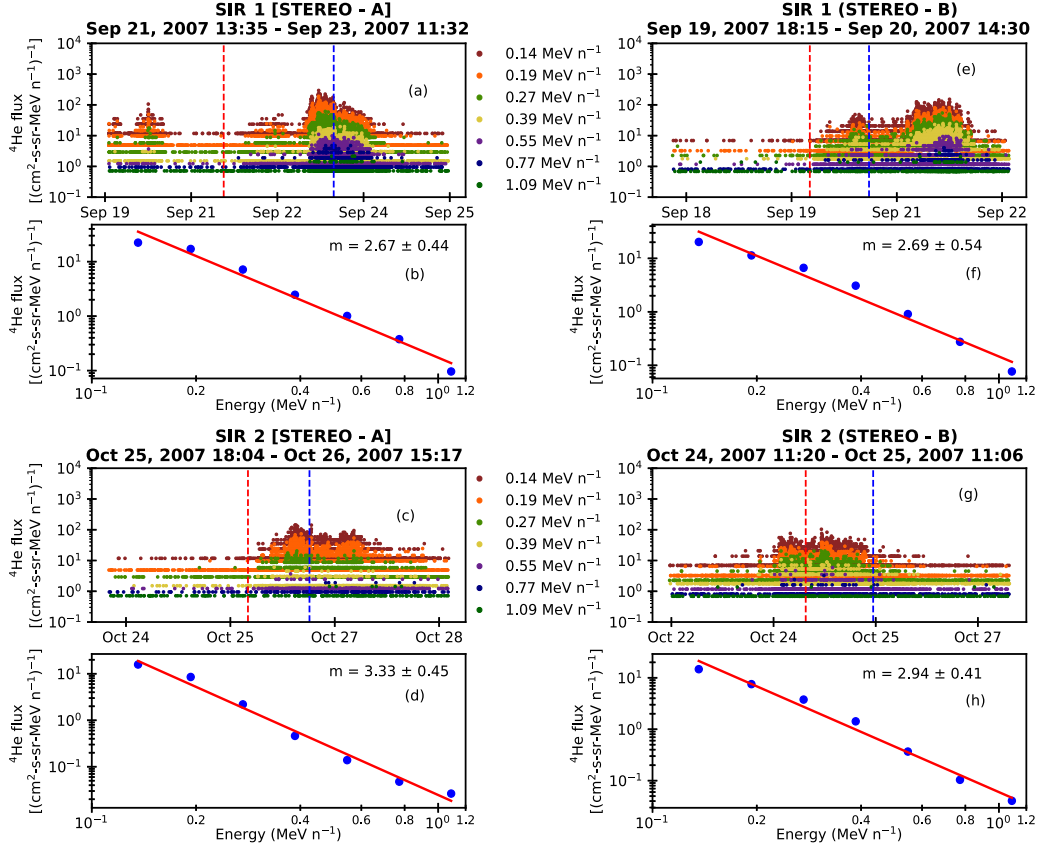


Figure 6. Temporal variations of the ${}^4\text{He}$ fluxes at different energies (mentioned in between) measured in panels (a) and (c) by STEREO-A and in panels (e) and (g) by STEREO-B, corresponding to two pairs of SIR events (SIR 1; STEREO-A and STEREO-B) and SIR 2; STEREO-A and STEREO-B) observed by these two spacecraft when they were very close to each other. The spectra of ${}^4\text{He}$ during the enhanced periods associated with SIR 1 (STEREO-A and STEREO-B) and SIR 2 (STEREO-A and STEREO-B) are shown in panels (b) and (f) and panels (d) and (h), respectively. The spectral indices (m) with MoEs are also mentioned.

papers, Fisk & Gloeckler (2006, 2008, 2014) argued that compressional turbulences could accelerate particles when in steady state, these particles do equal the amount of work on the turbulences. The source of free energy in this process is the pressure variation in the core particles. This free energy flows upward in energy through suprathermal tails (energy cascading) that exhibit a power-law index of 1.5 (see Fisk & Gloeckler 2006 for more details). However, this condition is evidently not satisfied for suprathermal particles associated with the other SIR events that were investigated in this work. Mason et al. (2008b) and Filwett et al. (2019) did not find any clustering of the spectral indices near 1.5. Most interestingly, the pump mechanism introduced by Fisk & Gloeckler (2008) that they claimed is responsible for the 1.5 spectral index is valid only for the quiet solar wind, that is, it is devoid of any shocks or large-scale compression regions. Because we observe a spectral index very close to 1.5 in the ${}^4\text{He}$, O, and Fe spectra in connection with an SIR event (SIR 12), we can rule out the role of the pump mechanism in this case. In the following part, we explore some other possibilities for the 1.5 spectral index for different species.

In order to investigate SIR 12, we show Figure 7. This figure shows the images of the solar corona in 19.5 nm (extreme-ultraviolet) light observed by the Sun-Earth Connection Coronal and Heliospheric Investigation (SECCHI) instrument

on board STEREO-A on 2012 June 12 at around (a) 04:55 UT and (b) 05:05 UT. One can see from Figure 7 that a large coronal hole was present around this time. The hole extends from the northeast to the southwest mid-latitudes of the Sun and encompasses the equatorial region as well. The locations of STEREO-A, the Earth, and STEREO-B around the same time are shown in Figure 8. During this time, the Carrington longitudes of the Earth and STEREO-A were 127.2 and 244.6, respectively. Therefore, this coronal hole was not visible from the Earth or from STEREO-B. It is possible that SIR 12 (starts on 2012 June 12 at 04:00 UT) is generated by the fast solar wind stream emanating from this large coronal hole. Interestingly, the SECCHI images also reveal the onset of a flare at 05:05 UT. The location of the flaring region was at the edge of this coronal hole (marked by “2” in Figure 7). Chertok et al. (2015) identified this flare event as an M4.6 class flare by analyzing the length of the blooming streak associated with this flare. As can be seen from Figure 8, the magnetic field line connecting the flare location (S15W126, from Chertok et al. 2015) propagates very closely to STEREO-A. Therefore, it is possible that the sharp enhancements in the suprathermal ${}^4\text{He}$, O, and Fe fluxes occur due to an impulsive solar energetic particle (ISEP) event associated with the solar flare, as shown in Figure 7. Mason et al. (2000, 2002) showed by using data obtained from ULEIS and the Solar Isotope Spectrometer (SIS)

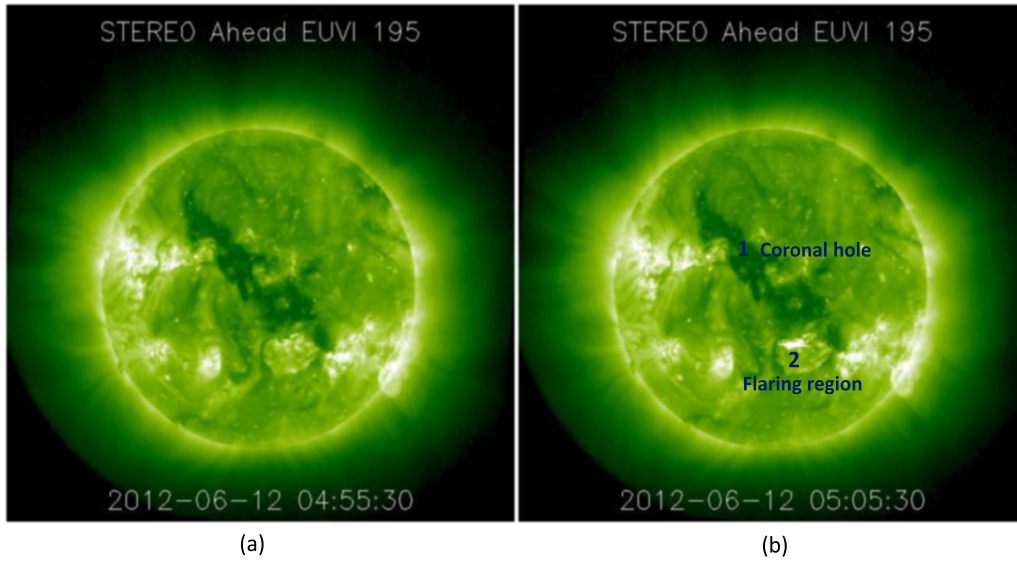


Figure 7. Solar corona observed in 19.5 nm by the EUVI of the SECCHI instrument (e.g., Wülser et al. 2004) on board STEREO-A at (a) 04:55:30 UT and (b) 05:05:30 UT on 2012 June 12. The dark region (1) represents a coronal hole. The bright region (just above the number 2) is a flaring region. The location of this flare region is S15W126 (Chertok et al. 2015).

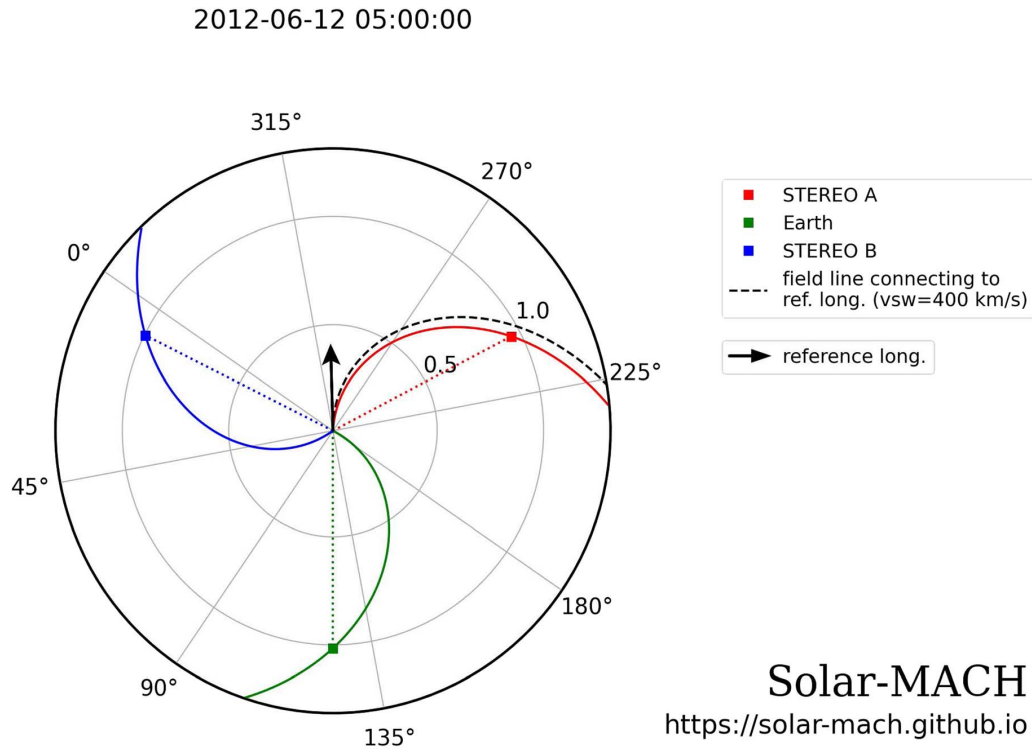


Figure 8. Positions of STEREO-A (red), the Earth (green), and STEREO-B (blue) on 2012 June 12 at 05:00 UT. The solid colored spirals connecting these three objects to the Sun are calculated based on a solar wind speed of 400 km s^{-1} . The solid arrow represents the location and direction of the solar flare mentioned in Figure 7. The dashed spiral (black) is the magnetic field line originating from the flare location. This figure indicates that it is possible that STEREO-A was magnetically connected to the flaring region when SIR 12 passed through it. Note that during this time, the Carrington longitudes of the Earth and STEREO-A were 127.2 and 244.6, respectively.

on board the ACE spacecraft that a particular class of ^3He -rich ISEP events exhibit power laws in the heavy ion spectra (e.g., ^3He , ^4He , O, and Fe) in the energy range $0.1\text{--}1.0 \text{ MeV n}^{-1}$.

Mason et al. (2002) reported an ISEP event observed by the ACE on 1998 September 9 where $<1.5 \text{ MeV n}^{-1}$ ^3He , ^4He , O, and Fe exhibit similar variations in their spectra, and the

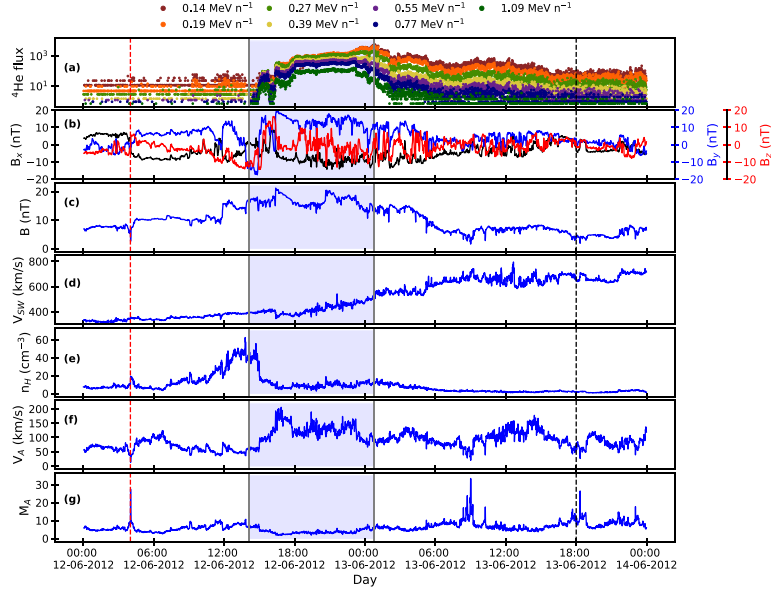


Figure 9. Variations in (a) ${}^4\text{He}$ fluxes corresponding to different energy channels, (b) the components (B_x , B_y , and B_z) of the IMF in the RTN coordinate system, (c) the magnitude of the magnetic field (B), (d) the bulk solar wind speed (V_{sw}), (e) the proton number density (n_H), (f) the Alfvén speed (V_A), and (g) the Alfvénic Mach number (M_A) during SIR 12. The dashed red and black lines indicate the start and end time of the SIR, as mentioned in Figure 1 and Table 1. The interval between the start of the ${}^4\text{He}$ flux enhancement and the time of the peak 0.14 MeV n^{-1} flux is shaded.

spectral indices lie in the range 1.15–1.38. Although the role of the solar flare-associated ISEP event looks promising in producing an identical spectral index, counterevidence exists in the literature. The typical time delay between the flare onset (measured by GOES X-ray fluxes) and an ISEP detection closure to the Earth is about 1 hr (e.g., Papaioannou et al. 2023). In the case of SIR 12, this delay is about 9 hr. Even in some ISEP events, the dispersionless enhancement of different energy channels is not guaranteed (see Mason et al. 2000). This essentially means that the enhancement of any particle (e.g., ${}^4\text{He}$) with a higher energy (e.g., 1 MeV n^{-1}) starts earlier than for a particle with lower energy (e.g., 0.5 MeV n^{-1}). When we assume a nominal Parker-spiral path length of 1.2 au between the flaring region shown in Figure 7 and the location of STEREO-A, the time delay between a 0.5 MeV n^{-1} and a 1 MeV n^{-1} particle (for any particle, because the energy unit is normalized by the mass number) is calculated to be more than an hour. However, we do not find any noticeable time delay in the ${}^4\text{He}$ flux enhancements corresponding to 0.55 MeV n^{-1} and 1.09 MeV n^{-1} in SIR 12. Therefore, the flux enhancements observed in SIR 12 do not appear to come directly from the flaring region. There may be another process at play in the IP medium that causes an insignificant time delay and the identical spectral index of three different elements with different FIP and m/q .

In this context, we believe that a more suitable mechanism that can explain this event would be acceleration of particles by merging and contraction of small-scale magnetic islands (SMIs; Drake et al. 2006a, 2006b; Cargill et al. 2006; Bian & Kontar 2013; Zank et al. 2014; Khabarova et al. 2015a; Le Roux et al. 2015, etc.). These SMIs can be induced in the vicinity of a heliospheric current sheet (Bemporad 2008; Cartwright & Moldwin 2008; Khabarova et al. 2015a, 2015b, 2016, etc.) by different active processes in the solar corona (e.g., a solar flare or CMEs) or by various instabilities in the current sheets (Eastwood et al. 2002;

Drake et al. 2006a). The typical length scale of such SMIs is 10^6 – 10^7 km (Khabarova et al. 2015a). Zank et al. (2014) showed analytically that particles accelerated due to merging and contraction of magnetic islands exhibit a power law, and the spectral indices depend on the Alfvénic Mach (M_A) number, which is independent of the m/q of the particles. At 1 au, a particular case of this theory ($M_A = 7$) predicts a velocity distribution spectrum that varies with V^{-5} (V is the particle speed), which is equivalent to a differential directional flux spectrum $\sim E^{-1.5}$ (E is the energy of the particle). To check the applicability of the theory of Zank et al. in our observation of the 1.5 spectral indices, we show Figures 9 and 10. In Figure 9, we plot (a) ${}^4\text{He}$ fluxes corresponding to different energy channels, (b) the components (B_x , B_y , and B_z) of the interplanetary magnetic field (IMF) in the RTN coordinate system, (c) the magnitude of magnetic field (B), (d) the bulk solar wind speed (V_{sw}), (e) the proton number density (n_H), (f) the Alfvén speed (V_A), and (g) the Alfvénic Mach number (M_A) during SIR 12. It can be seen from Figure 9 (g) that M_A varies in the range 5–10 several hours before the start of the ${}^4\text{He}$ flux enhancements. This is consistent with the hypothesis of Zank et al. (2014). More importantly, the very presence of magnetic islands is established from the hodograms (e.g., Khabarova et al. 2015a) shown in Figures 10(a) and (b), where rotation in the interplanetary magnetic field inside the magnetic islands (shaded interval in Figure 9) is evident. This type of rotation is not observed in other SIR events. We also calculate the typical length scale (l) by using Eq. 2 in Khabarova et al. (2015b), which reads $l = r \times (B/B_0)^{1/2}$ km, where r is distance in au, and $B = B(r)$ is the magnetic field, $B_0 = 10,000$ nT is the minimum coronal magnetic field provided by Jensen & Russell (2009). By taking the typical value of $B = 15$ nT inside the shaded region in Figure 9, we obtain $l \sim 6 \times 10^6$ km at 1 au.

Therefore, it appears that the identical spectral indices (very close to 1.5) for ${}^4\text{He}$, O, and Fe associated with SIR 12 are caused by local acceleration of these particles by the SMIs that

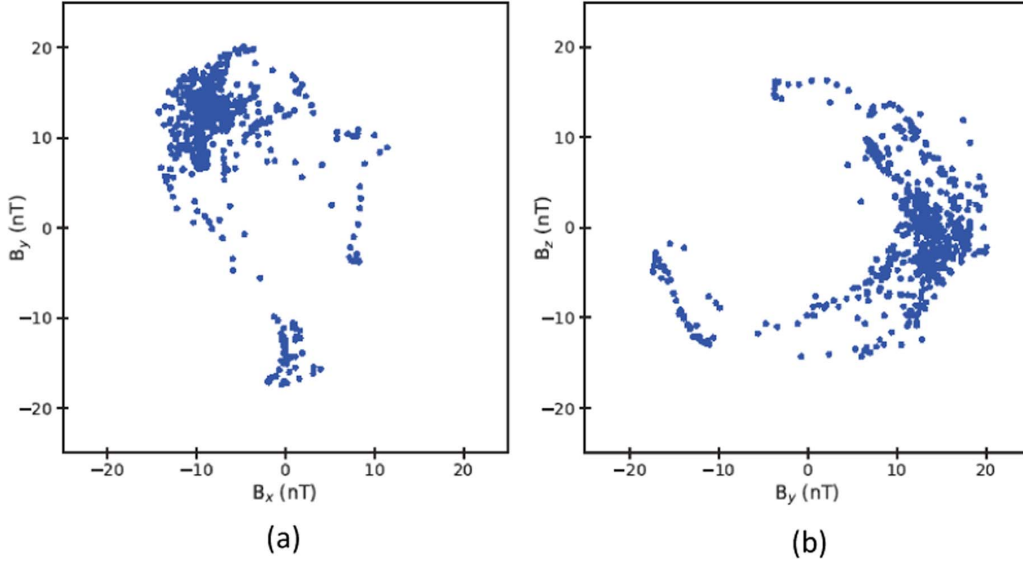


Figure 10. Hodograms of the IMF (a) B_x - B_y and (b) B_y - B_z during the shaded interval, as shown in Figure 9. The rotation in the magnetic field components establishes the existence of magnetic islands during this interval.

are generated by the flare (shown in Figure 7). The local acceleration of particles also supports the minimal modulation (no significant changes in the spectral indices) of these particles before they were detected by STEREO-A along with the characteristics of the source process.

6. Summary

This study investigated 20 SIR events observed by the STEREO-A spacecraft to better understand the energization process of suprathermal particles, especially those that are not linked to shocks. We analyze the differential directional flux of three distinct species (^4He , O, and Fe) in energy ranges from 0.14 to 1.09 MeV per nucleon and calculate their respective spectral indices for each event. Most of our events show significant variations in the spectral indices for each of the three species. Additionally, we observe that the spectral index for each species varies over a wide range: ^4He has a range of 1.55–4.08, O showed variability between 1.49 and 4.56, and Fe ranged from 1.46 to 4.04. We ascribe these spectral index variations to the stochastic nature of their origins and to interplanetary modulation, which depends on the m/q ratio.

In one of the 20 events, which we refer to as SIR 12, we observe that the spectral indices for all three species remain close to 1.5. We found that this event is associated with an M4.6 class solar flare that occurred approximately nine hours before the observed flux enhancement, and this connection is traced along the Parker spiral. Further investigation of this event revealed that during this period, the magnetic field rotated in the $y-z$ plane, perpendicular to the equatorial plane ($x-y$ plane). Additionally, we note that the solar wind Alfvénic Mach number (M_A) prior to the event remained within the range of 7–10. Taking all of these pieces of information into account, we conclude that the suprathermal population is generated locally through the merging and contraction of SIMs, which may have formed as a result of the flare and which are situated both above and below the heliospheric current sheet. For this particular case, we calculate

the size of the typical small-scale magnetic islands to be $\sim 6 \times 10^6$ km.

Acknowledgments

We are grateful to the principal investigators and all the members of the SIT, PLASTIC, and MAG (on board STEREO-A) team for constructing these instruments and for thereafter generating and managing the data sets used in this work. We thank Mihir I. Desai, Janet Luhmann, Peter Schroeder, and Glenn M. Mason for clarifying certain aspects of the SIT data used in this paper. We express our sincere gratitude to the Department of Space, Government of India, for supporting this work.

Data Availability

The list of SIR events used in this work is available at <https://stereo-dev.epss.ucla.edu/media/SIRs.pdf>. The suprathermal flux data are obtained from the SIT/IMPACT, the in situ data from PLASTIC/IMPACT, and the magnetic field data from MAG/IMPACT on board the STEREO-A are available at <https://cdaweb.gsfc.nasa.gov/index.html>. The IP shock list observed by the STEREO-A is available at <http://www.ipshocks.fi/database>. The EUVI/SECCHI images are available at <https://cdaw.gsfc.nasa.gov/>.

ORCID iDs

Bijoy Dalal <https://orcid.org/0000-0001-8993-9118>
 Dibyendu Chakrabarty <https://orcid.org/0000-0003-2693-5325>
 Nandita Srivastava <https://orcid.org/0000-0002-0452-5838>
 Avek Sarkar <https://orcid.org/0000-0002-4781-5798>

References

- Acuña, M., Curtis, D., Scheifele, J., et al. 2008, *SSRv*, 136, 203
 Agresti, A., & Coull, B. A. 1998, *The American Statistician*, 52, 119
 Allen, R. C., Ho, G. C., & Mason, G. M. 2019, *ApJL*, 883, L10

- Allen, R. C., Mason, G. M., Ho, G. C., et al. 2021, *A&A*, **656**, L2
- Belcher, J., & Davis, L., Jr 1971, *JGR*, **76**, 3534
- Bemporad, A. 2008, *ApJ*, **689**, 572
- Bian, N. H., & Kontar, E. P. 2013, *PhRvL*, **110**, 151101
- Bučík, R., Mall, U., Korth, A., & Mason, G. 2009, *AnGeo*, **27**, 3677
- Cargill, P. J., Vlahos, L., Turkmani, R., Galsgaard, K., & Isliker, H. 2006, in *Solar Dynamics and Its Effects on the Heliosphere and Earth*, ed. D. N. Baker et al., Vol. 124 (New York: Springer), 249
- Cartwright, M., & Moldwin, M. 2008, *JGRA*, **113**, A09105
- Chertok, I., Belov, A., & Grechnev, V. 2015, *SoPh*, **290**, 1947
- Dalal, B., Chakrabarty, D., & Srivastava, N. 2022, *ApJ*, **938**, 26
- Desai, M., Marsden, R., Sanderson, T., et al. 1998, *JGRA*, **103**, 2003
- Desai, M. I., Mason, G. M., Wiedenbeck, M. E., et al. 2004, *ApJ*, **611**, 1156
- Drake, J., Swisdak, M., Che, H., & Shay, M. 2006a, *Natur*, **443**, 553
- Drake, J., Swisdak, M., Schoeffler, K., Rogers, B., & Kobayashi, S. 2006b, *GeoRL*, **33**, L13105
- Eastwood, J., Balogh, A., Dunlop, M., & Smith, C. 2002, *JGRA*, **107**, 1365
- Ebert, R., Dayeh, M., Desai, M., & Mason, G. 2012, *ApJ*, **749**, 73
- Filwett, R., Desai, M., Ebert, R., & Dayeh, M. 2019, *ApJ*, **876**, 88
- Fisk, L., & Gloeckler, G. 2006, *ApJL*, **640**, L79
- Fisk, L., & Gloeckler, G. 2008, *ApJ*, **686**, 1466
- Fisk, L., & Gloeckler, G. 2014, *JGRA*, **119**, 8733
- Fisk, L., & Lee, M. 1980, *ApJ*, **237**, 620
- Fisk, L. A., & Gloeckler, G. 2007, *PNAS*, **104**, 5749
- Galvin, A. B., Kistler, L. M., Popecki, M. A., et al. 2008, *SSRv*, **136**, 437
- Giacalone, J., Jokipii, J. R., & Kota, J. 2002, *ApJ*, **573**, 845
- Gieseler, J., Dresing, N., Palmroos, C., et al. 2023, *FrASS*, **9**, 1058810
- Gloeckler, G. 2003, in *AIP Conf. Proc. 679, Solar Wind Ten: Proc. of the Tenth International Solar Wind Conf.*, ed. M. Velli, R. Bruno, & F. Malara (Melville, NY: AIP), 583
- Gosling, J., Borrini, G., Asbridge, J., et al. 1981, *JGR*, **86**, 5438
- Jensen, E., & Russell, C. 2009, *GeoRL*, **36**, L05104
- Jian, L., Luhmann, J., Russell, C., & Galvin, A. 2019, *SoPh*, **294**, 1
- Jian, L., Russell, C., Luhmann, J., Galvin, A., & Simunac, K. 2013, in *AIP Conf. Proc. 1539, Solar Wind 13: Proc. of the Thirteenth International Solar Wind Conf.*, ed. G. P. Zank (Melville, NY: AIP), 191
- Jian, L., Russell, C., Luhmann, J., & Skoug, R. 2006, *SoPh*, **239**, 337
- Khabarova, O., Zank, G., Li, G., et al. 2015a, *ApJ*, **808**, 181
- Khabarova, O. V., Zank, G. P., Li, G., et al. 2015b, *JPhCS*, **642**, 012033
- Khabarova, O. V., Zank, G. P., Li, G., et al. 2016, *ApJ*, **827**, 122
- Le Roux, J., Zank, G., Webb, G., & Khabarova, O. 2015, *ApJ*, **801**, 112
- Luhmann, J., Curtis, D., Schroeder, P., et al. 2008, *SSRv*, **136**, 117
- Mason, G., Desai, M., & Li, G. 2012, *ApJL*, **748**, L31
- Mason, G., Dwyer, J., & Mazur, J. 2000, *ApJ*, **545**, L157
- Mason, G., Korth, A., Walpole, P., et al. 2008a, *SSRv*, **136**, 257
- Mason, G. M., Leske, R. A., Desai, M. I., et al. 2008b, *ApJ*, **678**, 1458
- Mason, G. M., Wiedenbeck, M. E., Miller, J. A., et al. 2002, *ApJ*, **574**, 1039
- Papaioannou, A., Herbst, K., Ramm, T., et al. 2023, *A&A*, **671**, A66
- Richardson, I. G. 2018, *LRSF*, **15**, 1
- Schwadron, N. A., Dayeh, M., Desai, M., et al. 2010, *ApJ*, **713**, 1386
- Tsurutani, B., Smith, E., Pyle, K., & Simpson, J. 1982, *JGR*, **87**, 7389
- Wülser, J.-P., Lemen, J. R., Tarbell, T. D., et al. 2004, *Proc. SPIE*, **5171**, 111
- Zank, G. I., Le Roux, J., Webb, G., Dosch, A., & Khabarova, O. 2014, *ApJ*, **797**, 28

